Spectroscopic Studies of Exciton Electronic Structure and Charge Recombination in Solution Processed Semiconductors for Photovoltaics

Mark E. Ziffer

A dissertation

submitted in partial fulfillment of the

requirements for the degree of

Doctor of Philosophy

University of Washington

2018

Reading Committee:

David S. Ginger, Chair

David J. Masiello

Munira Khalil

Program Authorized to Offer Degree:

Chemistry

Abstract

University of Washington

Spectroscopic Studies of Exciton Electronic Structure and Charge Recombination in Solution Processed Semiconductors for Photovoltaics

Mark E. Ziffer

Chair of the Supervisory Committee:

Professor David S. Ginger
Department of Chemistry

Understanding the fundamental photophysical processes that occur in solution processed semiconductors is the key to realizing their full potential in optoelectronic devices and uncovering new design strategies for materials. In this thesis we study the fundamental photophysics of promising classes of solution processed semiconductor systems for photovoltaics: hybrid organic-inorganic perovskites and π-conjugated polymers, along with blends of π-conjugated polymers and small molecules. In hybrid perovskites, we will gain an understanding of the initial photoexcitations that occur upon absorption of light at the semiconductor band edge using electroabsorption spectroscopy. Through detailed analysis of the electric field modulated optical response we will determine the fundamental nature of excitons that form upon band edge photoexcitation, including their binding energy, their ionization under an electric field, and their tendency to scatter into free charge continuum states at room temperature. In π-conjugated polymers, we will study how chemical interactions in the solid state dictate the electronic properties of excitons that form upon photoexcitation. We will use a variety of spectroscopic techniques to gain a deep understanding of the through-bond (intrachain) and through-space (interchain) chromophore interactions that dictate how excitons delocalize in aggregates of polymers with different chemical structure. Finally, in blends of π-conjugated polymers and small

molecules, we will use time resolved spectroscopy methods to study the pathways that photogenerated charges take to recombine to the ground state. We will find that radiative recombination pathways can be accessed by photogenerated free charges in an efficient photovoltaic blend, which has largely been overlooked in the field of organic photovoltaics and is likely a key to improving the design of more efficient materials systems. We hope that the conclusions drawn from the studies provided in this thesis will help contribute to the fundamental understanding of the photophysics in these important emerging photovoltaic systems, and hopefully, provide inspiration for new avenues of investigation.

Table of Contents

List of Figures

Figure 3.4 ***a.)*** Normalized photoluminescence spectra (solid lines) and absorption spectra (dashed lines) of P1 and P2 at 295 K. The 0-0 and 0-1 emission peaks are labeled for clarity, along with the energy of the relative peak shifts between P1 and P2. ***b.)*** and ***c.)*** Temperature dependent photoluminescence spectra of P1 and P2 normalized to the 0-1 peak in order to compare the 0-0/0-1 ratio as a function of temperature. Vibronic emission peaks are labeled for clarity. ***d.)*** Redshift of the A1 absorption peak of P2 (see SI section S2), 0-0 emission peak of P2, and 0-1 emission peak of P2 as a function of decreasing temperature. The redshift is shown with respect to the energy of the peak of the 0-0, 0-1, or A1 transition at 295 K.

Figure 3.5 ***a.)*** and ***b.)*** Electroabsorption spectra of P1 and P2 measured at the second harmonic of the fundamental modulation frequency for a series of applied field strengths, normalized to the maximum peak amplitude of the spectrum. ***c.)*** and ***d.)*** EA data measured at 16 MV/m for P1 and P2 fit to Eq 1. using transfer matrix modelling (see SI section S4) to extract values for $\Delta\alpha_{g\rightarrow e}$.

Figure 4.1 ***a.)*** Chemical structures of PCE10 and FIDTT-2PDI. ***b.)*** TD-DFT calculation results of natural transition orbitals and the side-view of molecular geometry. ***c.)*** UV-vis absorption spectrum of thin films of PCE10, FIDTT-2PDI, and a 1:1 PCE10:FIDTT-2PDI blend. The energy level diagram of the molecules estimated by ultraviolet photoemission spectroscopy and optical absorption. Dotted line in ***c.)*** corresponds to AM1.5 global standard solar spectrum (ASTMG173).

Figure 4.2 ***a.)*** EQE_{PV} spectrum of a 1:1 PCE10:FIDTT-2PDI device (*inset:* EQE_{EL} of a 1:1 PCE10:FIDTT-2PDI device displayed as a function of injected current density near 1 sun injection conditions). ***b.)*** Photovoltaic performance of a device based on 1:1 PCE10:FIDTT-2PDI blend measured under AM1.5 illumination. ***c.)*** EQE_{PV} spectrum of 1:1 PCE10:FIDTT-2PDI measured using sensitive lock-in techniques to resolve the sub-bandgap absorption tail shown with the normalized electroluminescence spectrum. The blue line shows the EQE_{PV} tail recreated from the EL spectrum and blackbody radiation spectrum, demonstrating the reciprocity relationship between the sub-gap EQE_{PV} and EL spectrum.

Figure 4.3 ***a.)*** Time-resolved photoluminescence (PL) decays of neat PCE10 and 1:1 PCE10:FIDTT-2PDI following selective excitation of PCE10 at 735 nm (1.69 eV). The PCE10:FIDTT-2PDI blend exhibits a delayed luminescence tail extending beyond the 50 ns time window, (*inset:* early time (0-3 ns) time-resolved PL decay of PCE10 and PCE10:FIDTT-2PDI, showing fast initial quenching of the PCE10:FIDTT-2PDI luminescence). ***b.)*** time-resolved PL decay of 1:1 PCE10:FIDTT-2PDI extended into the microsecond time window, showing that the time-resolved PL tail lasts out to hundreds of nanoseconds and demonstrates fluence dependent kinetics characteristic of non-first order recombination. ***c.)*** Time-integrated spectra from the time-resolved PL measurements showing that the emission redshifts during the long-time tail of the PL decay (20-180 ns) compared to the early time spectrum (0-20ns). The steady-state PL spectrum of neat PCE10 and the EL spectrum of 1:1 PCE10:FIDTT-2PDI are shown overlaid on the 0-20ns and 20-180s spectra respectively, suggesting that while the early time PL intensity comes from unquenched PCE10, the recombination during the long-time tail is characterized by radiative emission from photogenerated charges. We note that the EL spectrum presented here is from the same data as Fig. 4.2 c. but is smoothed by a low-pass filter (see SI section S5 for details).

Figure 4.4 ***a.)*** Fluence dependent photoinduced absorption decay of the polaron spectral feature from transient absorption (TA) spectroscopy. Global fits based on the model in *b.)* are shown as black dashed lines. ***b.)*** Schematic of the bimolecular decay model used to globally fit the photoluminescence (PL) and TA data ***c.)*** fluence dependent delayed time-resolved PL data globally fit to the model in *b.)* using the bi-molecular charge recombination rate determined from fitting the fluence dependent TA data.

Figure 4.5 ***a.)*** 2D grazing-incidence X-ray diffraction patterns of neat and blend films at optimized conditions and ***b.)*** their 1D line-cuts in out-of-plane (solid lines) and in-plane (dotted lines) directions. ***c.)*** Thickness normalized and Lorentz-corrected resonant soft X-ray scattering profiles acquired at 283.4 eV. Unfused version of FIDTT-2PDI is included for comparison, which has similar long periods with lower domain purity. ***d.)*** Subgap EQE_{PV} spectra and ***e***.) EQE_{EL} with respect to applied voltage for neat and blend films Dotted lines in *d*. demonstrates an Urbach energy of 28 meV.

Dedication

I would like to dedicate this thesis with love in memory of Dr. Roberto Serruya, whose mentorship, love and support have helped me believe in myself through some of the most difficult times in my life. His loving ability to truly see the best in people will live on through all of those whose lives he touched.

Acknowledgments

I would like to acknowledge the many mentors throughout my life who have helped me to find and encouraged my passion for learning and scientific knowledge which has led me to accomplish the work presented in this thesis.

First, I would like to thank the foremost mentors in my life, my parents Robert and Regina Ziffer, whose unconditional love for me and support for my passions has allowed me to experience many wonderful learning opportunities in life that, at this moment, have culminated in the completion of my PhD. I will always being lovingly thankful for their support of me even in my worst times. I would also like to thank my sister Emily, whose love and visits to me in Seattle have meant so much to me through my years here, and who always has been and will be one of the closest people in my life.

I would also like to thank the mentors in my life who have inspired my scientifically. I found my first interest and passion for science from my godfather Dr. Mijail Serruya, who I always admired like a hero when I was young because of the amazing research he accomplished as a neuroscientist. It was his work and passion for his research that I saw growing up that inspired me to begin taking science classes at Colby College as an undergraduate, hoping to go the same route where I also planned to major in biology or biochemistry and pursue neuroscience research. However, it was my first organic chemistry class that I took at Colby that truly sparked a passion for learning that I had not quite experienced before, and which led me to choose a major in chemistry instead. I would like to acknowledge my mentors from Colby, in particular Prof. Rebecca Conry and Prof. Thomas Shattuck, who truly fostered my interest and passion in learning about chemistry and experiencing research first hand. Prof. Shattuck's physical chemistry class opened up a new side of me that sparked my obsession and fascination with understanding fundamental physics and aspects of physical chemistry. I would also like to thank my mentors at Argonne National Laboratory, Dr. Huiming Wu specifically, but many other people who I interacted with every day. My experience there showed me that my fundamental interests in science could also have the potential to make major impacts on technology and society, and cemented my decision to pursue a PhD.

Now to acknowledge my mentors from my PhD, the amount that my PhD advisor David Ginger has given me, in terms of support, personal growth as a scientist, and inspiration to accomplish truly great things scientifically, is not something that I can put into a reasonable number of words. David's mentorship has changed my life and changed me as a person and helped me become the kind of scientist I very honestly never dreamed I was capable of becoming. I cannot thank him enough for the gift of growth that he has given me as a scientist, and if I ever have a successful career as a scientist in the future much of that will be indebted to what I learned from him. I would also like to thank the other faculty mentors at UW who have helped me grow as a scientist, specifically Prof. David Masiello, Prof. Munira Khalil, and Prof. Bruce Robinson. I have learned so much from them that I will take with me throughout my career and I appreciate their mentorship and encouragement throughout my PhD.

Finally, I would also like to thank the many wonderful friends who I have made during my years in the Ginger lab who have made my life here very special and memorable. There have been so many people who I have formed deep and special friendships with in this group. At the risk of leaving anybody out I will not mention names specifically, but just thank those people who have meant so much to me over the years during the PhD process, and who have truly brought joy to my life and made me excited to come to work every day even during difficult times. I cannot thank you enough and I hope we will always keep in touch.

I would also like to acknowledge Kathryn Guye for sacrificing her time to help me to format and arrange this thesis during the days leading up to the end of my PhD, which have been some of the most stressful in my life, and which made it possible for me to submit this thesis on time! I truly appreciate her support and help with his, along with the support of so many of my other colleagues.

Chapter 1: Introduction

Solution processable semiconductors offer one of the most exciting areas of research for chemists, physicists, materials scientists, and engineers due to the potential breakthrough technological applications and fundamental scientific questions that these systems pose. The potential technological applications of solution processable semiconductors are myriad, and could arguably be said to have potential in nearly every area of modern electronics that rely on the functionality of semiconductors. This thesis will primarily focus on the properties of solution processed semiconductors as they relate to optoelectronic technologies – devices whose main function is to convert photonic energy into electrical energy, and vice versa. Examples of these devices, in particular ones in which solution processed semiconductors have already had a commercial technological impact or are show great promise for commercial applications, include flexible circuits and bio-compatible/biomimetic electronics,[1-3] light emitting diodes for display technologies,[4-5] and low-cost photovoltaic devices for solar energy conversion.[6-9]

This thesis will primarily focus on the study of solution processable semiconductors that are relevant as absorber materials for solar energy applications. The primary function of a solar cell absorber material is to efficiently convert the energy of photons from the sun (by absorption of light primarily covering the visible to near-IR regions of the electromagnetic spectrum) into electrical charges that can be extracted from a device with minimal loss of energy and deliver the highest available power to an electrical load. While one could draw a simple circuit diagram for a device that would accomplish this task, in reality the processes of charge generation, energy loss prior to extraction, and recombination that affects the maximum power output, are all complicated microscopic physical processes that can occur inside the semiconductor absorber material itself. A full understanding of how to design a material that can optimize the aforementioned processes requires a deep knowledge of photophysical events that occur inside the absorber material on time scales spanning nearly twelve orders of magnitude, from the coherent properties of the electronic states that are accessed during the initial photon absorption event itself,[10-11] to the ultrafast transfer of electronic excitation energy and generation of charge,[12-13] to the energy loss during charge transport[14] and subsequent recombination of charge.[15-16] Therefore, various forms of time resolved, steady state and non-linear optical spectroscopies are the tools of choice to deeply understand the fundamental properties of a photovoltaic absorber material that govern its working mechanism in a device.

The work included in this thesis will study two of the most currently relevant materials systems for solution processable semiconductors for solar cells, namely organic-inorganic hybrid perovskites and π-conjugated semiconducting polymers (along with blends of π-conjugated polymers and small molecules). The scientific areas addressed will comprise two of the photophysical aspects mentioned in the discussion above, namely (1) the nature and electronic properties of the primary photoexcited species that are formed upon absorption of a photon in these systems, and (2) the pathways accessed during the recombination of photogenerated free charge.

In this Introduction we will briefly review several important aspects of the materials systems in Section 1.1, followed by a review of the basic electronic properties of primary

photoexcitations in semiconductors (Section 1.2), and finally give a background on charge recombination in semiconductors (Section 1.3), which will be helpful in understanding the studies described in Chapters 2 through 4 of this thesis.

Section 1.1 Materials Systems Studied

Hybrid Organic-Inorganic Perovskites

Hybrid organic-inorganic perovskites are crystalline semiconductors with the general perovskite formula ABX_3. The systems most relevant for photovoltaic technology are the lead halide perovskites, where B= Pb^{2+}, X= I, Br, or Cl, and A is can be an organic cation (typically methylammonium $CH_3NH_3^+$ or formamidinium CH_5N_2+) or an inorganic cation (Cs); however all-inorganic $CsPbX_3$ perovskites typically deliver inferior performance and hence at least some stoichiometric ratio of organic:inorganic cation is used for the A site. Hybrid organic-inorganic perovskites have garnered enormous scientific interest because of the unprecedented fast rise in efficiency of solar cells made from these materials from <10% to over 22% in a time span of around only 5 years.[7] They are most attractive for commercial applications because of their solution processability from very inexpensive, earth abundant elements, and efficiencies that already have surpassed established commercial technologies; for this reason, perovskite solar cells are already on the path to commercialization.

As crystalline materials, hybrid-organic inorganic perovskites demonstrate some of the "textbook" physical properties of three dimensional low band-gap crystalline semiconductors,[17] which include band-like charge transport[18] and band-to-band radiative recombination.[19] However unlike conventional inorganic semiconductors, these materials exhibit unique properties such as an apparent robust tolerance to defects in terms their effects on charge carrier scattering[20] and luminescence efficiency.[21] One of the most pressing photophysics questions early on, especially in light of some of the intriguing "textbook" versus "non-textbook" photophysical behavior of these systems, was the nature of the primary excited states that form upon absorption of light – namely, if the photoexcited states are best described as excitons or free charges,[22] and whether or not a "textbook" exciton model for low bandgap inorganic semiconductors (the Wannier exciton model) best describes their electronic structure. This is the topic of the study presented in Chapter 2. Section 1.2 below will give a brief background on some of the classic exciton theories for semiconductors.

π-Conjugated Semiconducting Polymers

Pi-conjugated semiconducting polymers have been of great technological interest for a wide diversity of applications due not only to their low cost manufacturing from non-toxic elements, but also their mechanical flexibility which opens up a range of interesting possibilities for "plastic" electronic devices such as flexible touchscreen devices or artificial skin. Many of the basic electronic properties of π-conjugated polymers, especially with regards to the broad tunability of chemical structures, are still being discovered.

The basic chemical structure of π-conjugated polymers consist of one-dimensional repeating units of π -conjugated monomers such that an extended π - π orbital interaction is ideally maintained along the entire length of the polymer backbone.[23] The theory originally developed to model the primary photoexcited states of these systems treated the excited state orbitals in the framework of a modified form of one-electron band theory,[24] wherein excitation from the ground state valence orbitals leads to the promotion of an electron into a conjugated π^* orbital that extends across the entire backbone of the polymer chain, essentially resulting in the picture of a 1D free electron band. However this model failed to reproduce many experimental observations (particularly in terms of the luminescent and non-linear optical properties of π-conjugated polymers as well as structure in the linear absorption spectrum),[25] and thus, in general, models where excited state wavefunctions are constructed from Hamiltonians that consider transfer probabilities between different "sites" on the polymer backbone and also consider long-range Coulomb interactions were found to more accurately reproduce experimental results.[26] The result of such a model is that excitations result in tightly bound excitons (rather than free electrons). While the electronic structure of these excitons is complex,[27] extensive work done by Spano[28] showed that many of the spectral properties of π-conjugated polymers can be understood in the framework of simple exciton theories developed in the 1960's for molecular crystals,[29] and that these spectral signatures can in turn be used to understand key aspects about the exciton electronic structure.[28] These theories are reviewed in Section 1.3 below. The study in Chapter 3 of this thesis will relate to studying the spectral signatures excitons to establish basic aspects of their electronic structure.

Polymer:Small Molecule Blends

Pi-conjugated polymers perform very poorly as photovoltaic absorber materials on their own, due principally to the fact that (1) photoexcitations in these systems result in tighty bound excitons that cannot separate on their own into free charges, and (2) in general π-conjugated polymers do not sustain ambipolar transport of both electrons and holes (typical π-conjugated polymers only exhibit good transport of holes due to an abundance of electron-trapping defects), and therefore cannot be used on their own. A breakthrough discovery in 1995 from Heeger and coworkers[30] found that when a π-conjugated polymer (MEH-PPV) was mixed in solution with a small molecule electron acceptor (a functionalized C_{60} molecule) and spin cast as a thin film absorber layer in a solar cell, the incident photon-to-current-extraction efficiency improved by nearly two orders of magnitude compared to when MEH-PPV was used alone. Since then, the field of polymer photovoltaics has relied on this polymer:small molecule "bulk heterojunction" architecture to make efficient solar cells. For nearly 20 years most of the progress in polymer photovoltaics was made by improving the morphology and chemical structure of the polymer elecrton "donor" material, while C_{60} type molecules remained fixed as the "acceptor." Only in the last few years has research into alternative "non-fullerene" acceptor materials surged. As of the time of writing of this thesis, the highest power conversion efficiency for a single junction polymer solar cell has been achieved in a polymer/non-fullerene acceptor system with a power conversion efficiency of ~14%.[31]

In the early 2000's it became clear that both ground and excited state interactions between the polymer donors and small molecule acceptors in the intimate nanoscale mixture of phases that occurs in the bulk heterojunction architecture, result in the formation of excited state "charge transfer" complexes between the polymer and small molecule.[32] Following the absorption of light on either the polymer or small molecule, excitons diffuse to a donor/acceptor interface and transfer an excited state charge (either an electron or hole) to a ground state donor or acceptor molecule, which can result in a Coulombically bound "charge transfer" complex consisting of a polymer with an excess electron and an acceptor molecule with an excess hole bound together by the Coulomb interaction.[32] These charges can separate to form mobile charge in their respective donor or acceptor phases, which can recombine again at an interface again forming a charge transfer complex. Therefore, the current picture of the operation of organic photovoltaics considers charge transfer states to be an "intermediate" state which mediates both the separation of charge from the initial photoexcited species as well as the recombination of free charges to the ground state.[32] The minimization of excessive recombination pathways for free charge is directly related to the open circuit voltage that can be achieved in a solar cell, which we review below in section 1.3. Hence, understanding the nature of charge recombination pathways in an organic solar cell is critical to enhance performance, which is the topic of the study in Chapter 4 of this thesis.

Section 1.2 Fundamentals of Excited States in Semiconductors

As discussed in the above sections, understanding the nature of primary photoexcited states in solution processed semiconductors is not only an important question of fundamental scientific interest, but it is also critical towards understanding how free charge generated will be generated in a solar cell following the absorption of light. Will charge be generated spontaneously as in a "textbook" low band gap crystalline inorganic semiconductor, or will a bulk heterojunction be required to separate tightly bound excitons as in a polymer:small molecule solar cell? These are the topics of the studies in Chapters 2 and 3 of this thesis, and in order to introduce these concepts we review some of the fundamental theories of excited states in semiconductors below.

Band-to-Band Transitions

Band-to-band transitions are a result of the so-called "one electron" theory for crystalline semiconductors. For a clear and comprehensive explanation of one-electron theory the textbook by Yu and Cardona is an ideal reference.[17] We briefly outline several key aspects of one electron theory here in order to aid in the understanding of the theory of Wannier excitons below, specifically by introducing the concepts of an electron and hole effective mass and the band-to-band transition matrix element.

The basics of one electron theory can be understood from the Hamiltonian used to describe a wavefunction of an excited state in the crystal. The Hamiltonian for an electron in excited state "n" is given by:

$$\left[\left(\frac{p^2}{2m}\right) + V(r)\right]\phi_n(r) = E_n\phi_n(r) \qquad Eq.\,1$$

In Eq. 1, p is the momentum operator for electon "n", and $V(r)$ is the potential experienced by electron "n" at point "r." Importantly, the basis for one electron theory comes from assuming that the potential function $V(r)$ is simply an average potential experienced by the electron as it moves through the lattice, and does not contain any information about specific correlations with other electrons.[17] Many methods for estimating the average potential function exist which are reviewed by Cardona and Yu.[17]Another basic element of one electron theory considers that due to the translational invariance of the crystal structure between unit cells in the lattice, periodic functions of the form e^{ikx} expressed in terms of a wavevector (k) in the reciprocal lattice can be used to describe the translational invariance of the wavefunction between unit cells. Therefore, wavefunctions can be expressed in the form of a "Bloch" function, which considers a free electron wave function as a plane wave with wave vector (k) due to the translational invariance, modulated by a envelope function $u_k(x)$ which is a result of the average periodic potential in the Eq. 1:

$$\phi_k(x) = e^{ikx}u_k(x) \qquad Eq\ 2.$$

Because of the translational invariance between unit cells within the crystal, k can theoretically take on an infinite number of values between the boundaries of a primitive cell in reciprocal space (known as the Brillouin zone),[17] and so the Bloch functions correspond to a continuous "band" of energy states, referred to for electrons as the "conduction band." The same wavefunctions can be written for positive charges (holes) in the "valence band." The shape of the function that describes the energy band ($E(k)$) determines the effective mass of an electron in the valence band or hole in the conduction band, due to the fact that (k) represents the momentum corresponding to a Bloch electron, and the classical relationship between energy and momentum is expressed by $\frac{d^2E}{dk^2} = \frac{1}{m}$.[17]

Photoexcitations in one electron theory result in an electron in the conduction band and a hole in the valence band, and the overall transition probability is governed by an oscillator strength $\vec{P}_{cv}$, which can be calculated theoretically considering the outer shell atomic orbitals that constitute the bands themselves.[17] The transition rate is also governed by a so called joint density of states function, which considers the shape of both the valence and conduction bands in k-space which determines how many available states exist for a transition corresponding to states with wavevector in the interval $k + \Delta k$.[17] It is important to note that momentum must be conserved during the transition, which limits the form of the join-density of states function such that in the limit of no external interactions to scatter the electron or hole (such as electron-phonon scattering), transitions can only occur between states in the valence band with the same k index as states in the conduction

band.[17] With the basic understanding laid out here, we now move to discuss the concept of a Wannier exciton.

Wannier Excitons

A Wannier exciton is a first step beyond one-electron theory to consider the effect that the interaction between an electron in the conduction band and a hole in the valence band will have on the electronic structure of an excited state. The approach taken to model the electronic structure of the Wannier exciton describes the electron-hole pair in same way one considers the Hamiltonian for the relative coordinate wavefunction of a hydrogen atom.[17] The only difference between the hydrogen atom model and the Wannier exciton model is that the reduced mass used in the kinetic energy term in the Hamiltonian is the reduced effective mass of the electron and hole (calculated from the band structure as explained above), and the dielectric constant in the potential term in the Hamiltonian is the relative dielectric constant of the crystal as opposed to the vacuum dielectric constant used for the hydrogen atom. The effective mass Schrödinger equation for relative motion of the electron-hole pair in the Wannier exciton model is then given as:[33-34]

$$\left[-\left(\frac{\hbar}{2\mu}\right)\nabla^2 - \frac{e^2}{\epsilon r}\right]\phi_n(r) = E_n\phi_n(r) \qquad Eq.3$$

$$\mu = \ electron - hole\ reduced\ effective\ mass, \qquad \epsilon = \ relative\ dielectric\ constant$$

To resulting solutions to Eq. 3 will give spherical harmonic wavefunctions similar to the hydrogen atom with the typical $\frac{1}{n^2}$ proportionality between energy level spacings (where n is the principal quantum number of the state). The energy levels specifically are given by:

$$E_n = E_g - \frac{E_B}{n^2} \quad where\ E_B = \frac{\mu e^4}{2\hbar^2\epsilon^2} \qquad Eq.4$$

Here E_g is equivalent to the ionization continuum of the hydrogen atom, and the exciton binding energy is defined as the difference between the n=1 exciton level and the onset of the exciton ionization continuum similar to the definition of the hydrogen Rydberg.[17] Therefore absorption to a Wannier exciton state below E_g will result in the formation of a neutrally charged quasi-particle consisting of a bound electron-hole pair, while absorption of a photon above E_g will result in free electrons and holes. The study in Chapter 2 will concern the effects of an external electric field on the states of a Wannier exciton and the resulting changes in the absorption spectra in order to estimate the exciton binding energy.

Molecular Excitons: H- and J- Aggregates

In the treatment of the Wannier exciton we started from one-electron band theory to determine the energy band structure for free electrons and holes to calculate their reduced effective mass, and then considered the electron-hole interaction using the Hamiltonian in Eq. 3. This results in the

picture of the exciton as neutral quasiparticle where the distance between the electron and hole can span many lattice sites, as the original states started from free electron and hole wavefunctions which interact only by the long range Coulomb potential. In contrast, in the molecular exciton picture, rather than starting from a free particle picture, we start by considering the basic wave functions for the excitation in terms of non-interacting excited states on each molecule confined to a lattice site of the crystal. Here we briefly illustrate the basic aspects of the molecular exciton theory following the approach from Kasha and McRae.[35]

We consider a molecular crystal consisting of N molecules arranged in a periodic lattice. As noted above, we start with the picture of non-interacting molecular excited states and use and these to determine first order energy corrections as well as symmetry adapted linear stationary state wave wavefunctions for the exciton which will be used to calculate transition probabilities. The ground state wavefunction can be written as:

$$\Psi_G = \psi_1\psi_2\psi_3 \dots \psi_a \dots \psi_N = \prod_{n=1}^{N} \psi_n \qquad Eq.5$$

And a basis function describing an excited state of the system with the excitation localized on one molecule in the crystal can be written as:

$$\phi_a = \psi_a^\dagger \prod_{\substack{n-1 \\ n\neq a}}^{N} \psi_n = \psi_1\psi_2\psi_3 \dots \psi_n \dots \psi_N \qquad (a = 1,2,3 \dots \dots N) \qquad Eq.6$$

Here $\psi_a^\dagger$ is an excited state wavefunction on the "a"-th lattice site. A stationary state wavefunction for the crystal with index *k* can be written in terms of linear combinations of the ϕ_a functions:

$$\Psi_k = \frac{1}{\sqrt{N}} \sum_{a=1}^{N} C_{ak}\phi_a \qquad Eq.7$$

In Eq. 7 the C_{ak} terms are expansion coefficients. Due to the translational invariance in the lattice of molecules, these expansion coefficients can be written in terms of periodic functions of the form $e^{2\pi ika/N}$, where the wavevector *k* determines the number of nodes in the resulting function with respect to the position vector "a":

$$\Psi_k = \frac{1}{\sqrt{N}} \sum_{a=1}^{N} e^{2\pi ika/N}\phi_a \qquad \left(k = 0, +1, -1, +2 \dots\dots, \frac{N}{2}\right) \qquad Eq.8$$

By substituting in values for *k* we can already see what these wavefunctions will look like. For *k*=0 the phase factor $e^{2\pi ika/N}$ will be 1 for all terms in the sum, and the wavefunction will be nodeless, given by Eq. 9:

$$\Psi_{k=0} = \frac{1}{\sqrt{N}}\left[\left(\psi_1^\dagger\psi_2\psi_3 \dots \psi_N\right) + \left(\psi_1\psi_2^\dagger\psi_3 \dots \psi_N\right) + \cdots \left(\psi_1\psi_2\psi_3 \dots \psi_N^\dagger\right)\right] \qquad Eq.9$$

And for $\Psi_{N/2}$ the sum will constitute a wavefunction with will be a node in between every localized excited state wavefunction:

$$\Psi_{k=N/2} = \frac{1}{\sqrt{N}}\left[\left(\psi_1^{\dagger}\psi_2\psi_3 \ldots \psi_N\right) - \left(\psi_1\psi_2^{\dagger}\psi_3 \ldots \psi_N\right) + \cdots \left(\psi_1\psi_2\psi_3^{\dagger} \ldots \psi_N\right) -\right] \qquad Eq.10$$

These distinctions are important to point out in understanding the optical selection rules for the different excited state combinations. The transition dipole moment for a transition between the ground state wavefunction (Eq. 5) and one of the excited state wavefunctions (for example Eq. 9. and Eq. 10) can be written in terms of the individual transition dipole moments between the ground state and the ϕ_a functions that form the symmetry adapted wavefunctions in Eq. 9 and Eq. 10. With the transition dipole moment between the ground state and a particular ϕ_a function labeled was $\boldsymbol{M_{\phi_a}}$, the transition dipole moment for the symmetry adapted wavefunctions in Eq. 9 and Eq. 10 can be written as:

$$\boldsymbol{M_{k=0}} = \boldsymbol{M_{\phi_1}} + \boldsymbol{M_{\phi_2}} + \boldsymbol{M_{\phi_3}} \ldots\ldots + \boldsymbol{M_{\phi_N}} \qquad Eq.11$$

$$\boldsymbol{M_{k=N/2}} = \boldsymbol{M_{\phi_1}} - \boldsymbol{M_{\phi_2}} + \boldsymbol{M_{\phi_3}} - \boldsymbol{M_{\phi_4}} \ldots \qquad Eq.12$$

Here all of the $\boldsymbol{M_{\phi_a}}$ have the same magnitude, and when we consider the case where all of the $\boldsymbol{M_{\phi_a}}$ are oriented identically, and *an important result arises, that the transition between the $\Psi_{k=0}$ and the ground state is strongly symmetry allowed, while the transition between $\Psi_{k=N/2}$ and the ground state is symmetry forbidden.*

To calculate the first order energy for the symmetry adapted wavefunctions we start from the ϕ_a functions in Eq. 6. The perturbation potential in the Hamiltonian used to calculate the first order energy correction is a transition dipole-dipole interaction corresponding to the ground-to-excited state transition dipole moments for different ϕ_a states (the $\boldsymbol{M_{\phi_a}}$**'s**). We leave the mathematical details to the reader to explore in the clear references by Kasha[29, 35] and instead show the results diagrammatically below. We consider the aggregate to be a linear array of molecules (indeed the relevant geometry for a conjugated polymer). The interaction between the N-fold degenerate ϕ_a states will result in the splitting and formation of a band of energy levels of width 4β, where β is the transition dipole-dipole interaction energy between two different ϕ_a states.[36] The splitting of the different Ψ_k states depends on the phases of the transition dipoles $\boldsymbol{M_{\phi_a}}$ corresponding to a particular Ψ_k state (see Eq. 11 and Eq. 12). For a linear arrangement of molecules, when the transition dipoles orient in a *colinear* fashion, the dipole-dipole interaction in the $\Psi_{k=0}$ state has a net attractive interaction, resulting in the $\Psi_{k=0}$ state residing at the bottom of the exciton band (Fig. 1.1 a.). This is known as a ***J-aggregate***. When the transition dipoles between molecules are aligned in a *cofacial* fashion (Fig. 1.1 b.) the dipole-dipole interaction in the $\Psi_{k=0}$ state has a net *repulsive* attraction, resulting in the $\Psi_{k=0}$ state lying at the top of the exciton band. This is referred to as an ***H-aggregate***.

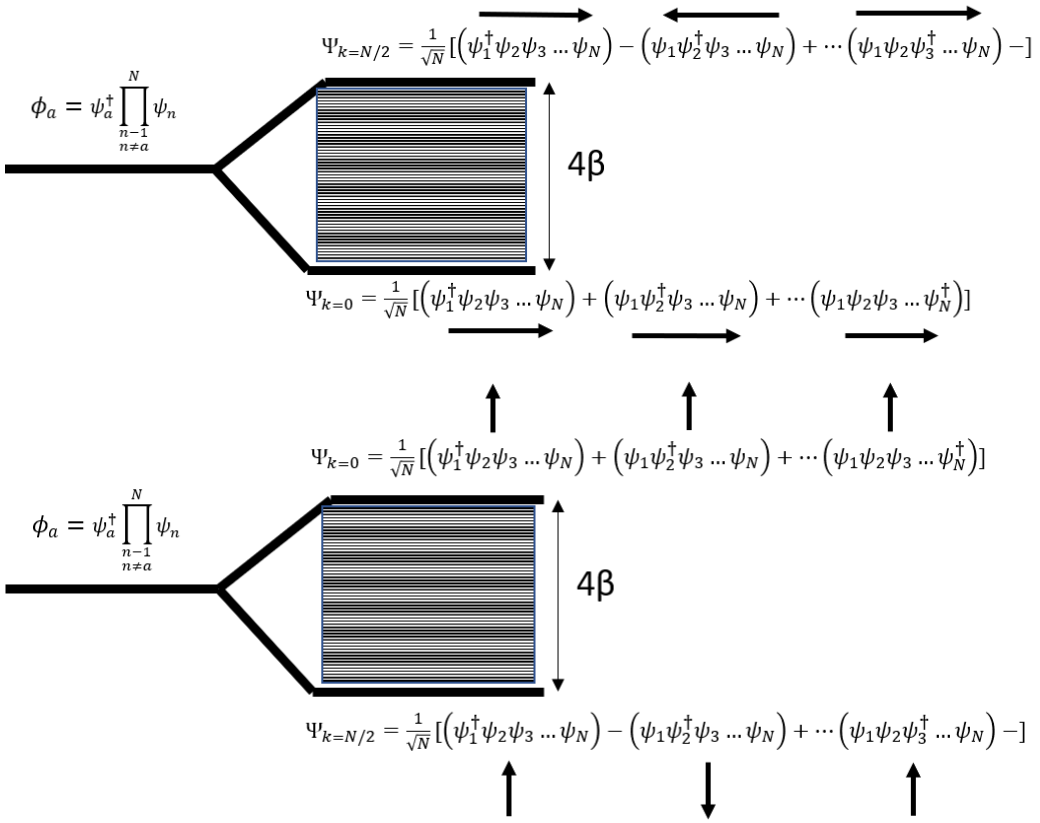

Figure 1.1 Energy level diagram corresponding to the splitting of the N-fold generate ϕ_a states to form an exciton band for a ***a.)*** *J-aggregate* and a ***b.)*** *H-aggregate*. Depending on the orientation of transition dipoles (*co-linear* in 1A or *co-facial* in 1B), the $\Psi_{k=0}$ state will reside either at the top or bottom of the exciton band.

The differences in the band structure between H- and J- aggregates shown in Figure 1.1 a. and Figure 1.1 b. have profound impacts on their respective optical properties. Conservation of momentum requires that transitions from the ground state to the exciton band can only occur to the $k = 0$ state.[36] Therefore, in a J-aggregate, optical absorption occurs to the bottom of the exciton band. On the contrary, for an H-aggregate absorption occurs to the top of the exciton band. Kasha's rule states that emission only occurs only from the bottom of the exciton band, is intraband cooling occurs on the time scale of picoseconds.[36] Therefore, in a J-aggregate, luminescence is strongly optically allowed since excitations emit from the k=0 state at the bottom of the exciton band. In contrast, in a H-aggregate, excitations quickly relax to the k=N/2 state, which is a symmetry forbidden transition to the ground state. *Hence, luminescence is severely quenched in a H-aggregate.* However, the ground state can absorb a phonon of wave vector *q*, wherein momentum can be conserved during a transition from the k=N/2 state. *The result is that luminescence in a H-aggregate can occur to a vibrationally excited ground state, but not to the vibrationally relaxed ground state (the so called 0-0 transition in a vibronic progression). On the other hand in a J-aggregate the 0-0 vibronic emission transition is strongly allowed.* An understanding of these basic

photophysics of H- and J- aggregates is necessary background to understanding the study in Chapter 3 of this thesis, were we explore H- and J-like spectroscopic signatures in the photoluminescence spectra of π-conjugated polymers.

Section 1.3 Charge Recombination in Semiconductors

In Section 1.2 above the basic properties of excited states in semiconductors were reviewed because these properties influence charge generation in a solar cell, which is a theme of the studies in Chapter 2 and Chapter 3 of this thesis. An equally important concern for the operation and efficiency of a solar cell is the recombination of charge. The maximum voltage that a solar cell can output is referred to as the open circuit voltage. For a solar cell under illumination, the open circuit voltage is defined as the voltage at which point the photogenerated current is balanced by an equal recombination current, such that no charge escapes the device.[37] The voltage at which this condition occurs is precisely equal to the chemical potential of a photogenerated electron-hole pair, in other words, the net photocurrent in the device is zero when the applied voltage is equal to the free energy associated with removing an electron-hole pair from the solar cell.[37] The chemical potential of an electron-hole pair is defined by the difference in quasi-Femi level for electrons in the conduction band, and holes in the valence band (the book by Wurfel[37] is recommended for a derivation). The concept of a quasi Fermi-level can be directly understood in terms of the generation and recombination of electrons and holes inside of a semiconductor. In Eq. 13 below we show a simple equation describing the time rate of change of electrons in the conduction band as a function of a generation rate (G) and recombination rate coefficient (k_{rec}):

$$\frac{dn(t)}{dt} = G - k_{rec}n(t) \qquad Eq.13$$

A similar equation can be written for the time dependent population of holes $p(t)$ in the valence band. Starting from an initial condition of $n(0) = 0$, the population $n(t)$ will increase in time until the quantity $k_{rec}n(t)$ is equal to G, at which point the population of electrons in the conduction band will reach a steady state. The recombination rate coefficient k_{rec} can embed many different pathways or recombination mechanisms. For the case of band-to-band recombination, k_{rec} is a pseudo rate constant which contains the band-to-band recombination constant (k_B) and the coupled time dependent population of holes, $k_{rec} = k_B * p(t)$, making the recombination order in Eq. 13 bimolecular (assuming the equal generation of holes and electrons). Here we remain agnostic to the particular pathways imbedded in $k_{rec}$and simply assume that it contains two different pathways, one intrinsic pathway k_1 (which could be a pseudo rate constant mentioned above reflecting the intrinsic band-to-band transition required by reciprocity with absorption in a simple semiconductor model)[37], and one extrinsic pathway k_2, which could reflect non-radiative recombination via extrinsic electron traps, for example.[37] Writing the overall rate constant k_{rec} as a sum of $k_1 + k_2$, we can see that the obvious effect of removing the extrinsic pathway k_2 would be to slow down the overall recombination, and hence lead to a larger population of n at steady state.

Under the assumption that excess photogenerated electrons in the conduction band are in thermal equilibrium, the population of electrons (n) in the conduction band under illumination can be written in terms of the integration over the density of states function of the conduction band ($D_c(E)$) multiplied by a Fermi distribution function giving the probability of an electron occupying a state at an energy E ($f_e(E)$):[37]

$$n = \int_{Ec}^{\infty} D_c(E) * f_e(E) dE \qquad Eq. 14$$

Using a density of states function that assumes a constant effective mass of the electron throughout the conduction band (which we label as N_c following the notation of Wurfel[37]), Eq 14 can be evaluated to a simple form (see the text by Wurfel[37]):

$$n = N_c \exp\left(-\frac{Ec - E_{fc}}{kT}\right) \qquad Eq. 15$$

In Eq 15., E_{fc} is the *quasi-Fermi energy* associated with the occupation probability of finding an electron at energy E in the conduction band. Rewriting Eq 15. to solve for the quasi-Femi energy, we arrive at Eq 16.:

$$E_{fc} = E_c - kTln\left(\frac{N_c}{n}\right) \qquad Eq. 16$$

Thus we can see that the effect of reducing the steady state population of electrons in the conduction band (n) is to reduce the quasi-Fermi energy for electrons in the conduction band. We note that the value of n (electrons in the conduction band) cannot exceed the available density of states in the conduction band N_c. An identical analysis can be applied for holes to obtain E_{fv} , the quasi-Fermi energy for holes in the valence band. The quantity $E_{fc} - E_{fv}$ defines the *quasi-Fermi splitting of electrons and holes*, which, as noted earlier directly corresponds to the free energy change associated with removing an electron-hole pair from the semiconductor and equivalently the maximum obtainable open-circuit voltage.

The study in Chapter 4 of this thesis will address the problem of extrinsic non-radiative recombination in organic photovoltaics, a which has posed a significant loss on the open circuit voltages achieved thus far in this technology.[38]

References

1. Arias, A. C.; MacKenzie, J. D.; McCulloch, I.; Rivnay, J.; Salleo, A., Materials and applications for large area electronics: solution-based approaches. *Chem Rev* **2010,** *110* (1), 3-24.
2. Rivnay, J.; Inal, S.; Salleo, A.; Owens, R. M.; Berggren, M.; Malliaras, G. G., Organic electrochemical transistors. *Nature Reviews Materials* **2018,** *3* (2), 17086.
3. Mannsfeld, S. C.; Tee, B. C.; Stoltenberg, R. M.; Chen, C. V.; Barman, S.; Muir, B. V.; Sokolov, A. N.; Reese, C.; Bao, Z., Highly sensitive flexible pressure sensors with microstructured rubber dielectric layers. *Nat Mater* **2010,** *9* (10), 859-64.
4. Burroughes, J. H.; Bradley, D. D. C.; Brown, A. R.; Marks, R. N.; Mackay, K.; Friend, R. H.; Burns, P. L.; Holmes, A. B., Light-emitting diodes based on conjugated polymers. *Nature* **1990,** *347* (6293), 539-541.
5. Wood, V.; Bulovic, V., Colloidal quantum dot light-emitting devices. *Nano Rev* **2010,** *1*.
6. Carey, G. H.; Abdelhady, A. L.; Ning, Z.; Thon, S. M.; Bakr, O. M.; Sargent, E. H., Colloidal Quantum Dot Solar Cells. *Chem Rev* **2015,** *115* (23), 12732-63.
7. Zhang, W.; Eperon, G. E.; Snaith, H. J., Metal halide perovskites for energy applications. *Nature Energy* **2016,** *1* (6), 16048.
8. Dennler, G.; Scharber, M. C.; Brabec, C. J., Polymer-Fullerene Bulk-Heterojunction Solar Cells. *Advanced Materials* **2009,** *21* (13), 1323-1338.
9. Hou, J.; Inganas, O.; Friend, R. H.; Gao, F., Organic solar cells based on non-fullerene acceptors. *Nat Mater* **2018,** *17* (2), 119-128.
10. Collini, E.; Scholes, G. D., Coherent intrachain energy migration in a conjugated polymer at room temperature. *Science* **2009,** *323* (5912), 369-73.
11. Jha, A.; Duan, H.-G.; Tiwari, V.; Nayak, P. K.; Snaith, H. J.; Thorwart, M.; Miller, R. J. D., Direct Observation of Ultrafast Exciton Dissociation in Lead Iodide Perovskite by 2D Electronic Spectroscopy. *ACS Photonics* **2017,** *5* (3), 852-860.
12. Miyata, K.; Meggiolaro, D.; Trinh, M. T.; Joshi, P. P.; Mosconi, E.; Jones, S. C.; De Angelis, F.; Zhu, X. Y., Large polarons in lead halide perovskites. *Sci Adv* **2017,** *3* (8), e1701217.
13. Gelinas, S.; Rao, A.; Kumar, A.; Smith, S. L.; Chin, A. W.; Clark, J.; van der Poll, T. S.; Bazan, G. C.; Friend, R. H., Ultrafast long-range charge separation in organic semiconductor photovoltaic diodes. *Science* **2014,** *343* (6170), 512-6.
14. Melianas, A.; Etzold, F.; Savenije, T. J.; Laquai, F.; Inganas, O.; Kemerink, M., Photo-generated carriers lose energy during extraction from polymer-fullerene solar cells. *Nat Commun* **2015,** *6*, 8778.
15. Rao, A.; Chow, P. C.; Gelinas, S.; Schlenker, C. W.; Li, C. Z.; Yip, H. L.; Jen, A. K.; Ginger, D. S.; Friend, R. H., The role of spin in the kinetic control of recombination in organic photovoltaics. *Nature* **2013,** *500* (7463), 435-9.
16. Wehrenfennig, C.; Eperon, G. E.; Johnston, M. B.; Snaith, H. J.; Herz, L. M., High Charge Carrier Mobilities and Lifetimes in Organolead Trihalide Perovskites. *Advanced Materials* **2014,** *26* (10), 1584-1589.
17. Yu, P. Y.; Cardona, M., *Fundamentals of Semiconductors*. Springer: Heidelberg, 2010.
18. Chen, Y.; Yi, H. T.; Wu, X.; Haroldson, R.; Gartstein, Y. N.; Rodionov, Y. I.; Tikhonov, K. S.; Zakhidov, A.; Zhu, X. Y.; Podzorov, V., Extended carrier lifetimes and diffusion in hybrid perovskites revealed by Hall effect and photoconductivity measurements. *Nat Commun* **2016,** *7*, 12253.

19. Davies, C. L.; Filip, M. R.; Patel, J. B.; Crothers, T. W.; Verdi, C.; Wright, A. D.; Milot, R. L.; Giustino, F.; Johnston, M. B.; Herz, L. M., Bimolecular recombination in methylammonium lead triiodide perovskite is an inverse absorption process. *Nat Commun* **2018,** *9* (1), 293.
20. Zhu, H.; Miyata, K.; Fu, Y.; Wang, J.; Joshi, P. P.; Niesner, D.; Williams, K. W.; Jin, S.; Zhu, X. Y., Screening in crystalline liquids protects energetic carriers in hybrid perovskites. *Science* **2016,** *353* (6306), 1409-1413.
21. Braly, I. L.; deQuilettes, D. W.; Pazos-Outón, L. M.; Burke, S.; Ziffer, M. E.; Ginger, D. S.; Hillhouse, H. W., Hybrid perovskite films approaching the radiative limit with over 90% photoluminescence quantum efficiency. *Nature Photonics* **2018**.
22. Stranks, S. D.; Eperon, G. E.; Grancini, G.; Menelaou, C.; Alcocer, M. J.; Leijtens, T.; Herz, L. M.; Petrozza, A.; Snaith, H. J., Electron-hole diffusion lengths exceeding 1 micrometer in an organometal trihalide perovskite absorber. *Science* **2013,** *342* (6156), 341-4.
23. Heeger, A. J., Semiconducting polymers: the Third Generation. *Chem Soc Rev* **2010,** *39* (7), 2354-71.
24. Heeger, A. J.; Kivelson, S.; Schrieffer, J. R.; Su, W. P., Solitons in conducting polymers. *Reviews of Modern Physics* **1988,** *60* (3), 781-850.
25. Sariciftci, N. S., *Primary Photoexcitations in Conjugated Polymers: Molecular Exciton Versus Semiconductor Band Model*. World Scientific: Singapore, 1997.
26. Chandross, M.; Mazumdar, S.; Jeglinski, S.; Wei, X.; Vardeny, Z. V.; Kwock, E. W.; Miller, T. M., Excitons in poly(para-phenylenevinylene). *Physical Review B* **1994,** *50* (19), 14702-14705.
27. Brédas, J.-L.; Cornil, J.; Beljonne, D.; dos Santos, D. A.; Shuai, Z., Excited-State Electronic Structure of Conjugated Oligomers and Polymers: A Quantum-Chemical Approach to Optical Phenomena. *Accounts of Chemical Research* **1999,** *32* (3), 267-276.
28. Spano, F. C.; Silva, C., H- and J-aggregate behavior in polymeric semiconductors. *Annu. Rev. Phys. Chem.* **2014,** *65*, 477-500.
29. Kasha, M.; Rawls, H. R.; Ashraf El-Bayoumi, M., The exciton model in molecular spectroscopy. *Pure and Applied Chemistry* **1965,** *11* (3-4).
30. Yu, G.; Gao, J.; Hummelen, J. C.; Wudl, F.; Heeger, A. J., Polymer Photovoltaic Cells: Enhanced Efficiencies via a Network of Internal Donor-Acceptor Heterojunctions. *Science* **1995,** *270* (5243), 1789-1791.
31. Li, S.; Ye, L.; Zhao, W.; Yan, H.; Yang, B.; Liu, D.; Li, W.; Ade, H.; Hou, J., A Wide Band-Gap Polymer with a Deep HOMO Level Enables 14.2% Efficiency in Polymer Solar Cells. *Journal of the American Chemical Society* **2018**.
32. Vandewal, K., Interfacial Charge Transfer States in Condensed Phase Systems. *Annual Review of Physical Chemistry* **2016,** *67*, 113-33.
33. Elliott, R. J., Intensity of Optical Absorption by Excitons. *Phys. Rev.* **1957,** *108* (6), 1384-1389.
34. Blossey, D., Wannier Exciton in an Electric Field. I. Optical Absorption by Bound and Continuum States. *Phys. Rev. B* **1970,** *2* (10), 3976-3990.
35. McRae, E. G.; Kasha, M., The Molecular Exciton Model. In *Physical Processes in Radiation Biology*, Augenstein, L.; Mason, R.; Rosenberg, B., Eds. Academic Press: New York, 1964; pp 23-42.

36. Pope, M.; Swenberg, C. E., *Electronic Processes in Organic Crystals and Polymers*. 2 ed.; Oxford University Press: New York, 1999.
37. Würfel, P., *Physics of Solar Cells*. Wiley-VCH: Weinheim, 2005.
38. Benduhn, J.; Tvingstedt, K.; Piersimoni, F.; Ullbrich, S.; Fan, Y.; Tropiano, M.; McGarry, K. A.; Zeika, O.; Riede, M. K.; Douglas, C. J.; Barlow, S.; Marder, S. R.; Neher, D.; Spoltore, D.; Vandewal, K., Intrinsic non-radiative voltage losses in fullerene-based organic solar cells. *Nature Energy* **2017,** *2* (6), 17053.

Chapter 2: Electroabsorption Spectroscopy Measurements of the Exciton Binding Energy, Electron-Hole Reduced Effective Mass, and Band Gap in the Perovskite $CH_3NH_3PbI_3$

This chapter contains the work published originally in "Electroabsorption spectroscopy measurements of the exciton binding energy, electron-hole reduced effective mass, and band gap in the perovskite $CH_3NH_3PbI_3$" by Ziffer, M. E.; Mohammed, J. C.; Ginger, D. S., in ACS Photonics 2016, 3 (6), 1060-1068 **DOI:** 10.1021/acsphotonics.6b00139

Section 2.1 Overview

We use electroabsorption (EA) spectroscopy to measure the exciton binding energy (E_B), electron-hole reduced effective mass (μ), and one-electron band gap (E_g) at the fundamental absorption edge of the hybrid organic-inorganic perovskite $CH_3NH_3PbI_3$ in its tetragonal phase at 300 K. By studying the second harmonic EA spectra at the fundamental absorption edge we establish that the room temperature EA response in $CH_3NH_3PbI_3$ follows the low-field Franz-Keldysh-Aspnes (FKA) effect. Following FKA analysis we find that $\mu = 0.12 \pm 0.03\, m_0$, $E_B = 7.4$ meV, and $E_g = 1.633$ eV. Our results provide direct experimental evidence that at room temperature primary transitions occurring in $CH_3NH_3PbI_3$ can essentially be described in terms of free carrier generation.

Section 2.2 Introduction

Hybrid organic-inorganic perovskite semiconductors are intriguing materials that have been demonstrated to have high performance in optoelectronic devices such as lasers,[1-2] LEDs,[3] and solar cells,[4-6] despite requiring only inexpensive and relatively crude processing conditions compared to current high-performance crystalline semiconductors. The archetypal material, $CH_3NH_3PbI_3$, has exhibited excellent power conversion efficiency in solar cells,[4] which has been attributed in part to good ambipolar charge transport,[7-8] long electron-hole diffusion lengths,[9-11] good radiative efficiency,[1, 12] photon recycling,[13] a high optical absorption coefficient,[14] and a low exciton binding energy.[15-19] Of these properties, the exciton binding energy (E_B) has been one of the most difficult to measure directly, particularly for the room temperature tetragonal phase of $CH_3NH_3PbI_3$.[20-21] Over the past several years a wide range of values have been estimated for E_B from 2-50 meV.[15, 17, 19, 22-31] Most recent work suggests E_B is small enough that $CH_3NH_3PbI_3$ solar cells can be broadly considered "non-excitonic" under ordinary working conditions[17-18, 32] and many time resolved spectroscopy studies on $CH_3NH_3PbI_3$ have been successfully interpreted considering radiative and non-radiative free carrier recombination kinetics alone.[19, 33-37] However, the degree to which bound excitonic states make up the primary photoexcited species at the direct absorption edge in the tetragonal phase is a fundamental physical question that is still a matter of study. Evidence for the room temperature coexistence of bound excitons and free charges at early time scales,[1, 38-39] and an excitonic bleach based on Elliott's model,[25, 40-41] have been reported quite recently in transient absorption measurements on polycrystalline thin films. In addition, recent

time-resolved terahertz spectroscopy measurements have been interpreted as evidence that bound excitons comprise the primary band edge photoexcitation species in $CH_3NH_3PbI_3$ single crystals,[23] while early rise times in time-resolved THz and microwave photoconductance studies on thin film samples have been attributed to exciton dissociation.[31, 42]

A classic method to unambiguously determine the binding energy of the Wannier exciton in bulk inorganic semiconductors is to measure the energy spacing between discrete hydrogenic energy levels of the Wannier exciton, which can be observed individually as peaks in the band edge absorption spectrum (according to Elliott's formula)[40-41]at cryogenic temperatures in very high purity samples.[43-45] Nicholas and coworkers[15-16] have recently been able to observe the 1s and 2s band edge exciton peaks of thin-film $CH_3NH_3PbI_3$ under high magnetic fields in the low temperature (2 K) absorption spectra, from which they determined E_B (14-16 meV) for the low temperature orthorhombic phase based on a model for a hydrogenic exciton in a strong magnetic field. As temperature increases and the discrete excitons peaks broaden due to exciton-phonon interactions[46-47]one can still study the band edge absorption spectra when only the $n = 1$ exciton peak is resolved,[48] however the reliability of this method decreases when the exciton binding energy is less than the half-width of the broadening function.[28, 45] While many authors have recently estimated E_B for the tetragonal phase of thin-film $CH_3NH_3PbI_3$ by fitting Elliott's formula to the band edge absorption spectra at temperatures >160K, in all cases the broadening half-width is still > E_B, and the values reported for E_B estimated from this method alone have varied from 6-25 meV.[19, 25-28]

It is well known that modulation spectroscopic techniques provide extremely sharp spectra of individual critical point (CP) absorption features in semiconductors due to the elimination of effects such as optical scattering and background absorption from broad neighboring critical point features[49] that appear in techniques such as ellipsometry or transmission/reflection spectroscopy. For this reason, modulation spectroscopy is often considered a superior technique for the determination of band edge properties in semiconductors.[50-51] Electric-field modulation spectroscopy is highly sensitive to Coulomb correlation effects of Wannier excitons, which makes it an interesting technique for studying exciton effects at critical points.[51-55] Here we use electroabsorption (EA) spectroscopy to provide sharp, derivative-like fundamental absorption edge spectra of $CH_3NH_3PbI_3$ from 210 K to 300 K. We find that the EA spectra at room temperature are represented by a form of the one-electron Franz-Keldysh-Aspnes (FKA) low-field theory[55-57] as opposed to the quadratic Stark effect,[58-60] which explains the third derivative-like $\chi^{(3)}$ EA response measured in our experiment. Using the FKA model with the experimental dielectric function measured from ellipsometry we extract a value for μ of $0.12 \pm 0.03\, m_0$. We further find that when the complex band edge dielectric function is modeled according to Elliott's formula,[40] a third-derivative-like EA analysis for the change in the dielectric function allows us to determine E_B = 7.4 meV (95% CI [6.8-9.2 meV]) and E_g=1.633 ± 0.002 eV.

Section 2.3 Low-field FKA response of $CH_3NH_3PbI_3$ at room temperature

EA sample preparation

We prepared $CH_3NH_3PbI_3$ thin film samples for EA in a dielectric capacitor structure, with a 150-nm-thick perovskite film sandwiched between two insulating layers in between semitransparent contacts (Appendix A and Appendix B section S14 for a schematic). The dielectric capacitor structure for the EA samples avoids injection of charge into the $CH_3NH_3PbI_3$ layer in order to ensure that the modulation response is due only to the applied field. The $CH_3NH_3PbI_3$ films were formed by spin-coating from a lead acetate trihydrate precursor solution,[61] which resulted in smooth, pinhole free films with good optical quality (Appendix B S15 for sample characterization).

$\chi^{(3)}$ EA response in $CH_3NH_3PbI_3$ due to Franz-Keldysh-Aspnes effect

Fig. 2.1 a. shows the room temperature EA spectra measured at linearly increasing AC field strengths, measured at the second harmonic of the fundamental modulation frequency (Ω=1.3 kHz, Appendix B section S12 for a discussion about the selection of the modulation frequency). Detection at the second harmonic is useful for a material such as $CH_3NH_3PbI_3$ that may exhibit piezoelectricity, since field-induced absorption changes due to piezoelectric effects are primarily a linear electro-optical effect and hence are not present in the second harmonic EA signal.[49, 62] The applied field strengths in our experiment (for applied peak-to-peak AC voltages in the range of 4-20 V) fall in the range of 1.4×10^5 V/m to 2.1×10^6 V/m, considering the uncertainty in the 1.3 kHz dielectric constant of $CH_3NH_3PbI_3$ (Appendix B section S6.2).[22, 63] In Fig. 2.1 b. we show the normalized EA spectra for the range of applied voltages used in our experiment. It is clear in Fig. 2.1 b. that the normalized spectra are nearly identical over the measured range of field strength, which demonstrates a field invariance in the functional form of the second harmonic EA response. In the inset of Fig. 2.1 b. we show a log-log plot of the amplitude scaling of peaks I, II, and III as a function of applied bias. The peaks all scale quadratically with field, with the slopes on the log-log plot for all peaks between ~1.9-2.0. The field invariant lineshape and quadratic amplitude scaling in the second harmonic signal demonstrated in Fig. 2.1 b. both identify the EA mechanism as a third-order ($\chi^{(3)}$) nonlinear optical response (Appendix B section S5).[57, 64-65] We note that several other authors have observed a $\chi^{(3)}$ EA response in $CH_3NH_3PbI_3$ (Appendix B section S13 for a discussion on differences between the reported lineshapes and those observed in our experiment).[63, 66]

The $\chi^{(3)}$ EA response is a well-known electro-optical effect that can be attributed either to the excitonic quadratic Stark effect[54, 60, 64-65] or the one-electron low-field Franz-Keldysh-Aspnes (FKA) effect.[49, 57, 67] The Stark effect is the perturbation treatment of an exciton in an electric field,[58] and applies theoretically when the potential drop across the exciton caused by the external electric field is small compared to either the Coulomb or confining potential of the exciton.[53-54, 58] The quadratic Stark effect is typically seen in EA spectra of small molecules,[60, 68] semiconducting polymers,[64, 69-70] and quantum well/dot systems.[71-72] The FKA effect is an exact solution for the change in the joint density-of-states (JDOS) function at critical points in the electronic band

structure when one-electron theory is used to describe the electronic states of a semiconductor.[50, 56, 73] The FKA effect has been observed in many bulk inorganic semiconductors at field strengths comparable with our experiment,[49-50, 55-56, 74] and is generally a complicated function of applied field. However in the early 1970's Aspnes and Rowe showed that when homogeneous broadening is introduced into the calculation for the change in the complex dielectric function ($\Delta\epsilon = \Delta\epsilon_r + i\Delta\epsilon_i$) based on the field-perturbed JDOS function, there is a low-field limit in which the electromodulation signal simplifies to a $\chi^{(3)}$ type response.[57, 75] In low-field FKA theory, the change in the optical dielectric function is related to the third derivative of the unperturbed complex dielectric function ($\epsilon = \epsilon_r + i\epsilon_i$): [57, 75]

$$\Delta\epsilon(E,F) = \frac{\hbar\Omega^3}{3}\frac{1}{E^2}\frac{d^3}{dE^3}\left(E^2\epsilon(E,0)\right) \qquad Eq(1.a.)$$

$$E = photon\ energy, \qquad F = applied\ external\ field\ strength$$

$$\hbar\Omega^3 = \frac{e^2F^2\hbar^2}{8\mu} \qquad Eq(1.b.)$$

The amplitude scaling term $\hbar\Omega$ in Eq. 1a. is the electro-optical energy, which is related to the energy gain of band electrons due to their acceleration by the applied electric field.[49] The electro-optical energy cubed $\hbar\Omega^3$ depends on the carrier reduced effective mass μ and the square of the electric field F^2 (Eq 1.b). The low-field limit is defined for $\hbar\Omega < \frac{1}{3}\Gamma$, where Γ is the homogeneous linewidth.[57] Given the most recent literature estimates of a small E_B in thin-film tetragonal $CH_3NH_3PbI_3$ on the order of ~10meV or less,[16, 25] we hypothesize that the EA response will be related to the FKA effect, as has been observed in other bulk semiconductors with $E_B <$ 10meV at comparable applied field strengths.[50]

One test of the validity of the low-field FKA model for EA analysis is to fit the experimental EA spectrum to Eq.1a. with the $\frac{d^3}{dE^3}E^2\epsilon$ term calculated numerically from the third derivative of the experimentally measured complex dielectric spectrum to yield a value for the reduced effective mass, μ.[75] In Fig. 2.1 c. we show the fit of Eq. 1a. to the EA data by varying only the amplitude $\hbar\Omega^3$, with the experimental complex ϵ obtained from ellipsometry shown in the inset (for details on the ellipsometry analysis see Appendx B section S3). We note that for this fit, and all other fits to the EA data and in this manuscript, the theoretical line shapes for $\Delta\epsilon$ were used in conjunction with the spectra of the complex refractive index measured from ellipsometry as input to a transfer matrix optical model[76] to simulate the resulting $\Delta T/T$. Transfer matrix optical modelling accounts for the effects of refractive index changes and thin film optical interference in the field modulated (ΔT) and unperturbed (T) transmittance through the device stack (see Appendix B section S4 for details), and thus allows for quantitative comparison between the measured $\Delta T/T$ and the modeled $\Delta\epsilon$ in Eq. 1.a. It is clear from examining Fig. 2.1 c. that all of the features in the EA spectrum, including their positions and relative heights, can be represented well by the third derivative form in Eq.1.a when we use the experimental complex ϵ measured from ellipsometry. Importantly, by fitting the amplitude $\hbar\Omega^3$ of the third derivative model in Eq 1.a. to the experimental data, we obtain a value for the carrier reduced effective mass of $\mu = 0.12 \pm$

$0.03m_0$ (Appendix B section S6.3 for details), where the error is determined by the uncertainty in the 1.3 kHz dielectric constant of our samples (Appendix B section S6.2). This value is in excellent agreement with recent experimental and theoretical estimates of the carrier reduced effective mass $(\sim 0.1 - 0.14m_0)$[15, 26, 77] and provides support for using the FKA model in our analysis.[75] Furthermore, we note that the value that we extract for the amplitude scaling term $\hbar\Omega$ (~5 meV for the maximum applied voltage V_{AC} = 20) is much smaller than the linewidth $\frac{1}{3}\Gamma$ for all reasonable values of Γ at room temperature (Appendix B section S11), which is consistent with the definition of the low-field limit in FKA theory. We note that the slight discrepancies between peak position and relative heights in the transfer matrix simulation and the EA spectrum shown in Fig. 2.1 c. can be largely attributed to interference effects resulting from the small uncertainty in the thicknesses and/or dielectric constants of the dielectric layers. The small errors in peak position from fitting the experimental complex ϵ to the EA spectrum will not affect our subsequent analysis of the exciton binding energy and band gap.

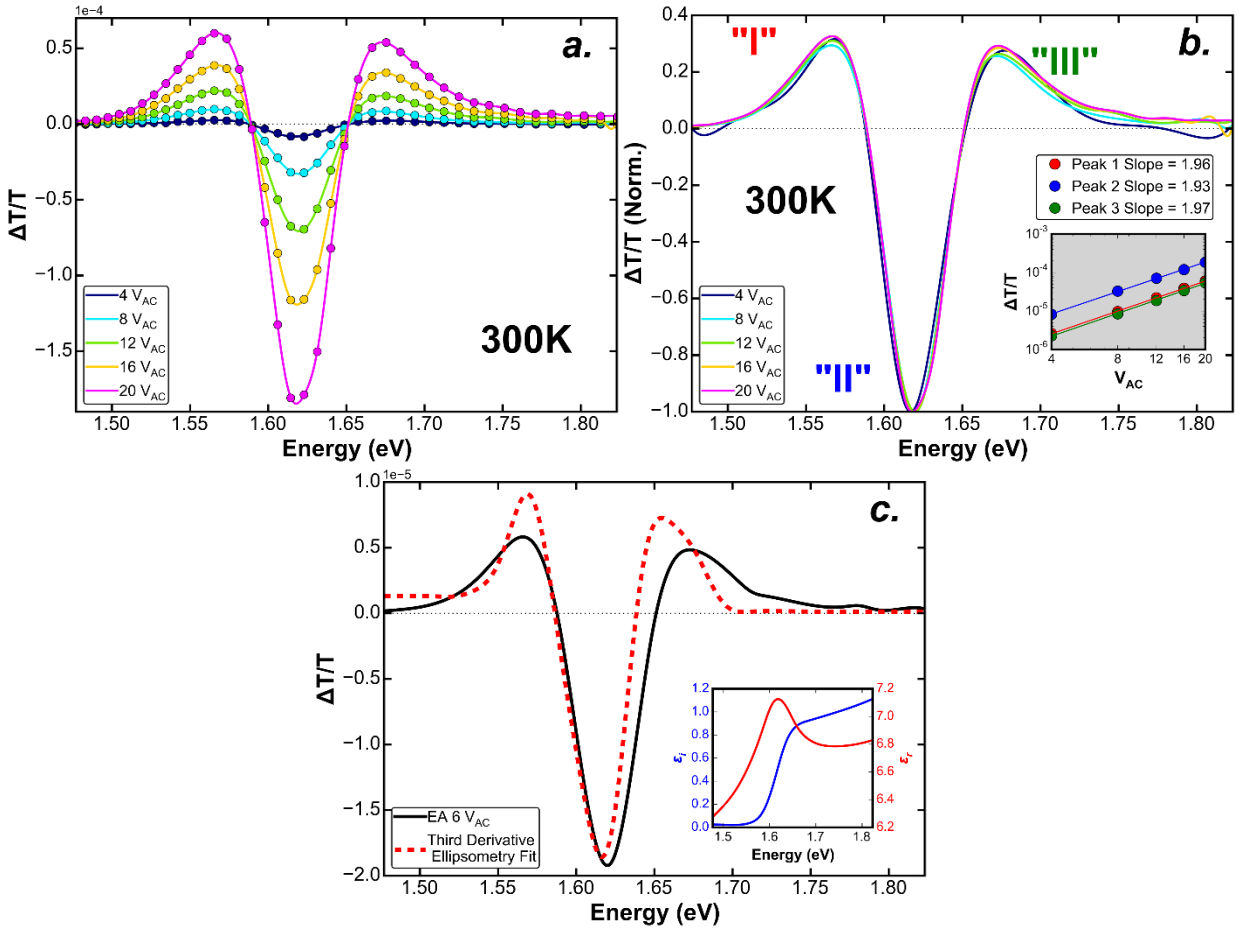

Figure 2.1 *a.)* EA spectra detected at the second harmonic of the electric-field modulation frequency for linearly increasing modulation voltages, measured at 300 K. The dots are the experimentally measured data points and the solid lines are spline fits to the data. *b.)* Amplitude normalized EA spectra (spline fits) showing the field invariance of the lineshape and (inset) quadratic field dependence of peak amplitudes, which demonstrates that the EA spectra are

characteristic of a $\chi^{(3)}$response. The colors of the markers in the inset correspond to the color labels of the peaks "I," "II," and "III." The extrema of Peaks "I", "II", and "III" were determined from the roots of the first derivative of the spline fits. *c.)* Comparison of the EA spectrum with the FKA third derivative formula of the unperturbed dielectric function (Eq. 1). The unperturbed complex dielectric function measured with ellipsometry (shown in the *inset*) was differentiated numerically and fit to the EA spectrum allowing $\hbar\Omega$ to vary.

Describing the Wannier excitonic contribution to the $\chi^{(3)}$ EA response with Elliot function

We now consider the excitonic contribution to the EA response within the framework of FKA theory. It has been shown both theoretically through a "contact exciton" model,[78-79] as well as experimentally through extensive electroreflectance studies on Ge,[80-81] that in the limit where the bound states of the exciton are effectively "mixed" with the continuum it is possible to describe Wannier exciton effects in the $\chi^{(3)}$ EA response using low-field FKA theory. In this limit, the EA response can be thought of largely in terms of the modulation of a Coulomb-modified continuum of states,[78, 80] and one can replace $\epsilon(E,0)$ in Eq 1.a. with a model dielectric function for a Wannier exciton.[80, 82] The "mixing" of the exciton bound states with the continuum in zero applied field is due to the ionization of bound states caused by excitonic interband scattering phenomena resulting from interactions between excitons and LO-phonons,[47] or by field ionization due to microscopic heterogeneity in the electrostatic potential energy surface from charged impurity sites within the polycrystalline sample.[83] To a first approximation, these ionization effects result in a homogeneous broadening of the exciton linewidth that can be modelled by a phenomenological parameter Γ when Elliott's function is used for $\epsilon(E,0)$. Given the accuracy of our calculated value of μ and good lineshape agreement from the $\chi^{(3)}$ FKA analysis for the room temperature data shown Fig. 2.1 c., we hypothesize that the low-field FKA model can be used to describe the $\chi^{(3)}$ EA response at 300 K by substituting Elliott's function[40] (Appendix B section S1) as a model dielectric function for $\epsilon(E,0)$ in Eq 1.a (which we will refer to as the "third derivative Elliott model").

In Fig. 2 a. we test this hypothesis by showing the fit to the room temperature EA spectrum obtained by varying the parameters E_B, E_g and Γ in the third derivative Elliott model and calculating $\Delta T/T$ from the modelled $\Delta\epsilon$ using transfer matrix modelling. The fit is excellent, giving best fit values of E_B = 7.4 meV and E_g = 1.633 eV with a 95% confidence interval spanning 6.8-9.2 meV for E_B and 1.631-1.635 eV for E_g as determined by a non-linear curve-fitting algorithm for Python.[84] This confidence interval is also consistent with a simple statistical analysis of the best fit values of multiple samples and field strengths (Appendix B section S4.2). Our value of E_B is in agreement with the observations from magneto-optical studies that the exciton binding energy in should fall below 16 meV for the tetragonal phase of $CH_3NH_3PbI_3$.[15] In order to confirm the accuracy of our fitting approach, we also fit a low-field electroreflectance (ER) spectrum of GaAs[85] (Fig. 2b.) from the literature (Appendix B section S2 for discussion on modeling the ER spectrum). The fit also captures the GaAs lineshape very well and the best fit parameters (E_B = 3.8 meV, E_g = 1.517) agree well with known values for GaAs (E_B = 4.2 meV, E_g = 1.5114).[86] We note that we used a global minimization algorithm for the fitting with boundaries over a wide parameter

space and no initial values. The accuracy of the best fit parameters for GaAs compared to the literature values demonstrates that in the low-field FKA limit, the third derivative Elliott method can be used to extract meaningful values for E_B and E_g.

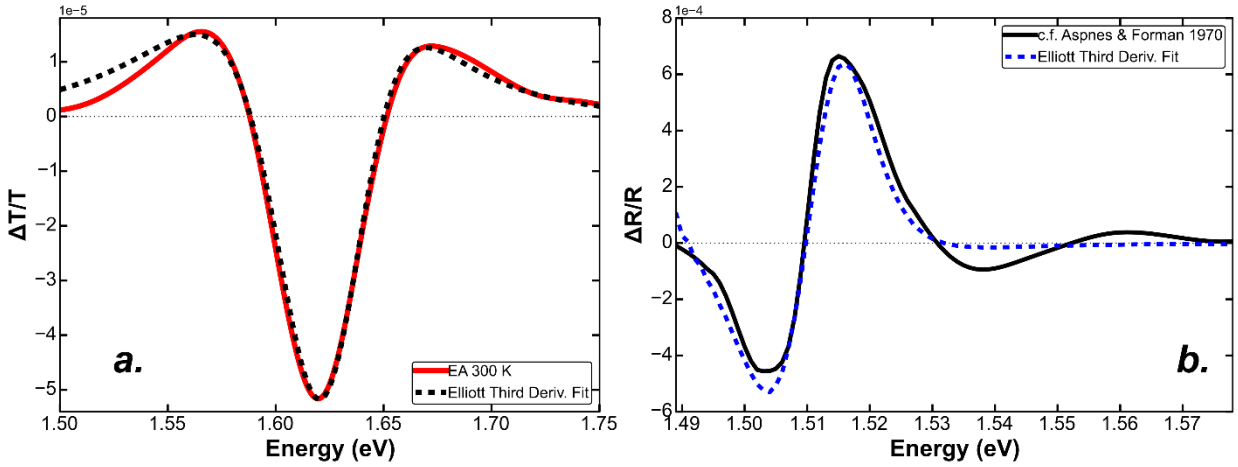

Figure 2.2 ***a.)*** Room temperature EA spectrum (solid line) and fit (dotted line) of $CH_3NH_3PbI_3$ using the third-derivative-Elliott with an exciton binding energy E_B = 7.4 ± 2 meV and band gap E_g = 1.633 ± 0.003 eV. ***b.)*** Fit of the low-field electroreflectance spectrum of GaAs from Forman *et al.*[72] to the third-derivative-Elliott model. The best fit parameters (E_B = 3.8 meV, E_g = 1.517) agree well with the accepted values for GaAs.

Having established the low-field FKA response of $CH_3NH_3PbI_3$ at room temperature based on the lineshape and effective mass analysis, and having demonstrated the use of the third derivative Elliott model to extract an accurate value of E_B in the low field FKA limit, we now have the information necessary (E_B and μ) to firmly validate our analysis on $CH_3NH_3PbI_3$ by comparing the EA response with exact predictions for a Wannier exciton in an electric field.[51, 54] Using the value of E_B calculated from the third derivative Elliott model along with the value of μ calculated from the third derivative of the ϵ_i spectrum measured with ellipsometry, we can estimate a value of 15 for the effective relative dielectric constant ϵ_{eff} that contributes to the screening of the electron-hole Coulomb interaction according to the hydrogenic exciton model.[54] Furthermore, knowing E_B, μ and ϵ_{eff}, we can calculate the ionization field of the exciton F_I (Eq. 2.), which is defined as the field required to cause a potential drop of E_B across the exciton radius.[54]

$$F_I = \frac{eE_B\mu}{4\pi\epsilon_0\epsilon_{eff}\hbar^2} \qquad Eq\ 2.$$

Section 2.4. Field ionization of the Wannier exciton at low temperature

In Appendix B, we show through numerical modelling of a Wannier exciton in an electric field[54] that based on the ratio of experimental applied field strengths to the ionization field of the exciton (F/F_I), we are right at the experimental threshold where theory predicts both the breakdown of the quadratic Stark shift and the quantum mechanical field ionization of the $n = 1$ exciton (Appendix B section S7 and S8). At reduced temperatures, where *thermal* ionization diminishes, we might then expect to see effects in the EA spectrum related to *field* ionization of the exciton, which are known to deviate from the predictions of one electron FKA theory.[51, 53-54] In Fig. 2.3 a. we show the normalized second harmonic EA spectra at 210 K for the same range of applied voltages as the room temperature experiments. We can see that in the high energy wing of the EA spectrum (Peak III) at 210 K, the lineshape begins to show deviations from field-invariant behavior, an effect which we observed at 210 K in multiple samples (Appendix B section S10 for full data) and is a deviation from low-field FKA theory. Notably, this field dependent increase in the relative amplitude of Peak III with respect to Peak I in the EA spectrum has been observed previously as an experimental signature of $n = 1$ exciton ionization in single crystals of PbI_2.[51, 87] In the inset of Fig. 2.3 a. we show that the amplitude scaling of Peak III with field at 210 K can also be seen to show deviation from a quadratic field dependence, consistent with the rapid broadening process of the $n = 1$ exciton near the field ionization threshold (Appendix B section S7).

The observation of signatures related to field ionization of the exciton at reduced temperatures in the EA spectrum is also consistent with the temperature dependent evolution of the absorption spectrum, where previous studies have noted the appearance of an exciton peak in the linear absorption spectrum at reduced temperatures.[17, 19, 88] In Fig. 2.3 b. we confirm that for our samples the development of a weak exciton feature becomes evident in the absorption spectrum upon cooling from room temperature to 210 K. The fact that we are able to observe signatures of field ionization of the $n = 1$ exciton in the EA spectrum at reduced temperatures as predicted based on our calculated value of the ionization field (F_I) provides firm experimental validation for our assigned values of E_B and μ, and further supports our use of low-field FKA analysis and third derivative Elliott fitting for the EA spectra at room temperature, where thermal ionization effects will become more important.[47]

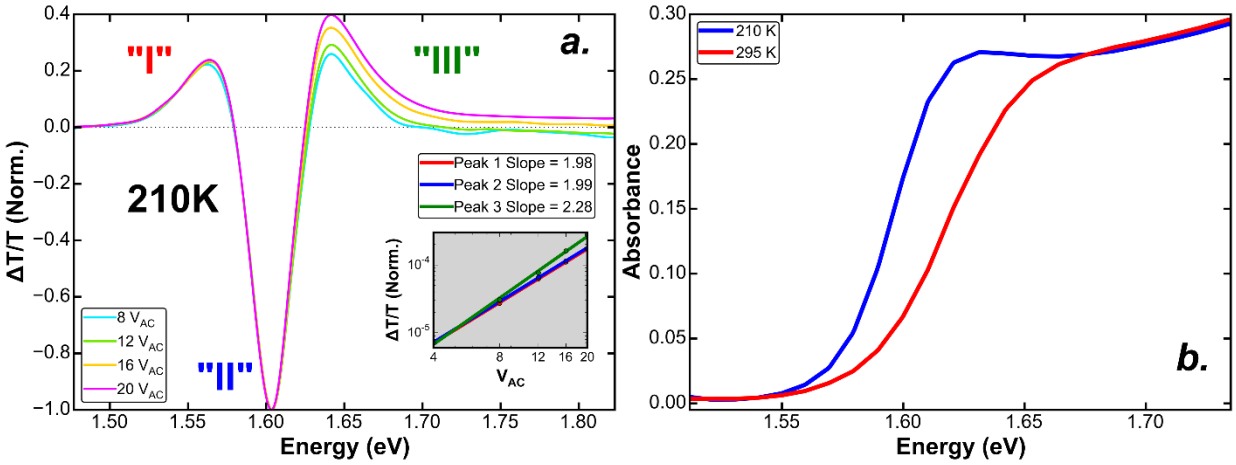

Figure 2.3 ***a.)*** Amplitude normalized EA spectra at 210K, showing the variation in lineshape with field for Peak "III," which can be attributed to field ionization of the $n = 1$ exciton. Inset: field dependence of peak amplitudes, showing deviation from quadratic scaling for Peak "III." ***b.)*** Temperature dependent absorption spectrum showing the development of a weak exciton peak at 210 K, consistent with the observations of field ionization of the exciton at 210 K in the EA spectrum.

Section 2.5. Conclusion

We have measured EA spectra at the fundamental absorption edge in thin film $CH_3NH_3PbI_3$ and have shown that at 300K the $\chi^{(3)}$EA response can be interpreted in terms of the one electron low-field FKA theory. The observation of the low-field FKA effect in $CH_3NH_3PbI_3$ at room temperature provides direct experimental evidence that the primary *photo-excitations* (as opposed to recombination mechanisms) can be described in terms of free carrier generation as transitions to a Coulomb-modified continuum of states, as was indeed previously suggested by Saba *et al.* on the basis of analyzing recombination dynamics.[19] Using low-field FKA theory to interpret the EA spectrum with the complex dielectric function measured from ellipsometry, we have calculated a value for the electron-hole reduced effective mass of $\mu = 0.12 \pm 0.03 m_0$, which is in excellent agreement with previous experimental and theoretical estimates and indicates that the room temperature EA response is due to the low-field FKA effect. By utilizing Elliott's function as a model for the complex ϵ in the low-field FKA formula, we have measured an exciton binding energy of 7.4 meV (95% CI [6.8-9.2 meV]) and band gap of 1.633 ± 0.002 eV for the tetragonal phase of $CH_3NH_3PbI_3$ at room temperature. Additionally, the separate determination of E_B and μ allowed us to estimate a value for ϵ_{eff} of 15. Interestingly, we point out that our calculated value for ϵ_{eff} of 15 coincides with the value of ϵ_r measured by Wehrenfennig *et al.*[36] at the phonon resonances associated with vibrations of the Pb-I cage (~1 and 2 THz)[36, 89-90] in the low-frequency THz spectrum. This agreement may highlight the fact that at room temperature the exciton-phonon interactions need to be considered[15-16, 39, 88] and is in agreement with our conclusion from the observed FKA effect that exciton-phonon interactions may result in a substantial "mixing" of bound exciton states with the continuum at room temperature.[47]

Our values of E_B, μ and ϵ_{eff} are all in excellent agreement with the most recent experimental estimates based on magneto-absorption[16] and transient absorption measurements,[25-26] but our E_B = 7.4 meV (95% CI [6.8-9.2 meV]) tends to the lower end of the wide range (6 – 25 meV) of results that have been reported from linear absorption data alone.[19, 27-29] Compared to other measurements in the literature, we note that this value for E_B in particular has the advantage of the inherent sensitivity of the third derivative-like EA response to the curvature of the dielectric function at the band edge critical point, removing background effects due to the nature of the modulation experiment and thus to overcoming some of the uncertainty inherent in fitting transmittance/reflectance or ellipsometry measurements.[50] Our collective results also strongly suggest that the room temperature EA response is not related to the quadratic Stark shift of an exciton. If the room temperature $\chi^{(3)}$ EA response were due to the quadratic Stark effect, we would not expect to see a breakdown in the quadratic field dependence or field invariance of the EA lineshape as temperature is reduced. In contrast, we observe a $\chi^{(3)}$ EA response at room temperature that satisfies the predictions of low-field FKA analysis, along with signatures of field induced ionization of the $n = 1$ exciton when the sample is cooled to 210 K. These results are consistent with a picture of phonon-mediated "mixing" between bound and continuum states of the Wannier exciton that results in a continuum-like band-edge response at room temperature.[47] These results provide an insight into the fundamental physical mechanism responsible for the EA response and the physical nature of band edge photoexcitations in $CH_3NH_3PbI_3$.

In this project, we have focused on characterization of $CH_3NH_3PbI_3$ perovskite samples fabricated by a popular lead acetate precursor route that produced films with good optical and optoelectronic quality.[61] Recent studies have suggested that the exciton binding energy in $CH_3NH_3PbI_3$ films may depend on film microstructure.[39] We therefore anticipate that a future study could use the methods presented herein to test this hypothesis by comparing systematically the binding exciton energies and bandgaps obtained from perovskites prepared by a range of growth processes. Our study provides a framework for the interpretation of future electroabsorption and other spectroscopic experiments on hybrid organic-inorganic perovskites.

Appendix A

Experimental Methods and Supplementary Information for Chapter 2

References

1. Deschler, F.; Price, M.; Pathak, S.; Klintberg, L. E.; Jarausch, D. D.; Higler, R.; Huttner, S.; Leijtens, T.; Stranks, S. D.; Snaith, H. J.; Atature, M.; Phillips, R. T.; Friend, R. H., High Photoluminescence Efficiency and Optically Pumped Lasing in Solution-Processed Mixed Halide Perovskite Semiconductors. *J. Phys. Chem. Lett.* **2014,** *5* (8), 1421-6.
2. Xing, G.; Mathews, N.; Lim, S. S.; Yantara, N.; Liu, X.; Sabba, D.; Gratzel, M.; Mhaisalkar, S.; Sum, T. C., Low-temperature solution-processed wavelength-tunable perovskites for lasing. *Nat. Mater.* **2014,** *13* (5), 476-80.
3. Cho, H.; Jeong, S. H.; Park, M. H.; Kim, Y. H.; Wolf, C.; Lee, C. L.; Heo, J. H.; Sadhanala, A.; Myoung, N.; Yoo, S.; Im, S. H.; Friend, R. H.; Lee, T. W., Overcoming the electroluminescence efficiency limitations of perovskite light-emitting diodes. *Science* **2015,** *350* (6265), 1222-5.
4. Zhou, H.; Chen, Q.; Li, G.; Luo, S.; Song, T. B.; Duan, H. S.; Hong, Z.; You, J.; Liu, Y.; Yang, Y., Interface engineering of highly efficient perovskite solar cells. *Science* **2014,** *345* (6196), 542-6.
5. Yang, W. S.; Noh, J. H.; Jeon, N. J.; Kim, Y. C.; Ryu, S.; Seo, J.; Seok, S. I., High-performance photovoltaic perovskite layers fabricated through intramolecular exchange. *Science* **2015,** *348* (6240), 1234-7.
6. Bi, D.; Tress, W.; Dar, M. I.; Gao, P.; Luo, J.; Renevier, C.; Schenk, K.; Abate, A.; Giordano, F.; Correa Baena, J. P.; Decoppet, J. D.; Zakeeruddin, S. M.; Nazeeruddin, M. K.; Gratzel, M.; Hagfeldt, A., Efficient luminescent solar cells based on tailored mixed-cation perovskites. *Sci. Adv.* **2016,** *2* (1), e1501170.
7. Lee, M. M.; Teuscher, J.; Miyasaka, T.; Murakami, T. N.; Snaith, H. J., Efficient hybrid solar cells based on meso-superstructured organometal halide perovskites. *Science* **2012,** *338* (6107), 643-7.
8. Etgar, L.; Gao, P.; Xue, Z.; Peng, Q.; Chandiran, A. K.; Liu, B.; Nazeeruddin, M. K.; Gratzel, M., Mesoscopic $CH_3NH_3PbI_3/TiO_2$ heterojunction solar cells. *J. Am. Chem. Soc.* **2012,** *134* (42), 17396-9.
9. Stranks, S. D.; Eperon, G. E.; Grancini, G.; Menelaou, C.; Alcocer, M. J.; Leijtens, T.; Herz, L. M.; Petrozza, A.; Snaith, H. J., Electron-hole diffusion lengths exceeding 1 micrometer in an organometal trihalide perovskite absorber. *Science* **2013,** *342* (6156), 341-4.
10. Guo, Z.; Manser, J. S.; Wan, Y.; Kamat, P. V.; Huang, L., Spatial and temporal imaging of long-range charge transport in perovskite thin films by ultrafast microscopy. *Nat. Commun.* **2015,** *6*, 7471.
11. Xing, G.; Mathews, N.; Sun, S.; Lim, S. S.; Lam, Y. M.; Gratzel, M.; Mhaisalkar, S.; Sum, T. C., Long-range balanced electron- and hole-transport lengths in organic-inorganic $CH_3NH_3PbI_3$. *Science* **2013,** *342* (6156), 344-7.
12. Tvingstedt, K.; Malinkiewicz, O.; Baumann, A.; Deibel, C.; Snaith, H. J.; Dyakonov, V.; Bolink, H. J., Radiative efficiency of lead iodide based perovskite solar cells. *Sci. Rep.* **2014,** *4*, 6071.
13. Pazos-Outon, L. M.; Szumilo, M.; Lamboll, R.; Richter, J. M.; Crespo-Quesada, M.; Abdi-Jalebi, M.; Beeson, H. J.; Vrucinic, M.; Alsari, M.; Snaith, H. J.; Ehrler, B.; Friend, R. H.; Deschler, F., Photon recycling in lead iodide perovskite solar cells. *Science* **2016,** *351* (6280), 1430-3.

14. Ball, J. M.; Stranks, S. D.; Hoerantner, M. T.; Huettner, S.; Zhang, W.; Crossland, E. J. W.; Ramirez, I.; Riede, M.; Johnston, M. B.; Friend, R. H.; Snaith, H. J., Optical properties and limiting photocurrent of thin-film perovskite solar cells. *Energy Environ. Sci.* **2015,** *8* (2), 602-609.
15. Miyata, A.; Mitioglu, A.; Plochocka, P.; Portugall, O.; Wang, J. T.-W.; Stranks, S. D.; Snaith, H. J.; Nicholas, R. J., Direct measurement of the exciton binding energy and effective masses for charge carriers in organic–inorganic tri-halide perovskites. *Nat. Phys.* **2015,** *11* (7), 582-587.
16. Galkowski, K.; Mitioglu, A.; Miyata, A.; Plochocka, P.; Portugall, O.; Eperon, G. E.; Wang, J. T. W.; Stergiopoulos, T.; Stranks, S. D.; Snaith, H. J.; Nicholas, R. J., Determination of the exciton binding energy and effective masses for methylammonium and formamidinium lead tri-halide perovskite semiconductors. *Energy Environ. Sci.* **2016,** *9* (3), 962-970.
17. D'Innocenzo, V.; Grancini, G.; Alcocer, M. J.; Kandada, A. R.; Stranks, S. D.; Lee, M. M.; Lanzani, G.; Snaith, H. J.; Petrozza, A., Excitons versus free charges in organo-lead tri-halide perovskites. *Nat. Commun.* **2014,** *5*, 3586.
18. Stranks, S. D.; Burlakov, V. M.; Leijtens, T.; Ball, J. M.; Goriely, A.; Snaith, H. J., Recombination Kinetics in Organic-Inorganic Perovskites: Excitons, Free Charge, and Subgap States. *Phys. Rev. Appl.* **2014,** *2* (3), 034007.
19. Saba, M.; Cadelano, M.; Marongiu, D.; Chen, F.; Sarritzu, V.; Sestu, N.; Figus, C.; Aresti, M.; Piras, R.; Lehmann, A. G.; Cannas, C.; Musinu, A.; Quochi, F.; Mura, A.; Bongiovanni, G., Correlated electron-hole plasma in organometal perovskites. *Nat. Commun.* **2014,** *5*, 5049.
20. Onoda-Yamamuro, N.; Matsuo, T.; Suga, H., Calorimetric and IR spectroscopic studies of phase transitions in methylammonium trihalogenoplumbates (II). *J. Phys. Chem. Solids* **1990,** *51* (12), 1383-1395.
21. Mitzi, D. B., Synthesis, Structure, and Properties of Organic-Inorganic Perovskites and Related Materials. *Prog. Inorg. Chem.* **1999,** *48*, 1-121.
22. Lin, Q.; Armin, A.; Nagiri, R. C. R.; Burn, P. L.; Meredith, P., Electro-optics of perovskite solar cells. *Nat. Photon.* **2014,** *9* (2), 106-112.
23. Valverde-Chávez, D. A.; Ponseca, C. S.; Stoumpos, C. C.; Yartsev, A.; Kanatzidis, M. G.; Sundström, V.; Cooke, D. G., Intrinsic femtosecond charge generation dynamics in single crystal $CH_3NH_3PbI_3$. *Energy Environ. Sci.* **2015,** *8* (12), 3700-3707.
24. Sun, S.; Salim, T.; Mathews, N.; Duchamp, M.; Boothroyd, C.; Xing, G.; Sum, T. C.; Lam, Y. M., The origin of high efficiency in low-temperature solution-processable bilayer organometal halide hybrid solar cells. *Energy Environ. Sci.* **2014,** *7* (1), 399-407.
25. Yang, Y.; Ostrowski, D. P.; France, R. M.; Zhu, K.; van de Lagemaat, J.; Luther, J. M.; Beard, M. C., Observation of a hot-phonon bottleneck in lead-iodide perovskites. *Nat. Photon.* **2015,** *10* (1), 53-59.
26. Price, M. B.; Butkus, J.; Jellicoe, T. C.; Sadhanala, A.; Briane, A.; Halpert, J. E.; Broch, K.; Hodgkiss, J. M.; Friend, R. H.; Deschler, F., Hot-carrier cooling and photoinduced refractive index changes in organic-inorganic lead halide perovskites. *Nat. Commun.* **2015,** *6*, 8420.
27. Green, M. A.; Jiang, Y.; Soufiani, A. M.; Ho-Baillie, A., Optical Properties of Photovoltaic Organic-Inorganic Lead Halide Perovskites. *J. Phys. Chem. Lett.* **2015**, 4774-4785.

28. Sestu, N.; Cadelano, M.; Sarritzu, V.; Chen, F.; Marongiu, D.; Piras, R.; Mainas, M.; Quochi, F.; Saba, M.; Mura, A.; Bongiovanni, G., Absorption F-Sum Rule for the Exciton Binding Energy in Methylammonium Lead Halide Perovskites. *J. Phys. Chem. Lett.* **2015,** *6* (22), 4566-72.
29. Yamada, Y.; Nakamura, T.; Endo, M.; Wakamiya, A.; Kanemitsu, Y., Photoelectronic Responses in Solution-Processed Perovskite $CH_3NH_3PbI_3$ Solar Cells Studied by Photoluminescence and Photoabsorption Spectroscopy. *IEEE J. Photovolt.* **2015,** *5* (1), 401-405.
30. Even, J.; Pedesseau, L.; Katan, C., Analysis of Multivalley and Multibandgap Absorption and Enhancement of Free Carriers Related to Exciton Screening in Hybrid Perovskites. *J. Phys. Chem. C* **2014,** *118* (22), 11566-11572.
31. Savenije, T. J.; Ponseca, C. S.; Kunneman, L.; Abdellah, M.; Zheng, K.; Tian, Y.; Zhu, Q.; Canton, S. E.; Scheblykin, I. G.; Pullerits, T.; Yartsev, A.; Sundström, V., Thermally Activated Exciton Dissociation and Recombination Control the Carrier Dynamics in Organometal Halide Perovskite. *J. Phys. Chem. Lett.* **2014,** *5* (13), 2189-2194.
32. Hu, M.; Bi, C.; Yuan, Y.; Xiao, Z.; Dong, Q.; Shao, Y.; Huang, J., Distinct exciton dissociation behavior of organolead trihalide perovskite and excitonic semiconductors studied in the same system. *Small* **2015,** *11* (18), 2164-9.
33. Yamada, Y.; Nakamura, T.; Endo, M.; Wakamiya, A.; Kanemitsu, Y., Photocarrier recombination dynamics in perovskite $CH_3NH_3PbI_3$ for solar cell applications. *J. Am. Chem. Soc.* **2014,** *136* (33), 11610-3.
34. Hutter, E. M.; Eperon, G. E.; Stranks, S. D.; Savenije, T. J., Charge Carriers in Planar and Meso-Structured Organic–Inorganic Perovskites: Mobilities, Lifetimes, and Concentrations of Trap States. *J. Phys. Chem. Lett.* **2015,** *6* (15), 3082-3090.
35. deQuilettes, D. W.; Vorpahl, S. M.; Stranks, S. D.; Nagaoka, H.; Eperon, G. E.; Ziffer, M. E.; Snaith, H. J.; Ginger, D. S., Impact of microstructure on local carrier lifetime in perovskite solar cells. *Science* **2015,** *348* (6235), 683-6.
36. Wehrenfennig, C.; Liu, M.; Snaith, H. J.; Johnston, M. B.; Herz, L. M., Charge-carrier dynamics in vapour-deposited films of the organolead halide perovskite $CH_3NH_3PbI_{3-x}Cl_x$. *Energy Environ. Sci.* **2014,** *7* (7), 2269.
37. La-o-vorakiat, C.; Salim, T.; Kadro, J.; Khuc, M. T.; Haselsberger, R.; Cheng, L.; Xia, H.; Gurzadyan, G. G.; Su, H.; Lam, Y. M.; Marcus, R. A.; Michel-Beyerle, M. E.; Chia, E. E., Elucidating the role of disorder and free-carrier recombination kinetics in $CH_3NH_3PbI_3$ perovskite films. *Nat. Commun.* **2015,** *6*, 7903.
38. Sheng, C.; Zhang, C.; Zhai, Y.; Mielczarek, K.; Wang, W.; Ma, W.; Zakhidov, A.; Vardeny, Z. V., Exciton versus free carrier photogeneration in organometal trihalide perovskites probed by broadband ultrafast polarization memory dynamics. *Phys. Rev. Lett.* **2015,** *114* (11), 116601.
39. Grancini, G.; Srimath Kandada, A. R.; Frost, J. M.; Barker, A. J.; De Bastiani, M.; Gandini, M.; Marras, S.; Lanzani, G.; Walsh, A.; Petrozza, A., Role of Microstructure in the Electron-Hole Interaction of Hybrid Lead-Halide Perovskites. *Nat. Photon.* **2015,** *9* (10), 695-701.
40. Elliott, R. J., Intensity of Optical Absorption by Excitons. *Phys. Rev.* **1957,** *108* (6), 1384-1389.
41. Elliott, R. J., Theory of Excitons: I. In *Polarons and Excitons*, Kuper, C. G.; Whitefield, G. D., Eds. Oliver and Boyd: Edinburgh, 1963; pp 269-293.

42. Ponseca, C. S., Jr.; Savenije, T. J.; Abdellah, M.; Zheng, K.; Yartsev, A.; Pascher, T.; Harlang, T.; Chabera, P.; Pullerits, T.; Stepanov, A.; Wolf, J. P.; Sundstrom, V., Organometal halide perovskite solar cell materials rationalized: ultrafast charge generation, high and microsecond-long balanced mobilities, and slow recombination. *J. Am. Chem. Soc.* **2014,** *136* (14), 5189-92.
43. Sell, D. D., Resolved Free-Exciton Transitions in the Optical-Absorption Spectrum of GaAs. *Phys. Rev. B* **1972,** *6* (10), 3750-3753.
44. Camassel, J.; Merle, P.; Mathieu, H.; Chevy, A., Excitonic absorption edge of indium selenide. *Phys. Rev. B* **1978,** *17* (12), 4718-4725.
45. Le Toullec, R.; Piccioli, N.; Chervin, J. C., Optical properties of the band-edge exciton in GaSe crystals at 10 K. *Phys. Rev. B* **1980,** *22* (12), 6162-6170.
46. Toyozawa, Y., Theory of Line-Shapes of the Exciton Absorption Bands. *Prog. Theor. Phys.* **1958,** *20* (1), 53-81.
47. Rudin, S.; Reinecke, T. L.; Segall, B., Temperature-dependent exciton linewidths in semiconductors. *Phys. Rev. B* **1990,** *42* (17), 11218-11231.
48. Sell, D. D.; Lawaetz, P., New Analysis of Direct Exciton Transitions - Application to Gap. *Phys. Rev. Lett.* **1971,** *26* (6), 311-314.
49. Aspnes, D. E., Third-Derivative Modulation Spectroscopy with Low-Field Electroreflectance. *Surf. Sci.* **1973,** *37* (1), 418-442.
50. Cardona, M., *Modulation Spectroscopy*. Academic Press: New York, New York, 1969.
51. Blossey, D., Wannier Exciton in an Electric Field. II. Electroabsorption in Direct-Band-Gap Solids. *Phys. Rev. B* **1971,** *3* (4), 1382-1391.
52. Dow, J. D.; Lao, B. Y.; Newman, S. A., Differential Electroabsorption. *Phys. Rev. B* **1971,** *3* (8), 2571-2581.
53. Dow, J.; Redfield, D., Electroabsorption in Semiconductors: The Excitonic Absorption Edge. *Phys. Rev. B* **1970,** *1* (8), 3358-3371.
54. Blossey, D., Wannier Exciton in an Electric Field. I. Optical Absorption by Bound and Continuum States. *Phys. Rev. B* **1970,** *2* (10), 3976-3990.
55. Aspnes, D. E., Modulation Spectroscopy/Electric Field Effects on the Dielectric Function of Semiconductors. In *Handbook on Semiconductors*, Balkanski, M., Ed. North-Holland Publishing Co.: Amsterdam, 1980; Vol. 2, pp 109-154.
56. Yu, P. Y.; Cardona, M., *Fundamentals of Semiconductors*. Springer: Heidelberg, 2010.
57. Aspnes, D. E.; Rowe, J. E., Resonant Nonlinear Optical Susceptibility: Electroreflectance in the Low-Field Limit. *Phys. Rev. B* **1972,** *5* (10), 4022-4030.
58. Landau, L. D.; Lifshitz, E. M., *Quantum Mechanics: Non-Relativistic Theory*. 2 ed.; Pergamon Press: Oxford, 1965.
59. Fauchier, J.; Dow, J. D., An analytic approach to the hydrogen Stark effect in weak, strong, and ultrastrong fields. *Phys. Rev. A* **1974,** *9* (1), 98-107.
60. Bublitz, G. U.; Boxer, S. G., Stark spectroscopy: applications in chemistry, biology, and materials science. *Annu. Rev. Phys. Chem.* **1997,** *48*, 213-42.
61. Zhang, W.; Saliba, M.; Moore, D. T.; Pathak, S. K.; Horantner, M. T.; Stergiopoulos, T.; Stranks, S. D.; Eperon, G. E.; Alexander-Webber, J. A.; Abate, A.; Sadhanala, A.; Yao, S.; Chen, Y.; Friend, R. H.; Estroff, L. A.; Wiesner, U.; Snaith, H. J., Ultrasmooth organic-inorganic perovskite thin-film formation and crystallization for efficient planar heterojunction solar cells. *Nat. Commun.* **2015,** *6*, 6142.

62. Kyser, D. S.; Rehn, V., Piezoelectric effects in electroreflectance. *Solid State Commun.* **1970,** *8* (18), 1437-1441.
63. Wu, X.; Yu, H.; Li, L. K.; Wang, F.; Xu, H. H.; Zhao, N., Composition-Dependent Light-Induced Dipole Moment Change in Organometal Halide Perovskites. *J. Phys. Chem. C* **2015,** *119* (2), 1253-1259.
64. Liess, M.; Jeglinski, S.; Vardeny, Z. V.; Ozaki, M.; Yoshino, K.; Ding, Y.; Barton, T., Electroabsorption spectroscopy of luminescent and nonluminescent π-conjugated polymers. *Phys. Rev. B* **1997,** *56* (24), 15712-15724.
65. Saito, K.; Yanagi, K.; Cogdell, R. J.; Hashimoto, H., A comparison of the Liptay theory of electroabsorption spectroscopy with the sum-over-state model and its modification for the degenerate case. *J. Chem. Phys.* **2011,** *134* (4), 044138.
66. Li, C.; Tscheuschner, S.; Paulus, F.; Hopkinson, P. E.; Kiessling, J.; Kohler, A.; Vaynzof, Y.; Huettner, S., Iodine Migration and its Effect on Hysteresis in Perovskite Solar Cells. *Adv. Mater.* **2016,** *28* (12), 2446-54.
67. Aspnes, D. E., Nonlinear Optical Susceptibilities from Electroreflectance Moments Analysis. *Phys. Rev. Lett.* **1971,** *26* (23), 1429-1432.
68. Liptay, W., Dipole Moments and Polarizabilities of Molecules in Excited Electronic States. In *Excited States*, Lim, E. C., Ed. Academic Press, Inc.: New York, New York, 1974; Vol. 1, pp 129-229.
69. Zhou, M.; Chua, L.-L.; Png, R.-Q.; Yong, C.-K.; Sivaramakrishnan, S.; Chia, P.-J.; Wee, A. T. S.; Friend, R. H.; Ho, P. K. H., Role of δ-Hole-Doped Interfaces at Ohmic Contacts to Organic Semiconductors. *Phys. Rev. Lett.* **2009,** *103* (3).
70. MacLeod, B. A.; Horwitz, N. E.; Ratcliff, E. L.; Jenkins, J. L.; Armstrong, N. R.; Giordano, A. J.; Hotchkiss, P. J.; Marder, S. R.; Campbell, C. T.; Ginger, D. S., Built-In Potential in Conjugated Polymer Diodes with Changing Anode Work Function: Interfacial States and Deviation from the Schottky-Mott Limit. *J. Phys. Chem. Lett.* **2012,** *3* (9), 1202-7.
71. Miller, D. A. B.; Chemla, D. S.; Damen, T. C.; Gossard, A. C.; Wiegmann, W.; Wood, T. H.; Burrus, C. A., Electric field dependence of optical absorption near the band gap of quantum-well structures. *Phys. Rev. B* **1985,** *32* (2), 1043-1060.
72. Sacra, A.; Norris, D. J.; Murray, C. B.; Bawendi, M. G., Stark spectroscopy of CdSe nanocrystallites: The significance of transition linewidths. *J. Chem. Phys.* **1995,** *103* (13), 5236.
73. Aspnes, D. E., Band nonparabolicities, broadening, and internal field distributions: The spectroscopy of Franz-Keldysh oscillations. *Phys. Rev. B* **1974,** *10* (10), 4228-4238.
74. Hamakawa, Y.; Nishino, T., Recent Advances in Modulation Spectroscopy. In *Optical Properties of Solids New Developments*, Seraphin, B. O., Ed. North-Holland Publishing Company: Amsterdam, 1976; pp 255-351.
75. Aspnes, D. E., Direct Verification of the Third-Derivative Nature of Electroreflectance Spectra. *Phys. Rev. Lett.* **1972,** *28* (3), 168-171.
76. Byrnes, S. J., Multilayer optical calculations. *arXiv e-prints* **2016,** *arXiv:1603.02720*.
77. Menéndez-Proupin, E.; Palacios, P.; Wahnón, P.; Conesa, J. C., Self-consistent relativistic band structure of the $CH_3NH_3PbI_3$ perovskite. *Phys. Rev. B* **2014,** *90* (4), 045207.
78. Rowe, J.; Aspnes, D., Approximate Treatment of Exciton Effects in Electric Field Modulation Via the Slater-Koster Interaction. *Phys. Rev. Lett.* **1970,** *25* (3), 162-165.
79. Penchina, C.; Pribram, J.; Sak, J., Electric Field Effects on Excitonic Absorption in Semiconductors. *Phys. Rev.* **1969,** *188* (3), 1240-1245.

80. Aspnes, D. E.; Frova, A., Ge-Aqueous-Electrolyte Interface: Electrical Properties and Electroreflectance at the Fundamental Direct Threshold. *Phys. Rev. B* **1970,** *2* (4), 1037-1052.
81. Aspnes, D. E., Schottky-Barrier Electroreflectance of Ge - Nondegenerate and Orbitally Degenerate Critical-Points. *Phys. Rev. B* **1975,** *12* (6), 2297-2310.
82. Fischer, J. E.; Aspnes, D. E., Electroreflectance: A Status Report. *Phys. Status Solidi B* **1973,** *55* (1), 9-32.
83. Dow, J.; Redfield, D., Toward a Unified Theory of Urbach's Rule and Exponential Absorption Edges. *Phys. Rev. B* **1972,** *5* (2), 594-610.
84. Newville, M.; Ingargiola, A.; Allen, D. B.; Stensitzki, T. LMFIT: Non-Linear Least-Square Minimization and Curve-Fitting for Python. http://cars9.uchicago.edu/software/python/lmfit/confidence.html.
85. Forman, R. A.; Aspnes, D. E.; Cardona, M., Transverse electroreflectance in semi-insulating silicon and gallium arsenide. *J. Phys. Chem. Solids* **1970,** *31* (2), 227-246.
86. Blakemore, J. S., Semiconducting and other major properties of gallium arsenide. *J. Appl. Phys.* **1982,** *53* (10), R123.
87. Blossey, D. F.; Handler, P., Electroabsorption. In *Semiconductors and Semimetals*, Willardson, R. K.; Beer, A. C., Eds. Academic Press: New York, New York, 1972; Vol. 9, pp 257-314.
88. Soufiani, A. M.; Huang, F. Z.; Reece, P.; Sheng, R.; Ho-Baillie, A.; Green, M. A., Polaronic exciton binding energy in iodide and bromide organic-inorganic lead halide perovskites. *Appl. Phys. Lett.* **2015,** *107* (23), 231902.
89. La-o-vorakiat, C.; Xia, H.; Kadro, J.; Salim, T.; Zhao, D.; Ahmed, T.; Lam, Y. M.; Zhu, J. X.; Marcus, R. A.; Michel-Beyerle, M. E.; Chia, E. E., Phonon Mode Transformation Across the Orthohombic-Tetragonal Phase Transition in a Lead Iodide Perovskite $CH_3NH_3PbI_3$: A Terahertz Time-Domain Spectroscopy Approach. *J. Phys. Chem. Lett.* **2016,** *7* (1), 1-6.
90. Brivio, F.; Frost, J. M.; Skelton, J. M.; Jackson, A. J.; Weber, O. J.; Weller, M. T.; Goni, A. R.; Leguy, A. M. A.; Barnes, P. R. F.; Walsh, A., Lattice dynamics and vibrational spectra of the orthorhombic, tetragonal, and cubic phases of methylammonium lead iodide. *Phys. Rev. B.* **2015,** *92* (14), 144308.

Chapter 3: H- and J- Aggregate Characteristics and Exciton Polarizability in π-Conjugated Polymers

This work contains contributions from several authors for a manuscript in preparation entitled "Tuning H- and J- Aggregate Behavior in π-Conjugated Polymers via Non-Covalent Interactions" by Mark E. Ziffer, Sae Byeok Jo, Yun Liu, Joseph C. Mohammed, Jeffrey S. Harrison, Alex K.-Y. Jen and David S. Ginger

Section 3.1 Overview

We study how tailoring non-covalent interactions through the regiochemistry of common donor/acceptor polymers can alter their excited-state electronic properties. Specifically, we compare two regioregular analogues (referred to as P1 and P2) of the widely used donor/acceptor copolymer poly[4,8-bis(5-(2-ethylhexyl)thiophen-2-yl)benzo[1,2-b:4,5-b']dithiophene-co-3-fluorothieno[3,4-b]thiophene-2-carboxylate] (PTB7-Th), which differ only in the orientation of a fluorine atom on the thieno[3,4-b]thiophene (FTT) acceptor units with respect to the benzodithiophene (BDT) unit. We show that in thin films this subtle change along the polymer backbone results in a transformation from typical H-like to an unusual HJ-like aggregate behavior, indicating significant differences in intrachain exciton coupling along the polymer backbone and interchain coupling between polymer chains. We also use electroabsorption spectroscopy to relate the dominant coupling mechanisms to differences in the excess polarization volume of the excitons in P1 and P2. Overall our results show that seemingly small changes in non-covalent interactions along a polymer backbone can have profound effects on the exciton electronic structure and dominant electronic coupling mechanisms in the solid state (intrachain versus interchain). Furthermore, these results provide evidence that interchain and intrachain coupling interactions may be correlated with electrostatic properties of the excitons in terms of their excited state polarization volume.

Section 3.2 Introduction

Probing and controlling the photoexcited states in semiconducting π-conjugated polymers has been a topic that has intrigued researchers for nearly 40 years.[1] While extensive research has established that the primary photoexcitations in π-conjugated polymers are best described as excitons,[2-3] the electronic structure of these primary neutral excitations, especially in relation to optoelectronic device relevant phenomena such as luminescence efficiency[4-6] and charge pair generation,[7-9] is a topic that continues to be debated and explored. Due to the fact that π-conjugated polymers are relevant for technological applications as thin film semiconductors, effects on the exciton electronic structure due to solid state interactions[5, 10-12] have been intensely studied and have been found to correlate sensitively with the morphological and molecular properties of a given polymer system.[11-14] These solid state interactions result in an interplay between intrachain versus interchain electronic coupling between chromophore units,[11, 13] which strongly influences the optical response and radiative properties of excitons in these materials.[11, 13] Therefore, a wealth of information about the electronic structure of excitons in these systems can be gained using

luminescence spectroscopy and various linear and non-linear optical spectroscopy techniques.[13, 15-16]

Notably, Spano and co-workers have analyzed the spectroscopic signatures of interchain versus intrachain electronic coupling in π-conjugated polymers,[11, 16-18] and have developed a framework for understanding the vibronic structure associated with electronic transitions in conjugated oligomers and polymer aggregates[17] by expanding on the classic molecular exciton theories developed by Kasha and others.[19-22] In particular, Spano showed that based on an analysis of the vibronic structure in the temperature dependent photoluminescence spectrum and the linear absorption spectrum, one can use a generalized HJ-aggregate model[13, 18] to classify the optical response in terms of H- or J-aggregate dominated behavior.[17-19] In π-conjugated polymers, H- or J-aggregation refers to the electronic coupling mechanisms that determine exciton formation – in H-aggregates excitons form due to interchain chromophore coupling, while in J-aggregates exciton formation arises from intrachain chromophore coupling.[11, 13, 17] In reality, both coupling mechanisms are at play in conjugated polymers, as is described formally by the generalized HJ-aggregate model.[18] Nevertheless, it is still possible to distinguish between H- or J- *dominated* behavior spectroscopically by studying the ratios of the vibronic peaks in the absorption spectra and luminescence spectra as a function of temperature.[11, 13, 18]

Furthermore, exotic phenomena such as thermally activated H- to J- transitions have been proposed within the generalized HJ aggregate model, which depends sensitively on the balance between interchain and intrachain coupling effects.[11, 13, 18] Systematic studies in a range of different polymer systems have shown that the strength of interchain versus intrachain interactions, resulting in modulation between predominately H- versus J-aggregate like behavior, can be tuned systematically by parameters such as solvent casting/annealing,[23-24] pressure,[25] regioregularity,[16] molecular weight,[13] and side chain engineering,[24] which can modulate aggregation both in the solid state and in solution.[26]

Recently one of our groups reported the regio-selective synthesis of two different regio-regular analogues (hereafter referred to as "P1" and "P2"),[27] of the widely used donor/acceptor copolymer PTB7-Th, which differ between each other only in the orientation of a fluorine atom on one of the fluorinated thieno[3,4-*b*]thiophene (FTT) acceptor units within the acceptor-donor-acceptor-donor (A-D-A-D) repeat structure in the polymer backbone (see Fig. 3.1). Significant differences in the field effect mobility and solid state packing investigated by GIWAXS are observed between the two polymers, which have been attributed to differences in planarization of the polymer backbone based on specific non-covalent interactions between the repeat units with different orientations of the fluorine atom.[27]

Herein we investigate the influence of these solid state interactions on the photophysics of P1 and P2 by studying the spectroscopic signatures of H- and J-like aggregate effects.[11] We find that what seems like a subtle change in non-covalent interactions between repeat units along the polymer backbone in P1 and P2 results in a transformation from a more typical H-like dominated exciton behavior for P1 to an unusual HJ-like hybrid behavior for P2, indicating significant differences in intrachain versus interchain electronic coupling in these two systems. Having established that P1 and P2 selectively exhibit either interchain or intrachain dominated electronic

coupling, we use electroabsorption spectroscopy to measure the excess polarizability associated with the transition to the lowest energy exciton. These results point towards interesting correlations between the degree of interchain versus intrachain coupling and the electrostatic properties of the exciton. Importantly, our results show that subtle tuning of the polymer backbone chemistry can lead to drastic changes in the behavior and electronic structure of primary photoexcitations.

Section 3.3 Chemical structures of P1 and P2

We start by reviewing the chemical structures of P1 and P2 which have been reported previously.[27] In order to highlight the chemical differences in backbone structure between P1 and P2, Fig. 3.1 shows a full A-D-A-D repeat unit of the P1 and P2 polymer chains. In P1, the hydrogen bonding between the fluorine atom on the FTT unit and a hydrogen atom on the neighboring benzodithiophene (BDT) unit "locks" each FTT unit in the plane of one BDT unit, such that there is a conformational degree of freedom about the C-C bond between every A-D pair in the A-D-A-D repeat structure. In contrast, in P2 *two* FTT units are hydrogen bonded to one BDT unit in the A-D-A-D backbone, such that a three unit A-D-A sequence becomes locked together in plane, as opposed to only a two unit A-D sequence in P1. The expected outcome of this design is that the P2 backbone will have a higher degree of "stiffness" and planarity compared to P1, which is consistent with the differences in crystallographic order and field effect mobility between P1 and P2 reported previously.[27] Yet, in addition to changing the thin film morphology, we also hypothesized that these differences in backbone planarity between P1 and P2 could modulate the degree of intrachain electronic coupling between monomer repeat units in the polymer backbone, as the exciton coherence length along a polymer chain has been shown to directly relate to the planarity of the chain in isolated molecules and in aggregates.[13] Therefore we hypothesize that the differences in backbone structure between P1 and P2 could lead to differences in solid state interactions that affect the exciton electronic structure, which we probe spectroscopically.

The aim of this study is to first establish that the differences in chemical structure between P1 and P2 do indeed affect the excited state electronic properties of aggregated polymer chains, which can be seen through the optical properties of thin films and dilute solutions. Next, we will study the effect of solid state interactions on exciton structure in more detail by analyzing temperature dependent photoluminescence measurements on P1 and P2 films in the framework of H- and J-aggregate-like behavior, which will allow us to characterize the unique differences in interchain versus intrachain dominated electronic coupling. Finally, having established the dominant electronic coupling behavior in P1 and P2, we use electroabsorption spectroscopy to probe the differences in exciton polarizability and excited state dipole characteristics resulting from the unique interchain and intrachain dominated electronic coupling in P1 and P2 respectively.

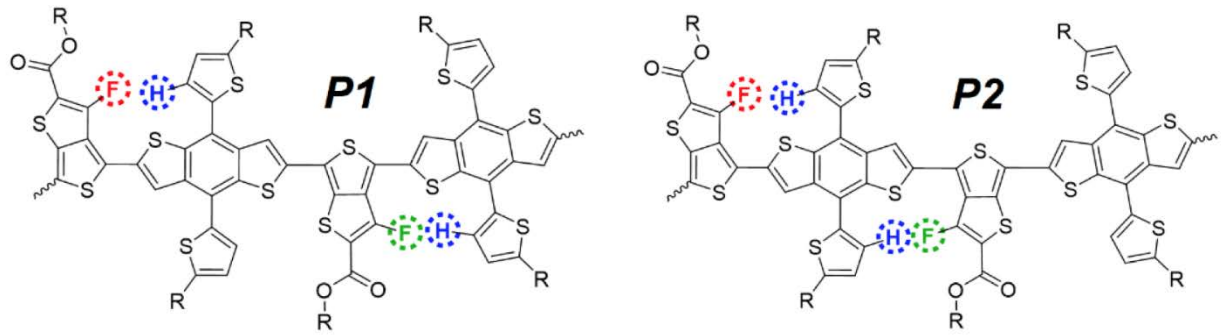

Figure 3.1. Chemical structures of A-D-A-D repeat units for P1 and P2 showing the effect of fluorination position on backbone structure. R=2-ethylhexyl.

Section 3.4 Characterization of Aggregation in Dilute Solution

To investigate the effects of aggregation on the excited state electronic properties of P1 and P2, we begin by studying the spectral signatures of the aggregate formation process itself using temperature dependent UV-Vis absorption spectroscopy for dilute solutions of P1 and P2. Fig. 3.2 a. and Fig. 3.2 b. compare the absorption spectra of thin films and dilute solutions (0.005 mg/mL [0.0038w%] in DCB) of P1 and P2 at room temperature. In Fig. 3.2 a., we show that at room temperature, the dilute solution and thin film absorption spectra are essentially identical for P2. This phenomenon, indicative of the formation of a planarized aggregate phase in solution,[26] has been observed in a number of donor-acceptor co-polymers,[28-30] in particular in PTB7[28-29] and PTB7-Th.[29] A detailed study by Fauvell *et al.* showed that the similarity between the dilute solution and thin film absorption spectra is due the strong self-aggregation of single PTB7 strands in solution.[28]

In contrast to P2, P1 exhibits a clear blue shift and shape change between its dilute solution spectrum at 25° C and its thin film absorption spectrum, which is a sign that in solution the polymers are not forming ordered aggregates, and possibly are in a state of completely de-aggregated coils.[26] In Fig. 3.2 c. we show the temperature dependent absorption spectrum of P1 from 25° C to 75° C in dilute solution. We observe that the red shoulder at ~1.8 eV in the absorption spectrum at 25° C decreases until the spectrum shows a single broad peak at ~2.1 eV at 75° C. This transformation to a single broad peak in solution that is blue shifted relative to either of the vibronic peaks in the thin film absorption spectrum indicates a phase transition in solution between disordered aggregates at low temperature to random de-aggregated coils with increasing temperature, a nearly universal behavior for conjugated polymers as demonstrated by Köhler and coworkers.[26] We note that solvatochromism effects do not appear make the comparison between solution and film spectra problematic, as the peaks in the P2 solution and film spectra not only have nearly identical shape but are also at nearly identical energies.

In contrast, the absorption spectra of a dilute P2 solution in DCB taken as function of increasing temperature (Fig. 3.2 d.) shows mainly a change in the ratio of the two primary vibronic peaks with no broad higher energy peaks growing in. We interpret the persistence of vibronic

structure in Fig. 3.2 d., even up to the highest temperatures, as evidence that the P2 polymer remains in an aggregated phase. The change in ratio of vibronic peaks is consistent with the polymer backbones within the aggregates becoming less planarized with increasing temperature.[26] Such dramatic contrast in the thermodynamics of aggregate formation in solution and the tendency to form aggregates with highly planar backbone structures for different polymers has been explained by factors such as differences in molecular weight and PDI,[26] differences in side chains,[26, 30] or by differences in backbone planarity and stiffness of a single polymer chain.[26] We note that the molecular weight and PDI of P1 and P2 are very similar (M_w P1 = 56kDa, M_w P2 = 62kDA, PDI P1 = 1.9, PDI P2 = 2.1), and their side chains are identical as shown in Fig. 3.1. Therefore we propose that the difference in the solution phase aggregation behavior between P1 and P2 is dominated largely by differences in backbone stiffness and planarity. In particular, we propose that the similarity between the dilute solution and film absorption spectra of P2, which indicates the formation of highly ordered aggregates in solution,[26] can be explained on the basis of a stiffer, more planarized backbone in the P2 molecule.

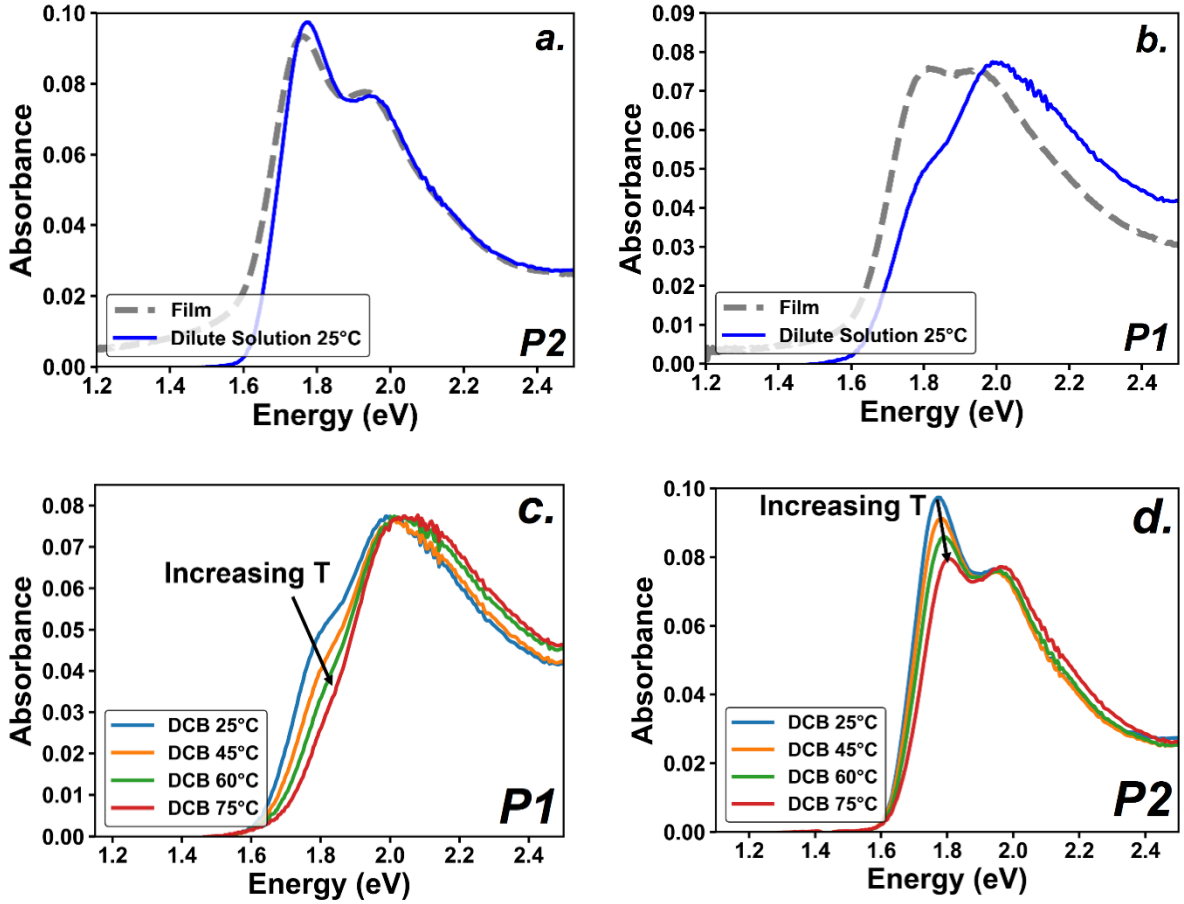

Figure 3.2 ***a.)*** & ***b.)*** Comparison of the thin film and dilute solution (0.005 mg/mL in DCB) UV-vis absorption spectra for P1 and P2 at room temperature. Thin film absorption spectra are scaled for comparison with the dilute solution spectra. ***c.)*** & ***d.)*** UV-vis absorption spectra of P1 and P2 in dilute solution (0.005 mg/mL in DCB) for a series of increasing temperatures. The 25° C spectra in ***c.)*** and ***d.)*** are the same as the spectra shown in ***a.)*** and ***b.)***.

Section 3.5 Characterizing Solid State Interactions with Spectroscopic Ellipsometry

To further explore the hypothesis that P2 tends to form aggregates constituting highly ordered polymer backbones, we turn to study the optical properties of P1 and P2 thin films using spectroscopic ellipsometry. Fig. 3.3 a. shows the spectra of the imaginary part of the complex dielectric function (ε_i) for P1 and P2 films derived from an isotropic model of the ellipsometry data measured at three angels of incidence (we note that anisotropic models did not improve the quality of the fit in the absorbing or transparent region, see SI Section S1 for more details on ellipsometry measurements and analysis). As opposed to k (the imaginary part of the complex refractive index) or the absorption coefficient, ε_i is directly related the optical susceptibility of the material, meaning that it can be directly compared to quantum mechanical theories for transition probabilities via the oscillator strength for a transition.[31] The ε_i spectrum of P2 shows a peak ε_i of ~5.1 and κ>1 (see SI section S1 for n and κ), which is notable for being unusually high for a conjugated polymer. The recent comprehensive study by Vezie *et al*,[31] showed that only for distinct cases of highly stiff backbones do conjugated polymers have $\varepsilon_i \geq 4$ or $\kappa \geq 1$. In contrast, P1 shows a maximum ε_i of ~3.25 and κ~0.8 (Fig. 3.3 a. and SI section S1). Similarly, we can observe differences in magnitude in the real part of the complex dielectric function (ε_r) and refractive index (see SI section S1) between P2 and P1 (Fig. 3.3 b.), which is consistent with the Kramers-Kronig relations. Vezie *et al.*[31] demonstrated that exceptional cases of high ε_i are possible in polymers with stiff conjugated backbones, where the persistence length along the polymer backbone (a characteristic length scale which describes the maximum segment of chain length that maintains co-linearity[32-34]) is directly responsible for the ability of these systems to sustain high optical absorption strength in the presence of solid state disorder.[31] We therefore propose that the high ε_i in P2 arises because its chemical structure promotes a longer persistence length along the conjugated backbone due to "locking" together three segment A-D-A units. This proposal is also consistent with the temperature-dependent aggregation behavior in solution, which also suggests a stiffer backbone chain in P2.

Further examining the ε_i spectra in Fig. 3.3 a., we observe not only clear differences in the magnitude of ε_i between the two polymers, but also differences in the shape of the vibronic structure in the spectra of P1 and P2. Specifically, in P2 the ratio of the lowest energy vibronic absorption peak ("A1", in the notation of Spano[11]) to the next lowest vibronic peak ("A2") is greater than 1 (specifically 1.25), where in contrast the A1/A2 ratio in P1 is almost exactly 1 (Fig. 3.3 a.). An A1/A2 absorption ratio greater than 1 is a typical signature of a J-aggregate, since the J-like coupling shifts oscillator strength to the 0-0 absorption transition relative to the higher lying states of the vibronic progression of a monomer unit.[17] In contrast, H-like coupling shifts oscillator strength to the A2 transition, resulting in a A1/A2 ratio typically less than or equal to 1.[17] While it is possible that individual monomer units of P1 and P2 could have different vibronic structure due to differences in structural rigidity arising from the distinct hydrogen bonding motifs between the FTT fluorine and BDT hydrogen (which could result in different Huang-Rhys factors[35] for the individual monomers), we note that the combined observations of a strongly enhanced A1/A2 ratio *and* an exceptionally high absorption strength for P2 suggest that long range intrachain correlations due to a structurally rigid and co-linear backbone are at play, which would be consistent with the characteristic vibronic structure of P2 resulting from J-like coupling. Furthermore, the absorption edge of P2 is ~60 meV redshifted from P1, which is consistent with enhanced J-like character in

P2, owing to the fact that optically allowed transitions in J-aggregates occur at the lower energy bottom of the exciton band, whereas in H-aggregates optical absorption occurs at the higher energy top of the exciton band.[17] Hence, we hypothesize that P1 and P2 exhibit characteristic differences in the amounts of interchain (H-like) versus intrachain (J-like) coupling, with P1 being H-like and P2 being J-like. We explore this hypothesis further by studying their temperature dependent photoluminescence spectra below.

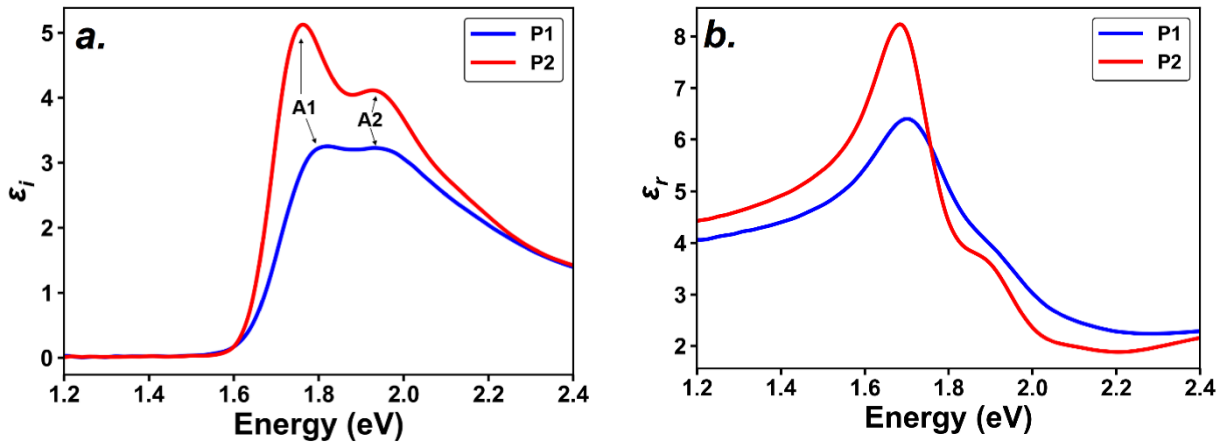

Figure 3.3 ***a.)*** *&* ***b.)*** Spectra of the imaginary (ε_i) and real (ε_r) components of the complex dielectric function ($\varepsilon = \varepsilon_r + i\varepsilon_i$) for thin films of P1 and P2 derived from modelling spectroscopic ellipsometry data measured at three angles of incidence (Appendix B S1 for details). The vibronic peaks A1 and A2 are labeled with arrows for P1 and P2.

Section 3.6 Characterizing H- and J- Like Coupling with Photoluminescence Spectroscopy

To further interrogate the H-like versus J-like behavior of P1 and P2, we turn to study the vibronic structure in their photoluminescence spectra. Fig. 3.4 a. shows the photoluminescence spectra of P1 and P2 along with their absorption edge spectra. The P2 photoluminescence shows two clear peaks separated by ~0.14 eV (in the range of typical C-C vibrational modes that are common for all conjugated polymers),[11, 18] with the highest energy peak only 0.16 eV redshifted from the absorption peak at 1.75 eV, which we assign as the 0-0 vibronic luminescence transition. The P1 photoluminescence spectrum shows a broad peak at 1.51 eV that is 60 meV blue shifted from the 0-1 peak of P2 (Fig. 3.4 a.). Comparing the absorption edge spectra of P1 and P2, we also notice that the absorption peak of P1 is blue shifted 60 meV relative to P2 (Fig. 3.4 a.). Therefore we assign the broad peak in the P1 photoluminescence spectrum at 1.51 eV to the 0-1 transition of P1. The 0-0 luminescence peak of P1 can seen upon close inspection as a shoulder on the blue edge of the photoluminescence spectrum (indicated with arrows in Fig. 3.4 a.).

In Fig. 3.4 b. and 3.4 c. we show the temperature-dependent photoluminescence spectra of P1 and P2, normalized to the 0-1 emission peak. Normalization of the spectra to the 0-1 emission

peak allows us to directly monitor the ratio of the 0-0/0-1 emission peaks as a function of temperature, which is a sensitive indicator of the strength and nature of the interchain versus intrachain excitonic coupling in the H- and J- aggregate models.[11, 18] Briefly, the ratio of the 0-0/0-1 peak in a H-aggregate *increases* with increasing temperature, owing to the fact that the 0-0 luminescence transition in a H-aggregate is optically forbidden and only becomes allowed in the presence of thermally activated disorder.[11] In contrast, in a J-aggregate the 0-0 luminescence transition is strongly allowed, and as a result the 0-0/0-1 peak ratio *decreases* with increasing temperature as disorder induced effects shift oscillator strength to the 0-1 transition.[17] In Fig. 3.4 b. we show that in P1 the shoulder on the blue edge of the photoluminescence spectrum (identified in Fig. 3.4 a.) grows in intensity with respect to the 0-1 peak as the temperature is raised from 80K to 295K: this intensity-ratio change is a classic signature of H-like behavior.[11] Furthermore, there is little to no discernable shift in the positions of the vibronic peaks of P1 as a function of temperature, an observation that we will return to when analyzing the photoluminescence spectra for P2. In Fig. 3.4 c. we show the temperature-dependent photoluminescence spectrum of P2 normalized to the 0-1 emission peak. Several aspects can be noted, the most prominent being that in contrast to P1, the intensity of the 0-0 emission peak relative to the 0-1 peak *decreases* with increasing temperature, which, in contrast to P1, is a clear signature of *J-like* behavior.[11] A second observation that we note about Fig. 3.4 c. is that the ratio of the 0-0/0-1 peak in P2 seems to "saturate" at around 160K without any noticeable increase in the 0-0/0-1 ratio between 160K to 80K. Finally, a third observation that we note is the apparent dramatic redshift of the 0-1 peak in P2 and comparatively more subtle redshift of the 0-0 peak with decreasing temperature.

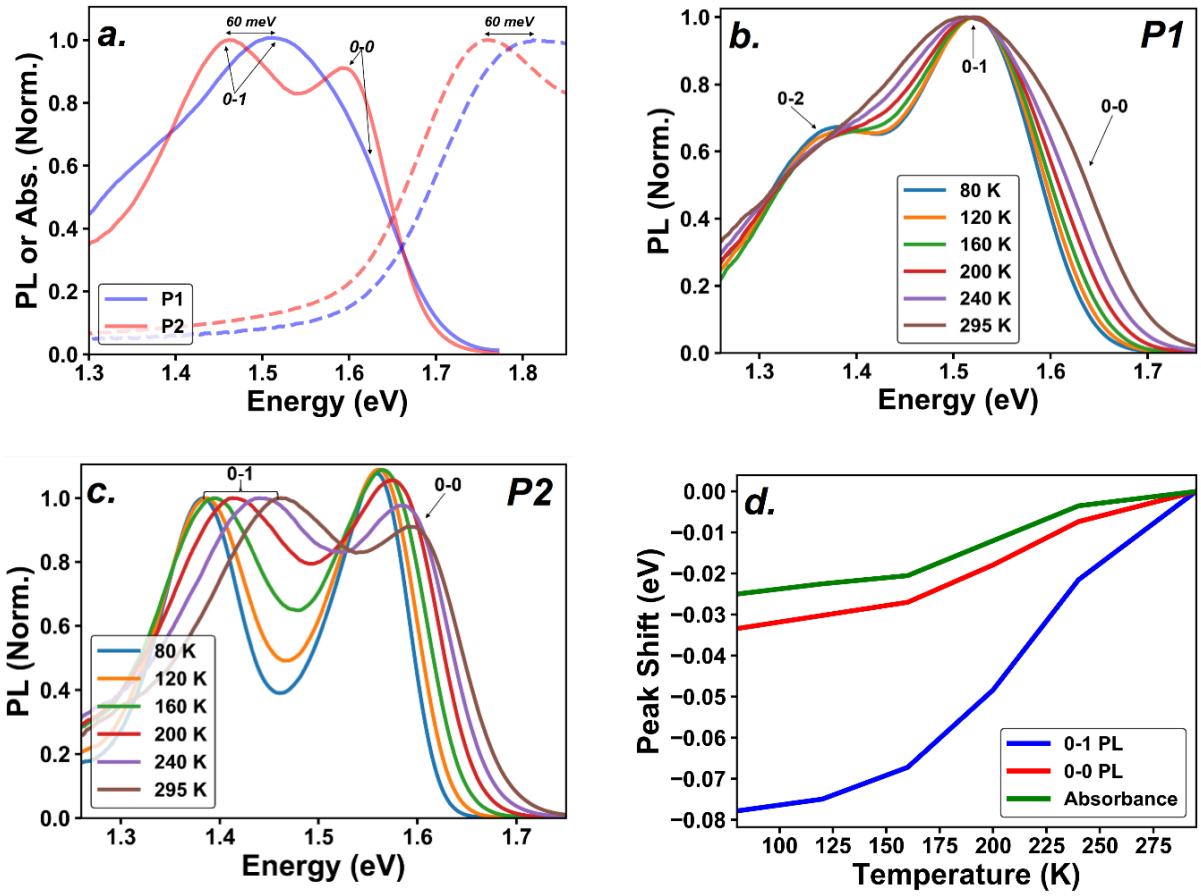

Figure 3.4 ***a.)*** Normalized photoluminescence spectra (solid lines) and absorption spectra (dashed lines) of P1 and P2 at 295 K. The 0-0 and 0-1 emission peaks are labeled for clarity, along with the energy of the relative peak shifts between P1 and P2. ***b.)*** and ***c.)*** Temperature dependent photoluminescence spectra of P1 and P2 normalized to the 0-1 peak in order to compare the 0-0/0-1 ratio as a function of temperature. Vibronic emission peaks are labeled for clarity. ***d.)*** Redshift of the A1 absorption peak of P2 (see SI section S2), 0-0 emission peak of P2, and 0-1 emission peak of P2 as a function of decreasing temperature. The redshift is shown with respect to the energy of the peak of the 0-0, 0-1, or A1 transition at 295 K.

We propose that the characteristics of the photoluminescence spectrum for P2 noted above arise from a J- to H- transition with decreasing temperature as predicted by the generalized HJ-aggregate theory put forth by Spano and Yamagata.[13, 18] The generalized HJ aggregate theory models a prototypical polymer aggregate as a "dimer" consisting of two linear polymer chains (J-aggregates) coupled together through interactions between monomer units on the adjacent chain in the dimer pair (H-like interactions). The electronic structure of the resulting "HJ dimer" can be described as two J-aggregate bands split by an energy ΔE caused by the dimer interaction.[18] Similar to the H-coupled molecular dimer originally described by Kasha,[22] the lower energy state caused by the split (or in this case the lower energy J-band), will be optically forbidden with respect to

transitions to/from the zero-phonon ground state at the k=0 point, whereas the higher energy J-band will have optically allowed transitions at the k=0 point. Therefore, the "H- to J-" transition seen in photoluminescence occurs when the available thermal energy is greater than ΔE, such that the upper J-band can be thermally populated and optically allowed transitions from the k=0 point of the upper J-band to the zero phonon ground state (the 0-0 vibronic photoluminescence) can occur, resulting in *thermally activated* J-like behavior.[18]

Returning to the data in Fig. 3.4 c., we propose that the steady increase of the 0-0/0-1 ratio with decreasing temperature (J-like behavior) and subsequent saturation at 160 K is indicative of a temperature dependent J- to H- transition for P2 as predicted by the generalized HJ aggregate model.[18] Interestingly, Spano noted that the thermal energy (k_BT) associated with the temperature onset where saturation in the 0-0/0-1 ratio occurs should approximately correspond to the splitting between the energy of the two J-bands in the HJ dimer (ΔE).[18] Therefore, assuming an onset of ~160K, we can estimate ΔE to be ~14 meV. Interestingly, this value is very close to the value of ΔE estimated for the red phase of MEH-PPV (~12 meV) by Spano, Bässler, and Köhler,[36] which suggests that our estimate for ΔE is within a physically plausible range for the dimer splitting of J-bands in a HJ aggregate.[36] While H- to J- transformations have been reported in polymers as a function of extrinsic controls such as morphological phase transitions in solution,[36] or morphological phase transitions in the solid state induced by solvent vapor annealing,[24] to our knowledge the thermally activated J- to H- transition based purely on the electronic structure of the dimer split J- exciton bands as predicted by Spano in the HJ aggregate model,[18] which we observe here, has not been reported before in a conjugated polymer system.

Finally, we address the redshift of the 0-0 and 0-1 photoluminescence peaks in P2 with decreasing temperature. A redshift of the optical transitions in P2 with decreasing temperature is to be expected, as a reduction in temperature can increase the intrachain exciton coherence length in a J-aggregate, resulting in an energetic lowering of the exciton bands.[37] In Fig. 3.4 d. we compare the magnitude of the redshift of the A1 absorption peak with the 0-0 and 0-1 photoluminescence peaks. We see that both the A1 peak in absorption and the 0-0 emission peak indeed follow a similar trend, which is consistent with the generalized HJ aggregate model. In a HJ aggregate, absorption and 0-0 emission both occur to and from the highest energy optically allowed J-band at the k=0 point,[11] and therefore the spectral shifts of the absorption and emission should move together. The small differences in the overall magnitude of the redshift between the A1 absorption peak and the 0-0 emission peak may be due to the fact that initial photoexcitations in conjugated polymers typically migrate to lower energy sites in the solid state, resulting in an additional energetic relaxation of the emission spectrum.[38] On the other hand, Fig. 3.4 d. also shows that the 0-1 emission peak clearly redshifts more strongly and with a different trend with decreasing temperature than either the 0-0 emission peak or the A1 absorption peak (which is also obvious from inspecting Fig. 3.4 c.).

This curious behavior of the 0-1 emission peak is not consistent with a simple single band J-aggregate model, where the spacing between vibronic peaks in emission is determined solely by the energy of the vibrational oscillator coupled to the electronic transition, and thus a shift in energy of the exciton band should result in a uniform shift of the vibronic peak positions. However,

we speculate that in a HJ aggregate, this assumption may not be valid, due to the fact that the 0-1 luminescence transition is optically allowed from either the higher or lower energy J-band split by the HJ dimer interaction. Therefore the redshift of the 0-1 luminescence transition with temperature could also reflect not only a shift in energy of the electronic bands, but also the temperature dependence of the Boltzmann population of excitons in the two split off J-bands, both of which can contribute to 0-1 emission. More detailed experimental and theoretical work will be needed to understand this unique energy shift of the 0-1 peak with temperature. We furthermore remark that the absence of any dramatic redshift of the 0-1 emission peak in the photoluminescence spectrum of P1 is consistent with purely H-like behavior used above to describe the temperature dependence of the 0-0/0-1 peak ratio in P1.

Therefore, based on the full analysis of the temperature dependent photoluminescence spectra of P1 and P2, we conclude that in P2, intrachain interactions are the dominant electronic coupling mechanism, such that J-like behavior is observed from room temperature down to 160K, and a full HJ-aggregate analysis is needed to describe the photophysics behind the photoluminescence spectrum. In contrast, P1 appears to show exclusively H-aggregate like behavior, indicating that interchain interactions are dominant.

Having established that P1 and P2 are respectively dominated by interchain and intrachain electronic coupling at room temperature, we now turn to electroabsorption spectroscopy to probe the electronic transitions in these materials in more detail.

Section 3.7 Electroabsorption Spectroscopy

Electroabsorption (EA) spectroscopy is a modulation spectroscopy technique that measures the change in the optical transmittance of a sample due to a perturbing low frequency AC electric field.[39-41] In Figures 5A and 5B, we show the normalized EA spectra measured at the second harmonic of the fundamental modulation frequency for P1 and P2 over a series of increasing electric field strengths. In the SI we also show the scaling of the EA features as a function of applied fields (see SI section S3). For both P1 and P2 the shape of the EA spectrum remains invariant with applied field and the amplitude of the EA peaks scale close to quadratically with electric field strength. We therefore assign the EA signal to a $\chi^{(3)}$ electro-optic response, as is typically observed in EA studies of small molecules,[42] semiconducting polymers,[41, 43] molecular crystals,[44] as well as in crystalline semiconductors.[40]

In the case of semiconducting polymers and molecular excitons,[41, 43-44] the $\chi^{(3)}$ EA response is almost always due to the quadratic Stark shift of an electronic exciton band, as the energy spacing between low energy electronic exciton bands in polymer semiconductors and molecular crystals are typically large enough such that the interaction potential due to the electric field can be treated as a small perturbation on the exciton energy. In particular, Vardeny and coworkers have shown that the EA spectrum in a wide variety of π-conjugated polymers (including a donor/acceptor copolymer[45]), consists of a derivative-like Stark shift of the lowest optically allowed exciton and its vibronic replicas, followed by a broad induced absorption feature at higher energies due to the symmetry breaking of transition dipole for the higher energy optically

forbidden exciton.[41, 45] Here we also observe this general lineshape for both P1 and P2 in Fig. 3.5 a. and 3.5 b., where the low energy derivative-like feature and vibronic shoulder can be seen between ~1.6-2.1 eV, followed by a broad induced absorption at around 2.2eV. Interpreting our spectra in the context of Vardeny *et al.*'s assignments,[41, 45] we therefore analyze our spectra by focusing on the region of the EA spectrum below 2.1 eV corresponding to the lowest electronic exciton level.

The full treatment to analyze the Stark effect in electroabsorption measurements on an isotropic ensemble of molecules (or in this case aggregates[44]) comes from the formula of Liptay,[42, 46] which we show in terms of the change in the imaginary part of the refractive index (*k)* in Eq. 1 (see SI section S5 for details). As mentioned earlier, we note that the ellipsometry modelling did not benefit from using anisotropic models, therefore we consider the assumption of a largely isotropic ensemble of absorbers to be reasonable.

$$\Delta k = F^2 \left\{ A_\chi k + \frac{B_\chi}{15}\frac{dk}{dE} + \frac{C_\chi}{30}\frac{d^2k}{dE^2} \right\} \qquad Eq\ 1.$$

Here, the coefficients B_χ, and C_χ (where χ is the angle between the polarization of light and the applied field, which we maintained at χ=55°) respectively contain quantitative values for the difference between the ground to excited state polarizability tensor ($\Delta\alpha_{g\rightarrow e}$, also referred to as the excess polarization volume), and the difference between the ground and excited state dipole moment ($\Delta\mu_{g\rightarrow e}$). In Figs 5C and 5D we show fits to the EA spectrum for the region of the spectrum corresponding to the low energy exciton and its vibronic features using Eq. 1 with transfer matrix modelling[40] (where the field strength is calculated from the applied voltage and dielectric constants of layers in the EA device stack, see SI section S4 and S5). The fits give very good agreement with the shape and magnitude of the EA spectrum, although we note two possible sources of error that could result in the small discrepancies between the fits and the data: first, errors in the fit may arise due to small errors in the modelled *k* spectra from ellipsometry whose derivatives we calculate numerically to use in Eq. 1 and in the transfer matrix model. Second, it has been argued that in heterogeneous systems (such as a polymer thin film consisting of a variety of aggregate types), electroabsorption preferentially probes the species of the system whose electronic structure results in the largest EA response, which in the case of semiconducting polymers is typically assigned to the aggregates or chains with the highest excess polarizability.[41] Therefore it is possible that the species which are preferentially probed by EA contain different optical properties from the bulk and hence will deviate from the Liptay model assumed using *k* measured from bulk ellipsometry.

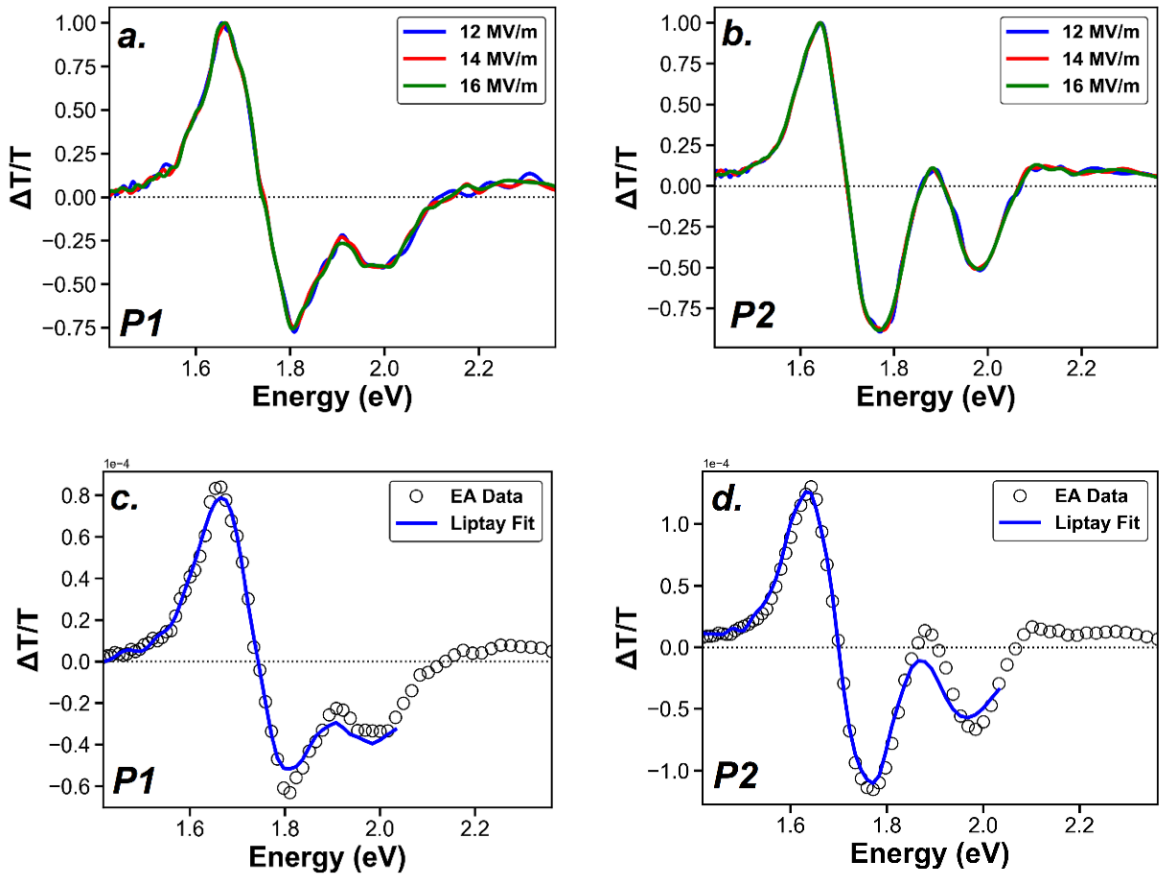

Figure 3.5 ***a.)*** and ***b.)*** Electroabsorption spectra of P1 and P2 measured at the second harmonic of the fundamental modulation frequency for a series of applied field strengths, normalized to the maximum peak amplitude of the spectrum. ***c.)*** and ***d.)*** EA data measured at 16 MV/m for P1 and P2 fit to Eq 1. using transfer matrix modelling (see SI section S4) to extract values for $\Delta\alpha_{g\rightarrow e}$.

Nevertheless, despite these caveats, the fits show very good agreement with the data and show primarily first-derivative like character (typical for conjugated polymers[41]), indicating a large contribution from the B_χ term in Eq. 1, from which we can directly extract a best fit value for the excess polarization volume for P1 of $\Delta\alpha_{g\rightarrow e}$=1047 ± 77 Å^3 and for P2 of $\Delta\alpha_{g\rightarrow e}$=645 ± 80 Å^3. The error on the values of $\Delta\alpha_{g\rightarrow e}$ is obtained by evaluating the 95% confidence interval for the statistical boundaries of the parameters in the fit.[47] These values for $\Delta\alpha_{g\rightarrow e}$ fall within the common range of values that have been reported in polymers such as PPVs, PDA, and polythiophenes, which tend to fall in the range of 10^2-10^4 Å^3.[41, 48-51] The spread in values for a 95% confidence interval on the value of $\Delta\mu_{g\rightarrow e}$ in P1 was rather large, and reflects that the dominant contribution to the electroabsorption response comes from the first derivative B_χ term, which reflects the contribution of $\Delta\alpha_{g\rightarrow e}$.[41] Therefore, we chose to only compare the $\Delta\alpha_{g\rightarrow e}$ values between P1 and P2.

We find it interesting that we measure a ~1.6 fold higher $\Delta\alpha_{g\rightarrow e}$ in P1 compared to P2, because this observation seems counterintuitive to the proposal that P2 shows evidence for strong intrachain exciton coupling, which one might assume would lead to higher excess polarizability along the chain backbone. One intriguing possibility that this observation suggests is that the exciton polarizability is influenced more strongly via *interchain* coupling. This hypothesis is consistent with seminal studies from Sirringhaus and coworkers[52-53] and Vardeny and coworkers[54] on regioregular polythiophene polymers, which showed that interchain coupling is correlated with the formation of more delocalized charged excitations (so called "2D polarons" or "interchain polarons").[52] From the results of our work, we put forth that the delocalization of charged excitations previously correlated with interchain coupling may also reflect in the excess polarization volume of the neutral excitation, and that therefore exciton polarizability may be controlled by interchain coupling and could be more dominant in H-aggregates. Indeed, it is interesting to point out that the systems in which interchain polarons were reported have been in regioregular P3HT, which shows H-like exciton character.[16] We put forth this hypothesis as an avenue for future study, as further theoretical and experimental work would be required to explore this idea.

Section 3.8 Conclusion

In conclusion, we have performed a detailed study on the photophysical properties of two regioregular analogues of the polymer PTB7-Th (referred to as "P1" and "P2"), which differ only in non-covalent hydrogen bonding interactions between the FTT and BDT backbone units in a A-D-A-D repeat structure. As predicted by the chemical structure, P2 demonstrates characteristics of a stiffer polymer backbone and longer persistince length than P1 which we conclude based on temperature dependent UV-vis studies of dilute solutions and ellipsometry measurements on thin films. Based on a detailed study of the temperature-dependent photoluminescence spectra in P1 and P2, we find that P1 exhibits typical characteristics of an H-aggregate (interchain dominated exciton coupling), whereas P2 shows signatures of J-like behavior and characteristics of an unusual, thermally-activated H- to J- transition as predicted by the generalized HJ aggregate model of Spano.[18] The signatures of J-like behavior in P2 directly show an increased degree of intrachain exciton coupling as compared to P1, which we believe is consistent with the stiffer, more co-linear backbone structure of P2 which could also facilitate a larger intrachain conjugation length.[32] Conversely, the chemical structure of the P1 backbone has inherently more flexibility and conformational degrees of freedom, which is consistent with interchain dominated coupling, where it is well known that polymers which exhibit only short range intrachain order are prone to enhanced interaction between chromophores on adjacent chains and hence increased interchain interactions.[11]

Finally, we used electroabsorption spectroscopy to measure the excess polarization volume ($\Delta\alpha_{g\rightarrow e}$) upon excitation in both P1 and P2 We found that $\Delta\alpha_{g\rightarrow e}$ = 1030 ± 80 Å^3 for P1 and 630 ± 80 Å^3 for P2, and attributed the larger $\Delta\alpha_{g\rightarrow e}$ in P1 to increased interchain interactions, posing an interesting comparison to the well-known delocalized "interchain polarons" that occur in H-aggregates of P3HT.[52-54] This correlation poses interesting questions regarding the inherent ability

of P1 to generate charge in photovoltaic experiments, as a larger exciton polarizability may reflect in the ability of the exciton to dissociate efficiently. Further studies in this vein are currently underway.

Overall, our work shows that subtle chemical changes to the polymer backbone in donor/acceptor copolymers can have a profound effect on the photophysics of excitons due to strong differences in solid state interactions. Tuning between H- and J- like coupling is a highly desirable design tool to be able to utilize, as the dominance of interchain versus intrachain interactions can have a profound role on the operation of organic electronic devices such as transistors, solar cells, and LEDs. Ultimately, the P1 and P2 polymers are analogues of the widely used photovoltaic polymer PTB7-Th. Correlating the findings of this work to the charge generation efficiency in solar cells based on P1 and P2 is a promising avenue for future research. Recent studies have shown that solid state aggregation plays a deciding role in the performance of polymer based bulk-heterojunction systems.[30] Understanding how device performance in aggregated polymer systems is correlated with exciton physics may provide a new outlook on design rules for polymers for more efficient photovoltaic devices.

Appendix B

Experimental Methods and Supplementary Information for Chapter 3

Acknowledgments

This work was supported by the Office of Naval Research through grant number N00014-17-1-2201. Part of this work was conducted at the Molecular Analysis Facility, a National Nanotechnology Coordinated Infrastructure site at the University of Washington which is supported in part by the National Science Foundation (grant ECC-1542101), the University of Washington, the Molecular Engineering & Sciences Institute, and the Clean Energy Institute.

References

1. Sariciftci, N. S., Primary Photoexcitations in Conjugated Polymers: Molecular Exciton Versus Semiconductor Band Model. World Scientific: Singapore, 1997.
2. Chandross, M.; Mazumdar, S.; Jeglinski, S.; Wei, X.; Vardeny, Z. V.; Kwock, E. W.; Miller, T. M., Excitons in poly(para-phenylenevinylene). Phys. Rev. B **1994,** 50 (19), 14702-14705.
3. Brédas, J.-L.; Cornil, J.; Heeger, A. J., The exciton binding energy in luminescent conjugated polymers. Advanced Materials **1996,** 8 (5), 447-452.
4. Samuel, I. D. W.; Rumbles, G.; Collison, C. J., Efficient interchain photoluminescence in a high-electron-affinity conjugated polymer. Physical Review B **1995,** 52 (16), R11573-R11576.
5. Brédas, J.-L.; Cornil, J.; Beljonne, D.; dos Santos, D. A.; Shuai, Z., Excited-State Electronic Structure of Conjugated Oligomers and Polymers: A Quantum-Chemical Approach to Optical Phenomena. Accounts of Chemical Research **1999,** 32 (3), 267-276.
6. Soos, Z. G.; Ramasesha, S.; Galvao, D. S., Band to correlated crossover in alternating Hubbard and Pariser-Parr-Pople chains: Nature of the lowest singlet excitation of conjugated polymers. Phys Rev Lett **1993,** 71 (10), 1609-1612.
7. Rolczynski, B. S.; Szarko, J. M.; Son, H. J.; Liang, Y.; Yu, L.; Chen, L. X., Ultrafast intramolecular exciton splitting dynamics in isolated low-band-gap polymers and their implications in photovoltaic materials design. J. Am. Chem. Soc. **2012,** 134 (9), 4142-52.
8. Köhler, A.; dos Santos, D. A.; Beljonne, D.; Shuai, Z.; Brédas, J. L.; Holmes, A. B.; Kraus, A.; Müllen, K.; Friend, R. H., Charge separation in localized and delocalized electronic states in polymeric semiconductors. Nature **1998,** 392, 903.
9. Grancini, G.; Maiuri, M.; Fazzi, D.; Petrozza, A.; Egelhaaf, H. J.; Brida, D.; Cerullo, G.; Lanzani, G., Hot exciton dissociation in polymer solar cells. Nat Mater **2013,** 12 (1), 29-33.
10. Ruini, A.; Caldas, M. J.; Bussi, G.; Molinari, E., Solid state effects on exciton states and optical properties of PPV. Phys Rev Lett **2002,** 88 (20), 206403.
11. Spano, F. C.; Silva, C., H- and J-aggregate behavior in polymeric semiconductors. Annu. Rev. Phys. Chem. **2014,** 65, 477-500.
12. Schwartz, B. J., Conjugated polymers as molecular materials: how chain conformation and film morphology influence energy transfer and interchain interactions. Annu Rev Phys Chem **2003,** 54, 141-72.
13. Paquin, F.; Yamagata, H.; Hestand, N. J.; Sakowicz, M.; Bérubé, N.; Côté, M.; Reynolds, L. X.; Haque, S. A.; Stingelin, N.; Spano, F. C.; Silva, C., Two-dimensional spatial coherence of excitons in semicrystalline polymeric semiconductors: Effect of molecular weight. Physical Review B **2013,** 88 (15).
14. Brown, P. J.; Thomas, D. S.; Köhler, A.; Wilson, J. S.; Kim, J.-S.; Ramsdale, C. M.; Sirringhaus, H.; Friend, R. H., Effect of interchain interactions on the absorption and emission of poly(3-hexylthiophene). Phys. Rev. B **2003,** 67 (6).
15. Grégoire, P.; Vella, E.; Dyson, M.; Bazán, C. M.; Leonelli, R.; Stingelin, N.; Stavrinou, P. N.; Bittner, E. R.; Silva, C., Excitonic coupling dominates the homogeneous photoluminescence excitation linewidth in semicrystalline polymeric semiconductors. Physical Review B **2017,** 95 (18).

16. Clark, J.; Silva, C.; Friend, R. H.; Spano, F. C., Role of intermolecular coupling in the photophysics of disordered organic semiconductors: aggregate emission in regioregular polythiophene. Phys Rev Lett **2007,** 98 (20), 206406.
17. Spano, F. C., The spectral signatures of Frenkel polarons in H- and J-aggregates. Acc Chem Res **2010,** 43 (3), 429-39.
18. Yamagata, H.; Spano, F. C., Interplay between intrachain and interchain interactions in semiconducting polymer assemblies: the HJ-aggregate model. J Chem Phys **2012,** 136 (18), 184901.
19. Kasha, M.; Rawls, H. R.; Ashraf El-Bayoumi, M., The exciton model in molecular spectroscopy. Pure and Applied Chemistry **1965,** 11 (3-4).
20. Davydov, A. S., The Theory of Molecular Excitons. Soviet Physics Uspekhi **1964,** 7 (2), 145-178.
21. Craig, D. P.; Walmsley, S. H., Excitons in Molecular Crystals. W. A. Benjamin, Inc.: New York, 1968.
22. McRae, E. G.; Kasha, M., The Molecular Exciton Model. In Physical Processes in Radiation Biology, Augenstein, L.; Mason, R.; Rosenberg, B., Eds. Academic Press: New York, 1964; pp 23-42.
23. Khan, A. L. T.; Sreearunothai, P.; Herz, L. M.; Banach, M. J.; Köhler, A., Morphology-dependent energy transfer within polyfluorene thin films. Physical Review B **2004,** 69 (8).
24. Eder, T.; Stangl, T.; Gmelch, M.; Remmerssen, K.; Laux, D.; Hoger, S.; Lupton, J. M.; Vogelsang, J., Switching between H- and J-type electronic coupling in single conjugated polymer aggregates. Nat Commun **2017,** 8 (1), 1641.
25. Niles, E. T.; Roehling, J. D.; Yamagata, H.; Wise, A. J.; Spano, F. C.; Moulé, A. J.; Grey, J. K., J-Aggregate Behavior in Poly-3-hexylthiophene Nanofibers. The Journal of Physical Chemistry Letters **2012,** 3 (2), 259-263.
26. Panzer, F.; Bassler, H.; Kohler, A., Temperature Induced Order-Disorder Transition in Solutions of Conjugated Polymers Probed by Optical Spectroscopy. J Phys Chem Lett **2017,** 8 (1), 114-125.
27. Zhong, H.; Li, C. Z.; Carpenter, J.; Ade, H.; Jen, A. K., Influence of Regio- and Chemoselectivity on the Properties of Fluoro-Substituted Thienothiophene and Benzodithiophene Copolymers. J Am Chem Soc **2015,** 137 (24), 7616-9.
28. Fauvell, T. J.; Zheng, T.; Jackson, N. E.; Ratner, M. A.; Yu, L.; Chen, L. X., Photophysical and Morphological Implications of Single-Strand Conjugated Polymer Folding in Solution. Chemistry of Materials **2016,** 28 (8), 2814-2822.
29. Bencheikh, F.; Duché, D.; Ruiz, C. M.; Simon, J.-J.; Escoubas, L., Study of Optical Properties and Molecular Aggregation of Conjugated Low Band Gap Copolymers: PTB7 and PTB7-Th. The Journal of Physical Chemistry C **2015,** 119 (43), 24643-24648.
30. Hu, H.; Chow, P. C. Y.; Zhang, G.; Ma, T.; Liu, J.; Yang, G.; Yan, H., Design of Donor Polymers with Strong Temperature-Dependent Aggregation Property for Efficient Organic Photovoltaics. Acc Chem Res **2017,** 50 (10), 2519-2528.
31. Vezie, M. S.; Few, S.; Meager, I.; Pieridou, G.; Dorling, B.; Ashraf, R. S.; Goni, A. R.; Bronstein, H.; McCulloch, I.; Hayes, S. C.; Campoy-Quiles, M.; Nelson, J., Exploring the origin of high optical absorption in conjugated polymers. Nat Mater **2016,** 15 (7), 746-53.
32. Rossi, G.; Chance, R. R.; Silbey, R., Conformational disorder in conjugated polymers. The Journal of Chemical Physics **1989,** 90 (12), 7594-7601.

33. Spiegel, D.; Pincus, P.; Heeger, A. J., Electronic properties of conjugated polymers in solution: Persistence lengths and photoinduced absorption. Synthetic Metals **1989,** 28 (1-2), 385-391.
34. Grosberg, A. Y.; Khokhlov, A. R., Statistical Physics of Macromolecules. AIP Press: Woodbury, NY, 1994.
35. Pope, M.; Swenberg, C. E., Electronic Processes in Organic Crystals and Polymers. 2 ed.; Oxford University Press: New York, 1999.
36. Yamagata, H.; Hestand, N. J.; Spano, F. C.; Kohler, A.; Scharsich, C.; Hoffmann, S. T.; Bassler, H., The red-phase of poly[2-methoxy-5-(2-ethylhexyloxy)-1,4-phenylenevinylene] (MEH-PPV): a disordered HJ-aggregate. J Chem Phys **2013,** 139 (11), 114903.
37. Yamagata, H.; Spano, F. C., Strong Photophysical Similarities between Conjugated Polymers and J-aggregates. J Phys Chem Lett **2014,** 5 (3), 622-32.
38. Kersting, R.; Lemmer, U.; Mahrt, R. F.; Leo, K.; Kurz, H.; Bassler, H.; Gobel, E. O., Femtosecond energy relaxation in pi -conjugated polymers. Phys Rev Lett **1993,** 70 (24), 3820-3823.
39. Cardona, M., Modulation Spectroscopy. Academic Press: New York, New York, 1969.
40. Ziffer, M. E.; Mohammed, J. C.; Ginger, D. S., Electroabsorption Spectroscopy Measurements of the Exciton Binding Energy, Electron–Hole Reduced Effective Mass, and Band Gap in the Perovskite $CH_3NH_3PbI_3$. ACS Photonics **2016,** 3 (6), 1060-1068.
41. Liess, M.; Jeglinski, S.; Vardeny, Z. V.; Ozaki, M.; Yoshino, K.; Ding, Y.; Barton, T., Electroabsorption spectroscopy of luminescent and nonluminescent π-conjugated polymers. Phys. Rev. B **1997,** 56 (24), 15712-15724.
42. Bublitz, G. U.; Boxer, S. G., Stark spectroscopy: applications in chemistry, biology, and materials science. Annu. Rev. Phys. Chem. **1997,** 48, 213-42.
43. Weiser, G.; Horvath, Á., Electroabsorption Spectroscopy On π-Conjugated Polymers. In Primary Photoexcitations in Conjugated Polymers: Molecular Exciton Versus Semiconductor Band Model, Sariciftci, N. S., Ed. World Scientific: Singapore, 1998; pp 318-362.
44. Petelenz, P.; Stradomska, A., Theoretical interpretation of electro-absorption spectra for intense optical transitions. Physical Review B **2005,** 71 (23).
45. Huynh, U. N. V.; Basel, T. P.; Ehrenfreund, E.; Li, G.; Yang, Y.; Mazumdar, S.; Vardeny, Z. V., Transient Magnetophotoinduced Absorption Studies of Photoexcitations in pi-Conjugated Donor-Acceptor Copolymers. Physical review letters **2017,** 119 (1), 017401.
46. Liptay, W., Dipole Moments and Polarizabilities of Molecules in Excited Electronic States. In Excited States, Lim, E. C., Ed. Academic Press, Inc.: New York, New York, 1974; Vol. 1, pp 129-229.
47. Newville, M.; Ingargiola, A.; Allen, D. B.; Stensitzki, T. LMFIT: Non-Linear Least-Square Minimization and Curve-Fitting for Python. http://cars9.uchicago.edu/software/python/lmfit/confidence.html.
48. Martin, S. J.; Bradley, D. D. C.; Lane, P. A.; Mellor, H.; Burn, P. L., Linear and nonlinear optical properties of the conjugated polymers PPV and MEH-PPV. Physical Review B **1999,** 59 (23), 15133-15142.
49. Feller, F.; Monkman, A. P., Electroabsorption studies of poly(2,5-pyridinediyl). Physical Review B **1999,** 60 (11), 8111-8116.

50. Horváth, Á.; Bässler, H.; Weiser, G., Electroabsorption in Conjugated Polymers. physica status solidi (b) **1992,** 173 (2), 755-764.
51. Wachsmann-Hogiu, S.; Peteanu, L. A.; Liu, L. A.; Yaron, D. J.; Wildeman, J., The Effects of Structural and Microenvironmental Disorder on the Electronic Properties of Poly[2-methoxy,5-(2‘-ethyl-hexoxy)-1,4-phenylene vinylene] (MEH−PPV) and Related Oligomers. The Journal of Physical Chemistry B **2003,** 107 (22), 5133-5143.
52. Sirringhaus, H.; Brown, P. J.; Friend, R. H.; Nielsen, M. M.; Bechgaard, K.; Langeveld-Voss, B. M. W.; Spiering, A. J. H.; Janssen, R. A. J.; Meijer, E. W.; Herwig, P.; de Leeuw, D. M., Two-dimensional charge transport in self-organized, high-mobility conjugated polymers. Nature **1999,** 401 (6754), 685-688.
53. Brown, P. J.; Sirringhaus, H.; Harrison, M.; Shkunov, M.; Friend, R. H., Optical spectroscopy of field-induced charge in self-organized high mobility poly(3-hexylthiophene). Phys. Rev. B **2001,** 63 (12).
54. Österbacka, R.; An, C. P.; Jiang, X. M.; Vardeny, Z. V., Two-Dimensional Electronic Excitations in Self-Assembled Conjugated Polymer Nanocrystals. Science **2000,** 287 (5454), 839-842.

Chapter 4: Long-lived, Non-Geminate, Radiative Recombination of Photogenerated Charges in a Polymer:Small-Molecule Acceptor Photovoltaic Blend

This chapter is based on the work of several authors for a manuscript in preparation entitled "Long-lived, Non-Geminate, Radiative Recombination of Photogenerated Charges in a Polymer:Small-Molecule Acceptor Photovoltaic Blend" by Mark E. Ziffer†, Sae Byeok Jo†, Hongliang Zhong, Long Ye, Hongbin Liu, Francis Lin, Jie Zhang, Xiaosong Li, Harald W. Ade, Alex K.-Y. Jen and David S. Ginger

†=Equal contribution for manuscript in preparation

Section 4.1 Overview

Minimization of open-circuit-voltage (V_{OC}) loss is required to transcend the efficiency limitations on the performance of organic photovoltaics (OPV). We study charge recombination in an OPV blend comprising a polymer donor with a small molecule/non-fullerene acceptor that exhibits both high photovoltaic internal quantum efficiency and high external electroluminescence quantum efficiency. Notably, this donor/acceptor blend, consisting of the donor polymer commonly referred to as PCE10 with a pseudo-planar small molecule acceptor (referred to as FIDTT-2PDI) exhibits relatively bright delayed photoluminescence on the microsecond time scale beyond that observed in the neat material. We study the photoluminescence decay kinetics of the blend in detail and conclude that this long-lived photoluminescence arises from radiative non-geminate recombination of charge carriers, which we propose occurs via a donor/acceptor CT state located close in energy to the singlet state of the polymer donor. Additionally, crystallographic and spectroscopic studies point towards low sub-gap disorder, which could be beneficial for low radiative and non-radiative losses. These results provide an important demonstration of photoluminescence due to non-geminate charge recombination in an efficient OPV blend, a key step in identifying new OPV materials and materials-screening criteria if OPV is to approach the theoretical limits to efficiency.

Section 4.2 Introduction

For a solar cell absorber to reach its theoretical maximum efficiency, the following requirements must be met: 1) the material must generate charge efficiently following the absorption of light, and; 2) the photogeneration of free charge should be balanced by recombination that occurs only via a necessary reciprocal radiative process.[126] These arguments, based on the principles of detailed balance,[27] apply to all solar cell materials, from single-crystal GaAs and hybrid perovskites to organic donor/acceptor blend systems. Indeed, Eq 1. quantifies the maximum achievable open circuit voltage for a material based on the external luminescence efficiency for free charge recombination (η_{ext}):[127]

$$V_{OC} = V_{OC,ideal} + \frac{kT}{q}\ln(\eta_{ext}) \qquad Eq\ 1.$$

This approach, emphasizing the importance of radiative free charge recombination, has been successfully applied to enhance open circuit voltages and power conversion efficiencies in a wide range of established and emerging photovoltaic technologies.[127-128] The current picture of organic photovoltaic operation focuses on free charge generation and subsequent recombination occurring through a manifold of weakly luminescent states formed at the interface between electron donor and acceptor phases (so-called "charge transfer" or "CT" states).[7a, 129]

From the analysis above, it follows that in an ideal organic photovoltaic material, 100% of photoexcitations should result in harvestable charges, and those photogenerated charges should recombine non-geminately via the CT state with 100% radiative efficiency, giving the blend a photoluminescence quantum efficiency (PLQE) of unity.

However, contrary to the relationship dictated by Eq 1., for the past 25 years, standard practice in the field of organic photovoltaics has been to screen blend materials by evaluating their photoluminescence *quenching* efficiency (compared to the PLQE of their neat components), as the quenching of singlet exciton emission from the donor and acceptor components of the blend indicates that a charge transfer event has taken place.[130] While this method has been very successful for identifying blends that can efficiently generate charge, one might argue that it has delayed progress by pushing the field towards pairings of materials such as fullerene acceptors with intrinsically low PLQE.[131] In such materials, charges inevitably recombine through CT states with large losses to non-radiative recombination channels, as the vibrational modes that facilitate non-radiative recombination in the parent materials can couple with the CT states,[132] leading to large deficits in the maximum achievable open circuit voltage (V_{OC}).[28, 129a] Indeed, for polymer/fullerene solar cells with typical external radiative efficiency values in the range of 10^{-9}-10^{-6}, this voltage loss due to non-radiative recombination is considerable (350-550 mV),[28, 133] and indeed quite close to the excess "voltage deficit" these materials exhibit below the radiative limit as one would estimate from Eq. 1.[28, 133] In this context, much work has focused on understanding and reducing non-radiative recombination pathways involving CT states at the interface between polymers and fullerenes.[28, 132, 134]

Recently, *non*-fullerene acceptors, both polymers and small molecules, have gained increasing attention, especially as their photovoltaic performance has matched and then exceeded that of polymer/fullerene blends.[22, 135] Frequent advantages are cited in that they exhibit tunable and complementary absorption spectra that can improve light harvesting, and that they offer wider and more facile ranges of energy level tuning compared to fullerene acceptors. However, another compelling advantage of non-fullerene acceptors is the possibility that these materials may move the field out of the local minimum of radiative efficiency that resulted from optimization on photoluminescence quenching using polymer/fullerene pairings. Although worries persist that the high density of vibrational states that classically facilitate non-radiative recombination in large

aromatic organic molecules[26] could lead to high rates of non-radiative recombination in an organic donor/acceptor system, it is encouraging to note that in the field of organic light emitting diodes, similar intermolecular donor/acceptor exciplex states with very high photoluminescence quantum efficiency (20%) have been achieved.[136] Furthermore, recent advances in OPV over the last several years using strongly absorbing non-fullerene acceptor molecules have led to devices with external electroluminescence quantum efficiencies (EQE_{EL}) on the order of $1x10^{-3}$%,[128c, 128d] which are high by the standards of polymer/fullerene blends.[23, 28]While the EQE_{EL} determines the non-radiative voltage loss of the solar cell itself,[126b] the non-radiative recombination currents in a device can be influenced by parameters such as interface recombination at contacts[137] and leakage currents,[138] which are not strictly related to the intrinsic properties of the absorber material. Therefore, from a materials screening perspective, it is important to study OPV absorber materials that demonstrate the process of radiative recombination of photogenerated free charge.

Herein we study this question using a model blend system based on the donor polymer poly[[2,6′-4,8-di(5-ethylhexylthienyl)benzo[1,2-b;3,3-b] dithiophene] [3-fluoro-2[(2-ethylhexyl)carbonyl] thieno[3,4-b]thiophenediyl]] (“PCE10”) and a pseudo-planar, small-molecule, non-fullerene acceptor consisting of an indacenodithieno[3,2-b]thiophene unit chemically fused with two perylene diimides (“FIDTT-2PDI”). This blend exhibits close to 80% photovoltaic internal quantum efficiency (IQE_{PV}) at short circuit, and exhibits relatively low V_{OC} loss (for organic photovoltaics) due to non-radiative recombination (ΔV_{nr}) of <300 mV (see below). Using time-resolved photoluminescence spectroscopy, we show that this blend exhibits *radiative* nongeminate recombination of photogenerated free charges out to microsecond time scales. Furthermore, we relate the low voltage losses to the microstructural and molecular properties of the blend and show that despite an apparently low driving force for charge transfer, the PCE10:FIDTT-2PDI system generates charge on early time scales. Together, these results demonstrate that the combined properties of efficient charge generation and photoluminescence due to non-geminate radiative recombination of charge are indeed possible in an efficient OPV blend, which demonstrates materials selection metrics that are needed in order to select OPV blends that will inherently achieve V_{OC}’s closer to the theoretical limits.

Section 4.3 Molecular properties of PCE10 and FIDTT-2PDI

Figure 4.1 a. shows the molecular structure of the polymer donor and small molecule acceptor we use for these studies. This system comprises a blend of the widely used low band gap donor-acceptor alternating copolymer, PCE10, and a small molecule acceptor based on an acceptor-donor-acceptor (A-D-A) type structure which we refer to as FIDTT-2PDI. A fused-ring aromatic indacenodithieno[3,2-b]thiophene (IDTT) unit is used as a central donor aromatically fused with two electron withdrawing units of perylene diimide (PDI). The detailed synthetic route for FIDTT-2PDI is described in the Supporting Information (SI section S12). The IDTT core has been widely utilized[135a] and its rigid ladder-type structure has the advantage of promoting π-π stacking. However, the introduction of bulky alkyl sidechains on it leads to the dominance of intermolecular interaction among the end groups.[135e, 139] With these factors in mind, we hypothesized that the aromatic fusing of IDTT and PDI unit could facilitate more crystalline solid state structures through the pseudo-planar configuration of wide π-plane of the PDI units. Figure 4.1 c. shows the UV-vis absorption spectra of thin films of FIDTT-2PDI, PCE10, and a 1:1 PCE10:FIDTT-2PDI blend. The FIDTT-2PDI acceptor has an optical absorption onset around 1.8 eV and strong absorption features in the range of 2.5-3.0 eV, which complements the absorption spectrum of the lower bandgap PCE10 and gives the PCE10:FIDTT-2PDI blend strong spectral absorption in the range of ~1.6-3.5 eV. Figure 4.2 a. shows the corresponding photovoltaic external quantum efficiency (EQE_{PV}) spectrum of a solar cell based on a 1:1 PCE10:FIDTT-2PDI blend. The device demonstrates a good incident photon to charge collection efficiency close to 70% at the absorption maximum of the PCE10:FIDTT-2PDI blend. Furthermore, the photovoltaic internal quantum efficiency (IQE_{PV}) is high at ~70-80% across the full absorption spectrum of PCE10:FIDTT-2PDI (see SI Fig. S3d. and Section S3), which demonstrates that the conversion of absorbed photons to free charges, and their resulting collection is efficient in this system. From the EQE_{PV} spectrum, we can also calculate the short-circuit current (J_{SC}) of the device using the AM1.5 solar spectrum, which we find to be 13.2 mA/cm^2, in good agreement with the results in Figure 4.2 b.

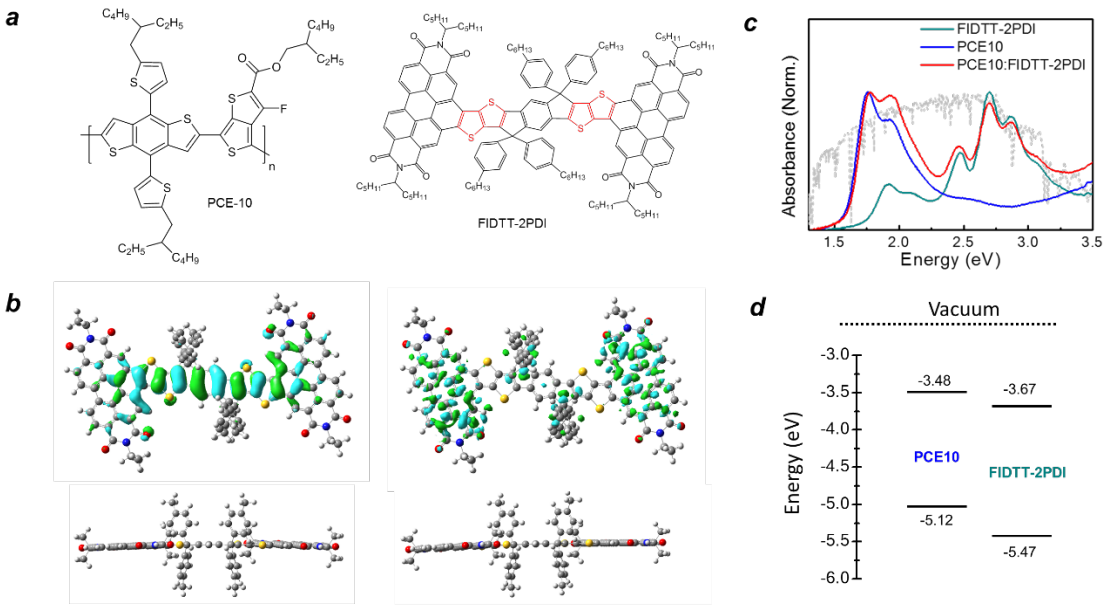

Figure 4.1 ***a.)*** Chemical structures of PCE10 and FIDTT-2PDI. ***b.)*** TD-DFT calculation results of natural transition orbitals and the side-view of molecular geometry. ***c.)*** UV-vis absorption spectrum of thin films of PCE10, FIDTT-2PDI, and a 1:1 PCE10:FIDTT-2PDI blend. The energy level diagram of the molecules estimated by ultraviolet photoemission spectroscopy and optical absorption. Dotted line in ***c.)*** corresponds to AM1.5 global standard solar spectrum (ASTMG173).

Section 4.4 Low non-radiative loss and efficient charge generation in PCE10:FIDTT-2PDI

Figure 4.2 c. plots the external electroluminescence quantum efficiency (EQE_{EL}) as a function of injected current density (J_{inj}) near the J_{SC} for the cell operating at AM1.5. This current density is equivalent to the recombination current in the solar cell under 1 sun illumination and biased at the open-circuit voltage (V_{OC}).[129a] Fig. 4.2 c. shows that the EQE_{EL} under 1 sun equivalent injection conditions is approximately 10^{-3}%. Although well below values for GaAs and perovskite materials, this value is still among the highest values reported to date in an OPV device[128c, 128d] and corresponds to a non-radiative voltage loss of only ~292 meV which is among the lowest reported for an OPV device.[28] A complete understanding of the V_{OC} loss can be gained by analyzing the sub-band gap EQE_{PV} spectrum and electroluminescence (EL) spectrum in the framework of the reciprocity relations between the photogeneration and radiative recombination of free charge.[126b, 133, 140] Following the approach taken by Nelson,[133a] Kirchartz,[133b] and Rau,[126b] we use the electroluminescence spectrum measured at 1 sun equivalent injection to recreate and extend the sub-bandgap tail of the EQE_{PV} spectrum measured using photocurrent spectroscopy in order to calculate the non-ideal radiative V_{OC} loss arising due to a non-step-like band edge (absorption edge broadening).[133]

We first experimentally validate the reciprocity between the electroluminescence of PCE10:FIDTT-2PDI and the sub-bandgap EQE_{PV} spectrum by using the EL spectrum measured at 1 sun equivalent injection conditions and the blackbody radiation spectrum at 295K to recreate the tail of the EQE_{PV} spectrum,[129a, 133a, 141] which is shown by the blue line labeled as ϕ_{EL}/ϕ_{BB} in Fig. 4.1 c. and overlaid on the tail of the measured EQE_{PV} spectrum (see SI section S2 for details on recreating the EQE_{PV} tail). Using the recreated EQE_{PV} spectrum extended down to low energies, we can then calculate the radiative saturation current J_0^{rad} in order to estimate the non-ideal *radiative* V_{OC} loss (ΔV_{OC}^{rad}) (i.e. that due to the non-ideal band shape) using Eqs 2 & 3:

$$J_{0,rad} = q\int_0^\infty EQE_{PV}(E)\emptyset_{BB}(E)\,dE \qquad Eq\ 2.$$

$$\Delta V_{OC}^{rad} = \frac{kT}{q}\ln\left(\frac{J_0^{SQ}}{J_0^{rad}}\right) \qquad Eq\ 3.$$

Using Eqs 2 & 3 we calculate ΔV_{OC}^{rad} to be ~68mV, which is on the very low end of most OPV systems[133] and indicates a sharp absorption edge suggesting a low degree of disorder at the band edge. Considering a Shockley-Quiesser limited V_{OC} of 1.381 V for a solar cell with a bandgap E_g^{PV}=1.655 eV (see Appendix B section S1 for determination of E_g^{PV}), our measured values for ΔV_{OC}^{rad} (~68 mV) and $\Delta V_{OC}^{non-rad}$ (292 mV) account quantitatively for the experimentally measured V_{OC} of 1.06 V (See Appendix B section S2 for full voltage loss analysis).

The collective device results demonstrate several important points about the PCE10:FIDTT-2PDI system: when incorporated in a solar cell, PCE10:FIDTT-2PDI shows not only efficient photoinduced free charge generation (IQE_{PV}), but also efficient luminescence (EQE_{EL}) due to the recombination of injected free charge. Furthermore, by demonstrating the reciprocity between the EL and the EQE_{PV} spectra in Figure 4.2 c., we conclude that the EL spectrum also represents the emission spectrum for the recombination of *photogenerated* free charge in PCE10:FIDTT-2PDI.[126b] These properties make the PCE10:FIDTT-2PDI system useful for studying the recombination of photogenerated free charge in photoluminescence, as we next turn to explore.

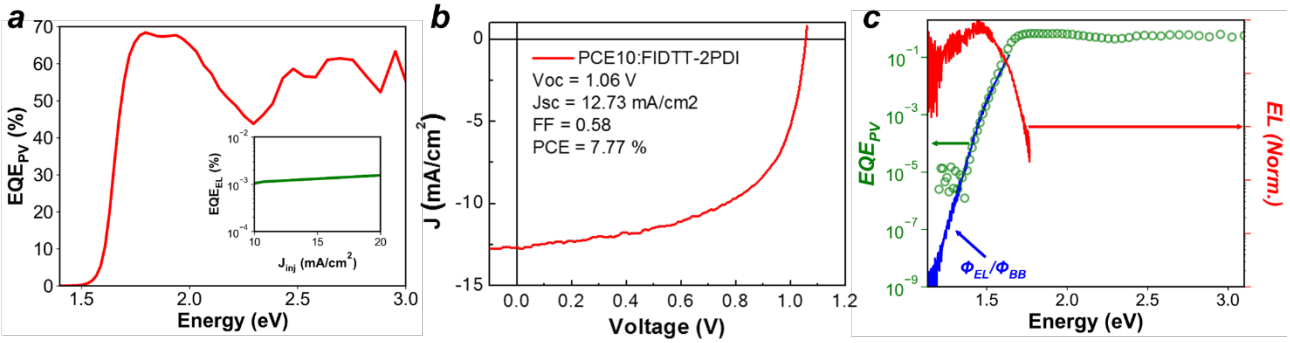

Figure 4.2 ***a.)*** EQE_{PV} spectrum of a 1:1 PCE10:FIDTT-2PDI device (*inset:* EQE_{EL} of a 1:1 PCE10:FIDTT-2PDI device displayed as a function of injected current density near 1 sun injection conditions). ***b.)*** Photovoltaic performance of a device based on 1:1 PCE10:FIDTT-2PDI blend measured under AM1.5 illumination. ***c.)*** EQE_{PV} spectrum of 1:1 PCE10:FIDTT-2PDI measured using sensitive lock-in techniques to resolve the sub-bandgap absorption tail shown with the normalized electroluminescence spectrum. The blue line shows the EQE_{PV} tail recreated from the EL spectrum and blackbody radiation spectrum, demonstrating the reciprocity relationship between the sub-gap EQE_{PV} and EL spectrum.

Section 4.5 Photoluminescence from Radiative Nongeminate Charge Recombination

We study the radiative decay kinetics of pristine films of PCE10:FIDTT-2PDI using time-resolved photoluminescence spectroscopy by selectively exciting the PCE10 donor at 735 nm (1.69 eV). Importantly, this blend and excitation scheme allow us to monitor the decay kinetics of PCE10 polymer excitons and CT states *without any competing kinetic processes due to energy transfer* from FIDTT-2PDI to PCE10. In particular, we chose 735 nm as the excitation wavelength to selectively excite PCE10 because of the high (~69%) IQE_{PV} of the PCE10:FIDTT-2PDI device at this wavelength compared to redder wavelengths in the IQE_{PV} spectrum, which maximizes the probability that charge generation that would occur upon photoexcitation. In Figure 4.3 a., we compare the time-resolved photoluminescence decay of neat PCE10 with PCE10:FIDTT-2PDI over a time window of 50 ns. At early times (~0-2 ns), we observe a faster decay in PCE10:FIDTT-2PDI than neat PCE10, which indicates fast quenching of the initial excited state (singlet excitons on PCE10) due to charge transfer, as is typically seen in donor/acceptor OPV blends.[142] However, beyond 2 ns, we observe a long-lived delayed luminescence tail that extends out past the 50 ns time window in the PCE10:FIDTT-2PDI blend. *In contrast, we observe no such tail in the neat PCE10 film*, where the photoluminescence decays to the noise level at around 10 ns.

Delayed luminescence in neat polymer films has been widely-studied, and is typically attributed to delayed fluorescence due to triplet-triplet annihilation[143] or phosphorescence[144] (the latter being observed only at cryogenic temperatures). On the contrary, delayed luminescence is less commonly reported in donor/acceptor blends: more often the photoluminescence of a donor/acceptor blend is strongly quenched due to charge transfer, resulting in a faster observed

photoluminescence decay in the blend than for either neat component.[145] There have been a few studies reporting long-time luminescence tails in organic donor/acceptor blends,[142a, 146] which have been explained almost exclusively as resulting from *geminate* recombination from a CT/exciplex state[142a, 146a-e, 146h] or very rarely as radiative non-geminate charge recombination via a similar intermediate state.[146f, 146g]

Here, we consider that the long luminescent tail that we observe in the PCE10:FIDTT-2PDI blends could arise from one of these possibilities, notably: (1) it could be the result of radiative non-geminate recombination of free charges; (2) it could result from slow geminate recombination of trapped CT states, or (3) it could result from the interplay of long-lived triplet states.

To test these possibilities further, we compare the photoluminescence decays at room temperature as a function of excitation fluence. Fig. 4.3 b. shows the photoluminescence decay of the PCE10:FIDTT-2PDI blend extended out to a 1 microsecond time window. In order to test if the delayed photoluminescence is due to a geminate or non-geminate process, we measure the photoluminescence decay as a function of pump fluence. Figure 4.3 b. shows the delayed luminescence kinetics at two pump fluences that differ by an order of magnitude (1.7 $\mu J/cm^2$/pulse and 17 $\mu J/cm^2$/pulse), which demonstrates a clear fluence-dependent increase in the photoluminescence decay rate with increasing pump fluence. A fluence-dependent increase in the apparent recombination rate is a clear indication of a non-first order process,[7a, 147] which suggests that the delayed photoluminescence does not arise from geminate CT recombination which should otherwise show first order kinetics.

Figure 4.3 c. shows the time-integrated spectra from the time-resolved photoluminescence data in Figure 4.3 b. during the prompt (0-20 ns) and delayed (20-180 ns) time ranges. The prompt emission spectrum (0-20 ns) overlays well with the steady-state photoluminescence spectrum of PCE10 (black dashed line in Figure 4.3 c.), which is consistent with comparatively bright initial emission from PCE10 at early times before quenching occurs (as shown in the inset of Figure 4.3 a.). Although the signal-to-noise is low in the delayed photoluminescence spectrum (20-180 ns), we see a clear redshift of the emission during the fluence-dependent emission tail, with the long-time spectrum showing good agreement with the electroluminescence spectrum of the PCE10:FIDTT-2PDI device (red dashed line in Figure 4.3 c.). As demonstrated earlier, the reciprocity between the electroluminescence spectrum and EQE_{PV} spectrum (Figure 4.2 c.) implies that the electroluminescence spectrum represents the emission spectrum for *photogenerated* free charges.[126b] We thus consider the good spectral alignment between the electroluminescence and the time-delayed photoluminescence, as evidence that the delayed photoluminescence in PCE10:FIDTT-2PDI arises from the non-geminate recombination of photogenerated charge carriers.

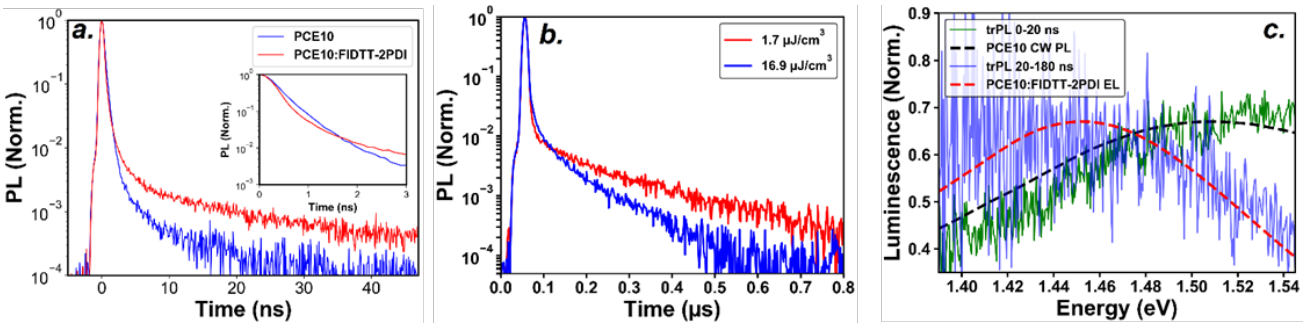

Figure 4.3 ***a.)*** Time-resolved photoluminescence (PL) decays of neat PCE10 and 1:1 PCE10:FIDTT-2PDI following selective excitation of PCE10 at 735 nm (1.69 eV). The PCE10:FIDTT-2PDI blend exhibits a delayed luminescence tail extending beyond the 50 ns time window, (*inset:* early time (0-3 ns) time-resolved PL decay of PCE10 and PCE10:FIDTT-2PDI, showing fast initial quenching of the PCE10:FIDTT-2PDI luminescence). ***b.)*** time-resolved PL decay of 1:1 PCE10:FIDTT-2PDI extended into the microsecond time window, showing that the time-resolved PL tail lasts out to hundreds of nanoseconds and demonstrates fluence dependent kinetics characteristic of non-first order recombination. ***c.)*** Time-integrated spectra from the time-resolved PL measurements showing that the emission redshifts during the long-time tail of the PL decay (20-180 ns) compared to the early time spectrum (0-20ns). The steady-state PL spectrum of neat PCE10 and the EL spectrum of 1:1 PCE10:FIDTT-2PDI are shown overlaid on the 0-20ns and 20-180s spectra respectively, suggesting that while the early time PL intensity comes from unquenched PCE10, the recombination during the long-time tail is characterized by radiative emission from photogenerated charges. We note that the EL spectrum presented here is from the same data as Fig. 4.2 c. but is smoothed by a low-pass filter (see SI section S5 for details).

In order to better test our hypothesis that the delayed photoluminescence arises from the non-geminate recombination of charges, we use transient absorption (TA) spectroscopy to characterize the intensity-dependent excited state kinetics on the ns-μs time scale. Fig. 4.4 a. shows the decay of the photoinduced absorption feature corresponding to the PCE10 polaron (see SI Section S10 for assignment of the TA feature). The polaron absorption measured via TA exhibits fluence-dependent kinetics on the same time scale as the delayed photoluminescence when excited at the same wavelength (735 nm) and comparable fluences (3.0 μJ/cm^2/pulse and 18.1 μJ/cm^2/pulse). Taken together, this data provides further evidence for the non-geminate recombination of photogenerated charge to explain the long photoluminescence tail.

In order compare the TA kinetics to the delayed photoluminescence in a more quantitative fashion, we use a simplified model for bimolecular recombination resulting in radiative and non-radiative decay to perform global fits of both the time-resolved photoluminescence data and the transient absorption data. In this approach, we fit all of the fluence-dependent TA and time-resolved photoluminescence data sets *simultaneously* using a common set of parameters using the bimolecular recombination model as shown in Fig. 4.4 b.

Briefly, we model the time-dependent free-carrier population (FC), PCE10 exciton population (S1), and CT state population (CT), using a set of coupled ordinary differential equations (see SI Section S4 for more details about the model and simulation parameters). As shown in Fig. 4.4 b., in this model, the luminescent recombination of charge in PCE10:FIDTT-2PDI occurs via a CT state (which is consistent with the observation of a redshifted electroluminescence spectrum in the PCE10:FIDTT-2PDI blend compared to either of the neat components, see Appendix B Fig. S5b.).

Figure 4.4 a. and 4.4 c. show the results of the global fits to the TA and time-resolved photoluminescence. The fits converge with a bimolecular charge recombination rate (k_{bi} = 2.23x10^{-11} cm^3/s), which is of similar order of magnitude for bimolecular charge recombination kinetics measured in a wide range of OPV blends.[148] Furthermore, by allowing the radiative and non-radiative recombination rates of the CT state to vary in the fit, we extract a monoexponential lifetime τ_{CT_mono} for the CT state of ~3.97 ns (where $\tau_{CT_{mono}} = 1/(k_{CT_{rad}} + k_{CT_{nonrad}})$) which is in good agreement with monoexponential CT lifetimes reported in the literature,[146c, 146i, 146j] and a PLQE for the CT state of 1.36x10^{-4}, which is consistent to the value that we estimate for the CT PLQE based on steady state photoluminescence measurements (see Appendix B section S7).

We point out that our model only requires the basic assumption of second order kinetics for non-geminate charge recombination (as opposed to many other models in the literature that require empirical reaction orders to fit non-geminate kinetics in OPV systems[149]), and based on this simplified model we consider the global fits to the TA and photoluminescence data to be very good. We consider that the agreement between the fit to the polaron decay in the TA data and the time-resolved photoluminescence data based on a set of common reasonable parameters, and the agreement between the delayed photoluminescence spectrum and the EL spectrum to be strong evidence in favor of the origin of the delayed photoluminescence in PCE10:FIDTT-2PDI being due to the radiative non-geminate recombination of free charge.

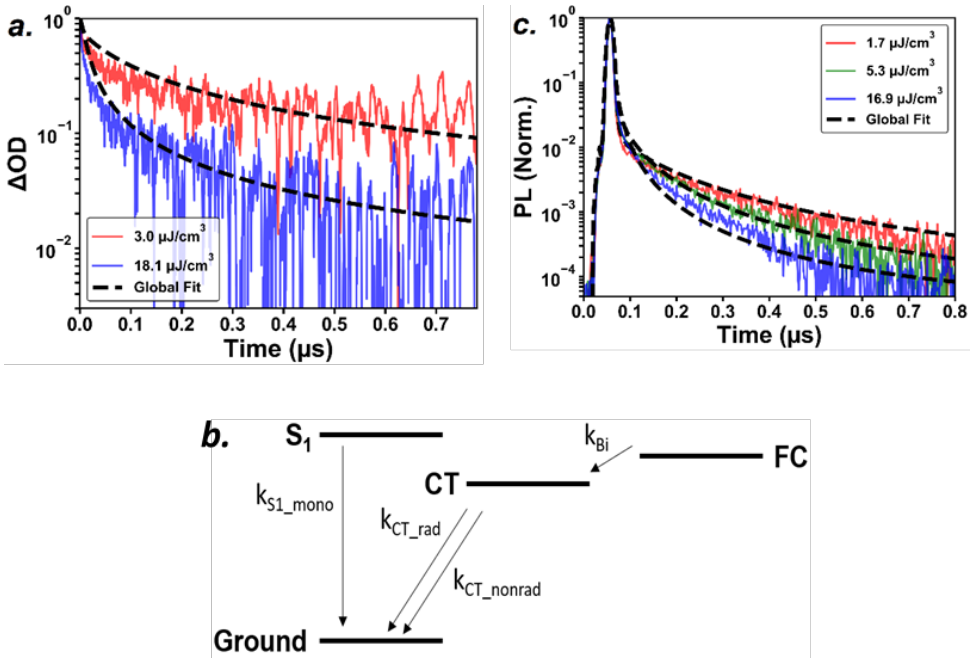

Figure 4.4 ***a.)*** Fluence dependent photoinduced absorption decay of the polaron spectral feature from transient absorption (TA) spectroscopy. Global fits based on the model in *b.)* are shown as black dashed lines. ***b.)*** Schematic of the bimolecular decay model used to globally fit the photoluminescence (PL) and TA data ***c.)*** fluence dependent delayed time-resolved PL data globally fit to the model in *b.)* using the bi-molecular charge recombination rate determined from fitting the fluence dependent TA data.

Returning to the possibility that the long non-geminate photoluminescence tail could arise from the dynamics of triplet states,[143, 146e] we note that Gelinas et al.[146e] observed fluence-dependent delayed luminescence in F8BT:PFB polymer:polymer blends at low temperature (10 K), which they attributed to triplet-triplet annihilation. We believe that triplet-triplet annihilation is an unlikely origin for the delayed photoluminescence observed in our system based on (1) the stronger delayed photoluminescence tail in the blend compared to the PCE10 which would be inconsistent with the formation of triplets via intersystem crossing from the PCE10 singlet; and (2), the radiative lifetime obtained for the emissive state in the delayed photoluminescence from our global fits to the data in Fig. 4.4, which is inconsistent with the expected radiative lifetime if the emissive state were due to triplet-triplet up-conversion, regardless of the origin of triplet formation (See Appendix B Section S8 for a detailed discussion).

We note that Keivanidis et al.[146f, 146g] have also observed delayed luminescence in polymer:small molecule blends of F8BT:PDI and related systems, which they also attributed to the non-geminate recombination of charge via exciplex emission. However, in contrast to the PCE10:FIDTT-2PDI system studied here, solar cells based on F8BT:PDI systems generally exhibit low charge generation efficiency (EQE_{PV} not exceeding ~17%) and poor device performance (PCE <0.1%),[150] raising the possibility that efficient radiative recombination of non-

geminate polarons and efficient charge separation/extraction might be mutually exclusive processes. Importantly, we point out that the PCE10:FIDTT-2PDI system we study here appears to generate photocurrent efficiently (EQE_{PV} approaching 70%), *and* exhibits photoluminescence due to the radiative non-geminate recombination of charge. Given that efficient charge generation and radiative non-geminate recombination of photogenerated charge are basic requirements needed to approach theoretical efficiency limits for solar cells, we believe that finding other organic donor/acceptor systems that exhibit maximum efficiencies for these processes simultaneously will be an important step towards selecting materials to realize higher V_{OC} and ultimately the highest power conversion efficiencies. We next turn to examine the possible molecular and morphological origins related to the low V_{OC} losses in the PCE10:FIDTT-2PDI blend.

Section 4.6 Molecular and Microstructural Aspects of Low Voltage Loss

In order to gain further insight into the voltage losses of the PCE10:FIDTT-2PDI blend with respect to the molecular properties of the FIDTT-2PDI acceptor, we investigate the microstructure of both neat acceptor and blend films, and the physical structure of donor/acceptor interfaces, using 2D grazing-incidence wide-angle X-ray scattering (2D GIWAXS) and resonant soft X-ray scattering (RSoXS).[151] Figure 4.5 a. depicts the 2D GIWAXS patterns of neat FIDTT-2PDI and the PCE10:FIDTT-2PDI blend films, and Figure 4.5 b. their 1D profiles in both the out-of-plane and in-plane directions. The neat FIDTT-2PDI film exhibits characteristic diffraction peaks at 0.33 $Å^{-1}$ (in-plane), 0.42 $Å^{-1}$ (out-of-plane) and 1.64 $Å^{-1}$ (out-of-plane). The *d*-spacings of these peaks of FIDTT-2PDI are slightly different from those of the lamellar stacking (0.29 $Å^{-1}$) and π-π stacking (1.59 $Å^{-1}$) of PCE10, respectively. Interestingly, both crystal diffraction peaks of FIDTT-2PDI are more pronounced in the blend, along with the formation of preferential face-on orientation of PCE10 as exhibited by the pronounced (010) peaks in the out-of-plane direction. This level of molecular order suggests the molecules in the bulk heterojunction have formed self-aggregated domains. However, due to the strong intermolecular interactions, it is also possible that unfavorable domains (larger than the exciton diffusion length) could form though in such cases one would expect a decrease in device performance.

We next probe the domain characteristics of the PCE10:FIDTT-2PDI blend with resonant soft x-ray scattering (RSoXS). Figure 4.5 c. shows the Lorentz-corrected RSoXS profile of the blend acquired at 283.4 eV, where the material contrast is maximum. The average domain purity can be quantified by a parameter called mean-square composition variance, which scales with the area integration of RSoXS profile normalized by film thickness and materials contrast.[151a] By comparing the blend morphology of IDTT-2PDI and its unfused version, we find that the mean-square variance of the PCE10:IDTT-2PDI system is ~1.5 times of that of its unfused counterpart. Additionally, the profile in Figure 4.5 c. is well fitted to a single lognormal distribution. Assuming the samples are globally isotropic in 3 dimensions, the length scale of domains can be estimated by 2π over *q* of the scattering peak. The long period extracted from the profile of the PCE10:IDTT-

2PDI film is estimated to be 33 nm, which agrees well with the size scale measured with transmission electron microscopy image with well-distributed crystal domains (Appendix B Figure S11). Consequently, these results indicate that crystalline domains maintaining reasonable long periods of approximately 33 nm and relatively higher domain purity are formed in the PCE10:FIDTT-2PDI blend.

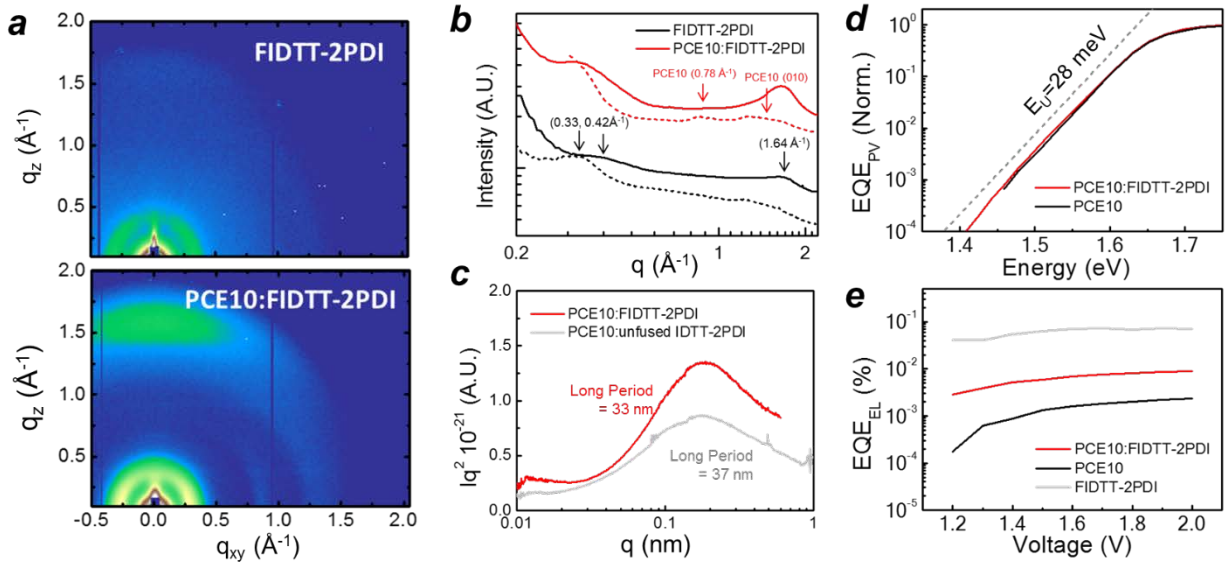

Figure 4.5 ***a.)*** 2D grazing-incidence X-ray diffraction patterns of neat and blend films at optimized conditions and ***b.)*** their 1D line-cuts in out-of-plane (solid lines) and in-plane (dotted lines) directions. ***c.)*** Thickness normalized and Lorentz-corrected resonant soft X-ray scattering profiles acquired at 283.4 eV. Unfused version of FIDTT-2PDI is included for comparison, which has similar long periods with lower domain purity. ***d.)*** Subgap EQE_{PV} spectra and ***e***.) EQE_{EL} with respect to applied voltage for neat and blend films Dotted lines in *d*. demonstrates an Urbach energy of 28 meV.

Importantly, the observation of high domain purity and ordered packing is also well-correlated with the low degree of disorder-induced broadening of the EQE_{PV} tails in the PCE10:FIDTT-2PDI blend. Figure 4.5 d. compares the sub-gap EQE spectra of neat PCE10 and PCE10:FIDTT-2PDI blend devices. As compared to the EQE_{PV} of neat PCE10, it is clear that the blend film exhibits only a subtle broadening of the band edge with an Urbach energy as low as 28 meV, which we attribute to a narrow density of sub-gap states in the PCE10:FIDTT-2PDI blend.[152] These results are consistent with the low non-ideal radiative voltage loss (ΔV_{OC}^{rad}) calculated based on the EL and EQE_{PV} reciprocity analysis in Fig. 4.2 c. above, and suggest a microstructural origin –specifically high local crystalline order – for the low loss. Furthermore, a comparison of the EL spectra between neat PCE10 and the PCE10:FIDTT-2PDI blend (Appendix B Figure S5b.) shows that the EL emission peak in the blend is only 45 meV redshifted compared to that of neat PCE10.

Based on these observations we hypothesize that charge recombination occurs via a narrow distribution of high energy charge transfer states (see above).

We note that, in the common theory used to analyze CT state absorption and emission, the peak of the electroluminescence spectrum occurs at an energy equal to ($E_{CT} - \lambda$), where E_{CT} is the CT state energy and λ is the reorganization energy, the latter is related to the geometric relaxation of the molecule following absorption or emission between the ground and excited CT complex.[140] Based on the position of the EL peak (1.45 eV) in the PCE10:FIDTT-2PDI blend, and considering that the upper limit of E_{CT} should not exceed E_g^{PV}=1.655 eV (the S_1 energy of PCE10), we can estimate an upper limit on λ of ~0.2 eV. We take this value for λ to be a conservative upper limit since the 45 meV redshifted electroluminescence spectrum suggests that E_{CT} is several 10's of meV lower than E_g^{PV}. Indeed, based on fitting the EQE_{PV} and EL spectra to the model derived by Vandewal and coworkers[140] where the value of λ is further constrained to fit the width of the EL spectrum and EQE_{PV} tail, we find that λ is closer to 0.15 eV (see SI Section S9 and Fig. S9), which falls on the very low end of values for λ that have been reported for polymer:small molecule acceptor blends (λ ~0.1 -0.4 eV).[140, 153] Recent work has highlighted the role of both high E_{CT} and small λ in mitigating non-radiative recombination from the excited state CT complex.[28, 132] We can speculate that the small λ for the CT transition may be associated with the structural rigidity of the FIDTT-2PDI acceptor due to its aromatically fused structure, which may be responsible for helping mitigate non-radiative recombination from the CT state.[132, 154] Most obviously, the suppression of non-radiative pathways in films of neat FIDTT-2PDI is evident from its PLQE of 5%, which exceeds that of neat PCE10 (PLQE = 3%, see SI section S6 for details about PLQE measurements of the neat materials) and is orders of magnitude higher than PLQE values measured for fullerenes.[131] In addition, the EQE_{EL} of neat FIDTT-2PDI (Figure 4.5 e.) reaches efficiencies up to 0.1%, which is comparable to the EQE_{EL} typically measured for crystalline silicon solar cells[133a] and for another common acceptor molecule with a rigid IDTT core, ITIC.[153b] Therefore, we postulate that the inherent properties of the neat FIDTT-2PDI molecule that allow it to achieve high radiative efficiency on its own may be helping to suppress non-radiative decay pathways via the CT state in the PCE10:FIDTT-2PDI blend.

Section 4.7 Conclusion

We have studied the voltage losses and nanosecond-to-microsecond scale charge recombination processes in a non-fullerene acceptor blend of the common donor polymer PCE10 and a relatively unstudied acceptor FIDTT-2PDI, comprising an IDTT core based A-D-A type molecule with a fully fused pseudo planar structure. In optimized blends, these materials exhibit good power conversion efficiencies over 7.5% with relatively high EQE_{PV} (70% max) and low V_{OC} loss compared to the Shockley-Queisser limit. This low voltage loss can be attributed to both a low non-ideal radiative loss (~68 meV) due to a sharp band edge, and a relatively low non-radiative loss (292 meV) due to an EQE_{EL} that reaches ~$1x10^{-3}$%. Importantly, this blend shows a long-lived tail out to ~1μs in the transient photoluminescence decay. From the analysis of the intensity-

dependent photoluminescence and intensity-dependent transient absorption kinetics, we conclude that this long emission tail results from the radiative non-geminate recombination of photogenerated free charge carriers.

We propose that the low non-ideal radiative voltage loss in PCE10:FIDTT-2PDI can be understood based on a high degree of interfacial crystallographic order in the blend due to favorable intermolecular interactions promoted by the extended π-conjugated structure of FIDTT-2PDI, which results in a small Urbach energy at the band edge (~28 meV) that we propose also leads to a narrow distribution of high energy sub-gap CT states. We also found that the radiative efficiency of the FIDTT-2PDI molecule itself is good, exhibiting a PLQE of 5% and EQE_{EL} of 0.1%. Based on these observations, we speculate that the low non-radiative voltage loss in the PCE10:FIDTT-2PDI blend is related to the molecular properties of FIDTT-2PDI itself. Recent work has emphasized the relationship between the radiative efficiency of the donor/acceptor CT state and the low-frequency intramolecular vibrational modes of the parent molecules that can induce structural reorganization and facilitate non-radiative decay to the ground state.[132, 154] We therefore hypothesize that the fully fused rigid structure of FIDTT-2PDI may be responsible for the good radiative properties of the molecule itself and the radiative efficiency of the PCE10:FIDTT-2PDI blend, while the narrowing of the CT density of states due to the highly crystalline interfaces may also help to suppress non-radiative recombination from tail sites with lower CT energies.[28]

Most importantly, our observation of photoluminescence due to non-geminate charge recombination in this system has important implications on the selection and evaluation of donor/acceptor pairs for future OPV blends. Photoluminescence due to the recombination of photogenerated free charge is a basic prerequisite for achieving maximum theoretical open circuit voltages in solar cells and is frequently used as a screening metric for high V_{OC} in crystalline inorganic materials that undergo band-to-band radiative recombination.[12, 155] However, photoluminescence due to non-geminate charge recombination has rarely been characterized in OPV blends based on the assumption that efficient generation of charge will be correlated with recombination via pathways that are predominantly non-radiative. In this sense, we propose that for the new generation of donor/acceptor systems based on more highly emissive polymer:non-fullerene acceptor blends, a new materials screening metric that is based on the efficiency of non-geminate free charge photoluminescence is necessary to push researchers in the path towards selecting blends that will maximize V_{OC}. To this end, selecting materials based on the photoluminescence quantum efficiency of the individual donor and acceptor parent molecules may help select blends with inherently more highly luminescent CT states, ultimately enhancing the radiative efficiency of free charge recombination. As pointed out by Keivanidis et al,[146g] in a blend where recombination of free charge occurs radiatively, the absolute intensity of photoluminescence due to free charge recombination will also scale with the charge generation efficiency. Therefore, we believe that ultimately, screening organic photovoltaic blends based on both the efficiency and intensity of photoluminescence due to non-geminate recombination of charge will help select blends that can achieve the highest power conversion efficiencies.

Appendix C

Experimental Methods and Supplementary Information for Chapter 4

Acknowledgments

This work was supported by the Office of Naval Research through grant number N00014-17-1-2201. Part of this work was conducted at the Molecular Analysis Facility, a National Nanotechnology Coordinated Infrastructure site at the University of Washington which is supported in part by the National Science Foundation (grant ECC-1542101), the University of Washington, the Molecular Engineering & Sciences Institute, and the Clean Energy Institute. Crystallographic studies were carried out at the beamlines 11.0.1.2 and 7.3.3, Advanced Light Source, Lawrence Berkeley National Laboratory, which is supported by U.S. Department of Energy under contract DE-AC02-05CH11231. Dr. L. Ye and Prof. H. Ade were supported by Office of Naval Research (ONR, Grant Nos. N00141412322 and N00141712204). Theoretical research by H. Liu and prof. X. Li was supported by the National Science Foundation (CHE-1565520 to X. L.). The use of advanced computational, storage, and networking infrastructure was provided by the Hyak supercomputer system and was funded by the STF at the University of Washington and the National Science Foundation (MRI- 1624430).

References

1. Shockley, W. & Queisser, H. J. Detailed Balance Limit of Efficiency of p-n Junction Solar Cells. *J. Appl. Phys.* **32**, 510-519, doi:10.1063/1.1736034 (1961).
2. Rau, U. Reciprocity relation between photovoltaic quantum efficiency and electroluminescent emission of solar cells. *Phys. Rev. B* **76**, doi:10.1103/PhysRevB.76.085303 (2007).
3. Würfel, P. *Physics of Solar Cells*. 19 (Wiley-VCH, 2005).
4. Miller, O. D., Yablonovitch, E. & Kurtz, S. R. Strong Internal and External Luminescence as Solar Cells Approach the Shockley–Queisser Limit. *IEEE J. of Photovolt.* **2**, 303-311, doi:10.1109/jphotov.2012.2198434 (2012).
5. Green, M. A. Radiative efficiency of state-of-the-art photovoltaic cells. *Prog. Photovoltaics* **20**, 472-476, doi:10.1002/pip.1147 (2012).
6. Abdi-Jalebi, M. *et al.* Maximizing and stabilizing luminescence from halide perovskites with potassium passivation. *Nature* **555**, 497-501, doi:10.1038/nature25989 (2018).
7. Baran, D. *et al.* Reduced voltage losses yield 10% efficient fullerene free organic solar cells with >1 V open circuit voltages. *Energy Environ. Sci.* **9**, 3783-3793, doi:10.1039/c6ee02598f (2016).
8. Liu, J. *et al.* Fast charge separation in a non-fullerene organic solar cell with a small driving force. *Nat. Energy* **1**, 16089, doi:10.1038/nenergy.2016.89 (2016).
9. Vandewal, K., Tvingstedt, K., Gadisa, A., Inganas, O. & Manca, J. V. On the origin of the open-circuit voltage of polymer-fullerene solar cells. *Nat. Mater.* **8**, 904-909, doi:10.1038/nmat2548 (2009).
10. Tvingstedt, K. *et al.* Electroluminescence from charge transfer states in polymer solar cells. *J. Am. Chem. Soc.* **131**, 11819-11824, doi:10.1021/ja903100p (2009).
11. Jailaubekov, A. E. *et al.* Hot charge-transfer excitons set the time limit for charge separation at donor/acceptor interfaces in organic photovoltaics. *Nat. Mater.* **12**, 66-73, doi:10.1038/nmat3500 (2013).
12. Vandewal, K. *et al.* Efficient charge generation by relaxed charge-transfer states at organic interfaces. *Nat. Mater.* **13**, 63-68, doi:10.1038/nmat3807 (2014).
13. Rao, A. *et al.* The role of spin in the kinetic control of recombination in organic photovoltaics. *Nature* **500**, 435-439, doi:10.1038/nature12339 (2013).
14. Bakulin, A. A. *et al.* The role of driving energy and delocalized states for charge separation in organic semiconductors. *Science* **335**, 1340-1344, doi:10.1126/science.1217745 (2012).
15. Burke, T. M., Sweetnam, S., Vandewal, K. & McGehee, M. D. Beyond Langevin Recombination: How Equilibrium Between Free Carriers and Charge Transfer States Determines the Open-Circuit Voltage of Organic Solar Cells. *Adv. Energy Mater.* **5**, 1500123, doi:10.1002/aenm.201500123 (2015).
16. Sariciftci, N. S., Smilowitz, L., Heeger, A. J. & Wudl, F. Photoinduced electron transfer from a conducting polymer to buckminsterfullerene. *Science* **258**, 1474-1476, doi:10.1126/science.258.5087.1474 (1992).
17. Halls, J. J. M. *et al.* Efficient photodiodes from interpenetrating polymer networks. *Nature* **376**, 498-500, doi:10.1038/376498a0 (1995).
18. Sun, Y. P. & Bunker, C. E. Fluorescence of (5,6)-fullerene-C70 in room-temperature solutions: quantum yields and well-resolved spectra as a function of excitation wavelength. *J. Phys. Chem.* **97**, 6770-6773, doi:10.1021/j100128a004 (1993).

19. Chen, X.-K. & Brédas, J.-L. Voltage Losses in Organic Solar Cells: Understanding the Contributions of Intramolecular Vibrations to Nonradiative Recombinations. *Adv. Energy Mater.* **8**, 1702227, doi:10.1002/aenm.201702227 (2018).
20. Benduhn, J. *et al.* Intrinsic non-radiative voltage losses in fullerene-based organic solar cells. *Nat. Energy* **2**, 17053, doi:10.1038/nenergy.2017.53 (2017).
21. Yao, J. *et al.* Quantifying Losses in Open-Circuit Voltage in Solution-Processable Solar Cells. *Phys. Rev. Appl.* **4**, doi:10.1103/PhysRevApplied.4.014020 (2015).
22. Rau, U., Blank, B., Müller, T. C. M. & Kirchartz, T. Efficiency Potential of Photovoltaic Materials and Devices Unveiled by Detailed-Balance Analysis. *Phys. Rev. Appl.* **7**, doi:10.1103/PhysRevApplied.7.044016 (2017).
23 Chen, X.-K., Ravva, M. K., Li, H., Ryno, S. M. & Brédas, J.-L. Effect of Molecular Packing and Charge Delocalization on the Nonradiative Recombination of Charge-Transfer States in Organic Solar Cells. *Adv. Energy Mater.* **6**, 1601325, doi:10.1002/aenm.201601325 (2016).
24. Yan, C. *et al.* Non-fullerene acceptors for organic solar cells. *Nat. Rev. Mater*, **3**, 18003, doi:10.1038/natrevmats.2018.3 (2018).
25. Sun, J. *et al.* Dithieno[3,2-b:2',3'-d]pyrrol Fused Nonfullerene Acceptors Enabling Over 13% Efficiency for Organic Solar Cells. *Adv. Mater.* **30**, e1707150, doi:10.1002/adma.201707150 (2018).
26. Xu, X. *et al.* Realizing Over 13% Efficiency in Green-Solvent-Processed Nonfullerene Organic Solar Cells Enabled by 1,3,4-Thiadiazole-Based Wide-Bandgap Copolymers. *Adv. Mater.* **30**, doi:10.1002/adma.201703973 (2018).
27. Yao, Z. *et al.* Dithienopicenocarbazole-Based Acceptors for Efficient Organic Solar Cells with Optoelectronic Response Over 1000 nm and an Extremely Low Energy Loss. *J. Am. Chem. Soc.* **140**, 2054-2057, doi:10.1021/jacs.7b13239 (2018).
28. Shi, X. *et al.* Design of a Highly Crystalline Low-Band Gap Fused-Ring Electron Acceptor for High-Efficiency Solar Cells with Low Energy Loss. *Chem. Mater.* **29**, 8369-8376, doi:10.1021/acs.chemmater.7b02853 (2017).
29. Dai, S. *et al.* Fused Nonacyclic Electron Acceptors for Efficient Polymer Solar Cells. *J. Am. Chem. Soc.* **139**, 1336-1343, doi:10.1021/jacs.6b12755 (2017).
30. Li, S. *et al.* A Wide Band-Gap Polymer with a Deep HOMO Level Enables 14.2% Efficiency in Polymer Solar Cells. *J. Am. Chem. Soc.*, doi:10.1021/jacs.8b02695 (2018).
31. Pope, M. & Swenberg, C. E. *Electronic Processes in Organic Crystals and Polymers*. 2 edn, (Oxford University Press, 1999).
32. Goushi, K., Yoshida, K., Sato, K. & Adachi, C. Organic light-emitting diodes employing efficient reverse intersystem crossing for triplet-to-singlet state conversion. *Nat. Photonics* **6**, 253-258, doi:10.1038/nphoton.2012.31 (2012).
33. Vandewal, K. Interfacial Charge Transfer States in Condensed Phase Systems. *Annu. Rev. Phys. Chem.* **67**, 113-133, doi:10.1146/annurev-physchem-040215-112144 (2016).
34. Kirchartz, T., Pieters, B. E., Taretto, K. & Rau, U. Mobility dependent efficiencies of organic bulk heterojunction solar cells: Surface recombination and charge transfer state distribution. *Phys. Rev. B* **80**, doi:10.1103/PhysRevB.80.035334 (2009).
35. Knesting, K. M. *et al.* ITO Interface Modifiers Can Improve V_{OC} in Polymer Solar Cells and Suppress Surface Recombination. *J. Phys. Chem. Lett.* **4**, 4038-4044, doi:10.1021/jz4021525 (2013).

36. Ok, K. H. *et al.* Ultra-thin and smooth transparent electrode for flexible and leakage-free organic light-emitting diodes. *Sci. Rep.* **5**, 9464, doi:10.1038/srep09464 (2015).
37. Han, G., Guo, Y., Song, X., Wang, Y. & Yi, Y. Terminal [small pi]-[small pi] stacking determines three-dimensional molecular packing and isotropic charge transport in an A-[small pi]-A electron acceptor for non-fullerene organic solar cells. *J. Mater. Chem. C* **5**, 4852-4857, doi:10.1039/C7TC01310H (2017).
38. Vandewal, K., Tvingstedt, K., Gadisa, A., Inganäs, O. & Manca, J. V. Relating the open-circuit voltage to interface molecular properties of donor:acceptor bulk heterojunction solar cells. *Phys. Rev. B* **81**, doi:10.1103/PhysRevB.81.125204 (2010).
39. Gong, W. *et al.* Influence of energetic disorder on electroluminescence emission in polymer:fullerene solar cells. *Phys. Rev. B* **86**, doi:10.1103/PhysRevB.86.024201 (2012).
40. Di Nuzzo, D. *et al.* Simultaneous Open-Circuit Voltage Enhancement and Short-Circuit Current Loss in Polymer: Fullerene Solar Cells Correlated by Reduced Quantum Efficiency for Photoinduced Electron Transfer. *Adv. Energy Mater.* **3**, 85-94, doi:10.1002/aenm.201200426 (2013).
41. Veldman, D., Meskers, S. C. J. & Janssen, R. A. J. The Energy of Charge-Transfer States in Electron Donor-Acceptor Blends: Insight into the Energy Losses in Organic Solar Cells. *Adv. Funct. Mater.* **19**, 1939-1948, doi:10.1002/adfm.200900090 (2009).
42. Partee, J. *et al.* Delayed Fluorescence and Triplet-Triplet Annihilation in π-Conjugated Polymers. *Phys. Rev. Lett.* **82**, 3673-3676, doi:10.1103/PhysRevLett.82.3673 (1999).
43. Rothe, C. & Monkman, A. P. Triplet exciton migration in a conjugated polyfluorene. *Phys. Rev. B* **68**, doi:10.1103/PhysRevB.68.075208 (2003).
44. Hertel, D., Bässler, H., Guentner, R. & Scherf, U. Triplet-triplet annihilation in a poly(fluorene)-derivative. *J. Chem. Phys.* **115**, 10007-10013, doi:10.1063/1.1415446 (2001).
45. Romanovskii, Y. V. *et al.* Phosphorescence of pi-conjugated oligomers and polymers. *Phys. Rev. Lett.* **84**, 1027-1030, doi:10.1103/PhysRevLett.84.1027 (2000).
46. Hertel, D. *et al.* Phosphorescence in Conjugated Poly(para-phenylene)-Derivatives. *Adv. Mater.* **13**, 65-70, doi:10.1002/1521-4095(200101)13:1<65::aid-adma65>3.0.co;2-q (2001).
47. Theander, M. *et al.* Photoluminescence quenching at apolythiophene/C60heterojunction. *Phys. Rev. B* **61**, 12957-12963, doi:10.1103/PhysRevB.61.12957 (2000).
48. Shaw, P. E., Ruseckas, A. & Samuel, I. D. W. Exciton Diffusion Measurements in Poly(3-hexylthiophene). *Adv. Mater.* **20**, 3516-3520, doi:10.1002/adma.200800982 (2008).
49. Hedley, G. J. *et al.* Determining the optimum morphology in high-performance polymer-fullerene organic photovoltaic cells. *Nat. Commun.* **4**, 2867, doi:10.1038/ncomms3867 (2013).
50. Arndt, A. P. *et al.* Time-Resolved Charge-Transfer State Emission in Organic Solar Cells: Temperature and Blend Composition Dependences of Interfacial Traps. *J. Phys. Chem. C* **119**, 13516-13523, doi:10.1021/acs.jpcc.5b03507 (2015).
51. Gerhard, M. *et al.* Temperature- and Energy-Dependent Separation of Charge-Transfer States in PTB7-Based Organic Solar Cells. *J. Phys. Chem. C* **119**, 28309-28318, doi:10.1021/acs.jpcc.5b09842 (2015).
52. Jarzab, D. *et al.* Low-Temperature Behaviour of Charge Transfer Excitons in Narrow-Bandgap Polymer-Based Bulk Heterojunctions. *Adv. Energy Mater.* **1**, 604-609, doi:10.1002/aenm.201100083 (2011).

53. Morteani, A. C., Sreearunothai, P., Herz, L. M., Friend, R. H. & Silva, C. Exciton regeneration at polymeric semiconductor heterojunctions. *Phys. Rev. Lett.* **92**, 247402, doi:10.1103/PhysRevLett.92.247402 (2004).
54. Gélinas, S. *et al.* The Binding Energy of Charge-Transfer Excitons Localized at Polymeric Semiconductor Heterojunctions. *J. Phys. Chem. C* **115**, 7114-7119, doi:10.1021/jp200466y (2011).
55. Keivanidis, P. E. *et al.* Delayed luminescence spectroscopy of organic photovoltaic binary blend films: Probing the emissive non-geminate charge recombination. *Adv. Mater.* **22**, 5183-5187, doi:10.1002/adma.201002389 (2010).
56. Keivanidis, P. E. *et al.* Correlating Emissive Non-Geminate Charge Recombination with Photocurrent Generation Efficiency in Polymer/Perylene Diimide Organic Photovoltaic Blend Films. *Adv. Funct. Mater.* **22**, 2318-2326, doi:10.1002/adfm.201102871 (2012).
57. Huang, Y. S. *et al.* Electronic structures of interfacial states formed at polymeric semiconductor heterojunctions. *Nat. Mater.* **7**, 483-489, doi:10.1038/nmat2182 (2008).
58. Veldman, D. *et al.* Compositional and electric field dependence of the dissociation of charge transfer excitons in alternating polyfluorene copolymer/fullerene blends. *J. Am. Chem. Soc.* **130**, 7721-7735, doi:10.1021/ja8012598 (2008).
59. Bernardo, B. *et al.* Delocalization and dielectric screening of charge transfer states in organic photovoltaic cells. *Nat. Commun.* **5**, 3245, doi:10.1038/ncomms4245 (2014).
60. Loi, M. A. *et al.* Charge Transfer Excitons in Bulk Heterojunctions of a Polyfluorene Copolymer and a Fullerene Derivative. *Adv. Funct. Mater.* **17**, 2111-2116, doi:10.1002/adfm.200601098 (2007).
61. Howard, I. A., Mauer, R., Meister, M. & Laquai, F. Effect of morphology on ultrafast free carrier generation in polythiophene:fullerene organic solar cells. *J. Am. Chem. Soc.* **132**, 14866-14876, doi:10.1021/ja105260d (2010).
62. Bartesaghi, D. *et al.* Competition between recombination and extraction of free charges determines the fill factor of organic solar cells. *Nat. Commun.* **6**, 7083, doi:10.1038/ncomms8083 (2015).
63. Etzold, F. *et al.* Ultrafast exciton dissociation followed by nongeminate charge recombination in PCDTBT:PCBM photovoltaic blends. *J. Am. Chem. Soc.* **133**, 9469-9479, doi:10.1021/ja201837e (2011).
64. Shuttle, C. G. *et al.* Bimolecular recombination losses in polythiophene: Fullerene solar cells. *Phys. Rev. B* **78**, doi:10.1103/PhysRevB.78.113201 (2008).
65. Keivanidis, P. E., Ho, P. K. H., Friend, R. H. & Greenham, N. C. The Dependence of Device Dark Current on the Active-Layer Morphology of Solution-Processed Organic Photodetectors. *Adv. Funct. Mater.* **20**, 3895-3903, doi:10.1002/adfm.201000967 (2010).
66. Ye, L. *et al.* Quantitative relations between interaction parameter, miscibility and function in organic solar cells. *Nat. Mater.* **17**, 253-260, doi:10.1038/s41563-017-0005-1 (2018).
67. Zhong, H., Li, C.-Z., Carpenter, J., Ade, H. & Jen, A. K. Y. Influence of Regio- and Chemoselectivity on the Properties of Fluoro-Substituted Thienothiophene and Benzodithiophene Copolymers. *J. Am. Chem. Soc.* **137**, 7616-7619, doi:10.1021/jacs.5b04209 (2015).
68. Kronemeijer, A. J. *et al.* Two-dimensional carrier distribution in top-gate polymer field-effect transistors: correlation between width of density of localized states and Urbach energy. *Adv. Mater.* **26**, 728-733, doi:10.1002/adma.201303060 (2014).

69. Graham, K. R. *et al.* Importance of the donor:fullerene intermolecular arrangement for high-efficiency organic photovoltaics. *J. Am. Chem. Soc.* **136**, 9608-9618, doi:10.1021/ja502985g (2014).
70. Zhao, W. *et al.* Fullerene-Free Polymer Solar Cells with over 11% Efficiency and Excellent Thermal Stability. *Adv. Mater.* **28**, 4734-4739, doi:10.1002/adma.201600281 (2016).
71. Vandewal, K. *et al.* Absorption Tails of Donor:C60 Blends Provide Insight into Thermally Activated Charge-Transfer Processes and Polaron Relaxation. *J. Am. Chem. Soc.* **139**, 1699-1704, doi:10.1021/jacs.6b12857 (2017).
72. Burke, T. M. & McGehee, M. D. How High Local Charge Carrier Mobility and an Energy Cascade in a Three-Phase Bulk Heterojunction Enable >90% Quantum Efficiency. *Adv. Mater.* **26**, 1923-1928, doi:10.1002/adma.201304241 (2014).
73. Sweetnam, S. *et al.* Characterization of the Polymer Energy Landscape in Polymer:Fullerene Bulk Heterojunctions with Pure and Mixed Phases. *J. Am. Chem. Soc.* **136**, 14078-14088, doi:10.1021/ja505463r (2014).
74. Ndjawa, G. O. N. *et al.* Open-Circuit Voltage in Organic Solar Cells: The Impacts of Donor Semicrystallinity and Coexistence of Multiple Interfacial Charge-Transfer Bands. *Adv. Energy Mater.* **7**, 1601995, doi:10.1002/aenm.201601995 (2017).
75. Sini, G. *et al.* On the Molecular Origin of Charge Separation at the Donor-Acceptor Interface. *Adv. Energy Mater.* **8**, 1702232, doi:10.1002/aenm.201702232 (2018).
76. Ran, N. A. *et al.* Harvesting the Full Potential of Photons with Organic Solar Cells. *Adv. Mater.* **28**, 1482-1488, doi:10.1002/adma.201504417 (2016).
77. Tamai, Y. *et al.* Ultrafast Long-Range Charge Separation in Nonfullerene Organic Solar Cells. *ACS Nano* **11**, 12473-12481, doi:10.1021/acsnano.7b06575 (2017).
78. M., S. J. *et al.* Photovoltaic Function and Exciton/Charge Transfer Dynamics in a Highly Efficient Semiconducting Copolymer. *Adv. Funct. Mater.* **24**, 10-26, doi:doi:10.1002/adfm.201301820 (2014).
79. Cha, H. *et al.* Influence of Blend Morphology and Energetics on Charge Separation and Recombination Dynamics in Organic Solar Cells Incorporating a Nonfullerene Acceptor. *Adv. Funct. Mater.* **28**, 1704389, doi:10.1002/adfm.201704389 (2018).
80. Gélinas, S. *et al.* Ultrafast Long-Range Charge Separation in Organic Semiconductor Photovoltaic Diodes. *Science* **343**, 512-516, doi:10.1126/science.1246249 (2014).
81. Zhang, J. *et al.* Control of Geminate Recombination by the Material Composition and Processing Conditions in Novel Polymer: Nonfullerene Acceptor Photovoltaic Devices. *J. Phys. Chem. A* **122**, 1253-1260, doi:10.1021/acs.jpca.7b11891 (2018).
82. Jakowetz, A. C. *et al.* What Controls the Rate of Ultrafast Charge Transfer and Charge Separation Efficiency in Organic Photovoltaic Blends. *J. Am. Chem. Soc.* **138**, 11672-11679, doi:10.1021/jacs.6b05131 (2016).
83. Gorenflot, J. *et al.* From Recombination Dynamics to Device Performance: Quantifying the Efficiency of Exciton Dissociation, Charge Separation, and Extraction in Bulk Heterojunction Solar Cells with Fluorine-Substituted Polymer Donors. *Adv. Energy Mater.* **8**, 1701678, doi:10.1002/aenm.201701678 (2018).
84. Katahara, J. K. & Hillhouse, H. W. Quasi-Fermi level splitting and sub-bandgap absorptivity from semiconductor photoluminescence. *J. Appl. Phys.* **116**, 173504, doi:10.1063/1.4898346 (2014).

85. Braly, I. L. *et al.* Hybrid perovskite films approaching the radiative limit with over 90% photoluminescence quantum efficiency. *Nat. Photonics*, doi:10.1038/s41566-018-0154-z (2018).
86. Forrest, S. R., Bradley, D. D. C. & Thompson, M. E. Measuring the Efficiency of Organic Light-Emitting Devices. *Adv. Mater.* **15**, 1043-1048, doi:10.1002/adma.200302151 (2003).
87. de Mello, J. C., Wittmann, H. F. & Friend, R. H. An improved experimental determination of external photoluminescence quantum efficiency. *Adv. Mater.* **9**, 230-232, doi:10.1002/adma.19970090308 (1997).
88. Alexander, H. *et al.* A SAXS/WAXS/GISAXS Beamline with Multilayer Monochromator. *Journal of Physics: Conference Series* **247**, 012007 (2010).
89. Gann, E. *et al.* Soft x-ray scattering facility at the Advanced Light Source with real-time data processing and analysis. *Review of Scientific Instruments* **83**, 045110, doi:10.1063/1.3701831 (2012).

Conclusion

We conclude this thesis by summarizing the works presented herein and also give an updated context to these studies while proposing future research directions.

In Chapter 2 we presented a detailed study into the nature of band edge photoexcitations in the prototypical photovoltaic hybrid organic-inorganic perovskite $CH_3NH_3PbI_3$. Using electroabsorption spectroscopy we found that the optical response to an applied electric field could be understood in terms of the low-field Franz-Keldysh-Aspnes effect, which predicts a third-derivative like lineshape whose amplitude scales quadratically with applied field and is in proportion to the electron-hole reduced effective mass. We found that the electroabsorption spectrum in $CH_3NH_3PbI_3$ could be best represented using a Franz-Keldysh-Aspnes (FKA) type model which is modified to take into account the response of a Coulomb-modified continuum of states,[1] which allowed us to model the electroabsorption response in terms of Elliott's formula[2] and calculate and exciton binding energy and one electron-band gap. Using this information we were able to predict an ionization field for the exciton based on a detailed analysis of the exact effects of an electric field on a Wannier exciton, which we were able to observe experimentally only upon lowering the temperature of the sample. This signified that at room temperature optical transitions occur directly into continuum states, resulting in the FKA-like response.

This study suggests several interesting avenues for further research. The implication that only as the sample cools down do field ionization effects become visible suggests that at room temperature the excitons are already ionized, as has been predicted in the theory of exciton line shapes by Segall and coworkers.[3] This suggests that detailed studies of exciton-phonon coupling effects, in particular as they relate to the initial photon absorption process, are of great importance for future study. Indeed we point out that more recently in a related compound, $CH_3NH_3PbBr_3$, as well as in two dimension hybrid-organic inorganic perovskites, signatures of coherent coupling between excitons and phonons have been observed in ultrafast transient absorption spectroscopy measurements.[4-5] Detailed analysis into the role that these interactions may play in photocarrier generation may be very interesting, especially in lower dimensional hybrid perovskite systems where the electronic properties alone of the exciton would otherwise preclude efficient dissociation.

In Chapter 3 we studied the nature of excitons in two isomers of the popular photovoltaic polymer known as "PCE10," which we referred to as "P1" and "P2". The isomers were designed specifically to promote different degrees of backbone rigidity, which was clearly reflected in absorption measurements on polymers in solution and on the difference in magnitude in the imaginary part of the optical dielectric function. Furthermore, the differences in backbone structure were found to lead to a dramatic difference in the exciton electronic structure with regards to differences in the predominance of interchain versus intrachain electronic coupling in the two polymer systems. Remarkably, we found that the differences were significant enough to result in J-aggregate like behavior in P2 and H-aggregate like behavior in P1. Notably, we found that the behavior in P2 could be described by predictions based on the generalized HJ aggregate model of Spano and coworkers,[6] which predicts a thermally activated transition from H-like to J-like

behavior in conjugated polymer aggregates. These results suggested that intrachain electronic coupling dominates in P2, whereas interchain electronic coupling dominates in P1. Using this knowledge, we performed electroabsorption spectroscopy measurements on the two polymers analyzed using the model of Liptay[7] allowing us to extract values for the change in polarizability ($\Delta\alpha_{g\rightarrow e}$) in the ground to excited state transition for P1 and P2. We found that interestingly, P1 showed a larger (1.6 fold difference) in excess polarizability than P2. This result suggests the fascinating possibility that interchain electronic coupling (as opposed to intrachain coupling) may dominate the polarizability of an exciton in conjugated polymers.

This study suggests certain intriguing avenues of further research. The observation of a thermally activated H- to J- transition suggests the exciting possibility of being able to observe the phenomenon of thermally activated super-radiance in a polymer system proposed by Spano and coworkers.[6] This would require a more detailed study involving comparing the radiative recombination rates of the polymer with its monomer analogue. An observation of this effect would be truly remarkable, as it defies the conventional notion that the destruction of intrachain exciton coherence due to thermal fluctuations in conjugated polymers would prevent the observation of a thermally activated superradiance phenomenon. This study also opens up the door to forming new interesting correlations between exciton electronic properties such as the exciton coherence length and bandwidth with electronic properties such as the polarizability of the exciton. A more detailed study would be needed to quantify the exciton coherence length and bandwidth. However, such correlations could provide new understanding into how these properties affect the electrostatic behavior of the exciton.

In Chapter 4 we studied charge recombination in a low V_{OC} loss polymer:small molecule photovoltaic blend and made a remarkable observation of photoluminescence due to the radiative non-geminate recombination of photogenerated charge. This process has been critically overlooked in the field of organic photovoltaics due to an assumption that recombination via charge transfer states will effectively quench photoluminescence. However the observation of photoluminescence due to the recombination of free charges is a fundamental prerequisite to achieving maximum open circuit voltages in solar cells. Therefore observing this phenomenon in an efficient photovoltaic blend may help researchers to rethink the screening and design criteria needed to maximize the efficiency of organic photovoltaic materials.

One very intriguing unanswered question is how the efficiency or intensity of *photoluminescence* due to non-radiative charge recombination in an organic photovoltaic material compares to the efficiency of *electroluminescence* when the material is incorporated into a device. Almost all studies estimating radiative efficiency report the electroluminescence quantum efficiency, and very few studies have reported photoluminescence quantum efficiencies of charge transfer states in organic photovoltaics. One that has reported PLQE of a CT state on a polymer:fullerene blend[8] reported values several orders of magnitude higher than the electroluminescence quantum efficiencies typically measured in polymer:fullerene blends. Indeed in our study, we also found from our model that the photoluminescence quantum efficiency for free charge recombination appears to be an order of magnitude higher than the electroluminescence quantum efficiency. While there may be reasonable explanations for this based on the possibility

of leakage currents or interface recombination in a device, it suggests that the intrinsic luminescence efficiency of charge transfer states in OPV systems may already be several orders of magnitude higher than is commonly quoted in the literature, and gives hope that advances in molecular engineering of CT states could lead to dramatic improvements in V_{OC} in organic photovoltaics in the near future.

In conclusion, we hope that the readers of this thesis were able to take away new ideas and that some of the work presented here may inspire new avenues of thought or research. It will truly be exciting to see how technologies based on the materials systems studied herein advance in the next several years, and whether or not these technologies become an important part of our daily lives in the long term future.

References

1. Rowe, J.; Aspnes, D., Approximate Treatment of Exciton Effects in Electric Field Modulation Via the Slater-Koster Interaction. *Phys. Rev. Lett.* **1970,** *25* (3), 162-165.
2. Elliott, R. J., Theory of Excitons: I. In *Polarons and Excitons*, Kuper, C. G.; Whitefield, G. D., Eds. Oliver and Boyd: Edinburgh, 1963; pp 269-293.
3. Rudin, S.; Reinecke, T. L.; Segall, B., Temperature-dependent exciton linewidths in semiconductors. *Phys. Rev. B* **1990,** *42* (17), 11218-11231.
4. Ni, L.; Huynh, U.; Cheminal, A.; Thomas, T. H.; Shivanna, R.; Hinrichsen, T. F.; Ahmad, S.; Sadhanala, A.; Rao, A., Real-Time Observation of Exciton-Phonon Coupling Dynamics in Self-Assembled Hybrid Perovskite Quantum Wells. *ACS Nano* **2017,** *11* (11), 10834-10843.
5. Batignani, G.; Fumero, G.; Srimath Kandada, A. R.; Cerullo, G.; Gandini, M.; Ferrante, C.; Petrozza, A.; Scopigno, T., Probing femtosecond lattice displacement upon photo-carrier generation in lead halide perovskite. *Nature Communications* **2018,** *9* (1), 1971.
6. Yamagata, H.; Spano, F. C., Interplay between intrachain and interchain interactions in semiconducting polymer assemblies: the HJ-aggregate model. *J Chem Phys* **2012,** *136* (18), 184901.
7. Liptay, W., Dipole Moments and Polarizabilities of Molecules in Excited Electronic States. In *Excited States*, Lim, E. C., Ed. Academic Press, Inc.: New York, New York, 1974; Vol. 1, pp 129-229.
8. Jarzab, D.; Cordella, F.; Gao, J.; Scharber, M.; Egelhaaf, H.-J.; Loi, M. A., Low-Temperature Behaviour of Charge Transfer Excitons in Narrow-Bandgap Polymer-Based Bulk Heterojunctions. *Adv. Energy Mater.* **2011,** *1* (4), 604-609.

Appendix A Supporting Information for Chapter 2

Experimental Methods

Preparation of thin-film $CH_3NH_3PbI_3$ samples

Substrates for EA measurements were prepared by depositing 80 nm of Al_2O_3 via atomic layer deposition onto ITO coated glass slides. Prior to thin-film deposition the Al_2O_3/ITO substrates were sonicated sequentially in acetone and isopropanol for 15 minutes each, blown dry with N_2, and then plasma cleaned with air for 5 mins. Glass microscope slides were used as substrates for ellipsometry and reflectance/transmittance spectroscopy measurements, which were cleaned by sonicating sequentially in detergent (International Products Co., Micro-90, 1% vol), deionized H_2O, acetone, and isopropanol for 20 minutes each, blown dry with N_2, and followed with air plasma treatment for 5 mins.

A 3:1 molar ratio of methylammonium iodide (Dyesol, AU): lead acetate trihydrate (Sigma-Aldrich, USA) was dissolved in anhydrous dimethylformamide to a concentration of 30 wt% in a N_2 filled glovebox and was stirred for ~1 hr at room temperature until all solids had dissolved. The resulting solution was spincoated at 2000 rpm for 45 seconds in a N_2 filled glovebox onto the substrates minutes after plasma treatment. The samples were dried at room temperature for 10 mins and then annealed on a hotplate at 100° C for 5 minutes, both in the glovebox.

Samples for EA measurements were then coated with 140 nm of PMMA (Sigma-Aldrich, USA) as an insulating dielectric layer by spincoating a 5 wt% PMMA solution in toluene at 8000 rpm for 1 min in the glovebox. These samples were dried overnight in a vacuum chamber inside the glovebox. Then, 60 nm of SiO_2 was deposited via e-beam evaporation on top of the PMMA as a second insulating dielectric. The PMMA/ SiO_2 double insulating layer was found to be necessary in order to construct a thin insulator with minimal leakage current. Finally, 15 nm of Ag was deposited via thermal evaporation to complete the semitransparent dielectric capacitor structure for EA measurements.

Electroabsorption Spectroscopy

White light from a 75 watt Xenon arc lamp (Newport Co., Oriel PhotoMax) was filtered by a grating monochromator (Acton Research Co., SpectraPro-2150i) to achieve a bandpass of ~3nm FWHM for the incident CW probe light. A function generator (Agilent, 33220A) was used as an AC voltage source to create a sinusoidal electric field (1.3 kHz) across the EA sample. The semitransparent sample for EA was mounted in a continuous flow N_2 cryostat (Janis Research Co.) custom fitted with electrical leads, and the temperature was controlled by a digital control unit (Lake Shore Cryogenics, Model 332). The CW probe light was focused onto the sample at normal incidence. The sample was masked by an aperture smaller than both semitransparent electrodes in the EA sample stack so that all transmitted light passed through an area between both electrodes. The transmitted light was focused onto a silicon photodiode (Thorlabs, FDS100) and the signal was amplified by a low noise current preamplifier (Stanford Research Systems, SR570). The AC component of the transmitted signal (ΔT) was demodulated by a lock-in amplifier (Stanford

Research Systems, SR830), which was phase referenced to the function generator at the second harmonic of the modulation fundamental frequency. The DC signal (T) was measured with a DC source-measure unit (Keithley, 2400). The in-phase component of the AC signal (ΔT) and the DC signal (T) were recorded simultaneously in a custom LabVIEW program. The AC signal (ΔT) was scaled by $\sqrt{2}$ to convert from RMS amplitude to peak amplitude before the normalized change in transmittance ($\Delta T/T$) was recorded. See SI Fig. S9.2 for a schematic of the EA set-up.

Ellipsometry, Total Reflectance/Transmittance, and Temperature Dependent Absorbance

Ellipsometry: The amplitude (Ψ) and phase (Δ) components of the complex reflectance ratio $\left(\frac{r_p}{r_s}\right)$ of light reflected at the $CH_3NH_3PbI_3$/Air interface were measured using a commercial spectroscopic ellipsometer (J.A. Woollam Co., M-2000) for three angles of incidence (55°, 65°, 75°). The normal incidence transmittance was also measured on the ellipsometer with the light source and detector at 90° relative to the sample chuck as an auxiliary data set for fitting (see SI section S3 for more details on the measurement and data analysis).

Total Reflectance/Transmittance: Near-normal incidence total reflectance and normal incidence transmittance spectra (SI section S3.1) were measured on a Cary 5000i UV-Vis-NIR spectrometer using the Internal Diffuse Reflectance Accessory (integrating sphere). For the total reflectance measurement, the incident angle was ~3°.

Temperature Dependent Absorbance: A home-built split-beam spectroscopy set up was used to measure temperature dependent absorbance (see SI Fig. S14.3 for schematic). The same monochromatic light source used in the EA measurement was used for the incident probe. The sample was mounted in the same continuous flow N_2 cryostat using the same temperature controller as EA. The probe light was chopped at 400Hz (Stanford Research Systems, SR450) and focused onto the sample plane at normal incidence. The light transmitted through the sample plane ("transmission" beam) was measured with a known area masked calibrated photodiode (OSI Optoelectronics) using a lock-in amplifier (Stanford Research Systems, SR830). In the light path between the source and sample plane, a glass microscope slide was placed at an angle to reflect some of the incident light onto a second known area masked calibrated photodiode (OSI Optoelectronics) as the "reference" beam, which was measured with a second lock-in amplifier (Stanford Research Systems, SR830). A wavelength dependent correction ratio was measured for the fraction of incident power per unit area measured by the "reference" photodiode compared to the incident power per unit area measured by the "transmission" photodiode without any sample present. The transmittance ($\frac{I_{trans}}{I_{inc}}$) of a sample could then be calculated in a single measurement from the "reference" and "transmission" signals, to avoid artifacts from instrument fluctuations. The absorbance ($-log_{10}\left(\frac{I_{trans}}{I_{inc}}\right)$) of $CH_3NH_3PbI_3$ was calculated by subtracting a glass blank spectrum.

Numerical Simulations

Numerical simulations for the Wannier exciton in an electric field (see SI section S7 and S8 for more information) were performed on an Intel Core i7-5960X Haswell-E 8-Core processor using in-house code written with scipy for Python. Specific details about the computational methods can be found in SI section S8.3.

Supplementary Information

S1. Elliott's Formula

The effective mass Schrödinger equation for relative motion of the electron-hole pair in the Wannier exciton model is given as:[1-2]

$$\left[-\left(\frac{\hbar}{2\mu}\right)\nabla^2 - \frac{e^2}{\epsilon r}\right]\phi_n(r) = E_n\phi_n(r) \qquad Eq\ S1\ a.$$

$$\mu = \ electron - hole\ reduced\ effective\ mass, \qquad \epsilon = \ relative\ dielectric\ constant$$

Elliott's formula gives the imaginary part of the optical frequency dielectric function ϵ_{img} in terms of the solutions to Eq S1a. $\phi_n(r)$ at the origin ($r = 0$).[1] Using the formulation of Blossey,[2] Elliott's function is given as:

$$\epsilon_{img} \propto \left|\frac{\hat{\epsilon}\cdot\vec{P}_{cv}}{m\omega a}\right|^2 {\phi_n}^2(0) \quad Eq\ S1\ b.$$

$$\vec{P}_{cv} = \ band - to - band\ matrix\ element,\ a = \ exciton\ Bohr\ radius$$

$${\phi_n}^2(0) = 4\pi\sum_{n=1}^{\infty} n^{-3}\delta\left[\frac{(\hbar\omega - E_g)}{E_B} + \frac{1}{n^2}\right] \ for\ \hbar\omega < E_g \quad Eq\ S1\ c.$$

$${\phi_n}^2(0) = \frac{2\pi}{1 - e^{-2\pi[(\hbar\omega - E_g)/E_B]^{-1/2}}} \ for\ \hbar\omega > E_g \quad Eq\ S1\ d.$$

$$E_B = \ exciton\ Ryderg\ energy\ (binding\ energy), \quad E_g = \ one - electron\ band\ gap$$

A dimensionless energy unit is defined as $x = \frac{(\hbar\omega - E_g)}{E_B}$.

When Eq S1 c. and S1 d. are convolved with a centered, area normalized broadening function $Br(x, \Gamma)$, where Γ describes the FWHM, we have:

$$[{\phi_n}^2(0)](x) = 4\pi\sum_{n=1}^{\infty} n^{-3} Br\left(x + \frac{1}{n^2}, \Gamma\right) \ for\ \hbar\omega < E_g \qquad Eq\ S1\ e.$$

$$[{\phi_n}^2(0)](x) = \int_0^{\infty} Br(x - x', \Gamma)\frac{2\pi}{1 - e^{-2\pi(x')^{-1/2}}}dx'\ for\ \hbar\omega > E_g \qquad Eq\ S1\ f.$$

In practice, Eq S1 f. is convolved numerically. The convolution integral can be cut off at a chosen energy as long as the numerical array for Eq S1d. is suitably padded.[3]

S2. Fitting the Elliott Third Derivative Model to GaAs

We fit the Elliott third derivative model for $\Delta\varepsilon$ to a literature electroreflectance (ER) spectrum of GaAs at 77K from Forman *et al.*[4] The GaAs spectra in Forman *et al.*[4] are among the first experimental observations of Aspnes' low field quadratic electro-modulation effect,[5] and hence offer a good test of the model. We use the Seraphin equation[6-7] (Eq S2 a.), which defines $\frac{\Delta R}{R}$ in terms of $\Delta\varepsilon_r$, $\Delta\varepsilon_i$, n and k by differentiating Fresnel's equations for reflectance at the Air/Sample interface.

$$\frac{\Delta R}{R} = \alpha(n,k)\Delta\varepsilon_r + \beta(n,k)\Delta\varepsilon_i \qquad Eq\ S2\ a.$$

Where:

$$\alpha = \frac{2\gamma}{(\gamma^2+\delta^2)} \qquad Eq\ S2\ b.$$

$$\beta = \frac{2\delta}{(\gamma^2+\delta^2)} \qquad Eq\ S2\ c.$$

$$\gamma = \frac{n}{n_0}(n^2 - 3k^2 - n_0) \qquad Eq\ S2\ d.$$

$$\delta = \frac{k}{n_0}(3n^2 - k^2 - n_0) \qquad Eq\ S2\ e.$$

To model the complex refractive index (n and k) of the GaAs fundamental absorption edge at 77K, we deconvolve a Gaussian of HWHM 21.6 meV from a standard GaAs ellipsometry spectrum at 300K[8] to simulate the reduction of homogeneous broadening with temperature. We also shift the energy scale by +83.5 meV to simulate the shift of the band gap. The magnitude of the Gaussian width for deconvolution was calculated using Eq 4 from Lautenschlager *et al.*,[9] while the energy shift of the spectrum was determined using the parameters from Table I and Eq 3a. in Lautenschlager *et al.*[9] The fit to the differential reflectance data of Forman *et al.*[4] is shown in Fig. 2 b. of the main text. The exciton binding energy, band gap, and broadening factor obtained from the parameters of the fit are compared with literature values for GaAs (Table S1), and the agreement is very good. Fig. S2 shows the spectra of $\Delta\epsilon_i$ and $\Delta\epsilon_r$ from the fit to the data in Fig. 2 b. of the main text.

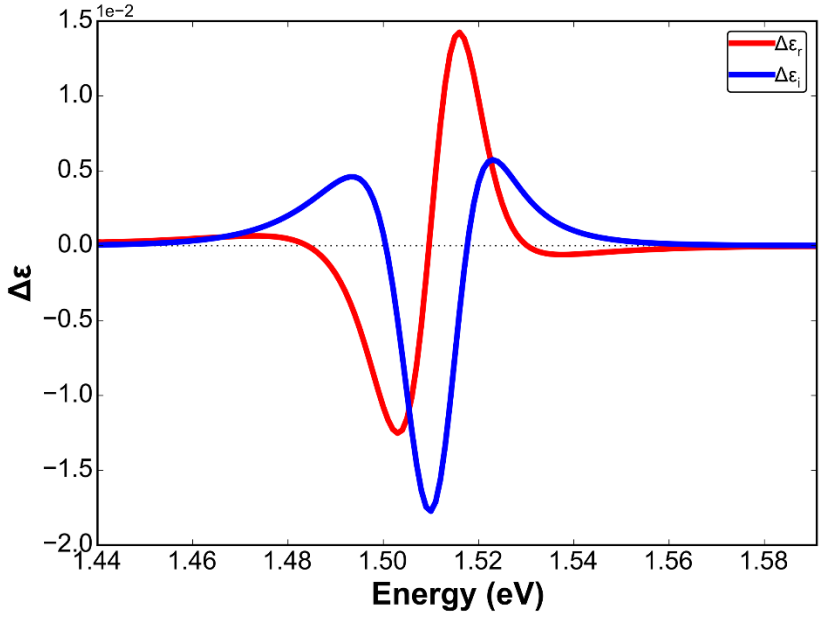

Figure S2. Changes in the real $\Delta\epsilon_r$ and imaginary $\Delta\epsilon_i$ components of the complex dielectric function based on the fit to the ER spectrum in Fig. 2.2 b.

Table S1.

	E_B (meV)	E_g (eV) (77K)	Γ_{FWHM} (meV) (77K)
Literature	4.2[9-10]	1.5114[9]	--*[9]
Elliott Third Derivative Fit	3.8	1.517	28.4

*Based on Table II in Lautenschlager et al.[9] there is a very large error for calcualting Γ from equation 4 in Lautenschlager et al.[9] If we take the broadening half-width to equal k_BT, we calculate that Γ_{FWHM}=~13 meV at 77K. However this value depends strongly on the phonon structure of GaAs.[9]

S3. Optical Modelling of Thin-Film $CH_3NH_3PbI_3$

S3.1 Ellipsometry and Reflectance/Transmittance Spectroscopy

Spectra of the amplitude (Ψ) and phase (Δ) components of the complex reflectance ratio $\left(\frac{r_p}{r_s}\right)$ were measured from light reflected at the $CH_3NH_3PbI_3$/Air interface on a Glass/$CH_3NH_3PbI_3$ sample (Fig. S3.1 a. and S3.1 b.) for three angles of incidence (55°, 65°, 75°). The backside of the glass substrate was covered with Scotch tape to scatter back-reflections at the Sample Chuck/Glass interface. The transmittance (Fig. S3.1 c.) of the Glass/$CH_3NH_3PbI_3$ sample was also measured on the ellipsometer with the light source and detector at 90° relative to the sample chuck. The transmittance provided an additional data set that was fit simultaneously with the sets of Ψ and Δ spectra using the CompleteEASE ellipsometry modelling software.[8]

For the analysis, the CP model from the ellipsometry analysis of $CH_3NH_3PbI_3$ by Shirayama *et al.*[11] was used as a "starting guess" for the model in CompleteEASE. A Kramers-Kronig (K-K) consistent B-Spline with a resolution of 0.05 eV was then adjusted from the starting guess of the Shirayama model to simultaneously fit the Ψ, Δ, and transmittance spectra. Given the good correspondence between the band edge *n* and *k* spectra obtained from the B-spline model (Fig. S3.1 d.) and spectra found in the literature,[11-14] along with the B-spline model satisfying the K-K relations, we found the modelled *n* and *k* to be satisfactory. The fitted thickness of the $CH_3NH_3PbI_3$ layer (149 nm) was also in excellent agreement with measurements on a profilometer (Bruker OM-Dektak XT), which gave a thickness of 150 nm. In order to verify that the *n* and *k* spectra from ellipsometry were correct, near-normal incidence total reflectance (*R*) and normal incidence transmittance (*T*) spectra were measured with an integrating sphere on a Cary 5000 instrument. The *R* and *T* spectra were fit by varying the thickness of $CH_3NH_3PbI_3$ in a transfer matrix model using the values of *n* and *k* obtained from ellipsometry. The transfer matrix fits to the transmittance and reflectance spectra using *n* and *k* from ellipsometry are very good (Fig. S3.2 a. and b.), and the fitted value of the thickness (150.7 nm) was again in excellent agreement with profilometry measurements.

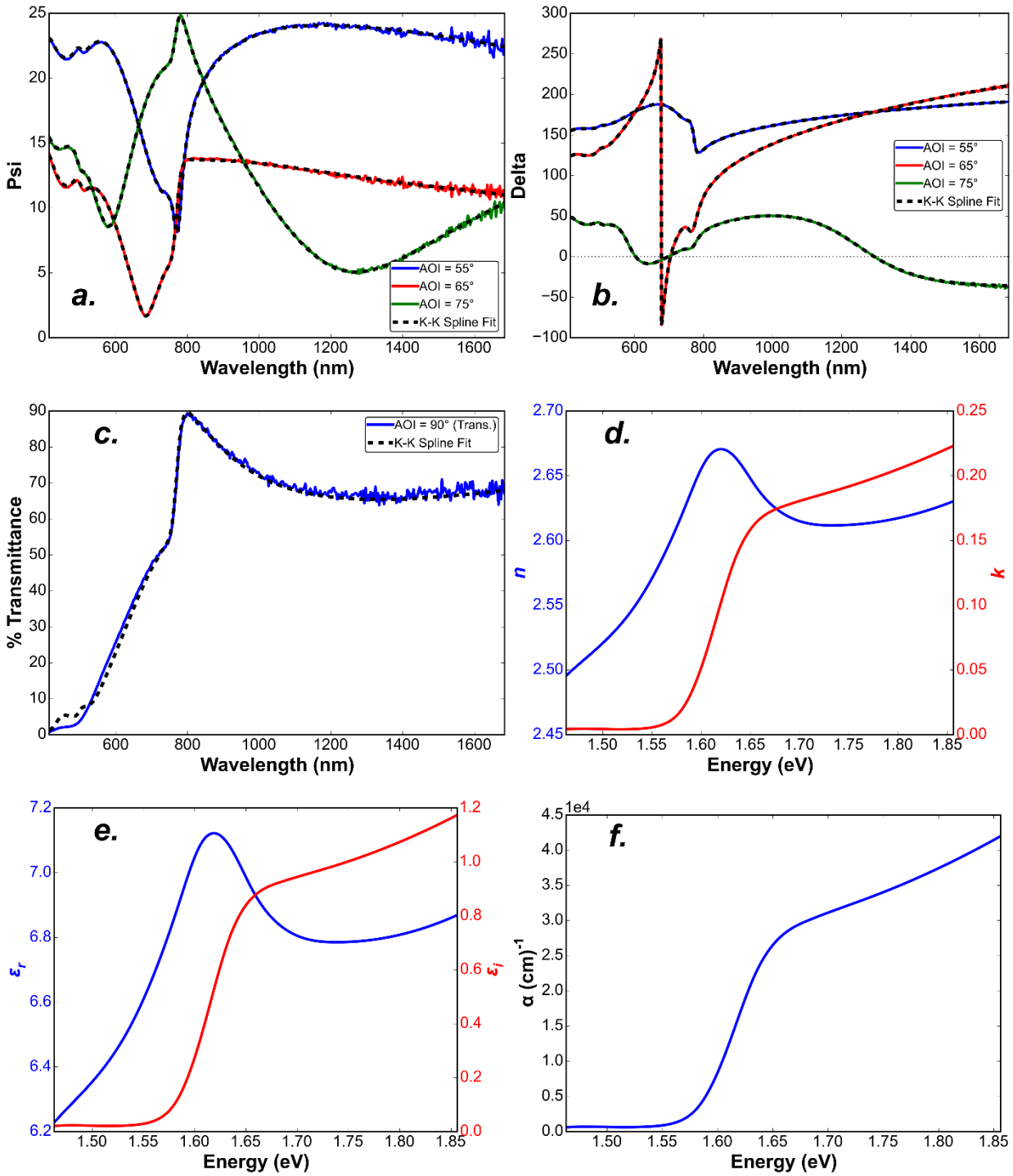

Fig. S3.1 a.-c.) Raw ellipsometry data (Psi, Delta, and Transmittance) showing the fits with a K-K consistent spline. d.-f.) Optical functions modelled from the fits to the ellipsometry data, showing the complex refractive index, complex dielectric function, and absorption coefficient.

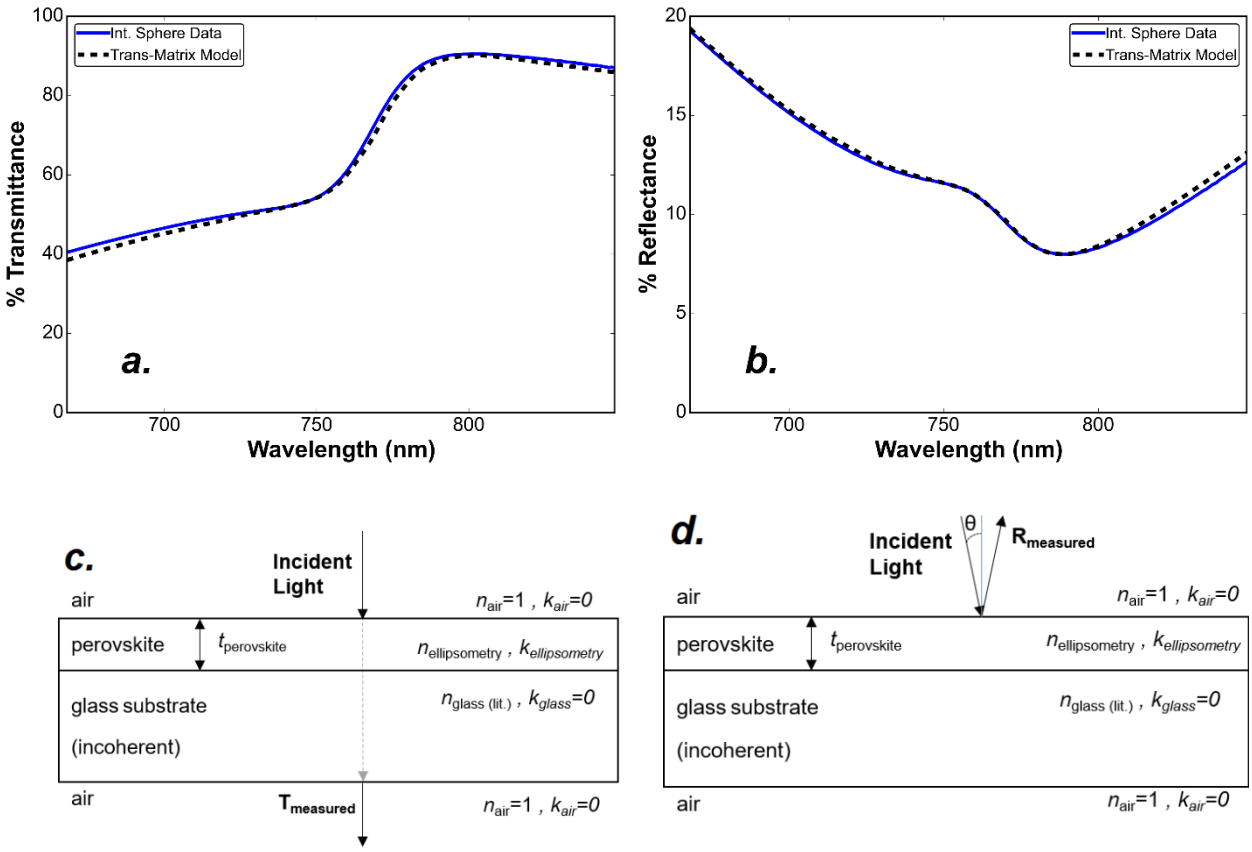

Fig. S3.2 a., b.) Normal incidence transmittance and near normal incidence total reflectance spectra measured with an integrating sphere on a Cary 5000i spectrometer. Fits are based on varying the perovskite thickness in a transfer matrix model using n and k derived from ellipsometry, and (c.) and (d)show a schematic for the transfer matrix modelling.

S4. Transfer Matrix Modelling of EA Data

S4.1 Schematic Model for Calculation of $\Delta T/T$ and Fitting $\Delta\epsilon$

The basic approach to calculate $\Delta T/T$ can be understood from the schematics in Figs S4.1a and S4.1b. T_0 is the transmittance in the absence of an external electric field and is calculated using a transfer matrix algorithm for Python[15] based on knowing the thickness (t_x for each layer "x") and spectra of the optical constants (n and k) of each layer in the stack. The optical constants of $CH_3NH_3PbI_3$ are taken from the experimentally measured n and k spectra from ellipsometry. The transmittance in an external field T_{field} is then calculated with transfer matrix modelling by changing the optical constants of the $CH_3NH_3PbI_3$ layer from $(n_{ellipsometry}, k_{ellipsometry})$ to $(n_{ellipsometry} + \Delta n, k_{ellipsometry} + \Delta k)$, where Δn and Δk are calculated from $\Delta\epsilon_i$ modelled by the third-derivative Elliott formula (see section S4.3 and S4.4 below for calculating $\Delta\epsilon_r$ from the modeled $\Delta\epsilon_i$ using the Kramers-Kronig relation and conversion to Δn and Δk). The change in transmittance is then calculated as $\Delta T = T_{field} - T_0$. The normalized change in transmittance is calculated as $\Delta T/T_0$. Parameters in the third derivative Elliott model (E_g, Γ, E_b, and an amplitude scaling factor) are then varied until optimal values are found that minimize the sum of the square of residuals between the measured EA spectra and the modelled $\Delta T/T_0$.

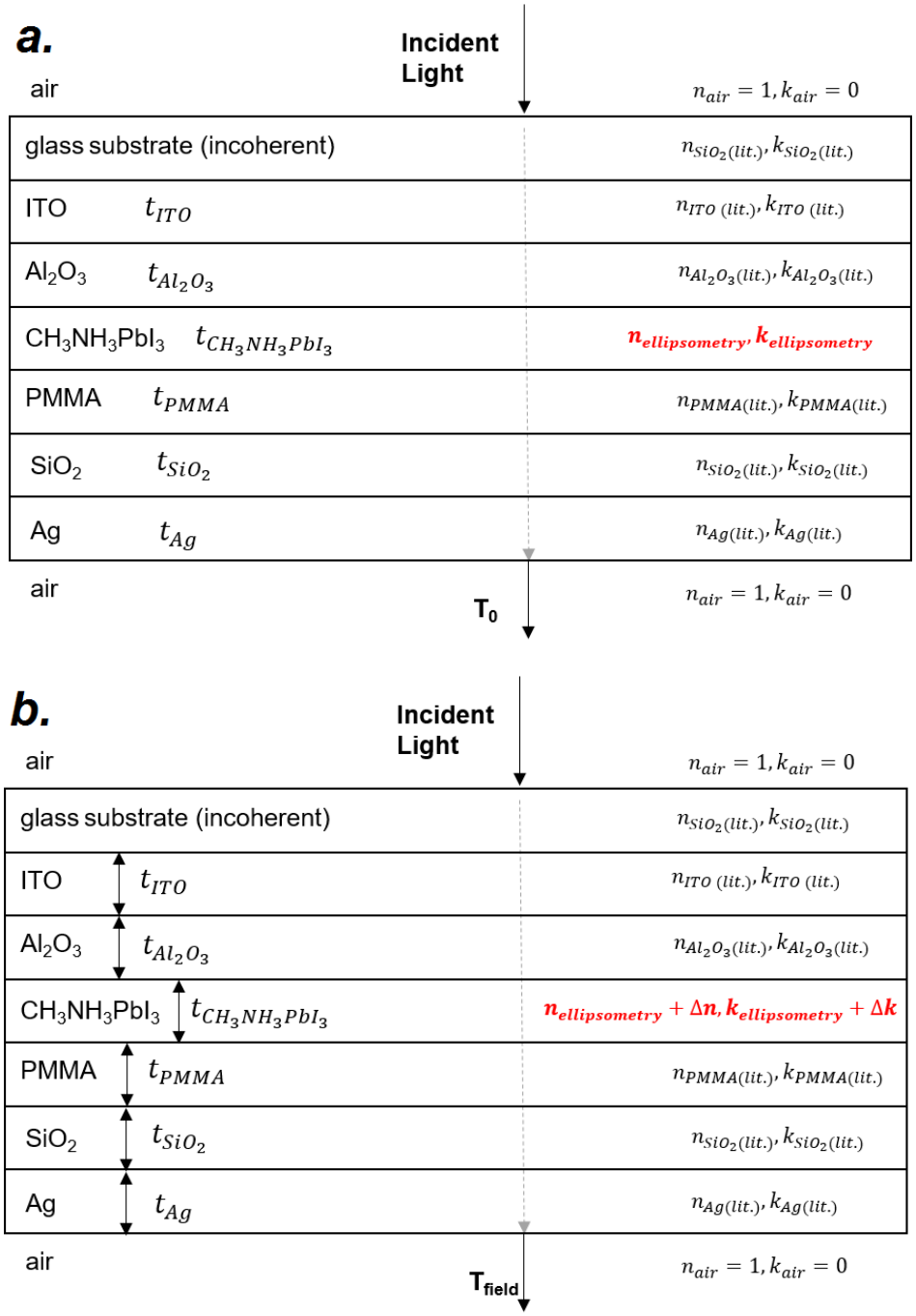

Fig. S4.1 a., b.) Schematics for the transfer matrix modelling for transmittance in zero field (a.) and an applied field (b.), which is used to calculate $\Delta T/T$.

S4.2 Determination of Error on E_B and E_g from the Third Derivative Elliott Model

The error on E_B and E_g reported in the main text was determined using the confidence interval algorithm[16] in LMFIT for Python. This method essentially follows the "constant chi square boundary" approach described by Press *et al.*[3], where in the LMFIT code the chi square boundary is determined using the F-test.[16] The LMFIT routine gave best fit values of E_B = 7.4 meV and E_g = 1.633 eV with a 95% confidence interval spanning 6.8-9.2 meV for E_B and 1.631-1.635 eV for E_g. We also calculated the error by fitting eight different room temperature EA spectra (2 samples, 4 field strengths each) and taking the mean and standard deviation of the best fit parameters for E_B and E_g. The field invariant lineshape and quadratic field scaling of the EA spectra from two samples (prepared from separate batches of precursor solutions) are shown in Fig. S4.2 a. and b. The value of E_B with this method was 7.61 ± 0.42 meV, while E_g was 1.637 ± 0.002 eV. We chose to report the larger error values from the LMFIT method, although the values from the two methods are generally in good agreement.

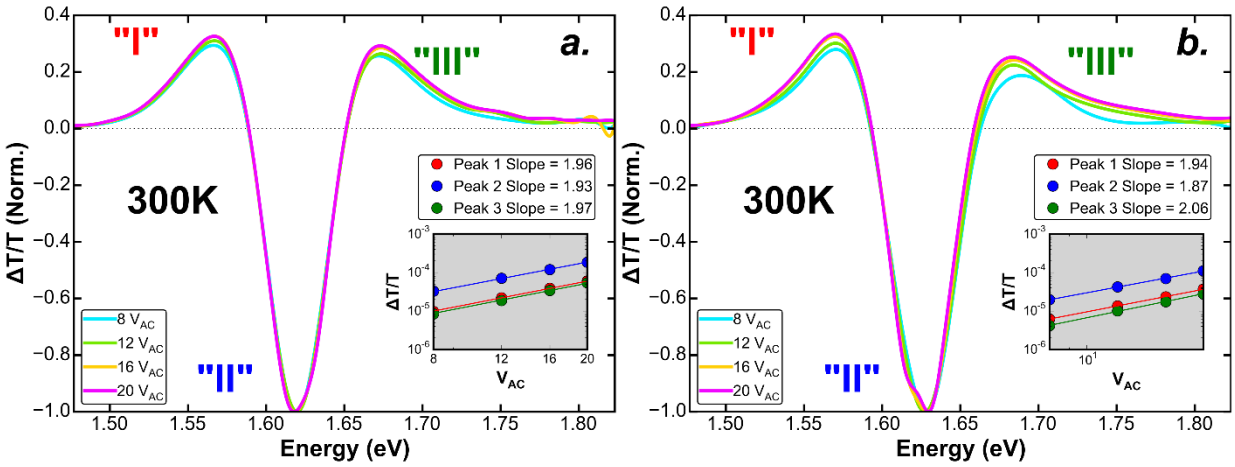

Fig. S4.2 a., b.) Second harmonic EA spectra of two different CH3NH3PbI3 films prepared from separate precursor batches. The data sets in a., b.) were used to supplement the error estimation for EB and Eg by assessing experimental variation.

S4.3 Calculating $\Delta\epsilon_r$ from $\Delta\epsilon_i$ and Calculating Δn and Δk from $\Delta\epsilon_r$ and $\Delta\epsilon_i$

The spectrum for $\Delta\epsilon_r$ is calculated from $\Delta\epsilon_i$ based on the differential form of the Kramers-Kronig (K-K) transform (Eq. S4.3 a.).

$$\Delta\epsilon_r(\omega, F) = \frac{1}{\pi}\int_{-\infty}^{\infty} \frac{\Delta\epsilon_i(\omega', F)}{\omega' - \omega} d\omega' \qquad Eq\ S4.3\ a.$$

$$\omega = \text{photon frequency}, \quad F = \text{applied field}$$

We derived Eq S4.3 a. following the approach taken by Seraphin and Bottka.[17] Our derivation used the Hilbert transform formulation of the K-K transform[18] rather than the form of the K-K transform used by Seraphin and Bottka, however the two forms are equivalent.[18] To calculate Δn and Δk from $\Delta\epsilon_r$ and $\Delta\epsilon_i$ we found the differential forms of the relations $\epsilon_i = 2nk$ and $\epsilon_r = n^2 - k^2$:

$$\Delta\epsilon_i = \frac{d\epsilon_i}{dk}\Delta k + \frac{d\epsilon_i}{dn}\Delta n \qquad Eq\ S4.3\ b.$$

$$\Delta\epsilon_r = \frac{d\epsilon_r}{dk}\Delta k + \frac{d\epsilon_r}{dn}\Delta n \qquad Eq\ S4.3\ c.$$

$$\Delta k = \frac{-\Delta\epsilon_r k + \Delta\epsilon_i n}{2(k^2 + n^2)} \qquad Eq\ S4.3\ d.$$

$$\Delta n = \frac{\Delta\epsilon_i k + \Delta\epsilon_r n}{2(k^2 + n^2)} \qquad Eq\ S4.3\ e.$$

S5. Second Harmonic Modulation Signal in the $\chi^{(3)}$ EA Response

Both the quadratic Stark effect[19] and the low-field FKA effect[5] relate the electromodulation response to the third order nonlinear optical susceptibility by virtue of its field invariant functional form and quadratic dependence on external electric field (Eq. S5 a.).

$$\Delta\epsilon(E) \propto \chi^{(3)}(E)F^2 \qquad Eq\ S5\ a.$$

Assuming the presence of static internal electric fields (F_0), the change in the complex dielectric function ($\Delta\epsilon$) can be expressed in terms of the fundamental (Ω) and second harmonic (2Ω) frequency of the AC modulation field ($F_{AC}\cos(\Omega t)$).[20] Here F_{AC} is calculated from the *peak* amplitude (as opposed to the peak-to-peak amplitude) of V_{AC} using Eq S6.2 (see section S6.2).

$$F = F_0 + F_{AC}\cos(\Omega t) \qquad Eq\ S5\ b.$$

$$\Delta\epsilon(E) \propto \chi^{(3)}(E)\left\{\frac{{F_{AC}}^2[1+\cos(2\Omega t)]}{2} + 2F_{AC}F_0\cos(\Omega t) + {F_0}^2\right\} \qquad Eq\ S5\ c.$$

The quadratic field dependence of the electroabsorption response is characterized by the observation of quadratic scaling of the second harmonic signal with field ($\frac{\Delta T}{T}_{2\omega} \propto {F_{AC}}^2$).

S6. Calculation of Experimental Ionization Field (F/F_I)

S6.1 Formula for F_I

The ionization field F_I is defined as the field required to cause a potential drop of one exciton Rydberg across the exciton Bohr radius (a). In keeping with the convention of the main text, we denote the exciton Rydberg as E_B rather than the commonly used symbol R.[2, 21-22] The equations in SI units for a (in units of m), E_B (in units of J), and F_I (in units of V/m) are given below:[22]

$$a = \frac{4\pi\epsilon_0\epsilon_r\hbar^2}{\mu e^2} \qquad Eq\ S6.1.a$$

*Where μ is the electron-hole reduced effective mass in units of kg, ϵ_r is the relative dielectric constant, ϵ_0 is the vacuum permittivity in units of (F/m), ħ is the reduced Planck constant in units of (J*s), and e is the elementary charge in units of C.*

$$E_B = \frac{\hbar^2}{2\mu a^2} \qquad Eq\ S6.1.b$$

$$F_I = \frac{E_B}{ea} \qquad Eq\ S6.1.c$$

We found that the formula for F_I in SI units from Blossey's work[2, 23] is missing a factor of 4π, so we used the corrected formula from Galbraith.[22]

S6.2 Calculating Electric Field and Dimensionless Field (F/F_I) Across the $CH_3NH_3PbI_3$ Layer

To calculate the electric field across the perovskite layer we model the layers in the device stack as four capacitors in series and use the applied voltage V_{AC}, known dielectric electric constants ϵ_x and thicknesses t_x for each layer "x". The thicknesses for each layer are shown in Fig. S14.1. For the applied field modulated at 1.3 kHz, we estimate the 1.3 kHz dielectric constant of $CH_3NH_3PbI_3$ from literature values to be in the range of $\epsilon_{perov\_1.3kHz} = 50 - 150$.[24-25] We note that in Eq S6.2 a. V_{AC} is the *peak* amplitude of the applied voltage (as opposed to the peak-to-peak amplitude).

$$F_{perov\_1.3kHz} = \frac{V_{AC}}{\epsilon_{perov\_1.3kHz}\left(\frac{t_{SiO_2}}{\epsilon_{SiO_2}} + \frac{t_{perov}}{\epsilon_{perov\_1.3kHz}} + \frac{t_{PMMA}}{\epsilon_{PMMA}} + \frac{t_{Al_2O_3}}{\epsilon_{Al_2O_3}}\right)} \qquad Eq\ S6.2$$

Taking $\epsilon_{perov\_1.35kHz} = 100 \pm 50$ as stated above, we calculate a minimum possible value for F/F_I of 0.25 (for 4 V_{AC} applied voltage and $\epsilon_{perov\_1.35kHz} = 150$), and maximum possible value of $F/F_I = 1.4$ (for 20 V_{AC} applied voltage and $\epsilon_{perov\_1.35kHz} = 50$). For the mean value of $\epsilon_{perov\_1.35kHz} = 100$, F/F_I is falls in a range of ~0.25-1.4 for applied voltages in the range of 4-20 V_{AC}.

S6.3 Calculating μ from the Amplitude of Δϵ from the Second Harmonic EA Response

From equation S5 c. we have for $\Delta\epsilon$ in second harmonic EA signal:

$$\Delta\epsilon_{2\Omega}(E) \propto \chi^{(3)}(E)\left\{\frac{{F_{AC}}^2[\cos(2\Omega t)]}{2}\right\} \qquad Eq\ S6.3\ a.$$

Using Eq 1.a. and 1.b. from the main text we can write:

$$\Delta\epsilon_{2\Omega}(E) = \frac{e^2\hbar^2}{8\mu}\frac{{F_{AC}}^2}{2}\frac{1}{3E^2}\frac{d^3}{dE^3}\left(E^2\epsilon(E,0)\right) \qquad Eq\ S6.3\ b.$$

$$\mu = \frac{e^2\hbar^2}{8\Delta\epsilon_{2\Omega}(E)}\frac{{F_{AC}}^2}{2}\frac{1}{3E^2}\frac{d^3}{dE^3}\left(E^2\epsilon(E,0)\right) \qquad Eq\ S6.3\ c.$$

Given that we can calculate a quantitative amplitude for $\Delta\epsilon_{2\Omega}(E)$ by fitting the EA spectrum with transfer matrix modelling, we can calculate a quantitative value for μ using Eq S6.3 c.

S7. Shift and Ionization Broadening of the $n = 1$ Wannier Exciton Level

In the following discussion we will demonstrate that the observed deviation from quadratic amplitude scaling for Peak III at 210 K (see Fig. 2.3 a. in the main text) is consistent with results from numerical simulations for a Wannier exciton in an electric field near the field ionization threshold of the $n = 1$ exciton. In Section S6.2 above we calculated a mean value for the dimensionless field F/F_I achieved in our experiment to be in the range of 0.25– 1.4, where F is the applied field and F_I is the exciton ionization field (see SI section S6.2). The dimensionless field F/F_I can be directly compared to theoretical models for a hydrogenic (Wannier) exciton in an electric field using both perturbation theory and exact numerical solutions.[2] In Fig. S7a. we show the exact shift of the $n = 1$ exciton peak as a function of F/F_I, calculated numerically using the method of Blossey[2] (see Section S8.2 and S8.3 for computational methods) along with the shift expected from perturbation theory[2] (the quadratic Stark effect, see Section S8.1). In Fig. S7a. the position of the $n = 1$ exciton peak is plotted for a dimensionless energy unit scaled to the exciton binding energy ($[E - E_g] \,/\, E_B$). Fig. S7a. shows that at F/F_I~0.3, the shift of the $n = 1$ exciton peak begins to deviate from the predicted quadratic Stark red shift, eventually blue shifting as F/F_I increases towards 1.[2, 26] In Fig. S7 b. we show the exciton absorption strength ($\phi_n(0)^2$, see Section S8.2 for details) as a function of dimensionless energy for the same range of F/F_I. We can see from Fig. S7 b. that the breakdown of the Stark shift at F/F_I~0.3 also corresponds to a rapid quenching and broadening of the exciton resonance with field, which represents the field ionization of the $n = 1$ exciton. Fig. S7.b shows that the broadening is asymmetric with respect to the center of the exciton peak for a given value of F/F_I, where the amplitude of the broadening function is larger on the blue side of the exciton peak relative to the amplitude on the red edge.

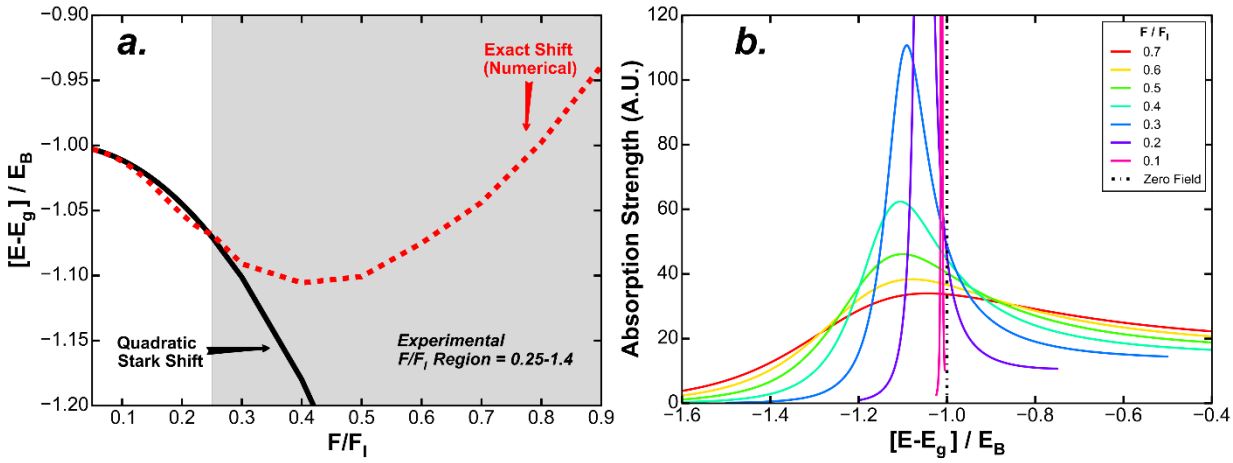

Fig. S7.1 a.) Shift of the n=1 exciton peak in dimensionless energy units as a function of dimensionless field, calculated using the result from perturbation theory (quadratic Stark effect) and numerical simulations for a Wannier exciton in an electric field. Breakdown of the Stark shift occrs around F/F_I~0.3. b.) Simulated spectrum of the absorption strength ($\phi_n(0)^2$) of the n=1 Wannier exciton in a dimensionless field. Rapid ionization is seen to occur starting at F/F_I~0.3, coinciding with the breakdown of the Stark effect.

In Fig. S7c. we show simulated ϵ_i spectra for values of F/F_I close to the $n = 1$ exciton ionization threshold. For these simulations the spectra are broadened by convolving a broadening function with a FWHM in dimensionless units (Γ/E_B).[2] Dow has pointed out that at low fields the numerical simulations of a Wannier exciton in an electric field are valid only for small broadening ($\Gamma/ E_B < 1$), due to the complicated broadening mechanisms of the Wannier exciton that cannot accounted for theoretically by simple convolution of the spectrum with a single homogeneous broadening function.[27-28] The value of Γ/E_B used in these simulations was $\Gamma/E_B = 1/3$. This is much smaller than the value we would expect in our experiment based on the linewidth at 210 K (linewidth found by fitting the 210K absorption spectrum to Elliott's formula) and exciton binding energy of $CH_3NH_3PbI_3$ (Γ ~21 meV, E_B~7meV, Γ/ E_B ~ 3). However, the simulations for small Γ/E_B are still able to point out general field dependent trends in ϵ_i that are consistent with our observations in the 210 K EA spectra. In Fig. S7 c. we show the simulated ϵ_i for zero applied field (black dashed curve) and F/F_I = 0.2, 0.3, and 0.7 (colored traces). The large peak at $\frac{[E-E_g]}{E_B} = -1.0$ corresponds to the $n = 1$ exciton resonance. For fixed values of F/F_I around the $n = 1$ ionization threshold, we can see that the field induced broadening at the red and blue edges of the $n = 1$ exciton peak give rise to the induced absorption features that correspond to the positive "wings" (Peaks I and III respectively) in the EA spectrum (see Fig. S7 c. and inset).

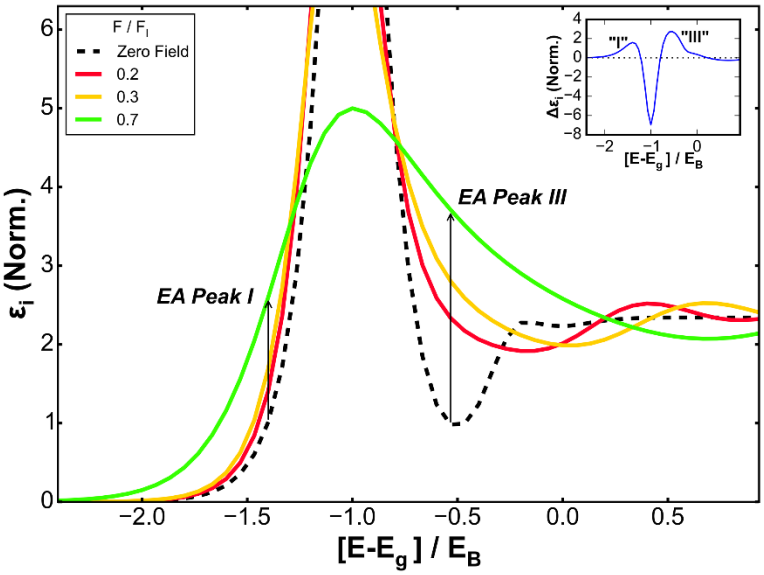

Fig. S7.2 Simulated ϵ_i for zero field and fixed values of dimensionless field near the n=1 exciton ionization threshold, showing that Peaks I and III in the EA spectrum are related to the broadening of the exciton peak from field ionization.

In Fig. S7 d. we show a log-log plot of the HWHM of the exciton peak on the blue side of the n=1 resonance as a function of F/F_I (for this simulation no broadening function was convolved with the simulated spectra). Fig. S7.d. also shows the derivative of HWHM as a function of F/F_I on a log-log scale, which gives the power law scaling of the HWHM as a function of field. We can see that initially the broadening is rapid, going like $(F/F_I)^{12}$ at $F/F_I = 0.1$ and then settling near $(F/F_I)^4$ around $F/F_I = 0.3$-0.6. We note that a HWHM cannot be measured above $F/F_I = 0.6$ as the amplitude on the blue side of the exciton peak becomes too large to assign a value at half of the peak maximum. In Fig. S7.e. we show a corresponding plot for the HWHM at the red edge of the exciton resonance as a function of field. Again, the initial broadening is fast, but slows to a nearly quadratic dependence ($(F/F_I)^2$) at $F/F_I = 0.3$-0.6.

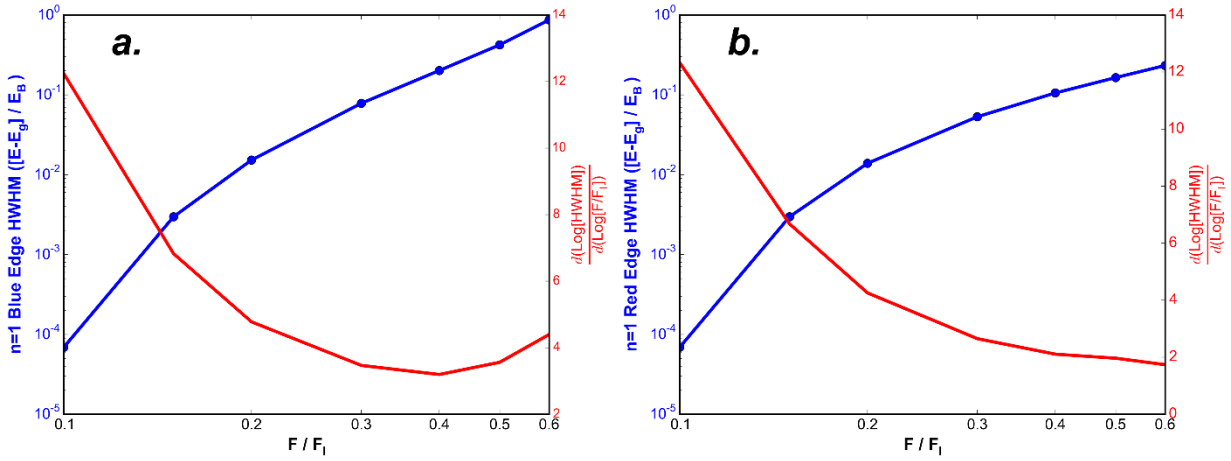

Fig. S7.3 *a., b.)* Log-log plot of the HWHM of the exciton peak at the blue (*a.*) and red (*b.*) edges as a function of dimensionless field. The derivative with respect to dimensionless field on a log-log scale gives the power law scaling of the HWHM as a function of dimensionless field.

This result is consistent with our general observations in the EA spectrum at 210 K. In our EA spectra we saw that Peak I (the induced absorption due to broadening at the red edge of the exciton peak) followed a quadratic field dependence, while Peak III (the induced absorption associated with broadening at the blue edge of the exciton peak) followed a power law dependence > 2. The simulations in Fig. S7 d. and S7 e. similarly show that near the $n = 1$ ionization threshold (F/F_I = 0.3-0.6), the broadening at the red edge of the exciton resonance approaches a quadratic power law field dependence, while the broadening a the blue edge follows a power law > 2. The difference between the magnitude of the power law scaling for Peak III calculated from these simulations versus that seen in the 210 K EA experiment (~4 vs ~2.3) is likely due to more complicated broadening effects from exciton-phonon interactions at 210 K.[28] The results of the simulations are however in general support of our hypothesis that the power law scaling >2 for Peak III in the 210 K EA spectrum can be associated with field ionization effects of the $n = 1$ exciton for a range of F/F_I around 0.3-0.6.

S8. Perturbation Theory and Numerical Solution for the Wannier Exciton in an Electric Field

S8.1 Perturbation Theory for the Wannier Exciton in an Electric Field in Parabolic Coordinates

Here we only briefly outline the approach for the perturbation theory solution for a Wannier exciton in an electric field, which is formally equivalent to the hydrogen Stark effect.[26] For more details on the perturbation theory solution in parabolic coordinates we refer the reader to Landau and Lifshitz,[29] Bethe and Salpeter,[30] Fong,[31] or Blossey.[2] In the parabolic band effective mass approximation[2, 21] the Schrödinger equation for the Wannier exciton in an electric field is formally equivalent to the Hydrogen atom in electric field, where μ is the electron-hole reduced effective mass based on the band dispersion and ϵ is the dielectric constant of the crystal (Eq S8.1 a.).

$$\left[-\left(\frac{\hbar}{2\mu}\right)\nabla^2 - \frac{e^2}{\epsilon r} - eFz\right]\phi_n(r) = E_n\phi_n(r) \qquad Eq\ S8.1\ a.$$

Due to the fixed direction of the field F along the z axis, Eq S8.1 a. is not separable in spherical coordinates (r, θ, ϕ), which are typically used for the Hydrogen atom.[29] The solution to Eq S8 a. is, however, separable in parabolic coordinates, which simplifies the computation of the perturbation theory solution by allowing non-degenerate perturbation methods to be used.[29, 31-32]

For the perturbation theory solution, one first finds the solution to the unperturbed Schrödinger equation for the Wannier exciton. In spherical coordinates this equation is formally equivalent to the Hydrogen atom:

$$\left[-\left(\frac{\hbar}{2\mu}\right)\nabla^2 - \frac{e^2}{\epsilon r}\right]\phi_n(r) = E_n\phi_n(r) \qquad Eq\ S8.1\ b.$$

A transformation is then made into parabolic coordinates (ξ, η, ϕ), which are given as:[2]

$$\xi = r + z, \qquad \eta = r - z, \qquad \phi = \tan^{-1}\left(\frac{y}{x}\right) \qquad Eq\ S8.1\ c.$$

Solutions to Eq S8.1 b. in parabolic coordinates can be found for three parabolic coordinate quantum numbers *n*, *i*, and *m*.[2] Here we use the parabolic quantum numbers defined by Blossey,[2] rather than the more commonly defined n_1, n_2, and *m*.[29-30]. The wavefunctions for the *n*, *i*, and *m* parabolic quantum numbers, with $m = 0$ are given below (Eq S8.1 d.). For the Wannier exciton, only the $m = 0$ states contribute to the optical absorption.[2]

$$\phi_{ni0} = \frac{exp\left(-\frac{1}{2n}(\xi + \eta)\right)}{n^2\sqrt{\pi}(n-i)!\,(i-1)!} L^0_{i-1}\left(\frac{\xi}{n}\right) L^0_{n-i}\left(\frac{\eta}{n}\right) \qquad Eq\ S8.1\ d.$$

Where $L^0_k(x)$ is the associated Laguerre function (see Blossey[2] or Landau and Lifshitz[29] for details).

Using the parabolic coordinate wavefunctions, the perturbation correction to the energy eigenvalue in Eq S8.1 a. for a state described by a given set of *n,i,m* parabolic quantum numbers in an electric field *F* can be found in closed form:[2]

$$E_{nim}/E_B = -1/n^2 - \frac{3}{2}(F/F_l)n(n-2i-m+1) - \frac{1}{32}(F/F_l)^2 n^4[17n^2 - 3(n-2i-m+1)^2 - 9m^2 + 19] \quad Eq\ S8.1\ e.$$

In SI Section S7, Eq S8.1e. is used to calculate the shift of the n=1 level according to perturbation theory. For the n=1 levels of the Wannier exciton, the parabolic quantum numbers are *n=1, i=1, m=0*.[2]

S8.2 Numerical Solution for the Wannier Exciton in an Arbitrarily Strong Electric Field

Here we will briefly discuss the exact numerical approach for solving the Wannier exciton in an electric field. For more details we refer the reader to the work of Dow *et al.*,[21, 26] Blossey *et al.*,[2, 33] and Ralph.[34] The optical frequency dielectric function can be simulated by finding solutions ($\phi_n(r)$) to the Schrodinger equation for a Wannier exciton in an electric field[2] and using Eq S1 b. (rewritten below) to calculate ϵ_{img} in terms of ${\phi_n}^2(0)$. We refer to ${\phi_n}^2(0)$ as the absorption strength in Section S7. Therefore all that is needed to simulate ϵ_{img} are the solutions for $\phi_n(r)$.

$$\epsilon_{img} \propto \left|\frac{\hat{\epsilon}\cdot\vec{P}_{cv}}{m\omega a}\right|^2 {\phi_n}^2(0)$$

Strictly speaking, the Wannier exciton in an electric field of any strength has only quasi-bound states,[26] as any finite electric field results in a quantum mechanical probability for ionization of the bound states into a region of unbounded potential energy (eFz).[26] The ionization probability can be visualized in the exciton spectrum as a broadening of the resonance peaks.[26] In weak electric fields the ionization probability is small, and perturbation theory can be used to describe the field induced shift of the resonance energy, which predominates over the field induced broadening for weak fields.[29] At arbitrarily strong fields, the perturbation theory fails to correctly describe the shift of the exciton, and ionization broadening causes the exciton spectrum to lose its quasi-discrete nature, becoming a continuous function of energy.[2] The numerical approach involves directly solving Eq S8.1 a. for continuous values of E_n by numerical integration after determining the correct boundary conditions. In this case the corresponding exact solutions to Eq S8.1 a. can be found for an arbitrarily strong electric field.

Here we will briefly summarize the setup of Blossey's equations[2] based on the transformation of the Schrodinger equation for a Wannier exciton in an electric field. The details of the computational methods that we employed for numerically solving Blossey's equations are given in the following section S8.3. The goal is to find direct numerical solutions to Eq S8.1 a. As noted in section S8.1, Eq S8.1 a. is separable in parabolic coordinates (Eq S8.1 c.). Therefore we look for solutions of the form:[2]

$$\phi_n(r) = Af_\nu(\eta)g_{\nu'}(\xi)e^{\pm im\phi} \qquad Eq\ S8.2\ a.$$

Where ν and ν' are eigenvalues related by the formula:[2]

$$\nu' = \nu + \frac{\mu e^2}{2\hbar^2} \qquad Eq\ S8.2\ b.$$

When Eq S8.1 a. is transformed into parabolic coordinates (see Blossey[2] for the Laplacian and volume element in parabolic coordinates), separable equations can be found for $f_\nu(\eta)$ and $g_{\nu\prime}(\xi)$ when Eq S8.2 a. is used as a trial solution for the wavefunction:

$$\frac{1}{\eta}\frac{d}{d\eta}\left(\eta\frac{df_\nu}{d\eta}\right) + \left(-\frac{m^2}{4\eta^2} - \frac{\nu}{\eta} + \frac{\mu E_n}{2\hbar^2} - \frac{\mu eF\eta}{4\hbar^2}\right)f_\nu(\eta) = 0 \qquad Eq\ S8.2\ c.$$

$$\frac{1}{\xi}\frac{d}{d\xi}\left(\xi\frac{dg_{\nu\prime}}{d\xi}\right) + \left(-\frac{m^2}{4\xi^2} - \frac{\nu'}{\xi} + \frac{\mu E_n}{2\hbar^2} + \frac{\mu eF\xi}{4\hbar^2}\right)g_{\nu\prime}(\xi) = 0 \qquad Eq\ S8.2\ d.$$

Blossey[2] then defines dimensionless variables for the energy and electric field. In this way the numerical solutions can be related to the dimensionless form of the perturbation solution in Eq S6.1e. The dimensionless energy (β) is defined as:

$$\beta = \frac{E - E_g}{\hbar\theta} \qquad Eq\ S8.2\ e.$$

Where $\hbar\theta$ is the electro-optical energy, reltated to the field strength F and the electron-hole reduced effective mass μ by the equation:

$$\hbar\theta = \left(\frac{\hbar^2 e^2 F^2}{2\mu}\right)^{1/3} \qquad Eq\ S8.2\ f.$$

The parabolic eigenvalues ν and ν' defined in Eq S8.2 b. are also transformed into dimensionless variables κ and κ', given by:

$$\kappa = \left(\frac{4\hbar^2}{\mu eF}\right)^{1/3}\nu \qquad and \qquad \kappa' = \kappa + 2(F/F_I)^{1/3} \qquad Eq\ S8.2\ g.$$

Where F_I is defined in Eq S5.1 c. Finally, a dimensionless distance x is defined, where:

$$x = (F/F_I)^{1/3}\left(\frac{\eta}{2a}\right), \qquad x > 0 \qquad Eq\ S8.2\ h.$$

$$x = (F/F_I)^{1/3}\left(\frac{\xi}{2a}\right), \qquad x < 0 \qquad Eq\ S8.2\ i.$$

The new set of second order ODEs to be solved is given by transformation of Eq S8.2 c. and d. into the dimensionless units:

$$\frac{1}{x}\frac{d}{dx}\left(x\frac{d}{dx}\begin{bmatrix}f\\g\end{bmatrix} + \left(-\frac{1}{x}\begin{bmatrix}\kappa\\\kappa'\end{bmatrix} + \beta\right)\right)\begin{bmatrix}f\\g\end{bmatrix} = 0, \qquad \begin{bmatrix}x > 0\\x < 0\end{bmatrix} \qquad Eq\ S8.2\ j.$$

S8.3 Computational Method for Numerically Solving Blossey's Equations (Eq S8.2 j.)

We use the method of "shooting to a fitting point"[3] for a two-point boundary value problem to find the eigenvalues κ that give continuous solutions for $f_{\kappa,\beta}(x)$ and $g_{\kappa',\beta}(x)$ according to the set of second order ODEs defined by Eq S8.2 j., which are continuous functions of the dimensionless energy β. The asymptotic form of the function $f_{\kappa,\beta}(x)$ for $x \gg \beta$ is already given by Blossey[2]:

$$f_{\kappa,\beta}(x) \sim (x-\beta)^{-3/4} \exp\left[-\frac{2}{3}(x-\beta)^{3/2} + \kappa(x-\beta)^{-1/2}\right]$$

Due to the regular singularities in the ODEs (Eq S8.2 j.) at the origin ($x = 0$), we look for a Frobenius series solution at the origin of the form[35]:

$$y(x) = x^s \sum_{k=0}^{\infty} A_k x^k$$

The Frobenius method yields two linearly independent solutions $y_1(x)$ and $y_2(x)$, so that the solution at the origin is a linear combination of the two[35]:

$$y(x) = C_1 y_1(x) + C_2 y_2(x)$$

We find that the two solutions have the form:

$$y_1(x) = C_1\left(1 + \kappa x + \left(\frac{1}{4}\kappa^2 - \frac{1}{4}\beta\right)x^2 + O(x^3)\right)$$

$$y_2(x) = C_2\left(\ln(x)\left(1 + \kappa x + \left(\frac{1}{4}\kappa^2 - \frac{1}{4}\beta\right)x^2 + O(x^3)\right) + \left(-2\kappa x + \left(\frac{1}{4}\beta - \frac{3}{4}\kappa^2\right)x^2 + O(x^3)\right)\right)$$

We can see that $y_2(x)$ and its first and second derivatives will diverge at $x = 0$, therefore we are only interested in the first solution $y_1(x)$ for the boundary conditions at the origin.

We then convert the second order O.D.E. for $f_{\kappa,\beta}(x)$ into to a set of two first order ODEs by the change of variables:

$$f_1 = f$$

$$f_2 = f_1'$$

$$f_2' = f_1''$$

To give a set of two first order ODEs:

$$\frac{df_1}{dx} = f_2$$

$$\frac{df_2}{dx} = -\left(\frac{1}{x}f_2 + \left(-\frac{\kappa}{x} + \beta - x\right)f_1\right)$$

We set up the boundary conditions at large x knowing the asymptotic solution for $x \to \infty$:

$$f_{1_{asym}}(x) = (x-\beta)^{-3/4}\exp\left[-\frac{2}{3}(x-\beta)^{3/2} + \kappa(x-\beta)^{-1/2}\right]$$

$$f_{2_{asym}}(x) = -\frac{e^{\frac{\kappa}{\sqrt{-\beta+x}}-\frac{2}{3}(-\beta+x)^{3/2}}(4\beta^2 + 2\kappa - 8\beta x + 4x^2 + 3\sqrt{-\beta+x})}{4(-\beta+x)^{9/4}}$$

For the boundary conditions at the origin, we use the Frobenius solutions and take an arbitrary value for $f_1(0)$:

$$f_1(0) = C_1$$

$$f_2(0) = \kappa f_1(0)$$

The numerical procedure then consists of integrating $f_1{}'$ and $f_2{}'$outward from the origin and inward from a large value of x ($x = 50$) to a fitting point. The fitting point is chosen at the first maximum of $f_1(x)$ from the inward integration. We note that the singularity in $f_2{}'$ at the origin can be dealt with analytically using the Frobenius solution. The outward solution for $f_1(x)$ is scaled to match the inward solution of $f_1(x)$at the fitting point, and the process is repeated, varying κ, until a value of κ is found for which the inward and outward solutions for $f_2(x)$ are also equal at the fitting point. This procedure is equivalent to solving for C_1 and κ by requiring that $f_{\kappa,\beta}(x)$ and $\frac{df_{\kappa,\beta}(x)}{dx}$ are continuous between the boundary points. Starting values for κ are found from the WKB eigenvalues, solved for using the method outlined by Blossey.[2] The numerical solutions for $f_{\kappa,\beta}(x)$ are then normalized by scaling $f_{\kappa,\beta}(x)$ so that $1 = \int_0^\infty {f_{\kappa,\beta}}^2(x)dx$, and the value of ${f_{\kappa,\beta}}^2(0)$ is taken from the normalized solution.

Once the eigenvalues κ are known, the eigenvalues $\kappa'$are known immediately for a chosen F/F_I via the relation $\kappa' = \kappa + 2\left(\frac{F_I}{F}\right)^{1/3}$.[2] To find the solutions for $g_{\kappa',\beta}(x)$, a similar approach may be taken for setting up the O.D.E.s as well as the boundaries at the origin. However, Blossey has pointed out that the normalization of $g_{\kappa',\beta}(x)$ is not possible numerically. The asymptotic solution for $g_{\kappa',\beta}(x)$ at large x is given as:

$$g_{\kappa',\beta}(x) \sim (-x+\beta)^{-3/4}\sin\left[\frac{2}{3}(-x+\beta)^{3/2} + \kappa'(-x+\beta)^{1/2} + \alpha\right]$$

where α is an arbitrary phase constant.

We follow the method of Winzer *et al.*[36] by integrating $g_1'$and g_2' outward from the origin, and then fitting the envelope of the numerical solution for $g_{\kappa',\beta}(x)$ to the envelope of the asymptotic solution. In this case the normalization constant and α are both solved for in the least squares sense and ${g_{\kappa',\beta}}^2(0)$can be taken directly from the obtained solution. This is equivalent to the normalization procedure of Blossey, where the normalization of $g_{\kappa',\beta}(x)$ is determined by the asymptotic solution.[2]

We verified that our solutions were correct by checking that we could reproduce the results in Blossey's report.[2] All calculations were carried out using in-house code written in scipy for Python.

S9. Temperature Dependent Absorbance

The absorbance $(-log_{10}\left(\frac{I_{trans}}{I_{inc}}\right))$ of $CH_3NH_3PbI_3$ was measured for all temperatures at which the EA spectra were measured and is shown below in Fig. S9. A weak exciton shoulder becomes noticeable at 210 K.

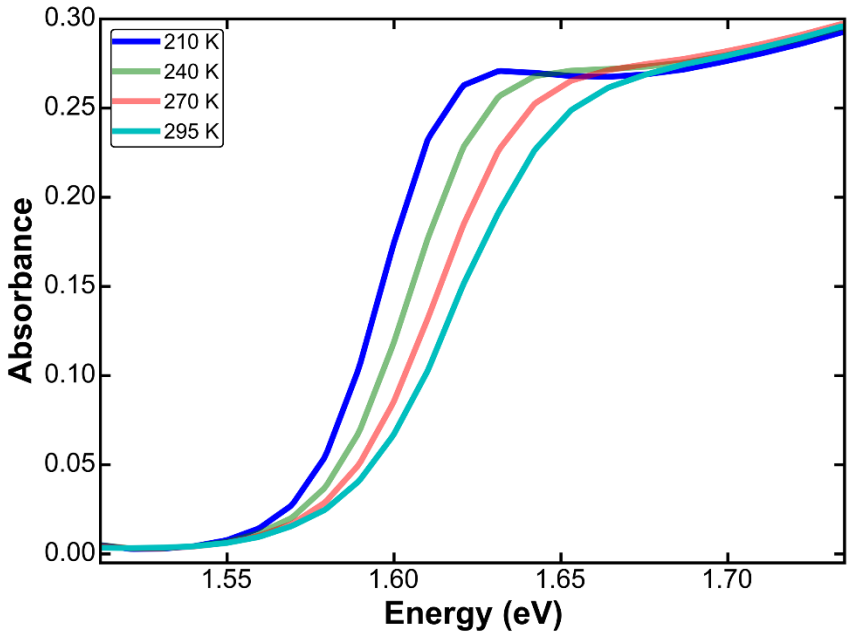

Fig. S9. Temperature dependent absorbance $(-log_{10}\left(\frac{I_{trans}}{I_{inc}}\right))$ of thin film $CH_3NH_3PbI_3$ from 210 - 295 K, highlighting the development of a weak exciton peak at 210 K.

S10. Observation of Field Ionization Signatures from 210-240K

We observed the signatures assigned to field ionization of the $n = 1$ exciton (see main text) in the EA spectrum at 210 K in multiple samples prepared from the same precursor route. In Fig. S10 a. we show the raw EA data corresponding to the amplitude normalized spectrum in Fig. 2.3 a. of the main text. In Figs. S10 b. and c. we show the raw data and amplitude normalized EA spectra for another sample at 210 K. The amplitude normalized spectrum demonstrates the same trend as Fig. 2.3 a. in the main text in terms of the variation in the line shape with field around Peak III, although the effect is slightly more subtle for this sample. The inset of Fig. S10 c. shows the increase in the power law scaling (>2) of Peak III with field at 210 K as discussed in the main text and section S7. In Fig. S10 d. we also show the amplitude normalized spectra from Fig. 2.3 a. in the main text, but with data from 4 V_{AC} included. At all temperatures the 4 V_{AC} data were noisy, making it difficult to compare lineshapes. However the trend is still in general agreement when the 4 V_{AC} data is included.

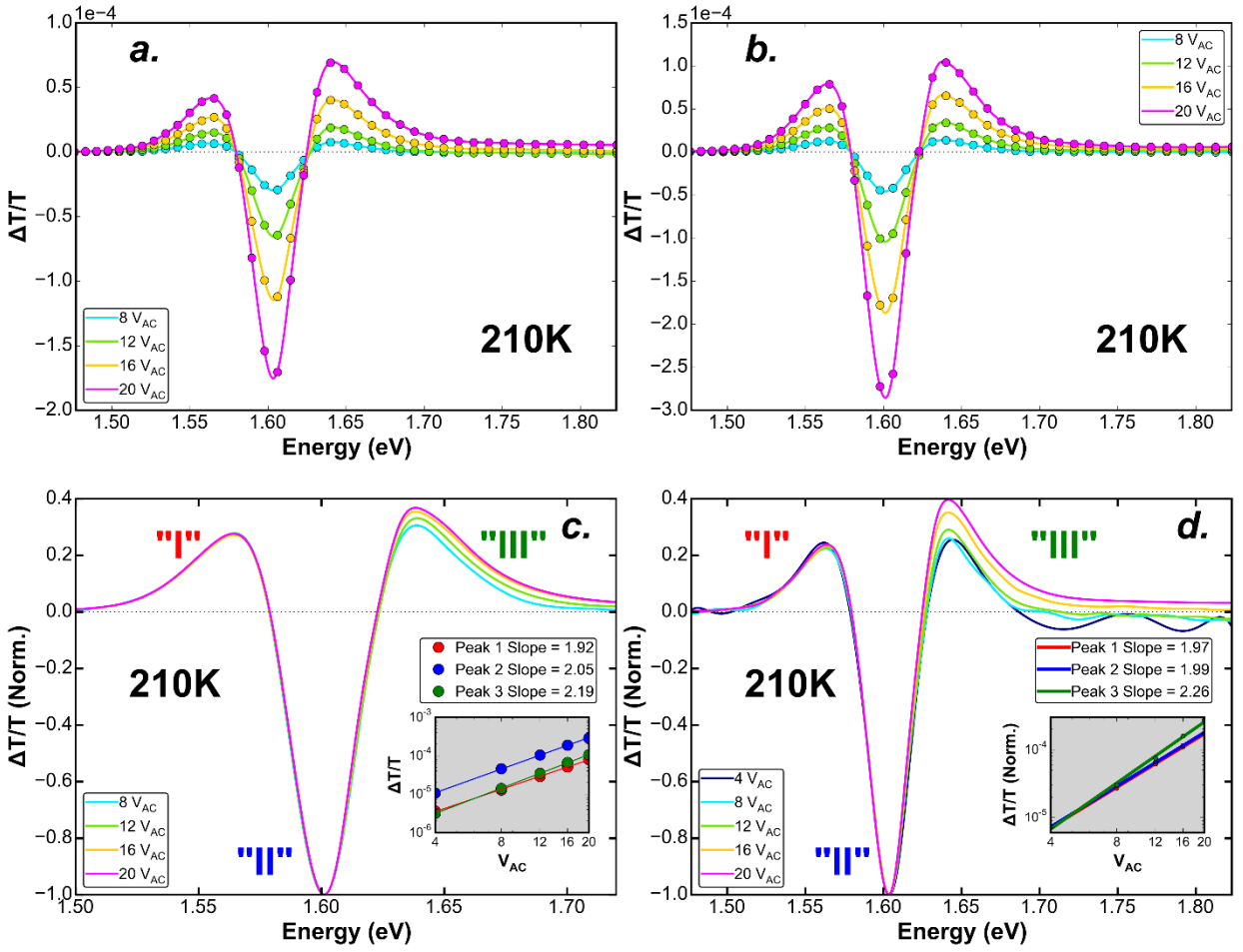

Fig. S10 *a., b.)* Raw data of the second harmonic EA spectra at 210 K for two different samples. *c., d.)* Amplitude normalized spectra for two different samples showing the field invariance of the lineshape at Peak III. The scaling of the paks with applied voltage are shown in the inset. Fig. *d.* is included to show the 4 V_{AC} lineshape, which was not reported in the main text due to the difficulty in fitting a reliable smoothing spline to the data to compare lineshapes.

S11. Comparison of $\hbar\Omega$ and Γ to Verify Conditions for Low-Field FKA Analysis

The condition defining the low-field limit of the FKA effect is $\hbar\Omega < \frac{1}{3}\,\Gamma$, where $\hbar\Omega$ is the electro-optic energy and Γ is the broadening half-width.[5, 37] From the low-field FKA analysis of the room temperature $\chi^{(3)}$ EA spectra using Eq 1 a. (main text) and the experimental complex ϵ, we calculated a maximum experimental value of $\hbar\Omega \sim 5$ meV. To estimate reasonable values for the linewidth Γ, we first fit the experimental ϵ_i spectrum from ellipsometry to Elliott's formula, fixing Γ at specific values and allowing all other parameters to vary. We constrain the boundaries on E_B from 1 – 200 meV for these fits. Looking at the fits to ϵ_i, we can then determine reasonable limits on Γ. In Fig. S11 we show the fits based on fixing Γ at 10, 20, 30, and 40 meV. We can see that reasonable fits can only be achieved starting at $\Gamma = 20$ meV, which satisfies the condition of the low-field FKA limit. Second, we can compare our calculated value of $\hbar\Omega$ with the value of Γ determined from the third derivative Elliott fit to the room temperature EA data, as shown in Fig. 2.2 a. of the main text. The value of Γ determined from the third derivative Elliott fit was 33-42 meV, depending on the broadening function used (Gaussian or Secant Hyperbolic).

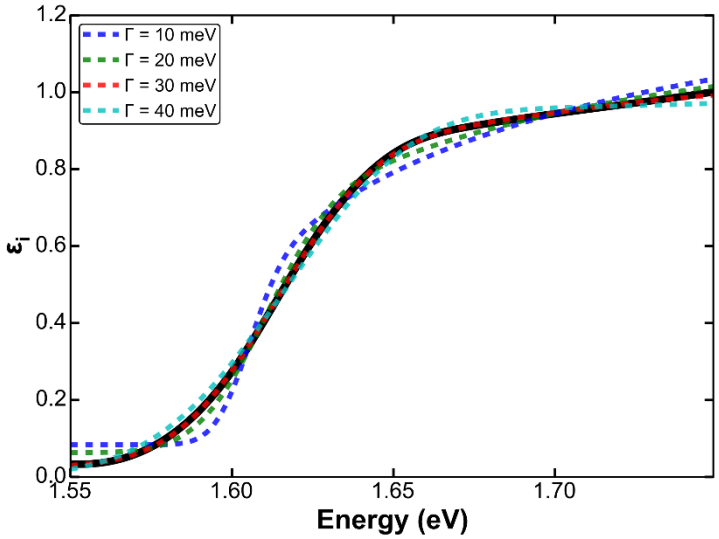

Fig. S11. Fits of Elliott's function (see section S1) to the ϵ_i spectrum of $CH_3NH_3PbI_3$ measured with ellipsometry, where the broadening parameter Γ is fixed at different values.

S12. Selection of V_{AC} Modulation Frequency

It has been shown through impedance spectroscopy measurements that at low frequencies $CH_3NH_3PbI_3$ exhibits a very large dielectric response, which has been attributed to mobile ion/defect migration[24] and associated defect dipoles[38], and the rotation of the polar $CH_3NH_3^+$ cation.[39] We studied the frequency dependence of the phase (θ) of the EA signal, referenced to the phase of the modulation voltage V_{AC} (10 V) applied by the function generator. Fig. S12 shows that below 1.3 kHz at 300K and 210K, the phase of the EA signal undergoes a gradual change as a function of frequency. Above 1.3 kHz the phase remains flat at 210 K and 300 K. Since the EA response is directly related to the polarization of the $CH_3NH_3PbI_3$ layer in response to V_{AC}, we attribute to the low frequency phase shift of the EA signal to similar mechanisms associated with the large low frequency dielectric response observed in impedance spectroscopy. The data in Fig. S12 suggests that 1.3 kHz is a suitable cutoff frequency to avoid any artifacts in the EA spectrum associated with the low frequency polarization mechanisms of $CH_3NH_3PbI_3$.

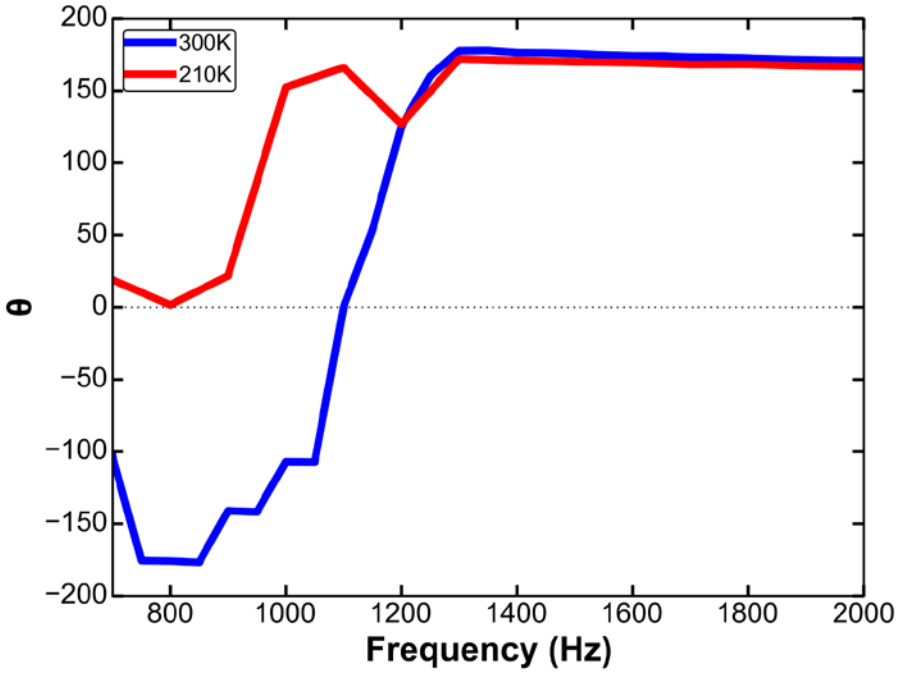

Fig. S12. Plot of the phase (θ) of the EA signal as a function of frequency. A modulation frequency of 1.3 kHz was chosen as the cut off frequency to avoid phase chages at low frequencies associated with low frequency dielectric effects in CH3NH3PbI3.

S13. Lineshape Differences in Transmission and Reflection Geometries

Recent literature reports of EA spectra in $CH_3NH_3PbI_3$ have reported first[40] and second[25, 41] derivative-like lineshapes, leading authors to interpret the EA response in terms of a linear or quadratic Stark shift following the theory of Liptay[42-43] and Weiser.[44] We have found that the differences between the lineshape measured in our EA spectra of $CH_3NH_3PbI_3$ and those measured in other reports in the literature[25, 40-41, 45] can be explained primarily on the basis of optical effects due to differences in measurement geometry and sample thickness. The other literature reports of EA spectra on $CH_3NH_3PbI_3$ have conducted the measurement on relatively thicker (~200-400 nm films) in a reflection geometry, where the sample is oriented at 45° incidence and the modulation of the reflected signal ($\Delta R/R$) is recorded. In these experiments, the probe light is reflected off of a thick (~100 nm) metal back electrode after making its first pass through the film, and then detected after second pass transmission back through the film to the air/glass interface. When measured in this geometry, the $\Delta R/R$ signal can be significantly distorted compared to the $\Delta T/T$ signal that would be measured in a single pass transmittance geometry, where a semi-transparent top electrode is used. The distortion is due entirely to effects from refractive index modulation (which can be expected for thicker films measured in reflection geometry) and optical interference effects. Price *et al.*[46] have also recently demonstrated the importance of accounting for refractive index changes in modulation spectra in $CH_3NH_3PbI_3$. In Fig. S13 a. we show the lineshapes simulated with transfer matrix modelling for our typical device stack (see section S4 for methods) for $\Delta T/T$ (15 nm Ag layer) and $\Delta R/R$ (45° incidence, 100 nm Ag layer). For this simulation a 300 nm thick $CH_3NH_3PbI_3$ layer is used and the complex $\Delta\epsilon$ is calculated from the low-field FKA formula using the complex ϵ measured from ellipsometry (see Fig. 2.1 c. and discussion in main text). It is clear that $\Delta T/T$ is very closely related to ϵ_i, whereas the signal measured in the $\Delta R/R$ geometry is significantly distorted from ϵ_i (we note that ϵ_i is the function that is directly calculated in theoretical models for the change in the optical response[5]). In Figs S13 b. and c. show simulations for $\Delta T/T$ and $\Delta R/R$ when the thickness of the $CH_3NH_3PbI_3$ layer is varied. We can see that the lineshape for $\Delta T/T$ changes very little depending on the thickness of $CH_3NH_3PbI_3$ (Fig. S13 b.), whereas the $\Delta R/R$ lineshape depends strongly on the perovskite thickness (Fig. S13 c.). The perovskite thickness dependence of the lineshape in the $\Delta R/R$ spectra can be explained by effects due to refractive index modulation (Δn) and optical interference. We note that in a crystal thicker than the penetration depth of light, an electro-modulation signal measured in the $\Delta R/R$ geometry will essentially represent the lineshape of Δn.[47] The lineshapes in Fig. S13 c. for certain thickness very closely resemble the second derivative-like lineshapes measured by other authors.[25, 41] In Fig. S13 d. we show the first and second derivative-like lineshapes calculated from the experimental complex ϵ measured from ellipsometry. While other authors have fit EA spectra of $CH_3NH_3PbI_3$ measured in reflection geometry using a classic Stark effect analysis based on the sum of zeroth, first, and second derivative-like lineshapes,[42-43] we can see that the spectra measured in transmission geometry cannot be fit with such an analysis. We note the first derivative-like response is always positive in the classic Stark effect EA analysis, as it represents a redshift of the absorption spectrum due to the exciton polarizability.[43]

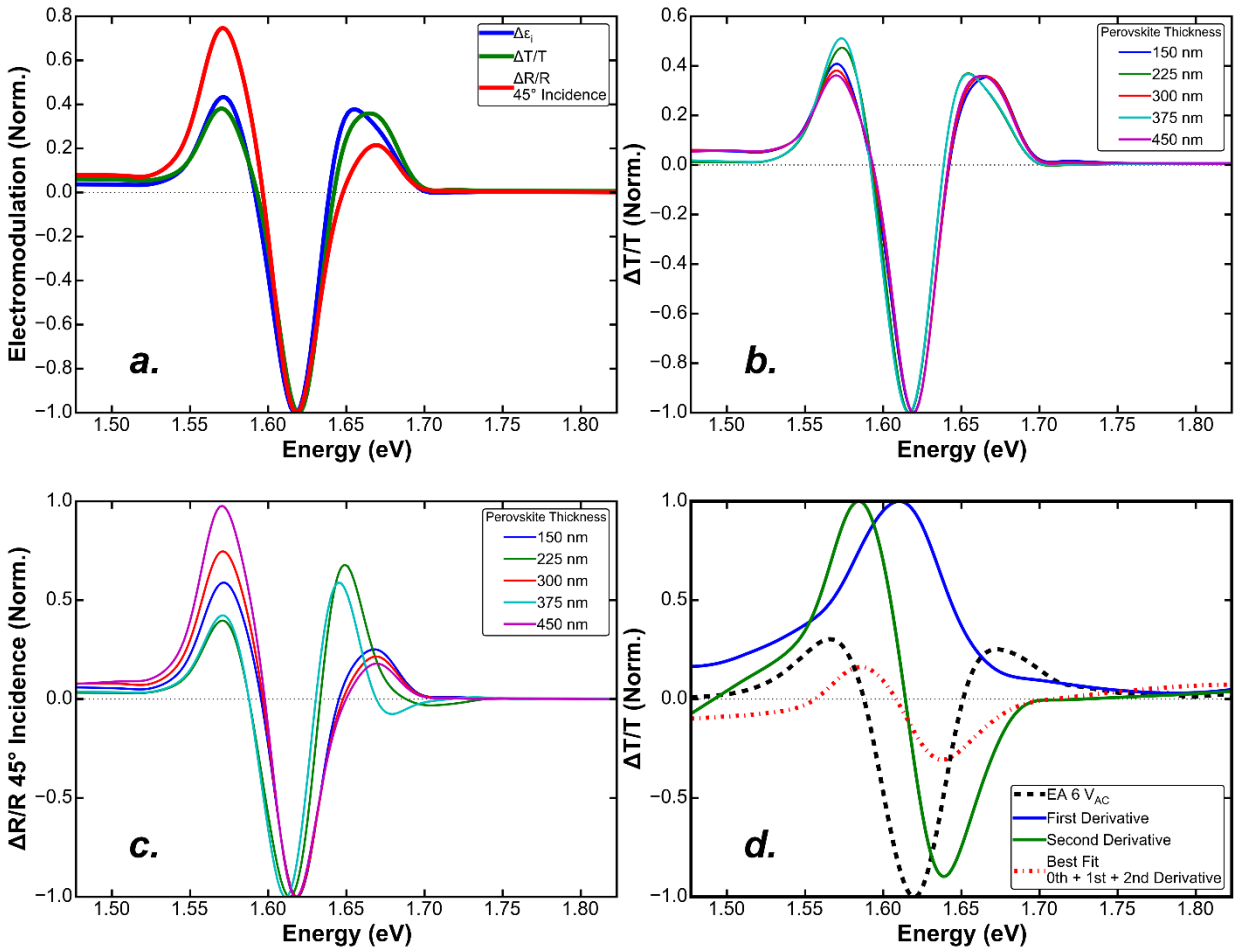

Fig. S13 a.) Comparison between normal incidence $\Delta T/T$ and 45° incidence $\Delta R/R$ simulated with transfer matrix modelling for a 300 nm thick CH3NH3PbI3 layer, where $\Delta\epsilon$ is calculated from the low-field FKA formula using the complex ϵ measured from ellipsometry as in Fig. 2.1 c. of the main text. It is clear that the $\Delta T/T$ lineshape closely resembles $\Delta\epsilon_i$, whereas $\Delta R/R$ is significantly distorted. b., c.) Plots showing the variation of $\Delta T/T$ and $\Delta R/R$ with perovskite thickness. It is clear that for certain thicknesses $\Delta R/R$ can resemble a second derivative-like shape, whereas the $\Delta T/T$ lineshape changes negligibly with perovskite thickness. d.) Comparison between the measured EA spectrum in transmission geometry and the first and second derivative-like lineshapes. The best fit of a sum of zeroth, first, and second derivative lineshapes to the EA data is also shown.

S14. Sample Configuration and Experimental Schematics

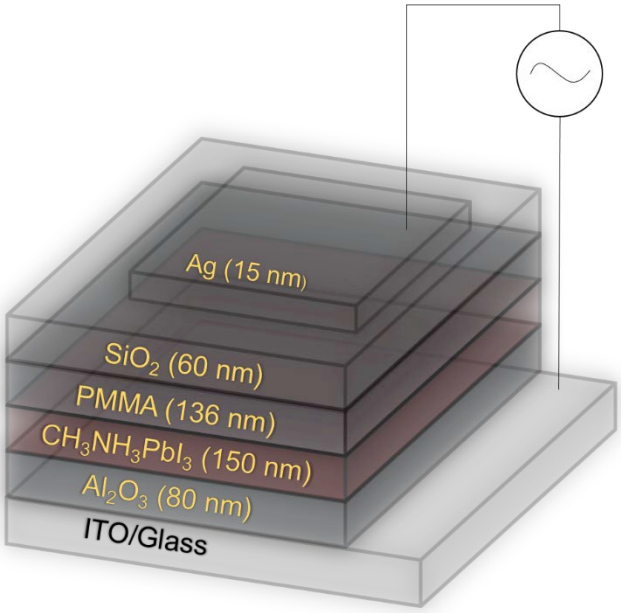

Fig. S14.1 Geometry of semi-transparent dielectric capacitor sample used in EA measurements.

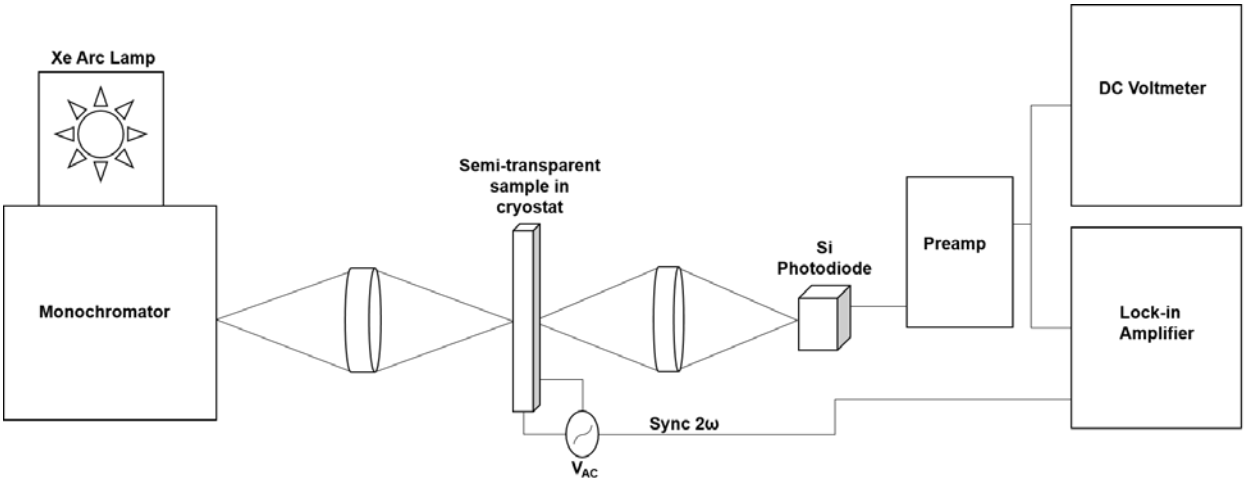

Fig. S14.2 Schematic of experimental set up for EA spectroscopy on home-built system.

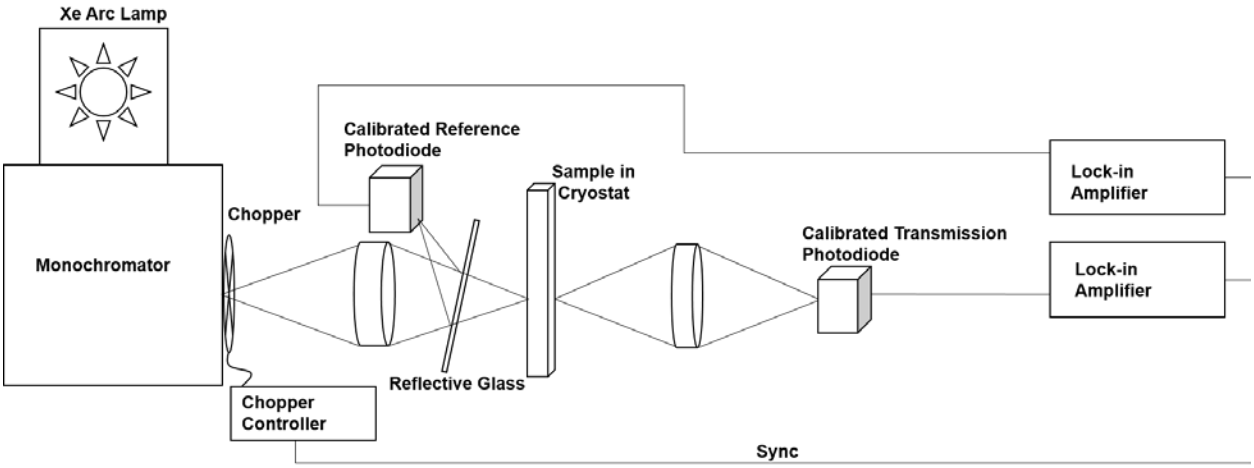

Fig. S14.3 Schematic of experimental set up for temperature dependent absorbance spectroscopy on home-built system.

S15. Structural, Morphological, and Additional Optical Characterization of $CH_3NH_3PbI_3$ Films Prepared via $Pb(CH_3CO_2)_2 \cdot 3H_2O$ Precursor Route

S15.1 X-Ray Diffraction

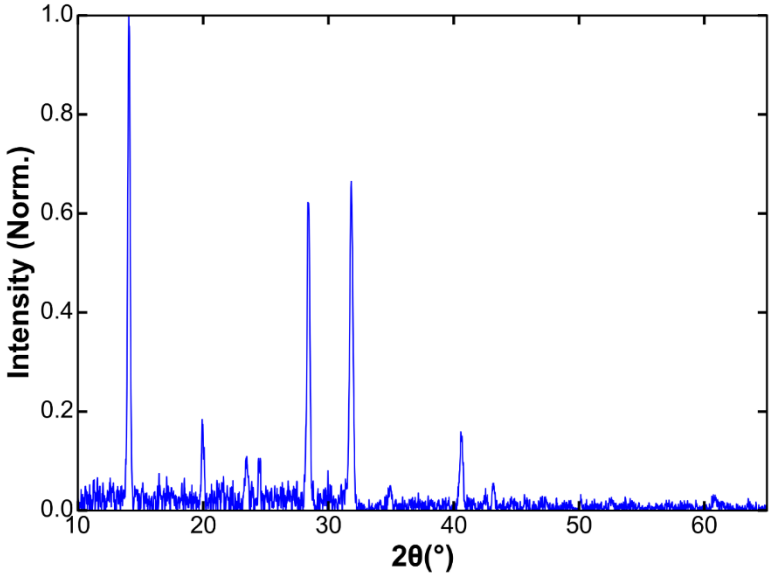

Fig. S15.1 X-ray diffraction pattern from a CH3NH3PbI3 film prepared on glass showing a characteristic pattern of tetragonal CH3NH3PbI3.48 The measurement was conducted on a Bruker D8 Discover with GADDS 2-D XRD system.

S15.2 SEM Top-View Morphology

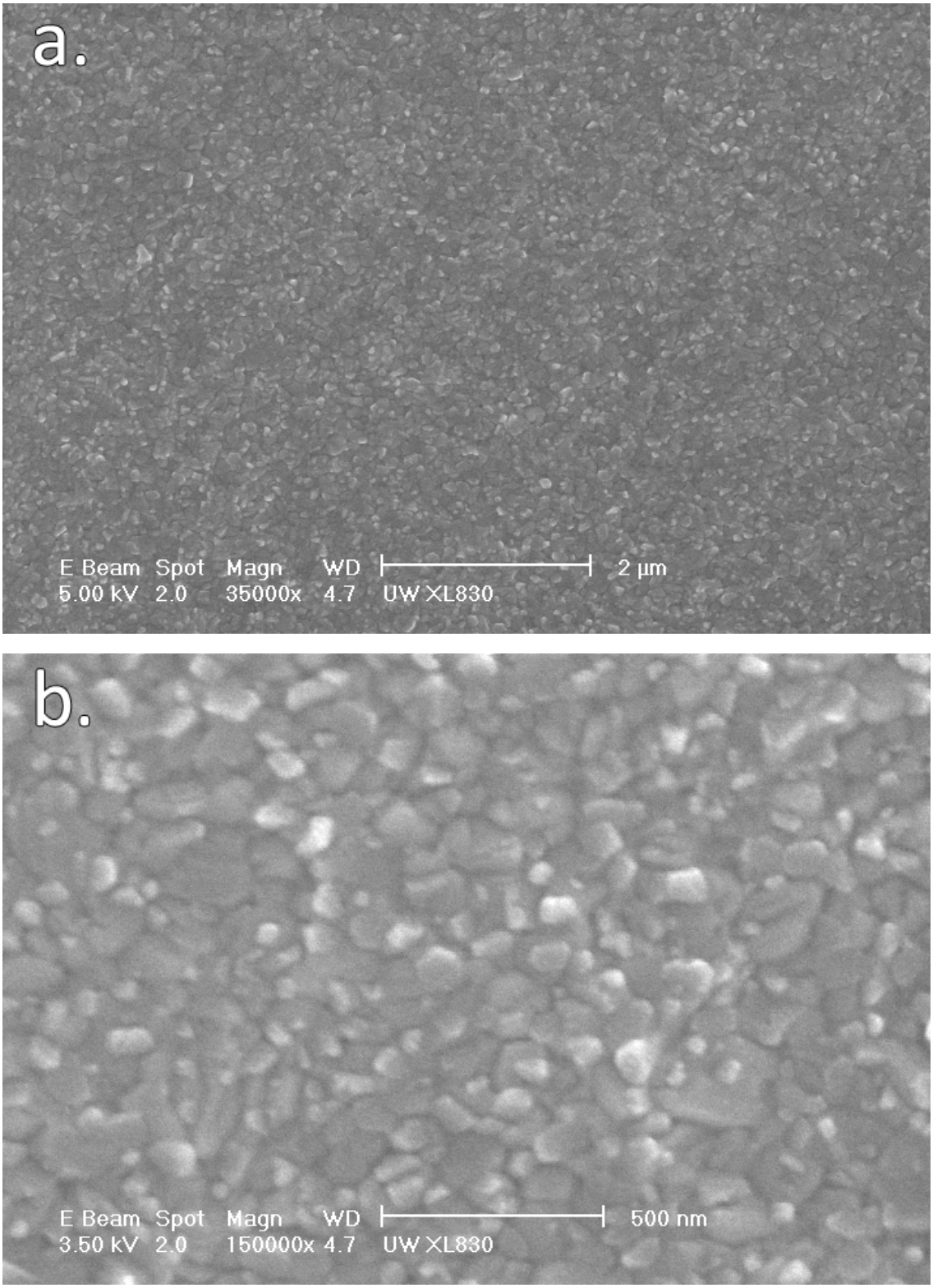

Fig. S15.2 *a., b.)* Top-view SEM images of a $CH_3NH_3PbI_3$ film prepared on glass showing a dense, pinhole free $CH_3NH_3PbI_3$ layer. Images were taken on a FEI XL830 Dual Beam FIB/SEM.

S15.3 AFM Surface Roughness

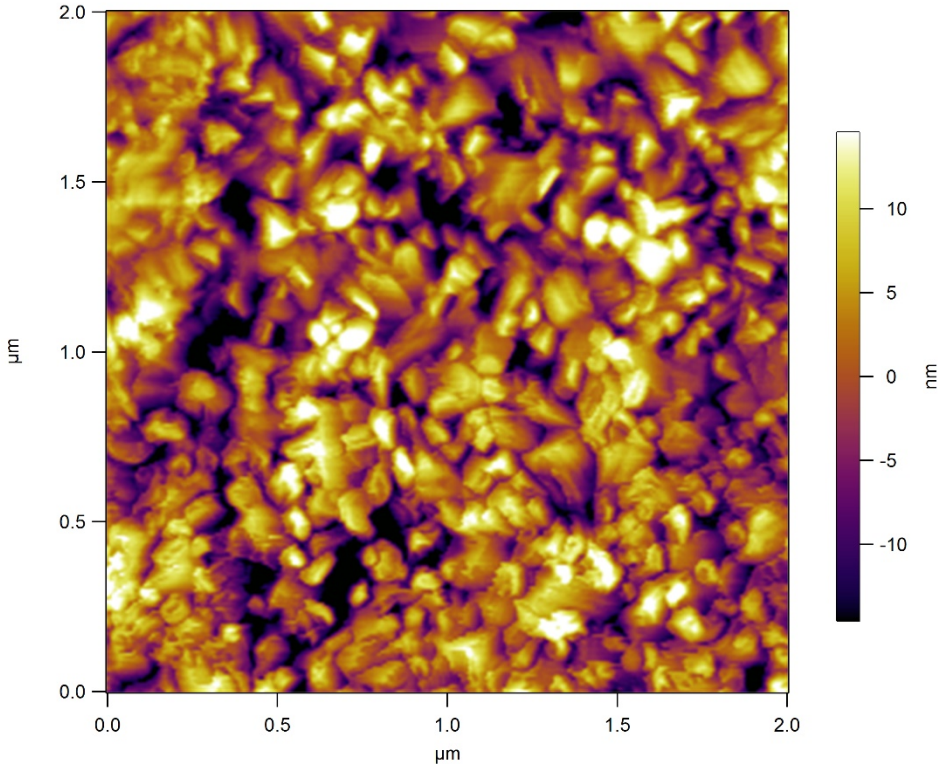

Fig. S15.3 AFM height image of a $CH_3NH_3PbI_3$ film prepared on glass showing a smooth $CH_3NH_3PbI_3$ layer. The RMS surface roughness was measured to be 7.3 nm. AFM measurements were taken with an Asylum Research MFP-3D BIO atomic force microscope (Oxford Instruments), using a 300 kHz frequency silicon cantilever with a conductive Pt coating (Budget Sensors).

S15.4 Steady-State Photoluminescence (PL) Spectrum and PL Lifetime

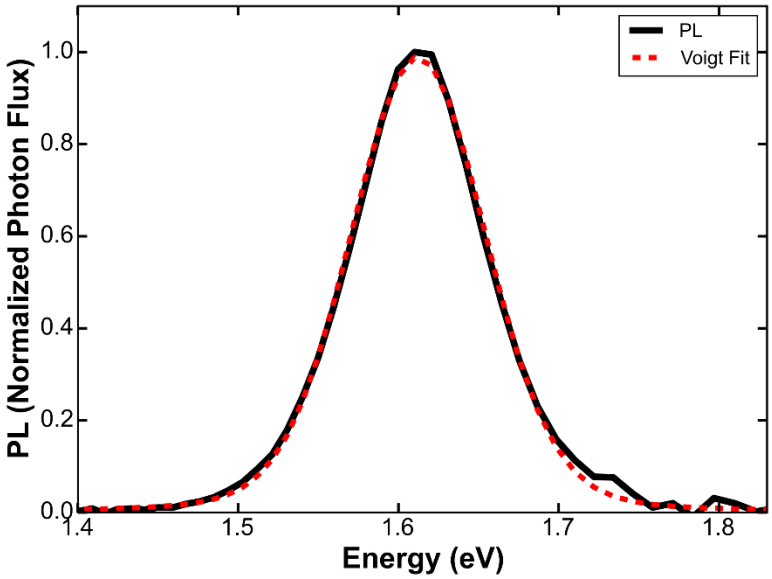

Fig. S15.4.1 Steady state photoluminescence (PL) spectrum of a $CH_3NH_3PbI_3$ film prepared on glass (447 nm LED excitation, Luxeon Rebel, 700 mW, LXML-PR01-0425). The PL spectrum is fit to a Voigt function with best fit parameters giving a total FWHM of 100 meV and a center of mass value at 1.612 eV, similar to previous reports.[49] The spectrum was corrected for the instrument response using a calibrated light source and the y-axis of the PL spectrum was scaled point-by-point using the Jacobian for converting the resolution from wavelength to eV. The measurement was conducted at room temperature with the sample under dynamic vacuum (<20 mTorr) using a system described previously.[50]

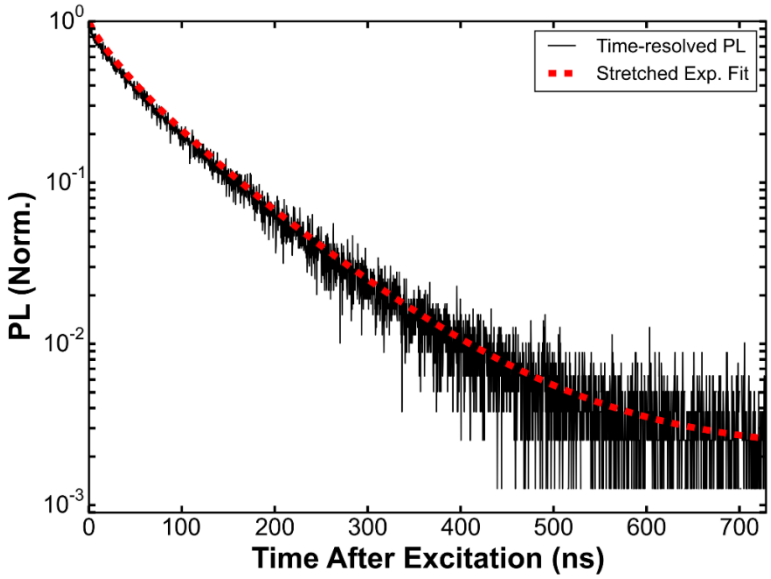

Fig. S15.4.2 Time-resolved photoluminescence decay of a $CH_3NH_3PbI_3$ film prepared on glass (470 nm pulsed diode laser excitation, 500 kHz repetition rate, 10 nJ/cm^2/pulse). The low-fluence PL decay was fit to a stretched exponential function[51] with best fit parameters giving an average lifetime of $\langle\tau\rangle$=64 ns, comparable to the monomolecular decay lifetime (τ=50-100ns) measured previously in films with similar morphology and crystallite size.[49, 52-53] The time-correlated single photon counting measurement was conducted with the sample under continuous N_2 flow on a custom-fitted confocal microscope set up described previously[51] with the excitation beam focused over an area of ~270μm^2.

Supplementary References

1. Elliott, R. J., Intensity of Optical Absorption by Excitons. Phys. Rev. 1957, 108, 1384-1389.
2. Blossey, D., Wannier Exciton in an Electric Field. I. Optical Absorption by Bound and Continuum States. Phys. Rev. B 1970, 2, 3976-3990.
3. Press, W. H.; Teukolsky, S. A.; Vetterling, W. T.; Flannery, B. P., Numerical Recipes 3rd Edition: The Art of Scientific Computing. 3 ed.; Cambridge University Press: New York, 2007.
4. Forman, R. A.; Aspnes, D. E.; Cardona, M., Transverse electroreflectance in semi-insulating silicon and gallium arsenide. J. Phys. Chem. Solids 1970, 31, 227-246.
5. Aspnes, D. E.; Rowe, J. E., Resonant Nonlinear Optical Susceptibility: Electroreflectance in the Low-Field Limit. Phys. Rev. B 1972, 5, 4022-4030.
6. Seraphin, B. O., Electroreflectance. In Semiconductors and Semimetals, Willardson, R. K.; Beer, A. C., Eds. Academic Press: New York, New York, 1972; Vol. 9, pp 1-149.
7. Hamakawa, Y.; Handler, P.; Germano, F., Interband Electro-Optical Properties of Germanium. II. Electroreflectance. Phys. Rev. 1968, 167, 709-716.
8. J. A. Woollam Co., I. CompleteEASE, 4.63; J. A. Woollam Co., Inc.: 2011.
9. Lautenschlager, P.; Garriga, M.; Logothetidis, S.; Cardona, M., Interband critical points of GaAs and their temperature dependence. Phys. Rev. B 1987, 35, 9174-9189.
10. Blakemore, J. S., Semiconducting and other major properties of gallium arsenide. J. Appl. Phys. 1982, 53, R123.
11. Shirayama, M.; Kadowaki, H.; Miyadera, T.; Sugita, T.; Tamakoshi, M.; Kato, M.; Fujiseki, T.; Murata, D.; Hara, S.; Murakami, T. N.; Fujimoto, S.; Chikamatsu, M.; Fujiwara, H., Optical Transitions in Hybrid Perovskite Solar Cells: Ellipsometry, Density Functional Theory, and Quantum Efficiency Analyses for CH3NH3PbI3. Phys. Rev. Appl. 2016, 5, 014012.
12. Jiang, Y.; Soufiani, A. M.; Gentle, A.; Huang, F.; Ho-Baillie, A.; Green, M. A., Temperature dependent optical properties of CH3NH3PbI3 perovskite by spectroscopic ellipsometry. Appl. Phys. Lett. 2016, 108, 061905.
13. Ball, J. M.; Stranks, S. D.; Hoerantner, M. T.; Huettner, S.; Zhang, W.; Crossland, E. J. W.; Ramirez, I.; Riede, M.; Johnston, M. B.; Friend, R. H.; Snaith, H. J., Optical properties and limiting photocurrent of thin-film perovskite solar cells. Energy Environ. Sci. 2015, 8, 602-609.
14. Loper, P.; Stuckelberger, M.; Niesen, B.; Werner, J.; Filipic, M.; Moon, S. J.; Yum, J. H.; Topic, M.; De Wolf, S.; Ballif, C., Complex Refractive Index Spectra of CH3NH3PbI3 Perovskite Thin Films Determined by Spectroscopic Ellipsometry and Spectrophotometry. J. Phys. Chem. Lett. 2015, 6, 66-71.
15. Byrnes, S. J., Multilayer optical calculations. arXiv e-prints 2016, arXiv:1603.02720.
16. Newville, M.; Ingargiola, A.; Allen, D. B.; Stensitzki, T. LMFIT: Non-Linear Least-Square Minimization and Curve-Fitting for Python. http://cars9.uchicago.edu/software/python/lmfit/confidence.html.
17. Seraphin, B.; Bottka, N., Franz-Keldysh Effect of the Refractive Index in Semiconductors. Phys. Rev. 1965, 139, A560-A565.
18. Peatross, J.; Ware, M., Physics of Light and Optics. 2013 ed.; available at optics.byu.edu: 2013.

19. Liess, M.; Jeglinski, S.; Vardeny, Z. V.; Ozaki, M.; Yoshino, K.; Ding, Y.; Barton, T., Electroabsorption spectroscopy of luminescent and nonluminescent π-conjugated polymers. Phys. Rev. B 1997, 56, 15712-15724.
20. Campbell, I. H.; Hagler, T. W.; Smith, D. L.; Ferraris, J. P., Direct Measurement of Conjugated Polymer Electronic Excitation Energies Using Metal/Polymer/Metal Structures. Phys. Rev. Lett. 1996, 76, 1900-1903.
21. Dow, J.; Redfield, D., Electroabsorption in Semiconductors: The Excitonic Absorption Edge. Phys. Rev. B 1970, 1, 3358-3371.
22. Galbraith, I. I., Excitonic electroabsorption and electrorefraction in semiconductors. Phys. Rev. B 1993, 48, 5105-5112.
23. Blossey, D., Wannier Exciton in an Electric Field. II. Electroabsorption in Direct-Band-Gap Solids. Phys. Rev. B 1971, 3, 1382-1391.
24. Lin, Q.; Armin, A.; Nagiri, R. C. R.; Burn, P. L.; Meredith, P., Electro-optics of perovskite solar cells. Nat. Photon. 2014, 9, 106-112.
25. Wu, X.; Yu, H.; Li, L. K.; Wang, F.; Xu, H. H.; Zhao, N., Composition-Dependent Light-Induced Dipole Moment Change in Organometal Halide Perovskites. J. Phys. Chem. C 2015, 119, 1253-1259.
26. Fauchier, J.; Dow, J. D., An analytic approach to the hydrogen Stark effect in weak, strong, and ultrastrong fields. Phys. Rev. A 1974, 9, 98-107.
27. Dow, J. D., Effects of final-state interactions on modulation spectra of semiconductors. Surf. Sci. 1973, 37, 787-803.
28. Rudin, S.; Reinecke, T. L.; Segall, B., Temperature-dependent exciton linewidths in semiconductors. Phys. Rev. B 1990, 42, 11218-11231.
29. Landau, L. D.; Lifshitz, E. M., Quantum Mechanics: Non-Relativistic Theory. 2 ed.; Pergamon Press: Oxford, 1965.
30. Bethe, H. A.; Salpeter, E. E., Quantum Mechanics of One- and Two-Electron Atoms. Springer-Verlag: Berlin, 1957.
31. Fong, P., Elementary Quantum Mechanics. Addison-Wesley: 1962.
32. Griffiths, D. J., Introduction to Quantum Mechanics. 1 ed.; Prentice Hall, Inc.: Upper Saddle River, NJ, 1995.
33. Blossey, D. F.; Handler, P., Electroabsorption. In Semiconductors and Semimetals, Willardson, R. K.; Beer, A. C., Eds. Academic Press: New York, New York, 1972; Vol. 9, pp 257-314.
34. Ralph, H. I., On the theory of the Franz-Keldysh effect. J. Phys. C Solid State 1968, 1, 378-386.
35. Hildebrand, F. B., Advanced Calculus for Applications. Prentice-Hall, Inc.: Englewood Cliffs, New Jersey, 1976.
36. Winzer, A. T.; Gobsch, G.; Goldhahn, R.; Fuhrmann, D.; Hangleiter, A.; Dadgar, A.; Krost, A., Influence of excitons and electric fields on the dielectric function of GaN: Theory and experiment. Phys. Rev. B 2006, 74.
37. Aspnes, D. E., Third-Derivative Modulation Spectroscopy with Low-Field Electroreflectance. Surf. Sci. 1973, 37, 418-442.
38. Li, L.; Wang, F.; Wu, X.; Yu, H.; Zhou, S.; Zhao, N., Carrier-Activated Polarization in Organometal Halide Perovskites. J. Phys. Chem. C 2016, 120, 2536-2541.

39. Juarez-Perez, E. J.; Sanchez, R. S.; Badia, L.; Garcia-Belmonte, G.; Kang, Y. S.; Mora-Sero, I.; Bisquert, J., Photoinduced Giant Dielectric Constant in Lead Halide Perovskite Solar Cells. J. Phys. Chem. Lett. 2014, 5, 2390-4.
40. Roiati, V.; Mosconi, E.; Listorti, A.; Colella, S.; Gigli, G.; De Angelis, F., Stark effect in perovskite/TiO2 solar cells: evidence of local interfacial order. Nano. Lett. 2014, 14, 2168-74.
41. Li, C.; Tscheuschner, S.; Paulus, F.; Hopkinson, P. E.; Kiessling, J.; Kohler, A.; Vaynzof, Y.; Huettner, S., Iodine Migration and its Effect on Hysteresis in Perovskite Solar Cells. Adv. Mater. 2016, 28, 2446-54.
42. Liptay, W., Dipole Moments and Polarizabilities of Molecules in Excited Electronic States. In Excited States, Lim, E. C., Ed. Academic Press, Inc.: New York, New York, 1974; Vol. 1, pp 129-229.
43. Bublitz, G. U.; Boxer, S. G., Stark spectroscopy: applications in chemistry, biology, and materials science. Annu. Rev. Phys. Chem. 1997, 48, 213-42.
44. Weiser, G., Absorption and electroabsorption on amorphous films of polyvinylcarbazole and trinitrofluorenone. Phys. Status Solidi A 1973, 18, 347-359.
45. Deschler, F.; Price, M.; Pathak, S.; Klintberg, L. E.; Jarausch, D. D.; Higler, R.; Huttner, S.; Leijtens, T.; Stranks, S. D.; Snaith, H. J.; Atature, M.; Phillips, R. T.; Friend, R. H., High Photoluminescence Efficiency and Optically Pumped Lasing in Solution-Processed Mixed Halide Perovskite Semiconductors. J. Phys. Chem. Lett. 2014, 5, 1421-6.
46. Price, M. B.; Butkus, J.; Jellicoe, T. C.; Sadhanala, A.; Briane, A.; Halpert, J. E.; Broch, K.; Hodgkiss, J. M.; Friend, R. H.; Deschler, F., Hot-carrier cooling and photoinduced refractive index changes in organic-inorganic lead halide perovskites. Nat. Commun. 2015, 6, 8420.
47. Aspnes, D. E.; Bottka, N., Electric-Field Effects on the Dielectric Function of Semiconductors and Insulators. In Semiconductors and Semimetals, Willardson, R. K.; Beer, A. C., Eds. Academic Press: New York, New York, 1972; Vol. 9, pp 457-543.
48. Stoumpos, C. C.; Malliakas, C. D.; Kanatzidis, M. G., Semiconducting tin and lead iodide perovskites with organic cations: phase transitions, high mobilities, and near-infrared photoluminescent properties. Inorg. Chem. 2013, 52, 9019-38.
49. Wehrenfennig, C.; Liu, M.; Snaith, H. J.; Johnston, M. B.; Herz, L. M., Homogeneous Emission Line Broadening in the Organo Lead Halide Perovskite CH3NH3PbI3-xClx. J. Phys. Chem. Lett. 2014, 5, 1300-6.
50. Sulas, D. B.; Yao, K.; Intemann, J. J.; Williams, S. T.; Li, C.-Z.; Chueh, C.-C.; Richards, J. J.; Xi, Y.; Pozzo, L. D.; Schlenker, C. W.; Jen, A. K. Y.; Ginger, D. S., Open-Circuit Voltage Losses in Selenium-Substituted Organic Photovoltaic Devices from Increased Density of Charge-Transfer States. Chem. Mater. 2015, 27, 6583-6591.
51. deQuilettes, D. W.; Vorpahl, S. M.; Stranks, S. D.; Nagaoka, H.; Eperon, G. E.; Ziffer, M. E.; Snaith, H. J.; Ginger, D. S., Impact of microstructure on local carrier lifetime in perovskite solar cells. Science 2015, 348, 683-6.
52. Liu, M.; Johnston, M. B.; Snaith, H. J., Efficient planar heterojunction perovskite solar cells by vapour deposition. Nature 2013, 501, 395-8.
53. D'Innocenzo, V.; Srimath Kandada, A. R.; De Bastiani, M.; Gandini, M.; Petrozza, A., Tuning the light emission properties by band gap engineering in hybrid lead halide perovskite. J. Am. Chem. Soc. 2014, 136, 17730-3.

Appendix B: Supporting Information for Chapter 3

Experimental Methods

Sample Preparation

P1 and P2 polymers were synthesized according to the methods reported previously.[27] The M_w and polydispersity index (PDI) for P1 and P2 were obtained using GPC (Waters 1515) operated with oDCB at 130°C, which was calibrated against a polystyrene standard. Thin film samples for UV-vis absorption, ellipsometry, and photoluminescence spectroscopy were prepared on glass microscope slides, which were cleaned by sequential sonication in detergent solution, DI-water, acetone, and isopropanol. Prior to spin coating polymer solutions, glass substrates were plasma cleaned for 5 minutes with air (Diener Femto). P1 and P2 solutions were prepared by dissolving 10mg/mL of material in anhydrous 1,2-dichlorobenzene and heating the solution at 80° C for several hours while stirring in a N_2 glovebox. Thin films of P1 and P2 were prepared by spin coating the solutions at 1800 rpm for 2 mins inside of a N_2 glovebox. Sample preparation for electroabsorption spectroscopy is described in detail in Section S4 of the Supporting Information.

Temperature Dependent UV-vis Absorption

Dilute solutions of P1 and P2 were prepared by dissolving 2 mg of polymer in 4 ml oDCB as a mother solution (0.5 mg/ml), followed by serial dilution in oDCB to obtain a concentration of (0.005 mg/ml). UV-vis absorption spectra of solutions were measured on an Agilent 8453 diode array spectrometer using a solvent blank. The UV-vis spectrometer was equipped with an Agilent 89090A Peltier temperature control accessory to vary the temperature of solutions. UV-vis absorbance spectra of films at room temperature were also measured using an Agilent 8453 spectrometer. See Section S2 of the Supporting Information for details about low temperature absorbance measurements.

Temperature Dependent Photoluminescence Spectroscopy

Photoluminescence spectroscopy was performed on a home-built set up consisting of a 660 nm DPSS laser used for excitation (CrystaLaser DL660-050-O), a set of f/3 achromatic lenses used for luminescence collection, and a fiber coupled (NA = 0.22) compact CCD spectrometer for detection (Ocean Optics USB 2000+). Long pass filters (700 nm cut-on) were used on the detector to block scattered excitation light. The excitation laser was linearly polarized using a broadband polarizer (Meadowlark Optics OWL), and a second polarizer (Meadowlark Optics OWL) was placed before the collection lenses with the polarization angle at 54.7° (magic angle) relative to the laser polarization. The spectrum of a calibrated white light source (Ocean Optics HL-3P-CAL-EXT) was also measured in the exact same set up and used to correct the photoluminescence spectra for the detector response. Samples were mounted in a continuous flow cryostat (Janis Research Co., STVP-100) with LN_2 used as a cryogenic gas and the temperature was controlled using a digital heating controller (Lakeshore Model 332).

Spectroscopic Ellipsometry

Spectroscopic ellipsometry measurements were performed in reflection geometry on P1 and P2 thin films on glass substrates using a J.A. Woollam M-2000 ellipsometer. Scotch tape was used on the back side of the glass substrates to scatter any backside reflections and spectra were measured at 3 angles of incidence (AOI = 55°, 65°, and 75°). Analysis of the ellipsometry data was performed using the CompleteEASE software from J.A. Woollam Co. Details about the analysis of the ellipsometry data can be found in Section S1 of the Supporting Information.

Electroabsorption Spectroscopy

Electroabsorption spectroscopy measurements were performed on a set up described previously in detail.[40] Briefly, a 75W Xenon arc lamp (Newport Oriel PhotoMax) and a monochromator (Princeton Instruments SP2150) were used to create a monochromatic probe CW beam which was "p" polarized relative to the plane of incidence on the EA sample using a broadband polarizer (Meadowlark Optics, OWL). The sample was mounted in the same cryostat used for photoluminescence measurements in a custom sample holder equipped with electrical leads, and was rotated such that the angle χ between the polarization of light and the vector of the applied electric field was 55°.[42] An aperture mask was used on the sample to ensure that light only passed through regions between the transparent electrodes. Details about the sample preparation and device architecture for electroabsorption measurements are discussed in detail in section S4 of the Supporting Information. An AC voltage (1kHz) was applied across the sample using a function generator (Agilent, 33220A) which resulted in a modulation of an electric field across the sample. A Si photodiode (Thorlabs, FDS100) was used to measure the signal from the transmitted monochromatic light through the EA sample. The signal was amplified using a transimpedance preamplifier (SRS SR570) and the second harmonic component of the AC signal was demodulated using a lock-in amplifier (SRS SR830) which was phase referenced to the function generator at the second harmonic of the fundamental modulation frequency. A Keithley 2400 voltmeter was used to measure the DC component of the transmitted light intensity. Normalizing the demodulated AC signal at the second harmonic to the DC signal resulted in the $\Delta T/T$ signal after appropriate scaling to convert to peak amplitude.[40]

Supplementary Information

S1. Ellipsometry on P1 and P2

We used spectroscopic ellipsometry to determine the complex dielectric function ($\varepsilon = \varepsilon_r + i\varepsilon_i$) and complex refractive index (n and k) for P1 and P2 by measuring the elliptical polarization state (represented as ψ and Δ) after polarized light was reflected from P1 and P2 thin films on glass substrates.

Isotropic Models

Modelling of the complex refractive index spectra was done using the CompleteEASE software from J.A. Woollam Co. A model for the glass substrate was constructed using two Tauc-Lorentz oscillators, which was used to simultaneously fit the ψ and Δ data along with the transmittance data of a blank glass substrate. Models for P1 and P2 were constructed using a region of the data where the glass substrate did not absorb (<~2.7 eV) in order to constrain the modelling to a spectral region where the complex refractive index of the substrate was not rapidly changing. First, models were constructed assuming an isotropic complex refractive index for P1 and P2. A preliminary model of ε_r and ε_i for the P1 and P2 data was constructed using an oscillator model consisting of four Gaussian oscillators, which was found to reproduce the general shape of the spectrum and vibronic structure seen in UV-vis absorbance spectra. Furthermore, the modelled thickness of the P1 and P2 layers were constrained to be close to the thicknesses measured from profilometry (~22 nm for P1 and ~46 nm for P2 measured using a Bruker Dektak profilometer). The oscillator models for P1 and P2 were then re-parameterized as Kramers-Kronig consistent B-splines[1] and the thicknesses and spline coefficients were allowed to vary, resulting in the ε_r and ε_i models shown in Figs. 3.3 a. and 3.3 b. of the main text, along with the data shown in Fig. S1.1 below. The final modelled thicknesses for P1 and P2 were found to be 18 nm and 41 nm, respectively.

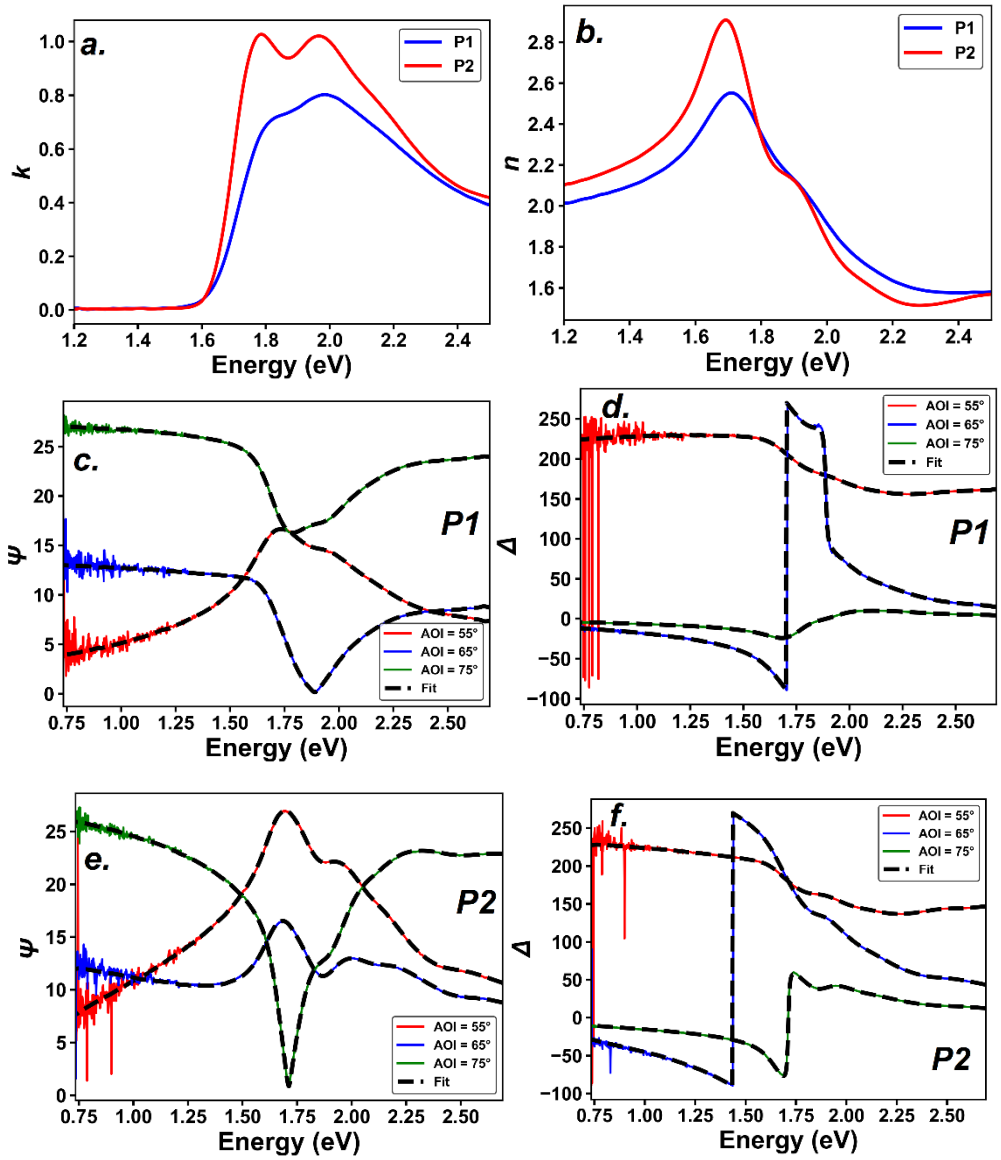

Fig. S1.1 Isotropic Models and Fits *a.) & b.)* *n* and *k* spectra of P1 and P2 with isotropic models described above. ***c.) - f.)*** Corresponding fits to the ψ and Δ data for P1 and P2 for isotropic modelling described above.

Anisotropic Models

We also tested uniaxial anisotropic models[2] for P1 and P2 to evaluate whether or not there would be substantial errors in our analysis due to the assumption of an isotropic complex refractive index. However, we found that anisotropic models did not substantially improve the quality of the fit to the ψ and Δ data, and furthermore resulted in models that appear to be unphysical. In Fig. S1.2 below we show the modelled ε_r and ε_i spectra for P2 using a four Gaussian oscillator model for the complex refractive index parallel to the plane of the film, and another four Gaussian oscillator model for the index perpendicular to the plane of the film. The modelled ε_r and ε_i for the index perpendicular to the plane of the film appear to show an unphysical vibronic line shape pattern, which we take as evidence that a uniaxial anisotropic model is not needed to describe the data and may be resulting in unphysical line shapes due to the introduction of too many free parameters in the model.

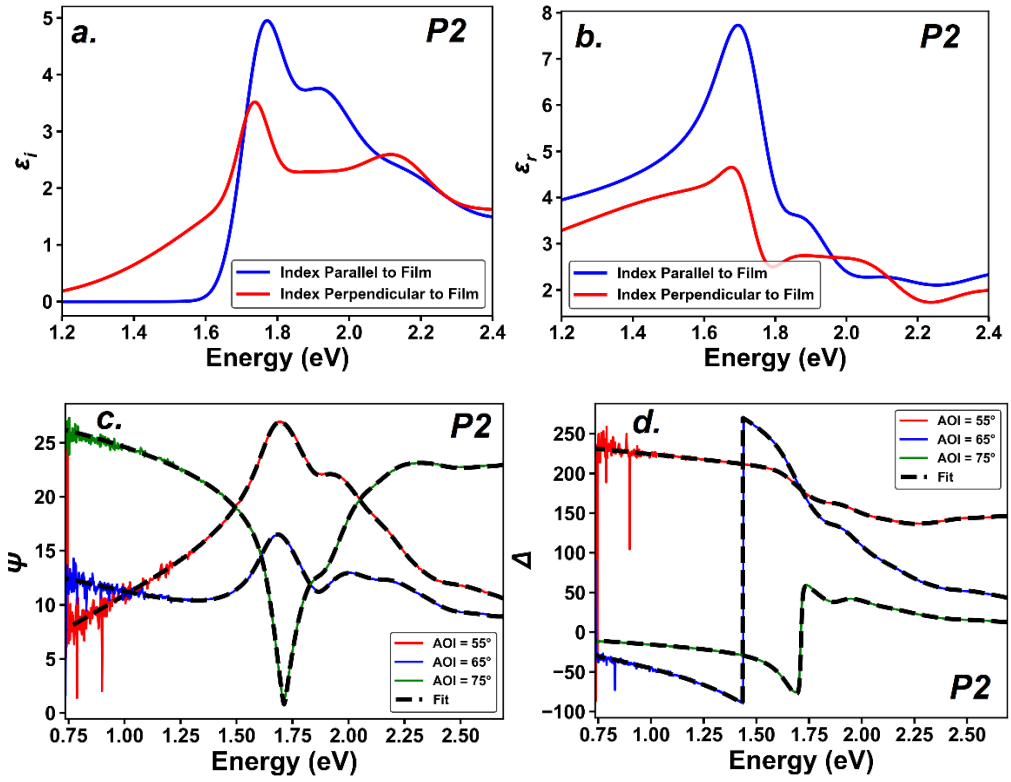

Fig. S1.2 Anisotropic Models and Fits for P2 ***a.) & b.)*** ε_r and ε_i spectra of P2 with uniaxial anisotropic models showing the dielectric functions parallel and perpendicular to the plane of the film. described above. ***c.) & d.)*** Corresponding fits to the ψ and Δ data for P2 using anisotropic modelling described above.

In Fig. .S1.3 below we show the modelled ε_r and ε_i spectra based on a uniaxial anisotropic model for P1 using the "four Gaussian" oscillator models for the complex refractive indices parallel and perpendicular to the plane of the film. Again we find that the quality of the fits to the ψ and Δ data do not improve. The shape of the ε_i spectrum parallel to the plane of the film represents a typical H-aggregate spectrum. The shape of the ε_i spectrum perpendicular to the plane of the film is potentially physically plausible, as its lack of vibronic structure could resemble the spectrum of completely amorphous regions of polymer similar to that seen in regio-regular P3HT.[3] However if this were the case we would expect the spectrum of amorphous polymer to be significantly blue shifted from the aggregate spectrum, which does not appear to be the case when comparing the parallel and perpendicular ε_i spectra. Furthermore, it would be implausible for the more disordered regions of the film to have higher ε_i than the aggregated regions based on the work of Vezie *et al.*[4] which demonstrated the correlation between chain planarity and ε_i. Therefore we stand by the conclusion that the isotropic models of the ε_i spectra used for P1 and P2 represent the more physically plausible results.

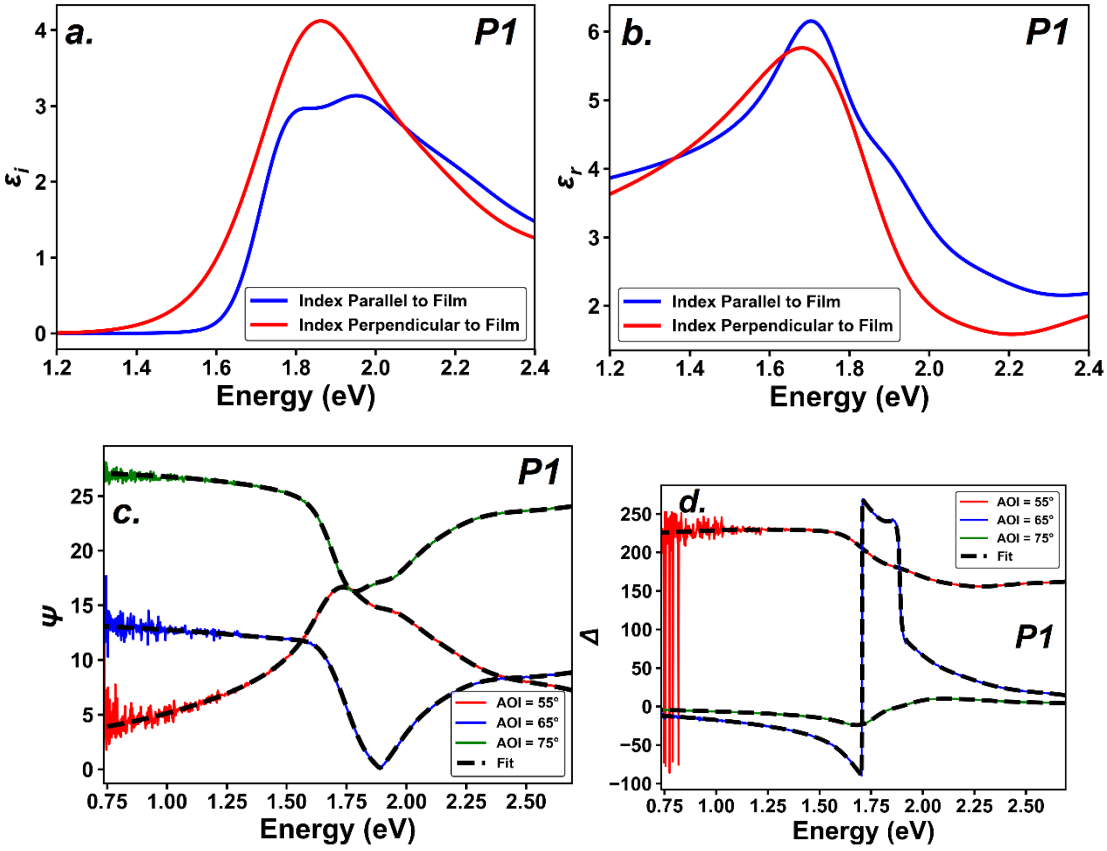

Fig. S1.3 Anisotropic Models and Fits for P1 *a.) & b.)* ε_r and ε_i spectra of P1 with uniaxial anisotropic models showing the dielectric functions parallel and perpendicular to the plane of the film. described above. *c.) & d.)* Corresponding fits to the ψ and Δ data for P1 using anisotropic modelling described above.

S2. Temperature Dependent Absorbance of P2

In the main text (Fig. 3.5 d.) we compared the temperature dependent redshift of the 0-0, 0-1, and A1 absorption peaks in P2 to study the anomalous behavior of the 0-1 redshift. In Fig. S2 below we show the temperature dependent absorption spectrum of P2 normalized to the A1 peak, from which the the data was used to plot the redshift of absorbance in Fig. 3.5 d. of the main text.

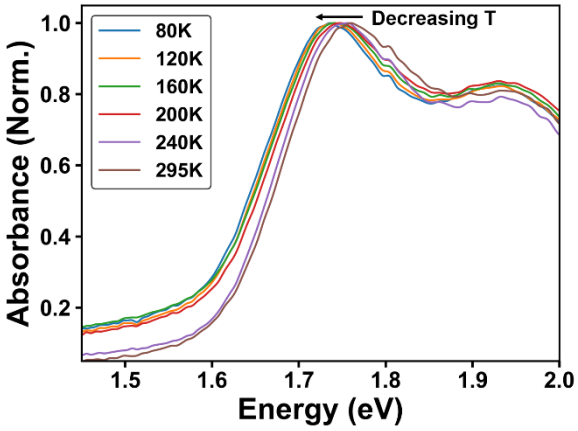

Fig. S2. Temperature dependent absorption spectrum of P2 corresponding to the peak redshift shown in Fig. 3.5 d. of the main text.

Experimental Methods for Low Temperature Absorbance

Low temperature absorbance was measured on a home built dual-beam spectrometer set up. Monochromatic light was created by a 75W Xenon arc lamp (Newport Oriel PhotoMax) and a monochromator (Princeton Instruments SP2150)and was partially split using a reflective glass slide. The split beam was chopped using an optical chopper and focused onto a silicon photodiode used to monitor intensity fluctuations in the lamp (referred to as the “monitor” photodiode). The rest of the beam was chopped with a second optical chopper and focused into a optical fiber which was then collimated and directed onto the sample at normal incidence. The transmitted light was focused onto another silicon photodiode, referred to as the “transmittance” photodiode. The signals from the monitor and transmittance photodiodes were measured simultaneously using two lock-in amplifiers and a custom LabVIEW code controlled the scanning of the monochromator and recording of data to generate a transmitted intensity spectrum. The transmitted intensity spectrum of a glass blank as also measured in order to calculate transmittance and absorbance. Samples were mounted in the same cryostat used for photoluminescence measurements (Janis Research Co., STVP-100) using the same temperature controller (Lakeshore Model 332).

S3. Quadratic Field Scaling of the Electroabsorption Signal in P1 and P2

In Figs. S3a and S3b below we show the scaling of the lowest energy EA peak with applied voltage (referred to as "Peak 1"), representing the peak at ~1.66 eV in P1 and peak at ~1.64 eV in P2, (see Fig. 3.5 a. and 3.5 b. in the main text). The logarithm of the amplitude of the EA signal versus the logarithm of the voltage is plotted on a linear scale and fit to a straight line to determine the order of the scaling with field. The scaling of P1 and P2 with voltage are both approximately quadratic, with P1 scaling as $F^{1.91}$ and P2 scaling as $F^{1.85}$. The small deviation from purely quadratic scaling could represent some contribution from linear Stark effects as opposed to purely quadratic Stark effects if there is some small degree of anisotropy of permanent dipole moments in the polymer films. However this effect is likely small given that the ellipsometry appears to indicate that the films are largely isotropic, and the scaling of peaks appears to be close to quadratic.

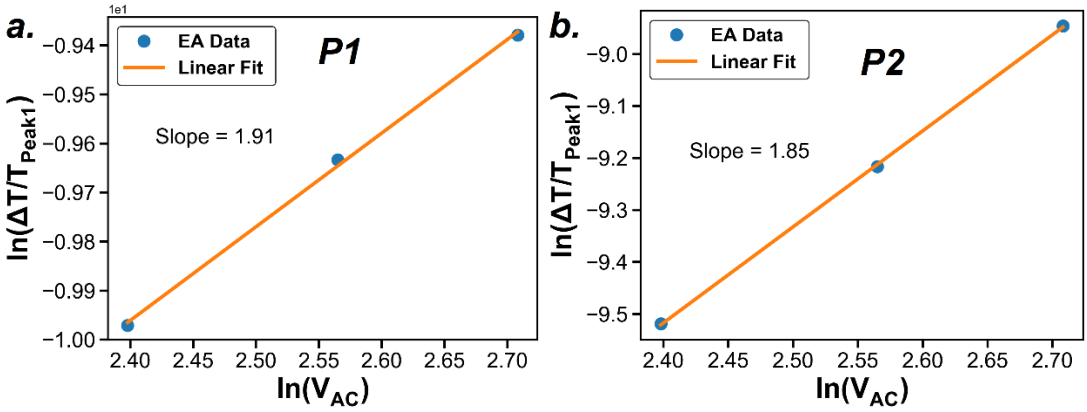

Fig. S3 ***a.)*** **&** ***b.)*** Log-log scaling of "Peak 1" in the EA spectrum for P1 and P2 with applied voltage (see description above for definition of "Peak 1")

S4 Device Structure for Electroabsorption Spectroscopy

Device Fabrication

Devices for electroabsorption spectroscopy were fabricated using a "dielectric capacitor" structure reported previously,[5] which sandwiches the electro-optical layer (P1 or P2) in between transparent thin film insulators and semitransparent contacts. This device structure allows for measurements to be performed in a transmittance geometry and also blocks the injection of charge from the electrodes, ensuring that the modulation signal is only due to field induced changes in the optical properties of the P1 or P2 layer. To construct the device, substrates were prepared by spin coating 58 nm layer of a transparent insulation polymer Cytop onto cleaned ITO/glass substrates. A second insulating layer of SiO_2 (100nm) was then deposited on top of the Cytop using e-beam evaporation. P1 and P2 solutions were spin coated onto these substrates following the Experimental Methods in the main text. After spin coating P1 and P2 films, another layer of 100 nm SiO_2 was e-beam evaporated on top and another layer of Cytop was spin coated (58nm). Finally, a semitransparent aluminum top contact (25 nm) was thermally evaporated. Figure S4 below shows the device architecture for the EA device.

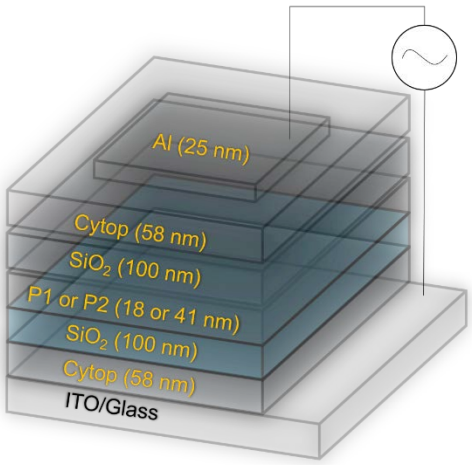

Fig. S4 Device architecture for samples used for electroabsorption spectroscopy

S5 Modelling of the Electroabsorption Spectra and Calculation of Parameters

To model the ΔT/T electroabsorption response, transfer matrix modelling was used following our previous work.[5] In order to model the EA spectrum with transfer matrix modelling, the complex refractive indices of all layers in the stack must be known (see Section S1 for P1 and P2 *n* and *k*), and also the change in the optical constants in the electro-optical layer as a function of field need to be know. In this work we used the Liptay equation to determine Δ*k* and Δ*n* based on the derivatives of the unperturbed *k* spectra. Below we discuss some aspects of the Liptay model and extraction of parameter values for $\Delta\alpha_{g\rightarrow e}$.

Coefficients of the Liptay Equation

The values for the change in dipole moment $\Delta\mu_{g\rightarrow e}$ and change in polarizability $\Delta\alpha_{g\rightarrow e}$ are given by the coefficients B_χ and C_χ. Here χ is the angle between the polarization vector of light and the applied electric field in the EA experiment, and the expressions for B_χ and C_χ are greatly simplified when χ is set to the magic angle (55°):[6]

$$B_{55^\circ} \cong \frac{15}{2} * \left((1/3) * \Delta\alpha_{g\rightarrow e}\right)$$

$$C_{55^\circ} \cong 5 * \left|\Delta\mu_{g\rightarrow e}\right|^2$$

These coefficients are found by fitting the electroabsorption spectrum to Eq. 1 in the main text using transfer matrix modelling (after Δ*n* has also been found, see below). The method for modelling the EA spectrum with transfer matrix modelling has been reported in detail in our previous work.[5] We note that we take into account the angle of incidence (55°) and "p" polarization of incident light as mentioned in the main text when using the transfer matrix algorithm.

Derivation of the Liptay Formula in Terms of Δk and Δn

The Liptay formula is typically written in the literature in terms of a change in absorption as a function of frequency, given by Eq. S4.1 below:[6]

$$\Delta A(\tilde{\nu}) = F^2\left\{A_\chi A(\tilde{\nu}) + \frac{B_\chi}{15hc}\tilde{\nu}\frac{d}{d\tilde{\nu}}\left(\frac{A(\tilde{\nu})}{\tilde{\nu}}\right) + \frac{C_\chi}{30h^2c^2}\tilde{\nu}\frac{d^2}{d\tilde{\nu}^2}\left(\frac{A(\tilde{\nu})}{\tilde{\nu}}\right)\right\} \qquad Eq.S4.1$$

To convert model the EA spectrum with transfer matrix modelling we need to convert the Liptay formula in terms of Δ*k and* Δ*n.* We start by noting that:

$$A = \frac{k*4\pi\ell}{\lambda} \qquad Eq.S4.2$$

$$\Delta k = \frac{\Delta A\lambda}{\ell 4\pi} \qquad Eq.S4.3$$

$$where\ \ell = thickness\ of\ film$$

We can substitute Eqs. S4.2 and S4.3 into Eq. S4.1 and arrive at:

$$\Delta k(\tilde{\nu}) = F^2\left\{A_\chi k(\tilde{\nu}) + \frac{B_\chi}{15hc}\frac{dk}{d\tilde{\nu}} + \frac{C_\chi}{30h^2c^2}\frac{d^2k}{d\tilde{\nu}^2}\right\} \qquad Eq.S4.4$$

To covert from frequency $\tilde{\nu}$ to energy (E), we note that:

$$E = hc\tilde{\nu} \qquad Eq.S4.5$$

$$\frac{d}{d\tilde{\nu}} = \frac{d}{dE}\frac{dE}{d\tilde{\nu}} = \frac{d}{dE}hc \qquad Eq.S4.6$$

$$\frac{d^2}{d\tilde{\nu}^2} = \frac{d}{d\tilde{\nu}}\frac{d}{d\tilde{\nu}} = \frac{d}{dE}hc * \frac{d}{dE}hc = \frac{d^2}{dE^2}h^2c^2 \qquad Eq.S4.7$$

Finally, substituting Eqs. S4.5-4.7 into Eq. S4.4, we arrive at the Liptay formula in terms of Δk:

$$\Delta k = F^2\left\{A_\chi k + \frac{B_\chi}{15}\frac{dk}{dE} + \frac{C_\chi}{30}\frac{d^2k}{dE^2}\right\} \qquad Eq.S4.8$$

To model the electroabsorption spectrum with transfer matrix modelling we also need a formula for Δn, which we obtain simply by taking the Kramers-Kronig transform of $Eq.S4.9$:

$$\Delta n(\omega) = \frac{1}{\pi}\int_{-\infty}^{\infty}\frac{\Delta k(\omega')}{\omega' - \omega}d\omega' \quad Eq.S4.9$$

Calculation of Field Across P1 and P2 Layers

To calculate the field across the P1 or P2 layers we modeled the EA stack as 5 capacitors in series and used the applied voltage and known thicknesses (given by "t" in Eq. S4.10 below) and dielectric constants of layers in the stack (see section S4 above for a diagram of the device stack).

$$F_{P1/P2} = \frac{V_{AC}}{\epsilon_{P1/P2}\left(\frac{t_{SiO_2}}{\epsilon_{SiO_2}} + \frac{t_{Cytop}}{\epsilon_{Cytop}} + \frac{t_{P1/P2}}{\epsilon_{P1/P2}} + \frac{t_{Cytop}}{\epsilon_{Cytop}} + \frac{t_{SiO_2}}{\epsilon_{SiO_2}}\right)} \qquad Eq.S4.10$$

For the P1 and P2 layers we assumed that the dielectric constant was 4, which is the value used in previous works for PTB7-Th.[7] However we were concerned that the dielectric constants of P1 and P2 could be different from one another, which could affect the fields calculated and resulting values obtained for $\Delta\alpha_{g\rightarrow e}$. So in order to evaluate whether or not there is a significant difference in dielectric constants between P1 and P2 we used electrochemical impedance spectroscopy (EIS). We applied a series of frequencies with ranging from 1 MHz to 1 Hz with a root mean squared amplitude of 10 mV. Recording the impedance of the device as a function of

frequency allowed us to accurately measure the capacitance of this system. We approximated the device under test as a parallel plate capacitor and used this assumption to fit the resultant impedance response to extract the capacitance. The results of this fit showed a capacitance of 1.75 nF for P1, while the capacitance of P2 was 1.6 nF. Using this information, we were able to extract the relative permittivity according to the following equation:

$$\varepsilon_r = \frac{C_{measured}}{C_0}$$

where $C_{measured}$ is the experimental measurement of capacitance and C_0 is the geometric capacitance of the device, replacing the dielectric with a vacuum. We calculate dC_0 using the known geometry of the device and using a parallel plate assumption.

$$C_0 = \frac{\varepsilon_0 A}{d}$$

Here, A is the area of the parallel plate which in this experiment is ~15 mm^2 while d is the plate separation. The plate separation for the P1 device is 334 nm while P2 is 357 nm. Using all these values we calculated the effective dielectric constant for P1 to be 4.4 while P2 had an effective dielectric constant of 4.3. As the only difference between the two devices is the identity of the material of interest, we concluded that the dielectric constants vary only very slightly.

Supplementary References

1. Johs, B.; Hale, J. S., Dielectric function representation by B-splines. *Phys. Status Solidi A* **2008,** *205* (4), 715-719.
2. Losurdo, M.; Bruno, G.; Irene, E. A., Anisotropy of optical properties of conjugated polymer thin films by spectroscopic ellipsometry. *Journal of Applied Physics* **2003,** *94* (8), 4923.
3. Clark, J.; Silva, C.; Friend, R. H.; Spano, F. C., Role of intermolecular coupling in the photophysics of disordered organic semiconductors: aggregate emission in regioregular polythiophene. *Phys Rev Lett* **2007,** *98* (20), 206406.
4. Vezie, M. S.; Few, S.; Meager, I.; Pieridou, G.; Dorling, B.; Ashraf, R. S.; Goni, A. R.; Bronstein, H.; McCulloch, I.; Hayes, S. C.; Campoy-Quiles, M.; Nelson, J., Exploring the origin of high optical absorption in conjugated polymers. *Nat Mater* **2016,** *15* (7), 746-53.
5. Ziffer, M. E.; Mohammed, J. C.; Ginger, D. S., Electroabsorption Spectroscopy Measurements of the Exciton Binding Energy, Electron–Hole Reduced Effective Mass, and Band Gap in the Perovskite $CH_3NH_3PbI_3$. *ACS Photonics* **2016,** *3* (6), 1060-1068.
6. Bublitz, G. U.; Boxer, S. G., Stark spectroscopy: applications in chemistry, biology, and materials science. *Annu. Rev. Phys. Chem.* **1997,** *48*, 213-42.
7. Pearson, A. J.; Hopkinson, P. E.; Couderc, E.; Domanski, K.; Abdi-Jalebi, M.; Greenham, N. C., Critical light instability in CB/DIO processed PBDTTT-EFT:PC 71 BM organic photovoltaic devices. *Organic Electronics* **2016,** *30*, 225-236.

Appendix C: Supporting Information for Chapter 4

Experimental Methods

Device and Sample Fabrication

Devices were fabricated using patterned ITO/glass substrates (Thin Film Devices, Inc. 15 Ω sq-1), while samples for spectroscopy were prepared on glass microscope slides, which were cleaned by sonication consecutively in detergent solution, DI-water, acetone, and isopropanol, followed by UV-O_3 treatment (Jelight 144AX). For devices, a zinc acetate dihydrate (1g) solution dissolved in 2-methoxy ethanol (10mL) and ethanolamine (280μL) was spin-coated on the cleaned substrates at 4000 rpm and sintered at 210 °C for 1 hour in air resulting in a 30nm thick ZnO film. The polymer:acceptor solutions were prepared by dissolving a 1:1 wt% ratio of PCE10 (1-Material, Inc.) and FIDTT-2PDI to a total concentration of 20mg/mL in anhydrous 1,2-dichlorobenzene with 3% by volume 1-chloronapthalene. Neat polymer solutions were prepared by dissolving 10mg/mL PCE10 in anhydrous 1,2-dichlorobenzene. Neat acceptor solutions were prepared by dissolving 10mg/mL FIDTT-2PDI in anhydrous chloroform. Solutions in 1,2-dichlorobenzene were blended at 90-100°C for 12 hours inside of a N_2 glovebox, while solutions in chloroform were stirred for several hours inside the glovebox. Polymer:acceptor blend and neat films were prepared inside of a N_2 glovebox by spincoating the solutions at 1600-1800 rpm for 2 mins on the ZnO/ITO/glass substrates for devices and on glass substrates for spectroscopy. For devices, 6 nm of MoO_X and 120nm of Ag were thermally evaporated (<1e-6 torr, Angstrom Engineering EvoVAC) through a patterned shadow mask to define the electrode pattern. The electrode area for devices defined by the overlap between the MoOx/Ag and ITO electrodes was approximately 0.06 cm^2. For spectroscopy, the films on glass were encapsulated inside of a N_2 glovebox using epoxy to seal a glass-to-glass bond between the perimeter of the sample substrate and a glass cover slide.

Photovoltaic Performance, Quantum Efficiency, and Optical Absorption Spectroscopy

Photovoltaic performance was evaluated by measuring the current-voltage characteristics (Keithley 2400) of the PCE10:FIDTT-2PDI solar cell under simulated AM1.5G illumination using a Class A solar simulator (Solar Light Co. 16S-300) inside of a N_2 glovebox. A calibrated reference silicon photodiode was used to calibrate the incident light intensity. Photovoltaic external quantum efficiency (EQE_{PV}) was measured using a custom built split-beam spectrometer with the device held under dynamic vacuum (<50 mTorr) inside a custom-built vacuum chamber with fused silica windows for optical spectroscopy. Light from a tungsten-halogen lamp (Horiba Scientific PowerArc) was spectrally filtered using a monochromator equipped with an order-sorting filter (Princeton Instruments SP-2150) and chopped at a frequency of 220Hz (Stanford Research Systems SR540). Long pass filters with cut-on wavelengths at 750, 800, and 850 nm were additionally used to filter any scattered light from the monochromator. The light was split using a fused silica optic so that a small fraction of the beam was focused onto a Si photodiode used to monitor intensity fluctuations from the incident light, while the remainder of the light focused onto a pixel of the device through a small area aperture mask. The photocurrent signal from the device was amplified with a transimpedance amplifier (Stanford Research Systems SR570) with no input bias, and the signal was demodulated by a lock-in amplifier (Stanford Research Systems SR830).

The photocurrent from a calibrated Si photodiode (OSI Optoelectronics) was then measured at the sample position through the same aperture mask to measure the incident power and calculate EQE_{PV}. Differences in lamp intensity between the two measurements were corrected using the signal recorded by the photodiode receiving the split-beam intensity. To calculate the internal quantum efficiency (IQE_{PV}) spectra, the complex refractive index spectra (*n* and *k*) of all layers in the device were determined using spectroscopic ellipsometry (J.A. Woollam Co. M-2000, see SI section S3 for details) and the fraction of absorbed light in the active layer was calculated using transfer-matrix modelling. UV-vis absorbance spectra were measured on encapsulated samples using a diode array UV-vis spectrometer (Agilent 8453). A sample consisting of two pieces of glass epoxied together around the perimeter was used as a blank for UV-vis absorbance.

Electroluminescence and Steady State Photoluminescence Spectroscopy

Electroluminescence spectra were measured driving the device with a DC voltage (Keithley 2400) while held under dynamic vacuum (<50 mTorr) inside a custom-built vacuum chamber with fused silica windows for optical spectroscopy. The device was aligned to the focal point of a custom-built spectrometer based on a f/3.9 spectrograph (Princeton Instruments SP-2300, slit width = 200 μm) and a f/4 lens system to collect the luminescence. The spectra were recorded with a LN_2 cooled CCD detector (Princeton Instruments Spec-10) and were corrected for the spectral response of the system using a calibrated white light source (Ocean Optics HL-3P-CAL-EXT). Electroluminescence quantum efficiency (EQE_{EL}) was measured inside of a N_2 glovebox using a custom built set-up consisting of a large area calibrated Si photodiode (Hamamatsu S3204-08), and two source-meters (Keithley 2400 and Keithley 237) used to simultaneously drive the device and measure photocurrent due to the photon flux indecent on the Si photodiode. Following standard procedures for OLED measurements,[86] the device was placed nearly flat on the photodiode with waveguided emission effectively blocked by the sample holder, while the small device area (~0.06cm^2) relative to the detector area (~1cm^2) ensured that the measurement was close to the condition of underfilling the detector. Steady-state photoluminescence spectroscopy was measured using a custom built set up consisting of a set of f/3 achromatic lenses used to collect and focus sample luminescence into a fiber optic cable (NA = 0.22) coupled to a compact CCD spectrometer (Ocean Optics, USB 2000+). The sample was excited with either a focused 730 nm diode laser (Thorlabs HL7302MG) or a collimated 532 nm DPSS laser (CrystaLaser). The excitation power was measured with a calibrated Si photodiode (OSI Optoelectronics) and the excitation area was measured with a beam profiler (Thorlabs BP209-VIS) to calculate the incident intensity. Photoluminescence quantum efficiency (PLQE) of neat FIDTT-2PDI and PCE10 thin films on glass was measured inside of a N_2 glovebox using a modified set up based around a Hamamatsu C9920-02 integrating sphere system. Briefly, a 532 nm DPSS laser (CrystaLaser) was fiber coupled into the integrating sphere, and the laser intensity as well as sample luminescence were simultaneously measured using a CCD spectrometer (Hamamatsu C10027) that was fiber coupled to the output port of the integrating sphere. Three measurements (sample in laser path, sample out of laser path, and sample removed from sphere) were made and the PLQE was calculated using the method of de Mello and coworkers.[87]

Time-Resolved Photoluminescence Spectroscopy

Time-resolved photoluminescence spectra were measured using a streak camera with excitation from an ultrafast tunable laser source. In brief, the fundamental output of a Ti:sapphire amplifier (Coherent, Inc. Libra-HE, 4.0 mJ, 1 kHz, 50 fs) was used to pump an optical parametric amplifier (Coherent, Inc./Light Conversion OPerA Solo) which was used to tune the laser excitation wavelength to 735 nm. Appropriate long-pass and band-pass filters were used after the OPA to ensure a clean laser spectrum, and the beam profile was measured prior to each experiment to quantify the excitation area (Thorlabs BC106N-UV). Luminescence from the sample was collected using a set of f/4 lenses which focused the light into a f/3.9 spectrograph (Princeton Instruments SP-2150, entrance slit width = 200 µm) coupled to a streak camera (Hammamatsu C10910, slow-sweep unit M10913-01). The streak camera was operated in photon-counting mode using maximum gain, and signal levels <5% above the photon counting threshold were maintained using neutral density filters in front of the detector in order to ensure single photon counting statistics. The time-resolved PL spectra were corrected for the spectral response of the system by measuring the spectrum of a calibrated white light source (Ocean Optics HL-3P-CAL-EXT) on the streak camera operated in focus mode. Appropriate subtraction of dark spectra were accounted for when correcting the white light and time-resolved PL spectra. All spectra were additionally corrected for the transmittance of a long-pass (800 nm) filter and any neutral density filters used on the detector. The IRF of the streak camera was measured using a ground glass slide to scatter part of the laser excitation into the detector with the signal attenuated by non-fluorescing neutral density filters.

Transient Absorption Spectroscopy

Transient absorption spectra were measured using a Helios/EOS spectrometer (Ultrafast Systems) built around the same laser amplifier used for time-resolved photoluminescence. In brief, the fundamental output of the Ti:sapphire amplifier (Coherent, Inc. Libra-HE, 4.0 mJ, 1 kHz, 50 fs) was split into two beamlines by an 80/20 beam-splitter. Part of the fundamental beam was used to pump an optical parametric amplifier (Coherent, Inc./Light Conversion OPerA Solo) which was used to tune the pump laser wavelength to 735 nm. For femtosecond transient absorption spectra, the other part of the fundamental beam was used to generate a white continuum probe using CaF_2 or sapphire plates. The delay between pump and probe pulses was controlled using a mechanical delay stage. For nanosecond transient absorption spectra, the white light continuum probe was generated using a supercontinuum pulsed light source which is electronically delayed relative to the pump. The ΔOD spectra were collected using fiber-coupled silicon CMOS and InGaAs array detectors while chopping the pump light at 500 Hz (for ultrafast measurements) or electronically modulating the probe at 2 kHz (for nanosecond measurements) to alternate collection of “pump-on” vs “pump-off” spectra. Appropriate long-pass and band-pass filters were used to ensure a clean pump laser spectrum and the beam area was quantified using a beam profiler (Thorlabs BC106N-UV). The spectra were processed by subtracting an average of 20 background noise spectra before time zero, performing chirp-correction and then correcting time zero. Global analysis was conducted for identifying initial overlapping spectral features and kinetics, by decomposing principle spectra and kinetics by Surface Xplorer software (Ultrafast Systems) using the corrected spectra in narrow wavelength range covering desired signals.

Morphological Characterization

Grazing-incidence wide-angle X-ray scattering (GIWAXS)[88] was used to investigate the molecular packing and crystalline properties. 2D GIWAXS data were acquired at beamline 7.3.3 at the Advanced Light Source, LBNL. Data were acquired just above the critical angle (~0.13^{o}) of the films with a hard X-ray energy of 10 keV. Ag Behenate (AgB) was used for geometry calibration. R-SoXS[89] measurements were performed at the beamline 11.0.1.2, Advanced Light Source (ALS), Lawrence Berkeley National Laboratory, following the previously established protocols. R-SoXS was performed in a transmission geometry with linearly polarized photons under high vacuum (1×10^{-7} torr) and a cooled (-45 °C) CCD (Princeton PI-MTE, 2048 pixels×2048 pixels) was used to capture the soft X-ray scattering 2D maps and PS300 was used for geometry calibration. The raw 2D X-ray data were processed with a modified version of NIKA into 1D scattering profiles I(q).

Supplementary Information

S1. Determination of the Photovoltaic Band Gap (E_g^{PV}) of PCE10: FIDTT-2PDI

We use the method of Rau and Kirchartz[1] to determine E_g^{PV} of PCE10: FIDTT-2PDI, which interprets the first derivative of the EQE_{PV} spectrum as a probability distribution function $P(E_g)$ for Shockley-Queisser band gaps (E_g) and uses the mean value of that distribution to define a photovoltaic bandgap (E_g^{PV}) according to Eq. S1. This method has been used to determine the photovoltaic band gap in both inorganic and organic solar cells.[1]

$$E_g^{\mathrm{PV}} = \int_a^b E_g P(E_g) dE_g \Big/ \int_a^b P(E_g) dE_g \quad \text{where } a \,\&\, b \text{ are the FWHM limits of } P(E_g) \qquad Eq\ S1$$

In Fig. S1 we show the EQE_{PV} spectrum and $P(E_g)$ for PCE10:FIDTT-2PDI determined from the first derivative of EQE_{PV}. Using Eq S1 we determine E_g^{PV} to be 1.655 eV for PCE10:FIDTT-2PDI.

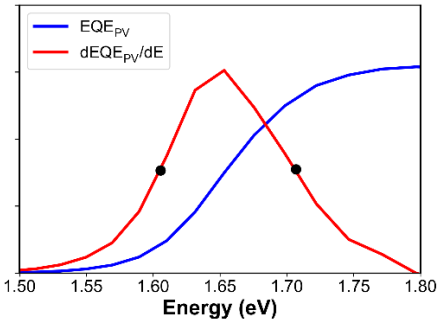

Fig. S1. Spectrum of EQE_{PV} and $d\mathrm{EQE_{PV}}/d\mathrm{E}$ for PCE10:FIDTT-2PDI, where $d\mathrm{EQE_{PV}}/d\mathrm{E}$ determines the probability distribution function for E_g according to the method of Rau and Krichartz.[1] The black dots represent the FWHM limits for the integral in Eq S1, which were determined by spline fits to $d\mathrm{EQE_{PV}}/d\mathrm{E}$.

S2. Quantitative Analysis of the V_{OC} Loss in PCE10:FIDTT-2PDI

Following the work of Rau and Kirchartz,[1] the V_{OC} of a solar cell can be described in several terms related to losses below the ideal V_{OC} calculated based on the Shockley-Queisser limit. Ultimately, the V_{OC} of a solar cell follows a simple formula (Eq S2.1) which depends on the short-circuit current under AM1.5 solar illumination (J_{SC}) and the dark saturation current (J_0) of the solar cell:

$$V_{OC} = \frac{kT}{q} \ln\left(\frac{J_{sc}}{J_0}\right) \qquad Eq\ S2.1$$

The V_{OC} in Eq S2.1 can also be equivalently written in terms of non-ideal deviations from ideal values for the short-circuit current and dark saturation current calculated based on the Shockley-Queisser limit[2] (J_{SC}^{SQ} and J_0^{SQ}, respectively) according to Eq S2.2:

$$V_{OC} = \frac{kT}{q}\ln\left(\frac{J_{SC}^{SQ}}{J_0^{SQ}} * \frac{J_{sc}}{J_{SC}^{SQ}} * \frac{J_0^{SQ}}{J_0^{rad}} * \frac{J_0^{rad}}{J_0}\right) \quad Eq\ S2.2$$

Here J_0^{rad} is the dark saturation current in the non-ideal radiative limit (defined in the main text in Eq 2) which takes into account that unlike in the Shockley-Queisser limit, the EQE_{PV} onset can have a non-step like shape below the photovoltaic band gap, which results in excess radiative contributions to the dark saturation current based on the principles of detailed balance (to be discussed below in more detail). Eq S2.2 can also of course be written equivalently as Eq S2.3, and the V_{OC} can be broken up into corresponding terms (Eq S2.4):[1]

$$V_{OC} = \frac{kT}{q}\ln\left(\frac{J_{SC}^{SQ}}{J_0^{SQ}}\right) + \frac{kT}{q}\ln\left(\frac{J_{sc}}{J_{SC}^{SQ}}\right) + \frac{kT}{q}\ln\left(\frac{J_0^{SQ}}{J_0^{rad}}\right) + \frac{kT}{q}\ln\left(\frac{J_0^{rad}}{J_0}\right) \quad Eq\ S2.3$$

$$V_{OC} = V_{OC}^{SQ} + \Delta V_{OC}^{SC} + \Delta V_{OC}^{rad} + \Delta V_{OC}^{nonrad} \quad Eq\ S2.4$$

The first term in Eqs S2.3 and S2.4 is the V_{OC} derived from the Shockley-Queisser limit which depends only on the bandgap (E_g^{PV}) of the solar cell and the temperature.[2] For PCE10:FIDTT2-PDI with E_g^{PV}=1.655 eV (see Section S1), the Shockley-Queisser V_{OC}=1.381 V at 295 K.

The second term in Eqs S2.3 and S2.4 (ΔV_{OC}^{SC}) is the loss due to less-than ideal above bandgap J_{SC}, which represents the V_{OC} loss due to an EQE_{PV} spectrum that is less than 100% above E_g^{PV}, a deviation from one of the assumptions in the Shockley-Quiesser limit. The short-circuit current in the Shockley Quiesser limit (J_{SC}^{SQ}) and the short circuit current of the device (J_{sc}) can be evaluated according to Eq S2.5, where $\emptyset_{AM1.5}(E)$ is the AM1.5 solar spectrum in units of photon flux per energy interval:

$$J_{SC} = q\int_{E_g^{PV}}^{\infty} EQE_{PV}(E)\emptyset_{AM1.5}(E)\,dE \quad Eq\ S2.5$$

To evaluate Eq S2.5 for J_{SC}^{SQ}, a Heaviside step function with an onset at E_g^{PV} is used to represent the EQE_{PV} spectrum in the Shockley-Quiesser limit (Fig. S2), while the experimentally measured EQE_{PV} spectrum for PCE10:FIDTT-2PDI (Fig. 4.2 a. in the main text) is used to calculate J_{sc}. The voltage loss corresponding to ΔV_{OC}^{SC} is found to be low (~13 mV), which is reasonable considering that the EQE_{PV} in PCE10:FIDTT-2PDI is reasonably high.

The third term in Eqs S2.3 and S2.4, ΔV_{OC}^{rad}, is the V_{OC} loss associated with a non-ideal radiative dark saturation current (J_0^{rad}), which is due to the energy loss associated with excess emission of thermal radiation from the solar cell in the dark (compared to that already considered in the Shockley-Quiesser limit). This excess loss is due to a broadened EQE_{PV} edge that extends further into the range of the blackbody emission spectrum at room temperature than the Shockley-Quiesser EQE_{PV}, which causes excess absorption of thermal radiation by the solar cell in the dark at low photon energies where the blackbody radiation spectrum increases in intensity. According to Kirchoff's radiation laws[3] the absorption of thermal radiation by a grey body in thermal

equilibrium with the ambient will also result in equivalent emission of radiation, which Rau[4] showed will manifest itself as a radiative equilibrium emission current in the solar cell (J_0^{rad}) that will ultimately increase the radiative dark saturation current (J_0) compared to that calculated from the Shockley Quiesser limit (J_0^{SQ}).[4] The non-ideal radiative dark saturation current (J_0^{rad}) can be evaluated using Eq S2.6, where $\emptyset_{BB}$(E) is the blackbody radiation spectrum given by Eq S2.7:

$$J_0^{rad} = q\int_0^{\infty} EQE_{PV}(E)\emptyset_{BB}(E)\,dE \qquad Eq\ S2.6$$

$$\emptyset_{BB}(E) = \frac{2\pi E^2}{h^3c^2} * \frac{1}{\exp\left(\frac{E}{kT}\right) - 1} \qquad Eq\ S2.7$$

To evaluate J_0^{rad}, it is necessary to know the EQE_{PV} spectrum down to energies where the blackbody radiation spectrum is appreciable at 295K. In order to do this, one can use the photovoltaic reciprocity relations described by Rau[4] where the electroluminescence spectrum is used to recreate and extend the EQE_{PV} spectrum by several orders of magnitude down to lower photon energies.[5] To explain this briefly, we can note that in Eq S2.6, J_0^{rad} is the integral of a spectral quantity $EQE_{PV}(E)\emptyset_{BB}(E)$, which defines the radiative equilibrium emission current as a function of energy ($J_{em,0}(E)$):

$$J_{em,0}(E) = qEQE_{PV}(E)\emptyset_{BB}(E) \qquad Eq\ S2.8$$

We can then define the electroluminescence spectrum ($\emptyset_{EL}(E)$) as the spectral photon flux resulting from the excess radiative current density as a function of voltage using the ideal diode law:[4]

$$\emptyset_{EL}(E) = \frac{J_{em,0}(E)}{q}\left(\exp\left(\frac{qV}{kT}\right) - 1\right) \qquad Eq\ S2.9$$

Combining Eqs S2.8 and S2.9 we find the relationship between the electroluminescence flux and the EQE_{PV} spectrum:

$$\emptyset_{EL}(E) = EQE_{PV}(E)\emptyset_{BB}(E)\left(\exp\left(\frac{qV}{kT}\right) - 1\right) \qquad Eq\ S2.10$$

From Eq S2.10 it is clear that $EQE_{PV}(E) \propto \frac{\emptyset_{EL}(E)}{\emptyset_{BB}(E)}$. Therefore, by simply dividing the electroluminescence spectrum by the blackbody radiation spectrum at 295K, we can recreate the shape of the low energy EQE_{PV} spectrum.[5] In practice, we divided a normalized electroluminescence spectrum by $\emptyset_{BB}(E)$ to get the shape of EQE_{PV}, and then scaled the resulting spectrum to match the tail of the EQE_{PV} spectrum measured with sensitive photocurrent spectroscopy in a region where the two overlap, resulting Fig. 4.2 c. of the main text. We then join the two spectra by interpolation in a region where the two overlap, resulting in the spectrum shown as the red trace in Fig. S2 below. To calculate J_0^{rad} for PCE10:FIDTT-2PDI we used this spectrum with Eq S2.6, while to calculate J_0^{SQ} we used the Heaviside step function (shown as the blue trace in Fig. S2) in Eq S2.6. Using Eqs S2.3 and S2.4 we found that ΔV_{OC}^{rad}=68 mV.

In the above analysis, we assumed the so-called "radiative limit," where the only dark saturation current that is considered is the radiative equilibrium current needed to satisfy Kirchoff's radiation laws. In a real device, there must also a contribution to the dark saturation current (J_0) that is due to non-radiative recombination as well, if we consider that there is a component of the injection current that recombines non-radiatively and follows the voltage dependence of the ideal diode law.[4] Therefore, the dark saturation current considering non-radiative recombination is a sum of radiative (J_0^{rad}) and non-radiative (J_0^{nonrad}) components:

$$J_0 = J_0^{rad} + J_0^{nonrad} \qquad Eq\ S2.11$$

Noting that the electroluminescence external quantum efficiency (EQE_{EL}) is simply equal to the fraction of recombination current which is radiative $\left(\frac{J_0^{rad}}{J_0^{rad}+J_0^{nonrad}}\right)$, we see that the fourth term in Eqs S2.3 and S2.4 (ΔV_{OC}^{nonrad}) is simply equal to $\frac{kT}{q}\ln(EQE_{EL})$. Based on the value that we measured for EQE_{EL} at 1 sun equivalent current injection (~1x10^{-5}), we find that ΔV_{OC}^{nonrad}=292 mV.

In Table S2 below we summarize the results of the calculations and find the total calculated V_{OC} to be ~1.01 V. This value is in close agreement to the measured V_{OC} of 1.06 V.

V_{OC}^{SQ} (V)	ΔV_{OC}^{SC} (V)	ΔV_{OC}^{rad} (V)	ΔV_{OC}^{nonrad} (V)	V_{oc} (V)
1.381	-0.013	-0.068	-0.292	1.008 *(calc.)*
--	--	--	--	1.06 *(measured)*

Table S2. Calculated voltage loss for PCE10:FIDTT-2PDI relative to the Shockley-Quiesser limit due to the different loss terms described above.

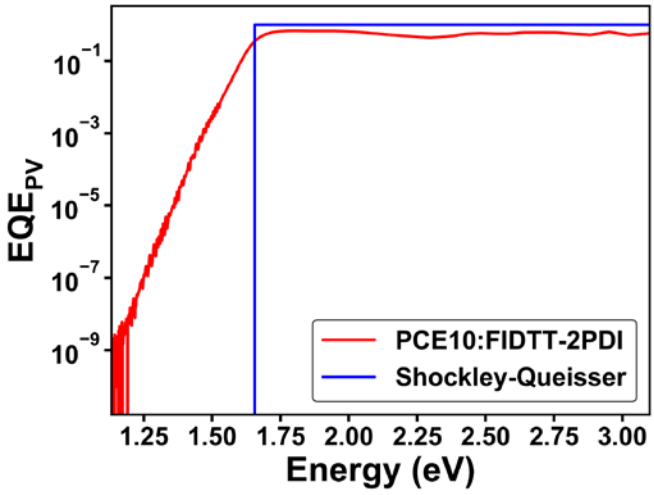

Fig. S2. Comparison of the EQEPV spectra used to calculate J_0^{rad} and J_0^{SQ} following Eq S2.6. The spectrum for PCE10:FIDTT-2PDI (red trace) is joined from the low energy recreation of EQEPV from the EL spectrum (see discussion above) and the EQEPV spectrum measured with photocurrent spectroscopy.

S3. Ellipsometry and IQE Analysis

The complex refractive index spectra (n and κ) for PCE10:FIDTT-2PDI were determined using spectroscopic ellipsometry. Spectroscopic ellipsometry measures a spectrum of the polarization state of elliptically polarized light (described by the parameters ψ and Δ) after it has been dispersed/dissipated by a material. For thin films, the raw ψ and Δ data obtained from the measurement can be fit based on models for the complex refractive indices and thickness of the thin film layers using transfer-matrix modelling. We performed spectroscopic ellipsometry on films of PCE10:FIDTT-2PDI spin coated onto Si substrates with 300 nm thermally grown SiO_2. The use of Si/SiO_2 substrates for ellipsometry has the advantage that substrate models for Si/SiO_2 wafers are very well defined, which minimizes uncertainty in the modelling of the PCE10:FIDTT-2PDI layer. Spectra were measured at 3 different angles of incidence (55°, 65°, and 75°). To model n and κ for PCE10:FIDTT-2PDI we used the CompleteEASE software from J.A. Woollam Co. We first fit the data in the transparent region (1300-1500 nm) to a Cauchy model, and constrained the modelled thickness of the PCE10:FIDTT-2PDI layer to be 78nm (close to that measured using a Bruker Dektak profilometer around ~75-80 nm). We then re-parameterized the Cauchy model in the transparent region using a Kramers-Kronig consistent B-spline[6] and extrapolated the B-spline into the absorbing region (400-1300) in increments of ~100 nm while keeping the model thickness fixed at 78 nm. Finally, after obtaining a B-spline model for the 400-1500 nm range with a fixed thickness of 78 nm, we allowed the thickness to vary to minimize the error in the fit. The final thickness was found to be ~73 nm, in reasonable agreement with the profilometry measurements. The fits to the ψ and Δ are shown in Fig. S3a. and the corresponding n and κ spectra are shown in Fig. S3b.

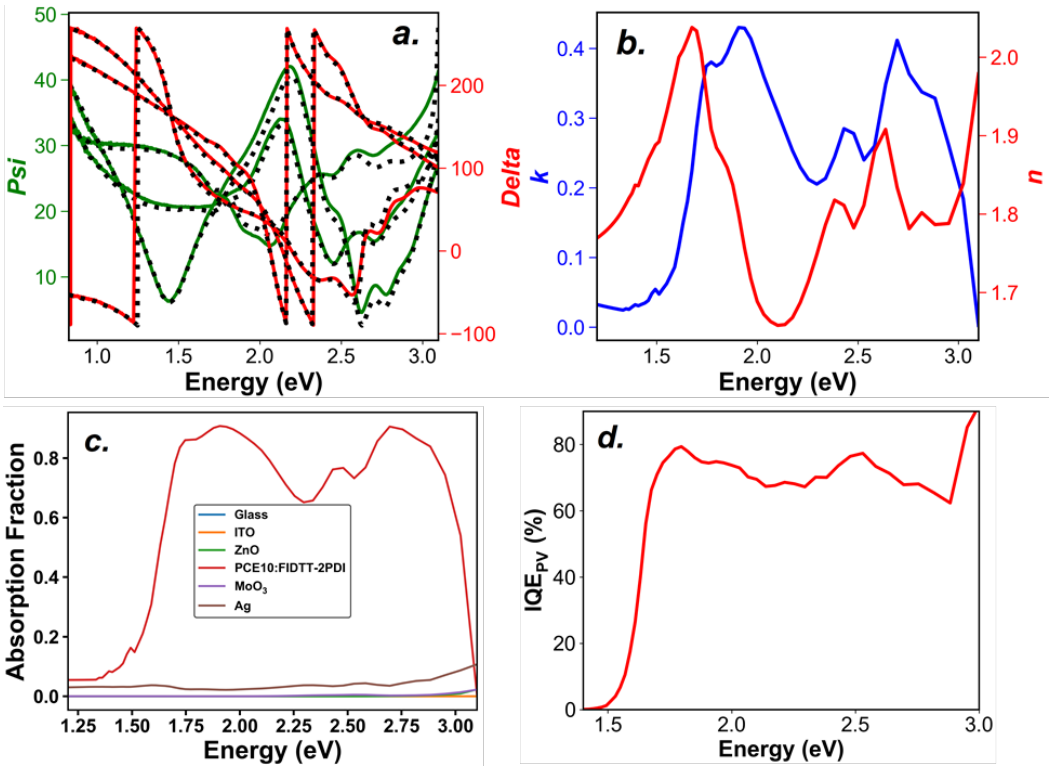

Fig. S3 ***a.)*** ψ and Δ spectra (ψ=green, Δ=red) measured at 55°, 65°, and 75° angle of incidence on Si/SiO_2(300nm)/PCE10:FIDTT-2PDI samples. Fits to the ψ and Δ spectra based on the final *n* and *κ* model are shown in black. ***b.)*** Final *n* and *κ* model determined for PCE10:FIDTT-2PDI. ***c.)*** Spectra of the fraction of absorbed light in each layer of the PCE10:FIDTT-2PDI solar cell calculated using transfer matrix modelling. ***d.)*** IQE_{PV} spectrum calculated using the fraction of absorbed light in the PCE10:FIDTT-2PDI layer and the EQE_{PV} spectrum shown in Fig. 4.2 a. of the main text.

To calculate the internal quantum efficiency (IQE_{PV}) for the PCE10:FIDTT-2PDI solar cell, a transfer-matrix algorithm[7] was used to calculate the fraction of absorbed light in each layer of the PCE10:FIDTT-2PDI device using their *n* and *κ* spectra across the wavelength range used for the EQE_{PV} measurements (Fig. S3 c.). The IQE_{PV} was then calculated by dividing the EQE_{PV} spectrum by the fraction of absorbed light in the PCE10:FIDTT-2PDI layer at each wavelength (Fig. S3 d.).

S4. Global Fitting of ns-μs PL and TA Data

To globally fit the fluence dependent polaron decay kinetics from transient absorption and the fluence dependent transient photoluminescence kinetics, we developed a model shown schematically in Fig. S2.1. This model is based on numerically solving a set of coupled ordinary differential equations (Eqs S2.1-S2.3) that govern the population dynamics of three species: the singlet excited state (S_1) on PCE10 (which is the primary excitation photogenerated by the 735 nm pump laser), the CT state (CT), and free charges (FC). To solve Eqs S2.1-S2.3, we assume that the initial excitation density is split into the three populations (S_1, geminate CT, and FC) within the instrument response time, so each of the three populations is given an initial condition at t=0. This is similar to the approach taken by Laquai and coworkers to model recombination dynamics in transient absorption experiments on polymer:fullerene blends;[8,9] however, our model differs in that we do not assume that the PCE10 S_1 population is quenched 100%. While a small fraction of unquenched singlet excited states would have only a small effect on the population kinetics of polarons monitored in transient absorption, any fraction of unquenched PCE10 S_1 states will have a significant effect on the photoluminescence transients, since the radiative recombination rate of the S_1 excited state is on the order of ~1000 times higher than that of a typical CT state.[10] Indeed, the effect of unquenched PCE10 S_1 states on the photoluminescence transients in PCE10:FIDTT-2PDI is clearly seen in Figs 3a., 3c., and 4c. in the main text, where the ~100 fold intensity difference between the initial PL intensity at t=0 and the delayed PL tail is due to the bright early time emission from unquenched PCE10 singlets, which can be seen spectrally as well in Fig. 4.3c. in the main text. In our model we also assume that recombination from the FC population occurs via the CT state as an intermediate, which is consistent with the general picture of charge recombination in organic photovoltaic blends.[11,12] In this assumption the CT and FC populations are coupled, so that non-geminate recombination of the FC population results population of the CT state with subsequent radiative and non-radiative decay to the ground state governed by the rate constants $k_{CT_{rad}}$ and $k_{CT_{nonrad}}$. We therefore are able to model the transient photoluminescence in terms of contributions from radiative decay of unquenched PCE10 and radiative decay of CT states coupled to the FC population using Eq S2.4. To model the decay of the PCE10 polaron feature in transient absorption, we assume that both free polarons (FC states) and polaron pairs (CT states) contribute to the polaron photoinduced absorption feature with equal absorption cross sections, in line with the assumptions of Laquai and coworkers.[8,9] We therefore model the transient absorption data using Eq S4.5, where we note that the FC population is multiplied by factor of ½ due to the fact that half of the free carriers are PCE10 positive polarons, while the other half are FIDTT-2PDI negative polarons, the latter of which are not monitored in the transient absorption kinetics from the PCE10 polaron feature that we track at 1150 nm (see SI section S10 and in particular Fig. S10.3b for assignment of the PCE10 polaron feature).

We fix certain parameters when fitting the model in order to constrain the number of free parameters being varied. Specifically, we allow only the bimolecular recombination rate of charges (k_{Bi}) and the monoexponential decay rate ($k_{CT_{mono}}$) and PL quantum efficiency of the CT state ($PLQE_{CT}$) to vary during the fit. We note that $k_{CT_{mono}}$ and $PLQE_{CT}$ are directly related to the radiative and non-radiative decay rates of the CT state ($k_{CT_{rad}}$ and $k_{CT_{nonrad}}$) by the relationships

$k_{CT_{mono}} = k_{CT_{rad}} + k_{CT_{nonrad}}$ and $PLQE_{CT} = \frac{k_{CT_{rad}}}{k_{CT_{rad}} + k_{CT_{nonrad}}}$. We choose to vary the parameters $k_{CT_{mono}}$ and $PLQE_{CT}$ instead of $k_{CT_{rad}} + k_{CT_{nonrad}}$ simply because there are more values reported in the literature for $k_{CT_{mono}}$ and $PLQE_{CT}$ which gives us a sense for reasonable boundaries for these parameters. We fix the parameters $k_{S1_{mono}}$ and $PLQE_{S1}$ for PCE10 to the values that we measure experimentally using time resolved photoluminescence and integrating sphere measurements (see section S6 below). We also fix the initial populations of S1, CT, and FC. For the initial population of S1, we use the steady state photoluminescence quenching fraction of PCE10 in the PCE10:FIDTT-2PDI blend excited at 730 nm (see section S7 below) to estimate the fraction of the initial excitation density that remains as S_1 states (Eq S4.6). For the initial population of FC states, we use the IQE_{PV} at 735 nm (68.6%) as an estimate for the fraction of excitations that split into free carriers, and set the initial FC population according to Eq S4.7 (noting that one excitation splits into one electron and one hole, giving two free carriers). The initial population of CT states is then calculated according to Eq S4.8. We note that the assumption that the initial FC population can be estimated based on the IQE_{PV} is likely to be a lower limit for the true initial FC population, since the IQE_{PV} also depends on the charge carrier extraction efficiency. We believe that varying the initial S_1 and FC populations in the fits would be meaningful for photoluminescence and transient absorption data spanning a much larger time range (sub-ps to μs) than we have addressed in this study; however, given the limited time range of the data that we are fitting (100's of ns to μs), we keep the initial S_1 and FC populations fixed to physically plausible estimates in order to constrain the possible limits on k_{Bi}, $k_{CT_{mono}}$, and $PLQE_{CT}$ to be within a physically meaningful range.

To fit the photoluminescence transients to the experimental data it is also essential to reconvolve the photoluminescence decay model with the experimentally measured instrument response function (IRF), which we do numerically.[13] Figure S4 a. shows the photoluminescence decay and fit for the lowest fluence (1.7 μJ/cm^3) from Fig. 4.3 c. in the main text along with the experimentally measured IRF. For the reconvolution fits, the noise baseline seen in the IRF is manually set to zero and a noise baseline is added to the reconvolution model to match the noise level of the photoluminescence decay. Figure S4 b. shows the photoluminescence models corresponding to the fits in Fig. 4.3 c. of the main text prior to reconvolution with the IRF. For numerical integration of the ODEs, solutions were found over a logarithmically spaced time array in order obtain accurate solutions for the relatively fast kinetics of the S_1 decay. Numerical integration of the coupled ODEs in Eq S4.1-S4.3, numerical convolution of the model generated from Eq. S4.4, and global fitting of the resulting models for transient photoluminescence and the model for TA (Eq S4.5) for a given set of parameters were done using custom written code for Python using features from the scipy scientific computing package. The parameters used for the best fit model (both fitted and fixed parameters) are listed in Table S4 below.

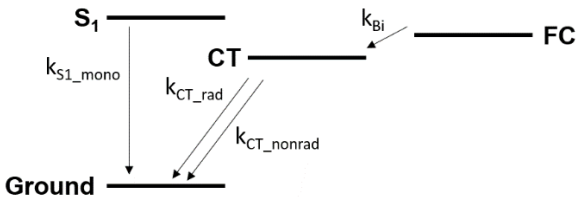

Fig. S4.1 Schematic diagram for the rate equations used to model the population dynamics of PCE10 singlets (S_1), CT states (CT) and free carriers (FC) corresponding to Eqs S4.1-S4.3.

$$\frac{dS_1}{dt} = -k_{S_{1_{mono}}}[S_1] \qquad Eq\ S4.1$$

$$\frac{dCT}{dt} = k_{Bi}[FC]^2 - \left(k_{CT_{rad}} + k_{CT_{nonrad}}\right)[CT] \qquad Eq\ S4.2$$

$$\frac{dFC}{dt} = -k_{Bi}[FC]^2 \qquad Eq\ S4.3$$

$$PL \propto -(PLQE_{S_1} * k_{S_{1_{mono}}}[S_1] + k_{CT_{rad}}[CT]) \qquad Eq\ S4.4$$

$$TA \propto \frac{[FC]}{2} + [CT] \qquad Eq\ S4.5$$

$$[S_1]_0 = [Excitations] * (1 - Fraction_{PCE10_{quench}}) \qquad Eq\ S4.6$$

$$[FC]_0 = 2.0 * [Excitations] * IQE_{735nm} \qquad Eq\ S4.7$$

$$[CT]_0 = [Excitations] - [S_1]_0 - \frac{[FC]_0}{2} \qquad Eq\ S4.8$$

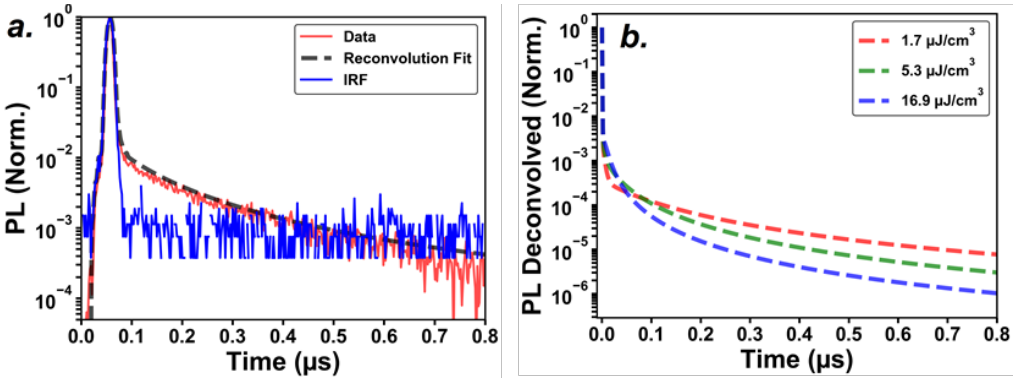

Fig. S4.2 *a*.) Decay and reconvolution fit for the lowest fluence (1.7 μJ/cm3) time resolved photoluminescence trace on PCE10:FIDTT-2PDI from Fig. 4.3 c. in the main text shown with the instrument response function (IRF) in blue. b.) PL models deconvolved from the IRF corresponding to the fits in Fig. 4.3 c. of the main text.

k_{Bi} (cm^3s^{-1})	$k_{CT_{mono}}$ (s^{-1})	$PLQE_{CT}$	$k_{S_{1_{mono}}}$ (s^{-1})	$PLQE_{S_1}$	$Fraction_{PCE10_{quench}}$	IQE_{735nm}
$2.228x10^{-11}$ (fit)	$2.52x10^{9}$ (fit)	$1.36x10^{-4}$ (fit)	$3.2258x10^{9}$ (fixed)	0.03 (fixed)	0.96 (fixed)	0.686 (fixed)

Table S4. Parameters used in the model described by Eqs S2.1-S2.8 for the global best fits to the fluence dependent transient photoluminescence and transient absorption data.

S5. Emission Spectra of PCE10:FIDTT-2PDI and Neat Materials

The photoluminescence and electroluminescence spectra of PCE10:FIDTT-2PDI, and neat PCE10 and FIDTT-2PDI are shown below in Fig. S5. For EL spectra, strong interference effects from the back-illuminated Si CCD detector (known as etaloning) are evident when the EL spectra are plotted on a linear scale, even after the raw data is spectrally corrected using a calibrated white light source. To correct the spectra for etaloning we low-pass filtered the EL spectra by Fourier transforming the data and multiplied the FFT with a Gaussian window function filter out the high frequency interference fringes, which after an inverse FFT generated the smoothed spectra shown in Fig. S5b as well as in Fig. 4.3 c. of the main text. A comparison of the raw and low-pass filtered spectra are shown as an example in Fig. S5c. We note that the unfiltered spectra were used for the recreation of the sub-gap EQE_{PV} spectrum in the main text due to the fact that low pass filtering can alter the shape of the EL spectrum near the end points of the data array. The peak maxima for the PCE10:FIDTT-2PDI and PCE10 EL spectra are determined by finding the roots (zero crossings) of derivatives of the spectra using spline representations. The EL peak maximum for PCE10:FIDTT-2PDI =1.452 eV and for PCE10 = 1.495 eV.

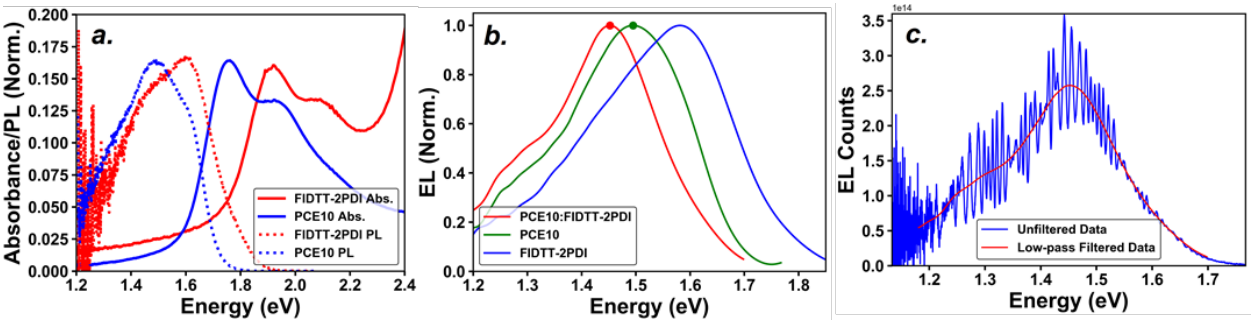

Fig. S5 ***a.)*** Absorption and PL spectra on films of neat PCE10 and FIDTT-2PDI. The excitation wavelength for PL spectra was 532 nm (see methods section in main text). ***b.)*** EL spectra of PCE10:FIDTT-2PDI and neat PCE10 and FIDTT-2PDI with peak maxima at 1.452 eV and 1.495 eV indicated by a dot on the PCE10:FIDTT-2PDI and PCE10 spectra. ***c.)*** Example of low-pass filtering of the EL spectrum for PCE10:FIDTT-2PDI.

S6. Radiative Lifetime and PLQE of PCE10 and FIDTT-2PDI

In order to calculate the radiative lifetime (τ_{rad}) of PCE10 and FIDTT-2PDI, we measured the photoluminescence quantum efficiency (PLQE) and monoexponential photoluminescence decay rate (k_{mono}) of films of neat PCE10 and FIDTT-2PDI. Noting that $\tau_{rad} = \frac{1}{k_{rad}}$, the radiative lifetime can be calculated using Eqs S7.1 and S7.2.[14]

$$PLQE = \frac{k_{rad}}{k_{rad} + k_{non-rad}} = \frac{k_{rad}}{k_{mono}} \qquad Eq\ S7.1$$

$$k_{rad} = PLQE * k_{mono} \qquad Eq\ S7.2$$

The PLQE was measured and calculated following the procedures of deMello et al.[15], where three measurements are made in an integrating sphere: (1) the sample is removed from the integrating sphere and only the excitation source intensity is measured, (2) the sample is placed in the integrating sphere out of the path of the excitation source to calculate the absorbed/emitted photon flux due to absorption of scattered excitation light by the sample, (3) the sample is placed in the integrating sphere in the path of the excitation source. The data is shown in Figs S6a and S6b below and the PLQE was calculated to be ~5% for FIDTT-2PDI and ~3% for PCE10.

The monoexponential lifetimes (k_{mono}) for PCE10 and FIDTT:2PDI were estimated by fitting the time resolved PL decays on neat films to either a stretched exponential or biexponential function. The fitting was done by numerically reconvolving the decay model with the IRF[13] (the noise baseline seen in the PCE10 IRF data was subtracted manually before reconvolution and a flat noise baseline was added as a parameter into the reconvolution fit). For PCE10, the time resolved PL was measured according to the same experimental methods described in the main text, where 735 nm pulsed excitation from an ultrafast tunable laser source was used to excite the sample and a streak camera was used for detection. For FIDTT-2PDI, time resolved PL was measured using a time correlated single photon counting set up (PicoQuant FluoTime 100) which consists of a visible PMT detector, a 470 nm pulsed diode laser excitation source (PicoQuant LDH470, driven by a PicoQuant PDL-800B at 20MHz pulse rate), and a time correlated single photon counting module (PicoHarp 300). For PCE10, the monoexponential lifetime is taken to be the lifetime of the first exponential component of the biexponential fit, which accounts for 96.3% of the total initial PL intensity (see Table S6.1). For FIDTT-2PDI, the monoexponential lifetime is taken to be the average lifetime calculated from the best fit parameters for the characteristic lifetime (τ_c) and β factor from the stretched exponential fit (stretched exponential fits are often used to describe relaxation dynamics in disordered systems).[16,17]

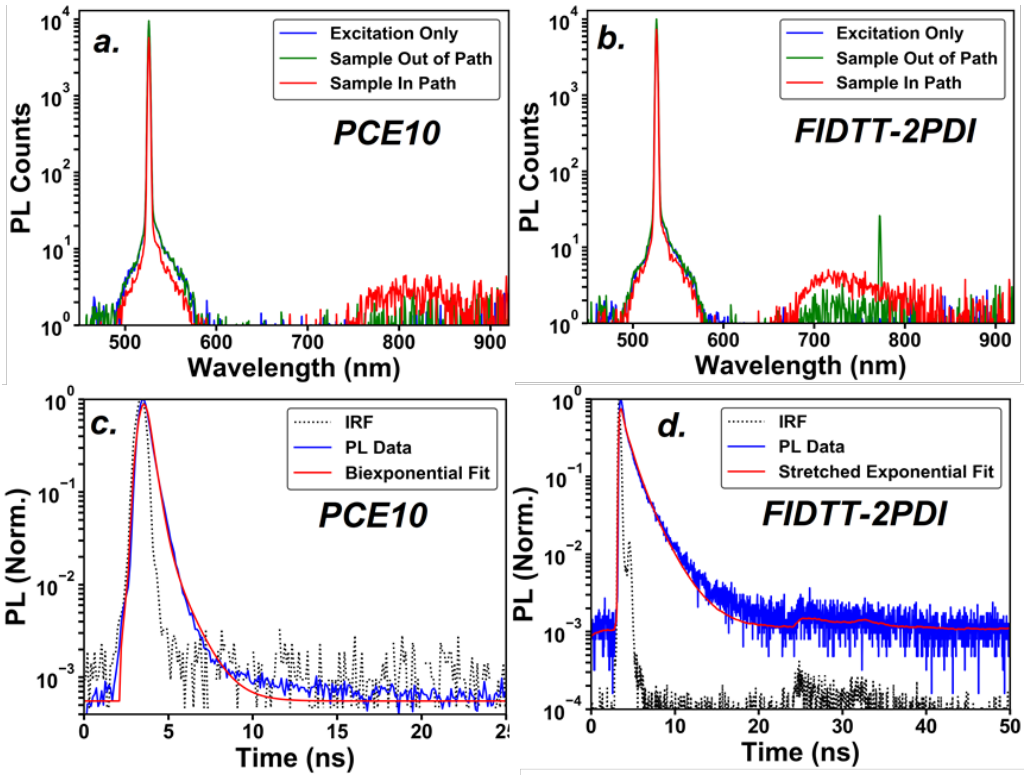

Fig. S6 ***a. & b.)*** PLQE of neat PCE10 and FIDTT-2PDI. ***c.& d.***) PL decay and its exponential fitting on neat PCE10 and FIDTT-2PDI

A_1 (%)	τ_1 (s)	A_2 (%)	τ_2 (s)
96.3	3.1×10^{-10}	3.7	1.04×10^{-9}

Table S6.1 Biexponential fit parameters for neat PCE10 PL decay (Fig. S6 c.)

τ_c (s)	β	τ_{avg} (s)
5.99×10^{-10}	0.672	7.9×10^{-10}

Table S6.2 Stretched exponential fit parameters for neat FIDTT-2PDI PL decay (Fig. S6 d.)

PCE10 *PLQE*	PCE10 k_{mono} (s)	PCE10 τ_{rad} (s)	FIDTT-2PDI *PLQE*	FIDTT-2PDI k_{mono} (s)	FIDTT-2PDI τ_{rad} (s)
3%	3.23×10^{9}	1.03×10^{-8}	5%	1.27×10^{9}	1.58×10^{-8}

Table S6.3 Summary of PLQE, monoexponential decay rates, and radiative lifetimes for PCE10 and FIDTT-2PDI

S7. Steady State PL Quenching and Determination of CT PLQE

In order to determine the steady state PL quenching fraction of PCE10 in the PCE10:FIDTT2-PDI blend, films of PCE10:FIDTT2-PDI and PCE10 were excited with a 730 nm CW diode laser and the steady state PL spectra were compared. Excitation at 730 nm selectively excites the PCE10 component in the PCE10:FIDTT-2PDI blend (see Fig. S5a.). Selective excitation of PCE10 allows us to estimate the quenching fraction of PCE10 alone which is a parameter necessary for the global fits to the time resolved PL data (see section S4 above), and it also simplifies the contributions to the steady state PL spectra of PCE10:FIDTT-2PDI into two components: PCE10 emission and CT emission (since energy transfer will not occur from the PCE10 singlet to FIDTT-2PDI, see Fig. S5a.). The PL spectra were normalized to the absorbed photon flux at 730 nm (Fig. S7 a. and b.) by dividing the PL spectra by the fraction of absorbed light (F_a) at 730 nm determined from the UV-vis absorption spectra of the films (where F_a is estimated as 1-transmittance). Due to the fact that the CT state emission overlaps with the singlet emission of PCE10 (Fig. S5b.), the quenching fraction of PCE10 in the blend (estimated by comparing the area under the PL/F_a curve in neat PCE10 to the area under the emission curve of PCE10 in the PL/F_a curve of the blend) can only be accurately calculating by decomposing the blend PL spectrum in terms of a linear combination of CT and PCE10 emission. We do this by fitting the PL spectrum of the PCE10:FIDTT-2PDI blend to a linear combination of the neat PCE10 PL spectrum and the PCE10:FIDTT-2PDI EL spectrum, the latter of which should represent the CT emission spectrum.[18] By fitting the PL/F_a curve of PCE10:FIDTT-2PDI in this way (Fig. S7 c.), we can compare the area under the CT emission curve to the PCE10 emission curve in the blend, and calculate both the quenching fraction of PCE10 in the blend and the PLQE of the CT state by noting that the PLQE of neat PCE10 is 3% (see section S6). Based on this analysis we estimate that PCE10 singlets are 96% quenched in the PCE10:FIDTT-2PDI blend, and that the PLQE of the CT state is ~$4x10^{-4}$.

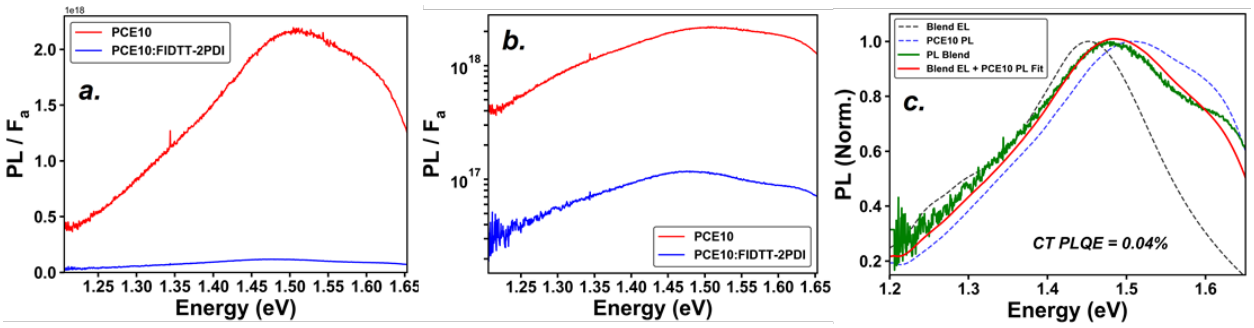

Fig. S7 ***a. & b.)*** PL spectra normalized to the fraction of absorbed light (F_a) at 730 nm for PCE10 and PCE10:FIDTT-2PDI on linear and semilogarithmic scales. ***c.)*** Fit of the PCE10:FIDTT-2PDI blend PL spectra in terms of a linear combination of the PCE10:FIDTT-2PDI EL spectrum and PCE10 PL spectrum to yield the CT PLQE and quenching fraction of PCE10 in the blend.

S8. Discussion of Triplet-Triplet Annihilation in the ns-µs Recombination Kinetics in PCE10:FIDTT-2PDI

Here we consider the possibility of whether or not the fluence dependent delayed photoluminescence in PCE10:FIDTT-2PDI could result from triplet-triplet annihilation. Triplet-triplet annihilation could occur from the formation of triplets via two different pathways: (1) triplets could form via intersystem crossing from the S_1 state of PCE10,[19] or (2) triplet formation could occur due to the non-geminate formation of triplet CT states (^{3}CT) via free charges, which could transfer energy to form triplet states on PCE10 or FIDTT-2PDI.[12,20] We can easily rule out the first possibility on the basis that it is not consistent with the observation of a much stronger delayed photoluminescence tail in the PCE10:FIDTT-2PDI blend as compared to neat PCE10, since in the blend other excited state deactivation pathways such as charge transfer would compete with triplet formation via intersystem crossing.

In terms of the second possibility, the non-geminate formation of triplets via ^{3}CT states is a well-studied phenomenon in polymer:acceptor blends[12] and could in principle result in the formation of triplets that could annihilate bi-moleculary and result in a fluence dependent delayed PL tail. However, our results from the modelling of the delayed PL argue against this scenario. Triplet-triplet annihilation is an upconversion process in which two triplets annihilate to form a singlet ground state (S_0) and a singlet excited state (S_1).[19] From our modelling of the time resolved PL, we found that the emissive state in the fluence dependent delayed PL tail had a monoexponential lifetime of 3.97 ns and a PLQE of 1.36×10^{-4}, which translates into a radiative lifetime of ~29 µs. This radiative lifetime is over 1000 times longer than that of neat PCE10 or FIDTT-2PDI, which have radiative lifetimes on the order of 10-20 ns (see SI Section S6 above). A radiative lifetime of 29 µs is far more consistent with that expected for CT states, as the exciplex states typically have lower oscillator strength than excitonic transitions, and thereby have long spontaneous emission lifetimes.[10,21] We additionally note that the possibility of triplet-triplet upconversion to the S_1 state of FIDTT-2PDI is highly unlikely to explain the observed phenomena on the basis of the spectral position of the delayed PL, which is far below the fluorescence peak of neat FIDTT-2PDI (see Section S5). We therefore argue that the delayed PL is due to radiative non-geminate recombination of charge via a CT state.

S9. Extracting CT State Parameters from EL and EQE_{PV} Fits

To estimate the reorganization energy (λ) and CT state energy (E_{CT}), we fit the EQE_{PV} tail and EL spectrum of PCE10:FIDTT-2PDI to the equations derived by Vandewal and coworkers[22] (Eqs S9.1 and S9.2), which describe the EL and EQE_{PV} spectra in terms of the shape and energetic position of the CT state absorption and emission spectra derived from the Marcus theory for photoinduced electron transfer.[22]

$$EQE_{PV}(E) = \frac{f}{E\sqrt{4\pi\lambda kT}} \exp\left(\frac{-(E_{CT} + \lambda - E)^2}{4\pi\lambda kT}\right) \qquad Eq\ S9.1$$

$$EL(E) = \frac{E}{\sqrt{4\pi\lambda kT}} \exp\left(\frac{-(E_{CT} - \lambda - E)^2}{4\pi\lambda kT}\right) \qquad Eq\ S9.2$$

In Eqs S9.1 and S9.2, E is the photon energy and f is a parameter that describes the electronic coupling between the ground and excited state CT complex.[22] To fit the data we normalized the EL spectrum and globally fit the EL and EQE_{PV} spectrum to a set of common parameters for λ and E_{CT} using a cost function based on the logarithm of the EQE_{PV} and EL spectra. The resulting fits are shown in Fig. S9 with best fit values for λ and E_{CT} of 0.15 eV and 1.60 eV, respectively. To check that the fits were reasonable we calculated the V_{OC} using the analytical solutions to the detailed balance limit in terms of E_{CT}, λ, and f derived by Vandewal and coworkers,[22] and included a non-radiative loss term based on the EQE_{EL} value reported in the main text:

$$V_{OC} = \frac{E_{CT}}{q} + \frac{kT}{q}\ln\left(\frac{J_{sc}h^3c^2}{fq2\pi(E_{CT} - \lambda)}\right) + \frac{kT}{q}\ln(EQE_{EL}) \qquad Eq\ S9.3$$

Using the values λ = 0.15 eV, E_{CT} = 1.60 eV, and f = 0.044 eV^2 obtained from the fits to the EQE_{PV} and EL spectra, we calculated a V_{OC} of 1.01 V, close to the value calculated in SI Section S2 using the methods of Kirchartz and Rau.[1]

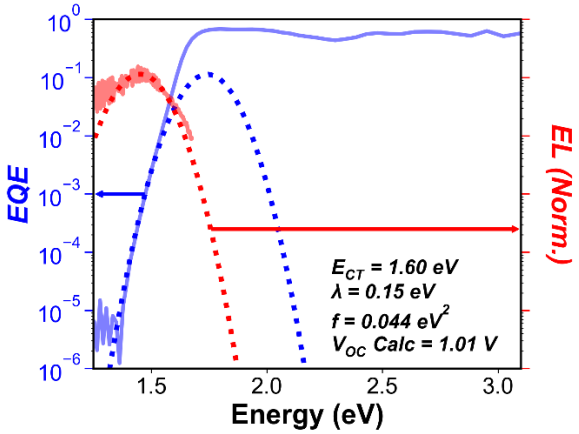

Fig. S9. Fits to the EQE_{PV} and EL spectra of PCE10:FIDTT-2PDI based on Eqs. S9.1 and S9.2. Values for λ, E_{CT}, and f are shown in the figure, along with the value for V_{OC} calculated from Eq. S9.3.

S10. Transient Absorption Spectroscopy Analysis

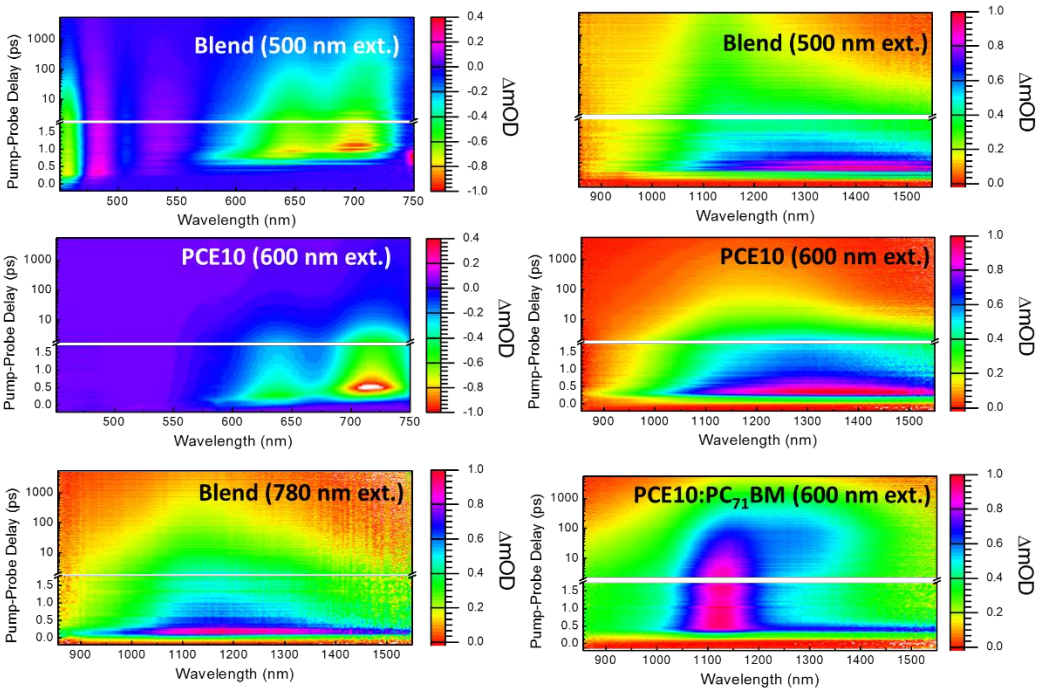

Figure S10.1. Pseudo-color plot of transient absorption spectra for neat and blend materials. The material and excitation conditions are described in in the figure. Spectra for PCE10:$PC_{71}BM$ is included for comparison. A clear formation of polaronic state (1100 nm) and decay of Singlet state (1400 nm) is observed. Similar behavior is observed in PCE10:FIDTT-2PDI blends, which exhibits prolonged polaronic peak of donor as well as the appearance of low energy excited state absorption (ESA) peak of FIDTT-2PDI.

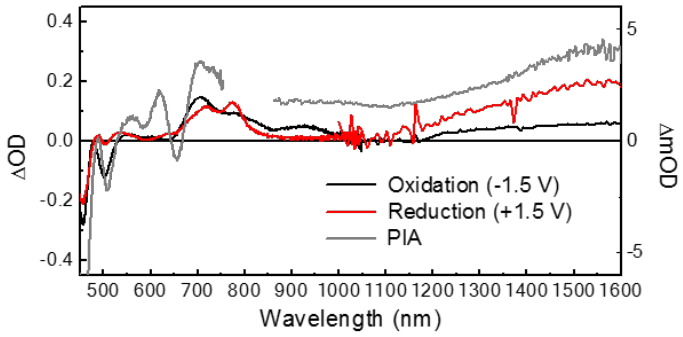

Figure S10.2. Sepctroelectrochemistry for neat FIDTT-2PDI films showing absorption of positively and negatively charged species. The films was cast onto an ITO/glass substrate and immersed into electrolyte solution (0.1M N-Bu_4PF_6 in acetonitrile solvent) and the difference in optical density was monitored with electrical oxidation/reduction. The photoinduced absorption signal and electrically charged absorption shows clear similarity. It can be understood that FIDTT-2PDI is capable of promoting spontaneous generation of charges, or weakly bound polaronic species.

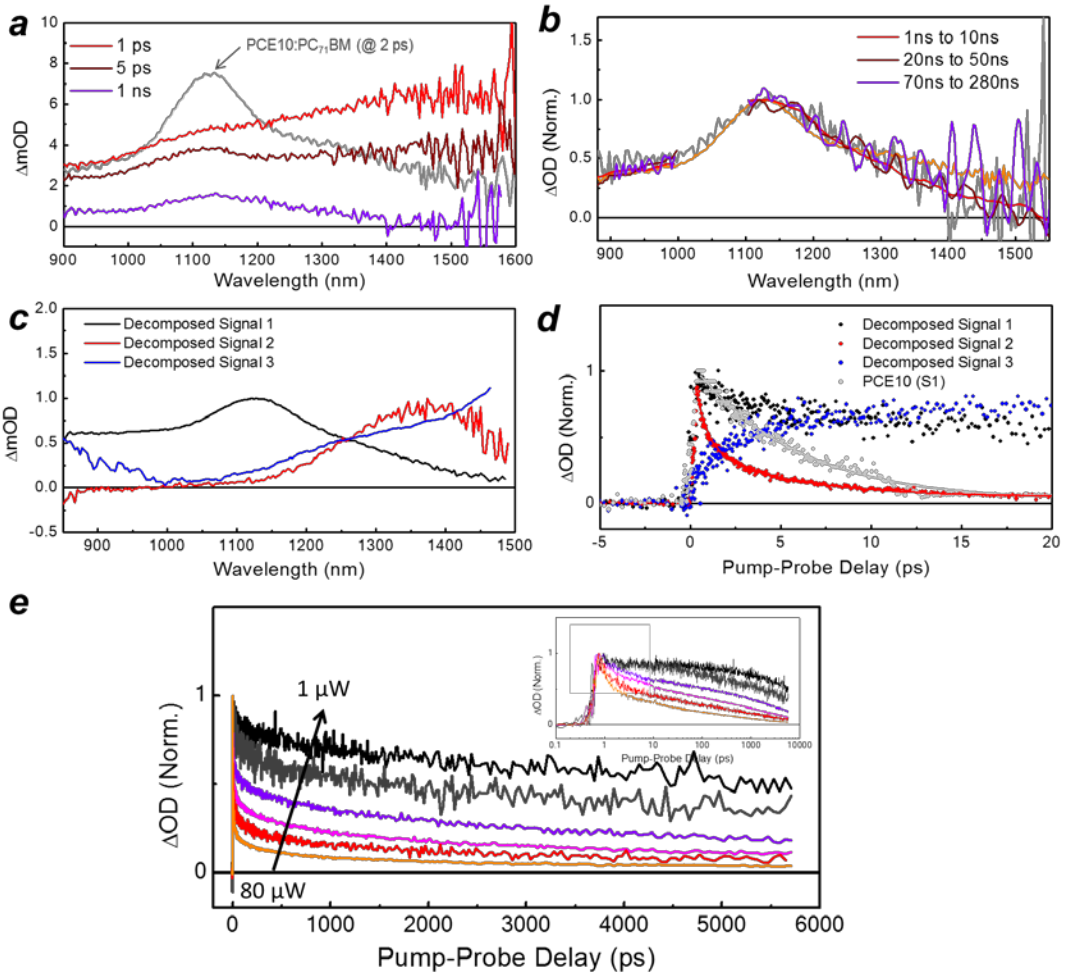

Figure S10.3. Photo-induced absorption spectra of PCE10:FIDTT-2PDI at different pump-probe delays measured by ***a.***) femtosecond transient absorption spectroscopy (500 fs to 5 ns) and ***b.***) nanosecond transient absorption spectroscopy (1 ns to 1 μs). Pump wavelength was 735 nm and the fluences were 2.7 μJ/cm^2 and 18.1 μJ/cm^2 for ***a.***) and ***b.***), respectively. For nanosecond transient absorption measurement, the signals were not recorded within 1000 nm to 1100 nm window due to the limited probe light spectra. For comparison purposes, spectra at 1 ns delay for PCE10:FIDTT-2PDI and PCE10:PC$_{71}$BM are included as grey and yellow solid lines, respectively. A clear signature of PCE10 polaron absorption appears predominantly around 1150 nm,[23] which is distinct from the broad spectral features of singlet and triplet excited state absorptions around 1300 nm. When closely examined, one can note that in the yellow trace corresponding to PCE10:PC$_{71}$BM, there is some additional photoinduced absorption between 1300-1500 nm, which is consistent with triplet absorption observed previously in PCE10:PC$_{71}$BM.[23] However in PCE10:FIDTT-2PDI, the photoinduced absorption appears to only contain predominant features from the PCE10 polaron peaked at 1150 nm, consistent with previous assignments.[23] ***c.***) Decomposed spectra and ***d.***) its initial kinetics from the global analysis of ***a.***). Clear features of PCE10 polaron, PCE10 singlet and the charged FIDTT-2PDI signals are acquired. The deconvoluted kinetics of charged A1 species from its overlapping spectral feature

of PCE10 singlet shows continuous generation of charges up until tens of ps, as in the GSB of the acceptor in the blend (main text). Deconvoluted kinetics of PCE10 (S1) from neat PCE10 film are also included as a reference. The singlet signals for blend and neat films were well fitted by bi and mono exponential decays. ***e.***) Fluence dependent kinetics of ESA feature (1150 nm) under excitation wavelength of 735 nm. With invariant peak position and fluence dependence, the polaronic feature does not sustain within geminately formed initial CT states but rather separates into free charge carriers. Inset shows log-scale time axis.

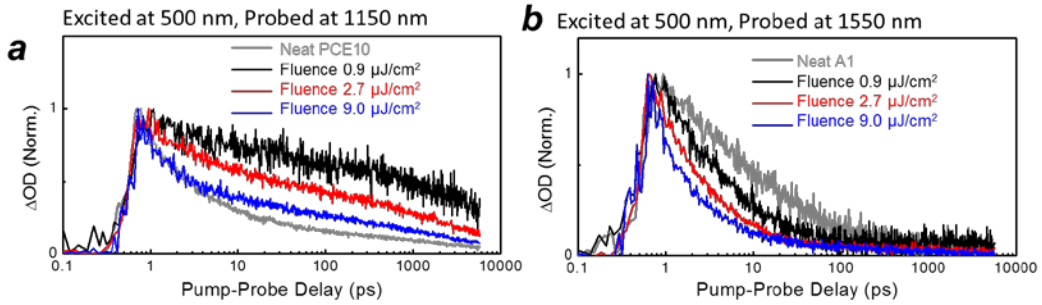

Figure S10.4. Fluence dependence of decay kinetics for ***a.***) the polaron of PCE10, and ***b.***) an ESA corresponds to the charged species in FIDTT-2PDI. They both exhibit clear fluence-dependence which is a sign of higher order recombination dominance. The features corroborates our assignment of ESAs.

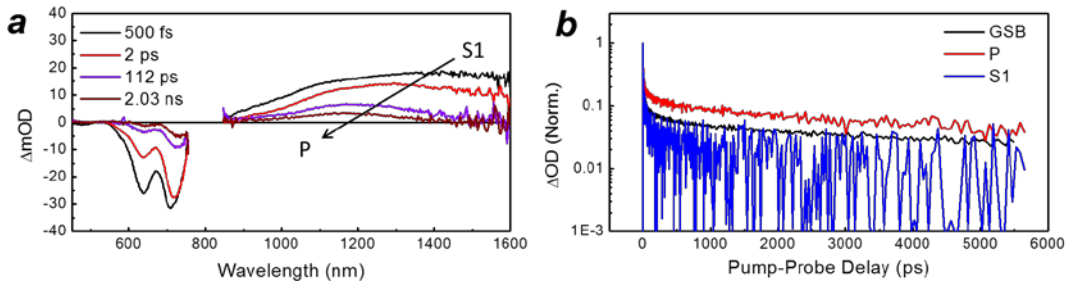

Figure S10.5. ***a.***) Photo-induced absorption spectra and ***b.***) decay kinetics of GSB and ESAs of neat PCE10 film at different pump-probe delays. Pump wavelength was 600 nm and the fluence was 8.8 μJ/cm^2. Clear evolution of polaronic features (1150 nm) as well as singlet (1400 nm) are observed, which has lifetime of around 20 ps and 2 ns, respectively. Due to multiple ESAs, the GSB decay can be fitted by multiexponential with time constants 17 ps (50%), 134 ps (20%), and 2.1 ns (30%).

S11. Morphology of PCE10:FIDTT-2PDI Blend

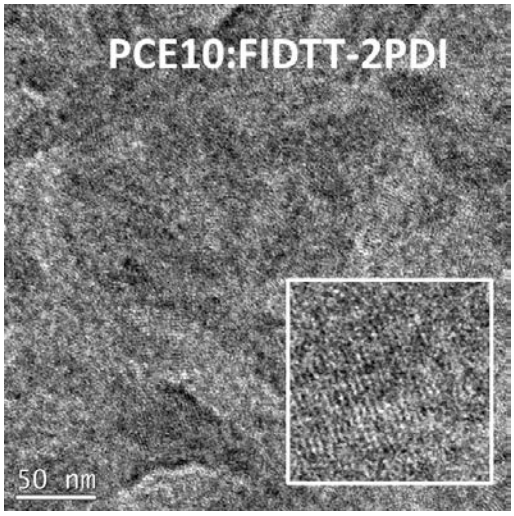

Figure S11. Transmission electron microscopy image of PCE10:FIDTT-2PDI blend at the optimized conditions. (measured with TECNI G2 F20 Supertwin TEM)

S12. Synthesis and Characterization of FIDTT-2PDI Molecules

S12.1 Computational Chemical Modelling

All the calculations are done in Gaussian 16 program[24] using B3LYP hybrid[25,26] functional with 6-31G(d) basis set.[27] The ground and excited state geometries are both confirmed to be true minimal using the frequency calculation. The excited state frequency and polarizabilities are calculated using the analytical hessian on the excited states.[28,29]

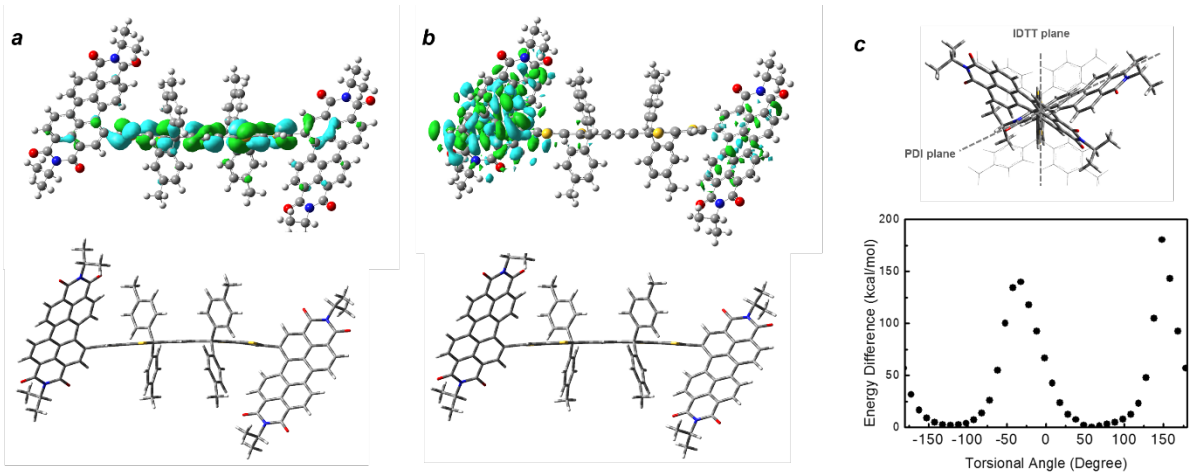

Figure S12.1. TD-DFT calculation results of natural transition orbitals and the side-view of molecular geometry for ***a.***) holes ***b.***) and electrons before the chemical fusing of PDI and IDTT. c. Torsional profile between PDI-IDTT. Strong steric hindrance is present between PDI acceptor and IDTT core that even breaks down the conjugation, and induce internal charge transfer with narrow localization of electrons and holes.

Molecule	Absorption (nm)	Emission (nm)	μ @ S_0 (Debye)	α @ S_0 ($Å^3$)	Δα @ S_1 ($Å^3$)	λ (eV)
FIDTT-2PDI	648	690	0.0189	255.5	722.62	0.11
IDTT-2PDI (before fusing)	704	818	0.7650	249.2	297.08	0.24

Table S12. TD-DFT results (B3LYP hybrid functional and the 6-31G(d) basis set) for the dipole moments of the ground state geometries, excess polarizability volume, structural reorganization energy. Unfused IDTT-2PDI is an intermediate state during the synthesis (Described in Scheme 1)

S12.2 Photoemission Spectroscopy

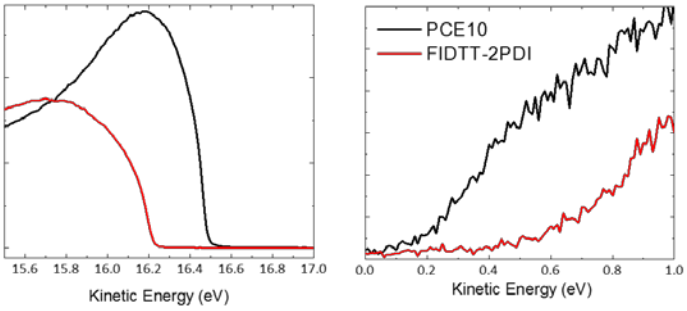

Figure S12.2. Ultraviolet photoemission spectra with excitation energy of 21.22 eV (He I). The spectra were corrected using gold 5d bands.

S12.3 Synthetic Procedure of FIDTT-2PDI

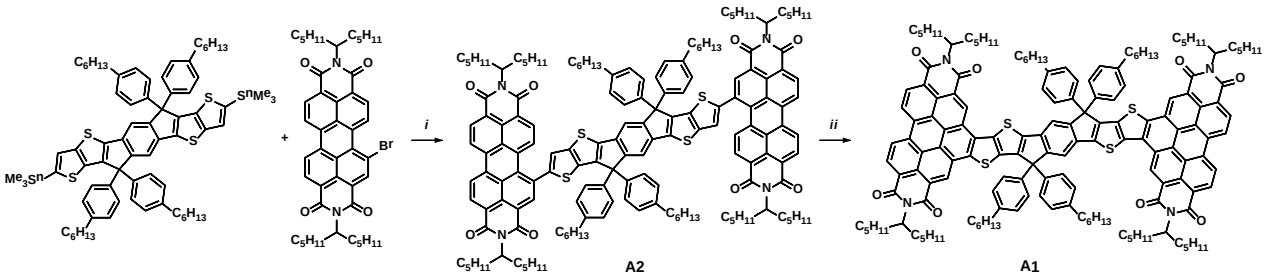

Scheme S12 Synthetic route of **FIDTT-2PDI**. Reagents and conditions: *i)* $PdCl_2(PPh_3)_2$, toluene, 110 °C. *ii)* $FeCl_3$, $MeNO_2$, toluene, 90 °C.

*Synthesis of unfused **IDTT-2PDI***

To a two-neck round button flask attached with a condenser was added 3,9-bis(trimethylstannyl)-5,5,11,11-tetrakis(4-hexylphenyl)-dithieno[2,3-*d*:2',3'-*d'*]-*s*-indaceno[1,2-*b*:5,6-*b'*]dithiophene (202 mg, 0.15 mmol), 1-bromo-*N*,*N*'-bis(6-undecanyl)-perylene-3,4,9,10-tetracarboxylic acid diimide (249 mg, 0.32 mmol) and $PdCl_2(PPh_3)_2$ (4.21 mg, 4 mol%), followed by addition of 15 mL anhydrous toluene under an argon atmosphere. The reaction mixture was then heated at 110 °C for 6 hours. After cooling to room temperature, methanol was added and the solid precipitate was collected by filtration. The crude product was further purified by column chromatography on silica gel eluted with CH_2Cl_2/hexanes (v/v = 2:1) to obtain **A2** as a dark brown solid (311 mg, 86%). ^{1}H NMR ($CDCl_3$, 500 MHz, 298 K) □□8.63 (m, 10H), 8.33 (m, 2H), 8.24 (m, 2H), 7.61 (s, 2H), 7.55 (br, 2H), 7.18 (d, *J* = 10.0 Hz, 8H), 7.12 (d, *J* = 10.0 Hz, 8H), 5.18 (m, 4H), 2.57 (m, 8 H), 2.23 (br, 8H), 1.86 (m, 8H), 1.60 (m, 8H), 1.28 (m, 76H), 0.84 (m, 36H); ^{13}C NMR ($CDCl_3$, 125 MHz, 323 K) □□146.8, 146.8, 144.6, 144.5, 142.4, 142.2, 142.1, 139.9, 139.9, 136.2, 135.4, 134.1, 133.7, 129.2, 128.8, 128.8, 128.6, 128.1, 127.9, 63.0, 54.8, 35.6, 32.3, 31.7, 31.3, 29.2, 26.7, 26.6, 22.6, 22.6, 22.5, 14.1, 14.0; we were not able to record a ^{13}C NMR spectrum with better S/N

ratio due to the limited solubility of the product in various solvents. HRMS (MALDI, *m/z*) Calcd for $C_{160}H_{178}N_4O_8S_4$ 2411.2528, found 2411.2420.

*Synthesis of fused molecule (**FIDTT-2PDI**)*

To a stirred solution of **IDTT-2PDI**(290 mg, 0.12 mmol) in 15 mL anhydrous toluene under an argon atmosphere was added a mixture of $FeCl_3$ (389 mg, 2.4 mmol) and 0.8 mL $MeNO_2$ freshly prepared in a glove box. The reaction was heated at 90 ºC for 8 hours then allowed to cool back to room temperature, and then extracted with water and $CHCl_3$. The combined extracts were washed with brine, dried over anhydrous $MgSO_4$, and then filtered. The volatiles were removed by rotary evaporation to give the crude product, which was further purified by column chromatography on silica gel eluted with $CHCl_3$/hexanes (v/v = 4:1) to obtain **FIDTT-2PDI** as a black solid (260 mg, 90%). ^{1}H NMR ($CDCl_3$, 500 MHz, 298 K) □□9.84 (m, 2H), 9.45 (br, 2H), 8.99 (m, 8H), 7.94 (s, 2H), 7.50 (d, *J* = 10.0 Hz, 8H), 7.33 (d, *J* = 10.0 Hz, 8H), 5.33 (br, 4H), 2.68 (t, *J* = 5.0 Hz, 8H), 2.41 (m, 8H), 2.03 (m, 8H), 1.69 (t, *J* = 5.0 Hz, 8H), 1.36 (m, 76H), 0.88 (m, 36H); ^{13}C NMR ($CDCl_3$, 125 MHz, 323 K) □□164.4, 164.3, 164.3, 154.6, 147.7, 147.2, 142.5, 141.2, 140.0, 136.6, 136.5, 134.9, 132.6, 132.5, 132.5, 130.5, 129.2, 128.4, 126.7, 126.3, 123.9, 123.8, 123.7, 123.6, 122.9, 118.2, 63.9, 55.2, 35.8, 32.7, 32.6, 32.0, 32.0, 31.8, 31.4, 29.2, 27.1, 26.9, 22.7, 22.7, 22.6, 14.1, 14.1, 14.0; we were not able to record a ^{13}C NMR spectrum with better S/N ratio due to the limited solubility of the product in various solvents. HRMS (MALDI, *m/z*) Calcd for $C_{160}H_{174}N_4O_8S_4$ 2407.2215, found 2407.2310.

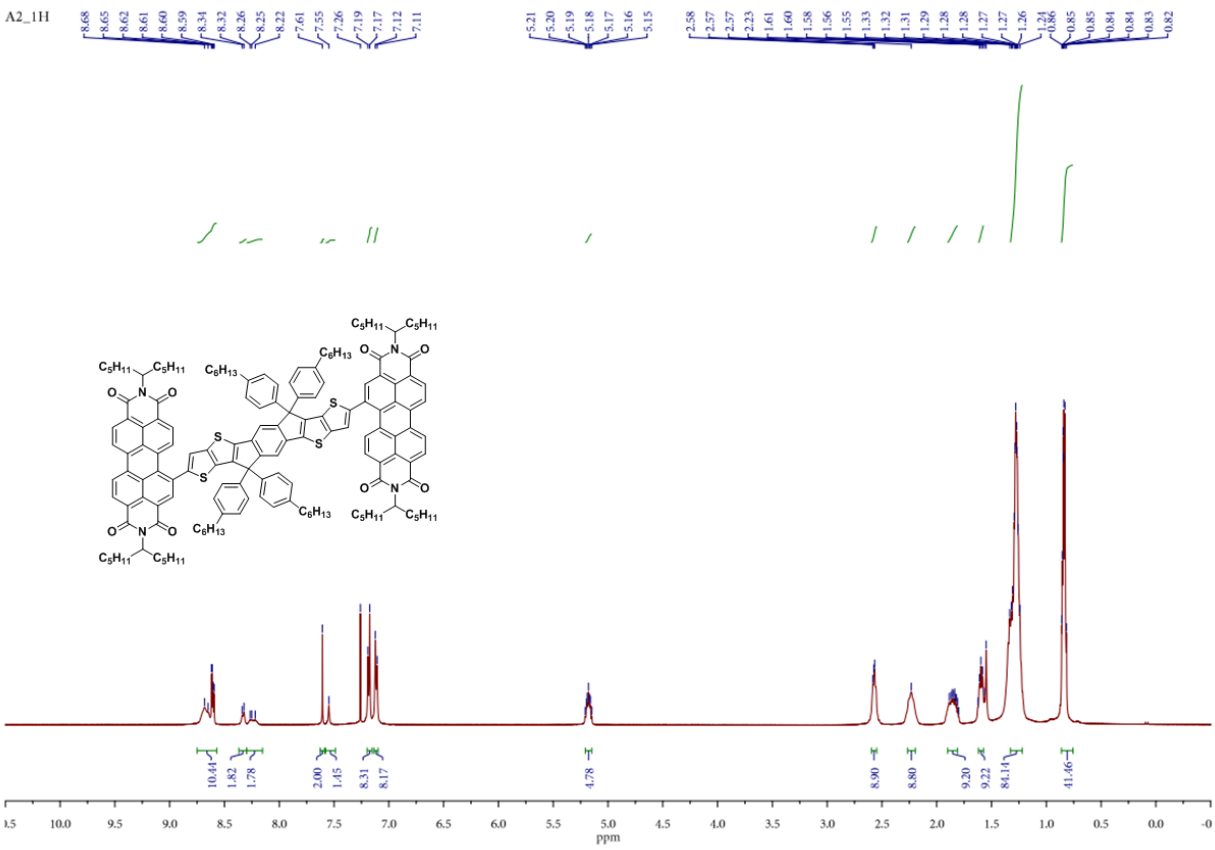
A2_1H
8.68
8.65
8.62
8.61
8.60
8.59
8.34
8.32
8.26
8.25
8.22
7.61
7.55
7.26
7.19
7.17
7.12
7.11
5.21
5.20
5.19
5.18
5.17
5.16
5.15
2.58
2.57
2.57
2.23
1.61
1.60
1.58
1.56
1.55
1.33
1.32
1.31
1.29
1.28
1.28
1.27
1.27
1.26
0.86
0.85
0.85
0.84
0.84
0.83
0.82
10.44
1.82
1.78
2.00
1.45
8.31
8.17
4.78
8.90
8.80
9.20
9.22
84.14
41.46
ppm

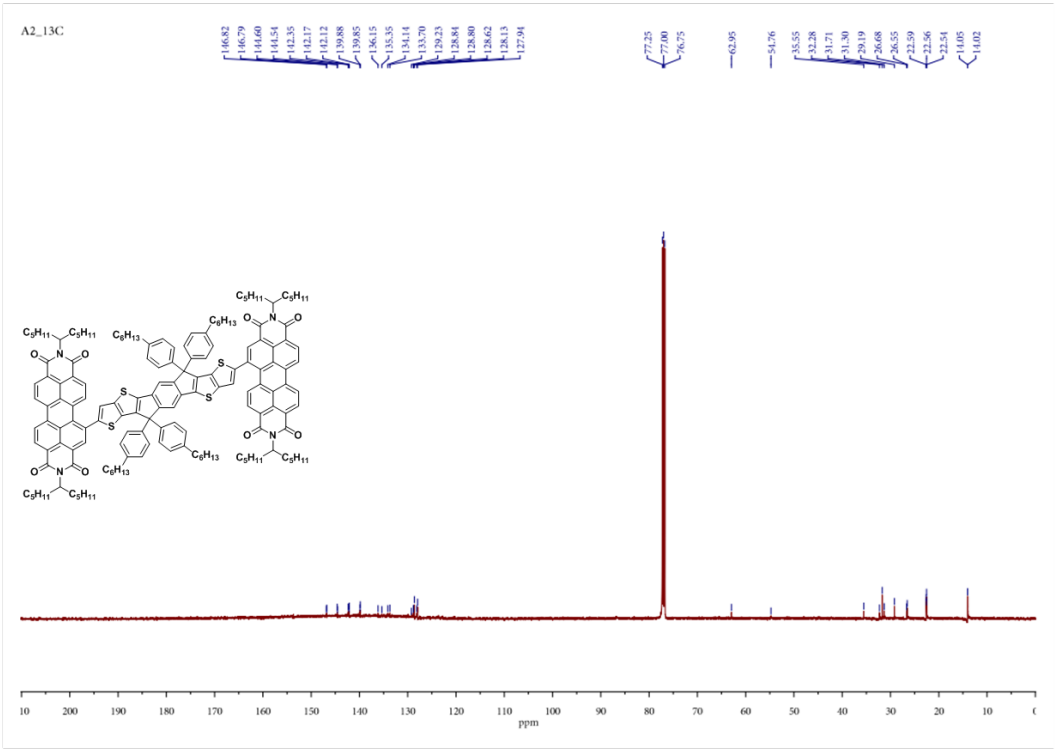
A2_13C
146.82
146.79
144.60
144.54
142.35
142.17
142.12
139.88
139.85
136.15
135.35
134.14
133.70
129.23
128.84
128.80
128.62
128.13
127.94
77.25
77.00
76.75
62.95
54.76
35.55
32.28
31.71
31.30
29.19
26.68
26.55
22.59
22.56
22.54
14.05
14.02
ppm

Supplementary References

1. Rau, U., Blank, B., Müller, T. C. M. & Kirchartz, T. Efficiency Potential of Photovoltaic Materials and Devices Unveiled by Detailed-Balance Analysis. *Phys. Rev. Appl.* **7**, doi:10.1103/PhysRevApplied.7.044016 (2017).
2. Shockley, W. & Queisser, H. J. Detailed Balance Limit of Efficiency of p-n Junction Solar Cells. *J. Appl. Phys.* **32**, 510-519, doi:10.1063/1.1736034 (1961).
3. Würfel, P. *Physics of Solar Cells*. 19 (Wiley-VCH, 2005).
4. Rau, U. Reciprocity relation between photovoltaic quantum efficiency and electroluminescent emission of solar cells. *Phys. Rev. B* **76**, doi:10.1103/PhysRevB.76.085303 (2007).
5. Yao, J. *et al.* Quantifying Losses in Open-Circuit Voltage in Solution-Processable Solar Cells. *Phys. Rev. Appl.* **4**, doi:10.1103/PhysRevApplied.4.014020 (2015).
6. Johs, B. & Hale, J. S. Dielectric function representation by B-splines. *physica status solidi (a)* **205**, 715-719, doi:10.1002/pssa.200777754 (2008).
7. Byrnes, S. J. Multilayer optical calculations. *arXiv e-prints* **arXiv:1603.02720** (2016).
8. Etzold, F. *et al.* Ultrafast exciton dissociation followed by nongeminate charge recombination in PCDTBT:PCBM photovoltaic blends. *J. Am. Chem. Soc.* **133**, 9469-9479, doi:10.1021/ja201837e (2011).
9. Howard, I. A., Mauer, R., Meister, M. & Laquai, F. Effect of morphology on ultrafast free carrier generation in polythiophene:fullerene organic solar cells. *J. Am. Chem. Soc.* **132**, 14866-14876, doi:10.1021/ja105260d (2010).
10. Chen, X.-K., Ravva, M. K., Li, H., Ryno, S. M. & Brédas, J.-L. Effect of Molecular Packing and Charge Delocalization on the Nonradiative Recombination of Charge-Transfer States in Organic Solar Cells. *Adv. Energy Mater.* **6**, 1601325, doi:10.1002/aenm.201601325 (2016).
11. Burke, T. M., Sweetnam, S., Vandewal, K. & McGehee, M. D. Beyond Langevin Recombination: How Equilibrium Between Free Carriers and Charge Transfer States Determines the Open-Circuit Voltage of Organic Solar Cells. *Adv. Energy Mater.* **5**, 1500123, doi:10.1002/aenm.201500123 (2015).
12. Rao, A. *et al.* The role of spin in the kinetic control of recombination in organic photovoltaics. *Nature* **500**, 435-439, doi:10.1038/nature12339 (2013).
13. Press, W. H., Teukolsky, S. A., Vetterling, W. T. & Flannery, B. P. *Numerical Recipes 3rd Edition: The Art of Scientific Computing*. 3 edn, 955-964 (Cambridge University Press, 2007).
14. Becker, H., Burns, S. E. & Friend, R. H. Effect of metal films on the photoluminescence and electroluminescence of conjugated polymers. *Phys. Rev. B* **56**, 1893-1905, doi:10.1103/PhysRevB.56.1893 (1997).
15. de Mello, J. C., Wittmann, H. F. & Friend, R. H. An improved experimental determination of external photoluminescence quantum efficiency. *Adv. Mater.* **9**, 230-232, doi:10.1002/adma.19970090308 (1997).
16. Epshtein, O., Nakhmanovich, G., Eichen, Y. & Ehrenfreund, E. Dispersive dynamics of photoexcitations in conjugated polymers measured by photomodulation spectroscopy. *Phys. Rev. B* **63**, doi:10.1103/PhysRevB.63.125206 (2001).
17. deQuilettes, D. W. *et al.* Impact of microstructure on local carrier lifetime in perovskite solar cells. *Science* **348**, 683-686, doi:10.1126/science.aaa5333 (2015).

18. Tvingstedt, K. *et al.* Electroluminescence from charge transfer states in polymer solar cells. *J. Am. Chem. Soc.* **131**, 11819-11824, doi:10.1021/ja903100p (2009).
19. Partee, J. *et al.* Delayed Fluorescence and Triplet-Triplet Annihilation in π-Conjugated Polymers. *Phys. Rev. Lett.* **82**, 3673-3676, doi:10.1103/PhysRevLett.82.3673 (1999).
20. Schlenker, C. W. *et al.* Polymer triplet energy levels need not limit photocurrent collection in organic solar cells. *J. Am. Chem. Soc.* **134**, 19661-19668, doi:10.1021/ja306110b (2012).
21. Strickler, S. J. & Berg, R. A. Relationship between Absorption Intensity and Fluorescence Lifetime of Molecules. *J. Chem. Phys.* **37**, 814-822, doi:10.1063/1.1733166 (1962).
22. Vandewal, K., Tvingstedt, K., Gadisa, A., Inganäs, O. & Manca, J. V. Relating the open-circuit voltage to interface molecular properties of donor:acceptor bulk heterojunction solar cells. *Phys. Rev. B* **81**, doi:10.1103/PhysRevB.81.125204 (2010).
23. Tamai, Y. *et al.* Ultrafast Long-Range Charge Separation in Nonfullerene Organic Solar Cells. *ACS Nano* **11**, 12473-12481, doi:10.1021/acsnano.7b06575 (2017).
24. Gaussian 16 Rev. A.03 (Wallingford, CT, 2016).
25. Lee, C., Yang, W. & Parr, R. G. Development of the Colle-Salvetti correlation-energy formula into a functional of the electron density. *Phys. Rev. B* **37**, 785-789, doi:10.1103/PhysRevB.37.785 (1988).
26. Stephens, P. J., Devlin, F. J., Chabalowski, C. F. & Frisch, M. J. Ab Initio Calculation of Vibrational Absorption and Circular Dichroism Spectra Using Density Functional Force Fields. *J. Phys. Chem.* **98**, 11623-11627, doi:10.1021/j100096a001 (1994).
27. Hehre, W. J., Ditchfield, R. & Pople, J. A. Self—Consistent Molecular Orbital Methods. XII. Further Extensions of Gaussian—Type Basis Sets for Use in Molecular Orbital Studies of Organic Molecules. *J. Chem. Phys.* **56**, 2257-2261, doi:10.1063/1.1677527 (1972).
28. Petrone, A., Lingerfelt, D. B., Williams-Young, D. B. & Li, X. Ab Initio Transient Vibrational Spectral Analysis. *J Phys Chem Lett* **7**, 4501-4508, doi:10.1021/acs.jpclett.6b02292 (2016).
29. Petrone, A., Williams-Young, D. B., Lingerfelt, D. B. & Li, X. Ab Initio Excited-State Transient Raman Analysis. *J Phys Chem A* **121**, 3958-3965, doi:10.1021/acs.jpca.7b02905 (2017).